CONSTITUTIVE-BASED MASONRY VAULT MECHANISMS

by

Peter Alan Mallinder,

B.Eng. (Hons.), M.Phil., C.Eng., M.I.C.E.

97

A thesis submitted in partial fulfilment of the requirements of Sheffield Hallam University for the degree of Doctor of Philosophy.

ACKNOWLEDGEMENT

The author wishes to express his sincere appreciation and thanks to Dr. Neil Taylor, Director of Studies, for his help and guidance over many years, particularly with regard to the brittle hinge mechanics.

Appreciation is also expressed to Mr. D. A. Richardson for his contribution to the geotechnical experimentation, and also to messrs. Broadhurst, Pridmore, Draper and Soar for their invaluable assistance in the author's information technology studies.

ABSTRACT

(Peter Alan Mallinder)

Constitutive-based Masonry Vault Mechanisms

The objective of the research programme has been to investigate the behaviour of masonry arch vault collapse mechanisms in the context of the problems besetting the national bridge stock. The programme has primarily involved masonry constitutive theoretical studies, supported by laboratory experimentation, which have led to the formulation of novel masonry hinge modelling. The modelling has been developed for practical application in a four hinge masonry vault mechanism analysis and subjected to testing. The technique has been applied in the field supported by a novel application of information technology (IT) image processing, reflecting the growing importance of IT within the construction industry. All theoretical studies have been mounted as micro-computer software with graphics. The accent is upon engineering requirements in practice.

Chapter One reviews the context and history of the masonry vault structural form, whose presence has long been commonplace in the United Kingdom, especially on the nation's road network. It is noted that elderly arched road bridges are under continual pressure to carry ever greater loads yet their strength is uncertain. Historically, structural analysts have attempted to resolve the arch's behaviour but present methods are still inexact.

Chapter Two describes how, traditionally, masonry has been assumed to possess either a linear stress-strain property or infinite stiffness and strength. An alternative, novel equation for modelling masonry stress-strain laws is presented which may be configured to mimic the behaviour of real materials as well as that of the infinite strength and linear laws it replaces. A numerical analytical procedure has been developed to 'solve' rectangular masonry sections under combined bending and thrust thereby rendering the earlier approximations unnecessary.

Chapter Three develops the theme further leading to the numerical determination of limit state hinge characteristics which furnish a static limit state axial thrust/bending moment interaction diagram and a corresponding serviceability limit state, prevention of cracking interaction diagram. Differentiation is thus made possible between hitherto identically-treated though varying natural materials and comparisons made. It is further postulated that any point on a static limit state interaction diagram locus represents a masonry hinge and an extensive series of laboratory model hinge tests is undertaken to demonstrate the point by testing the foregoing theoretical studies.

Chapter Four describes the incorporation of the hinge theory into a mechanism-type computer analytical tool. Crucially, the analysis is different from other mechanism analyses by virtue of the hinge modelling, enabling the effects of material properties on arch behaviour to be studied. The software is tested in Chapter Five against prototype data for laboratory model and full size masonry bridges.

Chapter Six introduces computer vision, an IT technique that is relatively novel to the structures field. It is adapted to monitor the above laboratory model arch tests and then extended to the monitoring of a multi-span arch bridge test in the field. Computer vision permits the formulation of a hypothesis regarding the unusual mode of failure that occurred and this is supported by a generalisation of the mechanism hinge theory, thereby demonstrating the merits of both techniques. Finally, Chapter Seven draws conclusions on the foregoing and makes suggestions for further work. Supporting documentation is given in the Appendices.

CONTENTS

Title Page

FIGURES INDEX

Number	Title	Page
6.2	Structure topology for analysis of Railtrack Bridge number 124	158
6.3	Bridge number 124: statical analysis - 1	159
6.4	Bridge number 124: statical analysis - 2	160
6.5	Bridge number 124: statical analysis - 3	161

PLATES INDEX

TABLES INDEX

CHAPTER ONE

Introduction

"Few of man's inventions are more basic than the bridge. The oldest engineering work devised by man, it is the only one universally employed in his pre-civilised state."

Joseph Gies (Bridges and Men, 1963)

1.1 Context

Just as the bridge is the oldest engineering work known to man, the arch is, after the simple timber beam, the oldest form of bridge. It was conceived in pre-history and prevailed until modern times as a unique structural form. Its great virtue lay in its ability to span without the need for tensile materials. The art (for it was hardly a science) of arch exploitation reached a zenith in the middle ages with the construction of monumental cathedrals throughout Europe.

It was not until relatively recently that the world's first significant non-masonry bridge was built - the cast iron arch at Ironbridge, Staffordshire. Cast iron's lack of tensile strength initially ensured, just as masonry's did, that the arch shape was still necessary. However, the rapid progress of the industrial revolution warranted that by the beginning of the twentieth century the arch form itself was obsolescent, being gradually replaced by flat spans of reinforced and prestressed concrete, and of steel.

The durability of the masonry arch form is such that, despite virtually none having been built for sixty or more years (with a few recent notable exceptions[1,2,3]), as a group they still constitute the most numerous form of public road bridge in the United Kingdom. As such they form a key part of the nation's communications infrastructure with a substantial capital replacement value, justifying considerable effort in their proper care and maintenance[4].

This continuing abundance of masonry arch bridges gives rise to serious problems for several reasons[5]. First, they were not "designed" in the modern sense. Most were probably constructed without calculations to traditional proportions or "rules of thumb" that were known to give safe results. Second, records of their construction, especially internally, have rarely survived to the present day - if they ever existed. Third, the loading of the day consisted of no more than a laden horse and cart, a far cry from a modern forty or forty-four tonne multi-axle tractor unit and trailer. Fourth, they suffer inevitable and progressive deterioration accompanying old age. Despite their durability, large margin of strength (relative to the loads of their day) and low maintenance demand, they can and do eventually fail[6]. The modern emphasis is therefore the safe load assessment of existing old bridges subjected to modern traffic loads, rather than of design[7,8].

Figure 1.1 shows the continuing abundance of this structural type in the United Kingdom bridge stock, and gives some idea of the scale of the structural assessment task. As the predominant bridge type, the arch is therefore an important national asset and the need for a good analytical tool, which is sufficiently accurate to be neither wasteful nor unsafe, is clearly considerable. The mainstream analytical method of recent years, MEXE, has its origins in the work of Professor Pippard and dates from the 1930's. The method, which is based on Pippard's model experiments and is partly empirical, will be considered in some detail in section 1.3.2. later.

The scale of the problem is comparatively greater in the U.K., whose older bridges have survived in greater numbers by virtue of not having suffered the wartime ravages as have occurred elsewhere. It is further compounded by continually increasing traffic loads, both in terms of vehicle weights and numbers.

The structural type is extremely old and its presence commonplace. Plate 1.1 depicts an ancient United Kingdom example, and Plate 1.2 a more renowned but similarly ancient Italian counterpart. Until relatively recently, modern structural analysis had not been applied to such structures. It can be said that it was a surprise to many that the modern techniques initially only yielded relatively poor results. Faced with these problems the current interest in masonry arch analysis emerged, stimulated particularly by the Department of Transport nationally, although arch bridge ownership in fact extends through local highway authorities, Railtrack and British Waterways Board. Under this impetus the first contemporary research began including a series of full scale tests-to-destruction by the Transport Research Laboratory[9].

FIGURE 1.1

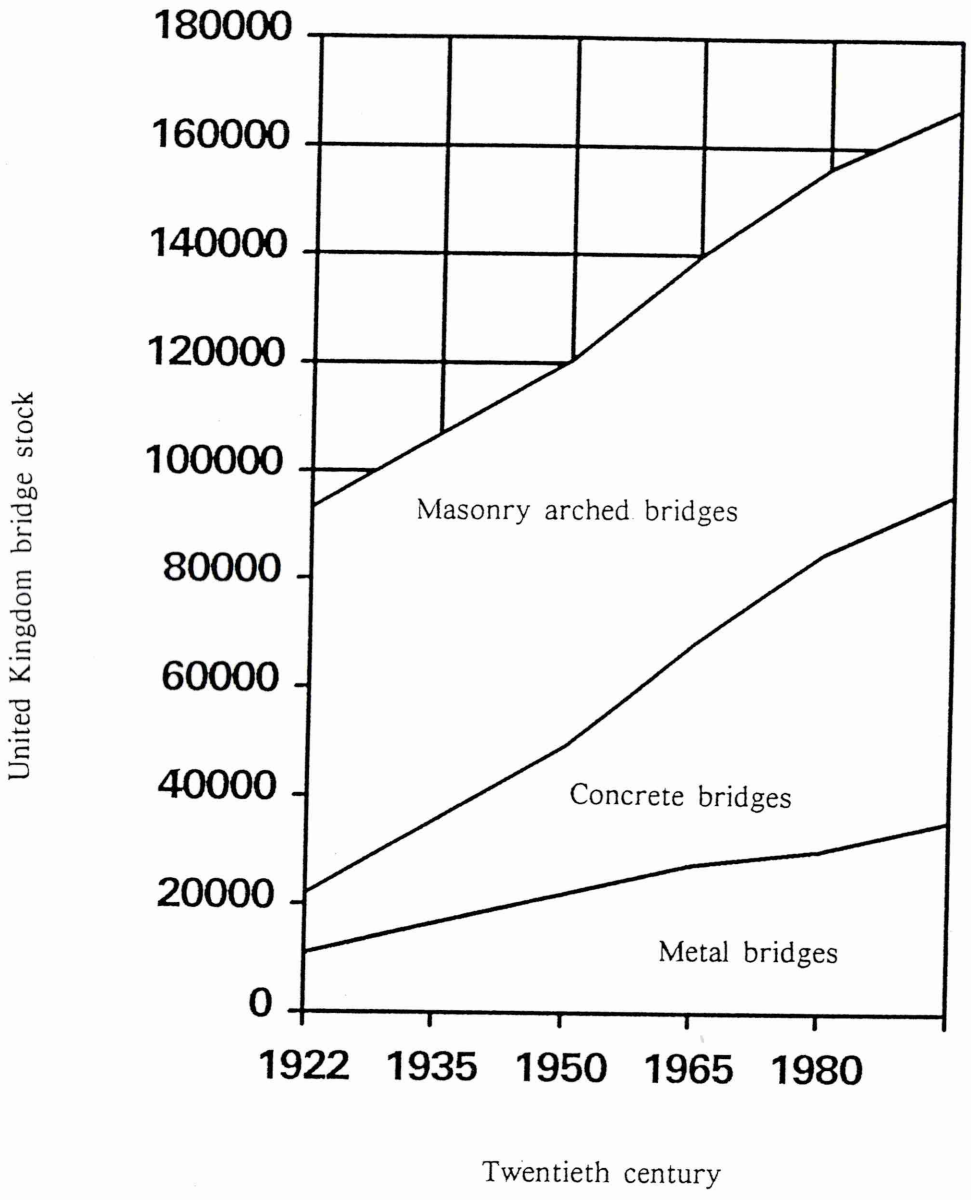

The United Kingdom bridge stock

PLATE 1.1

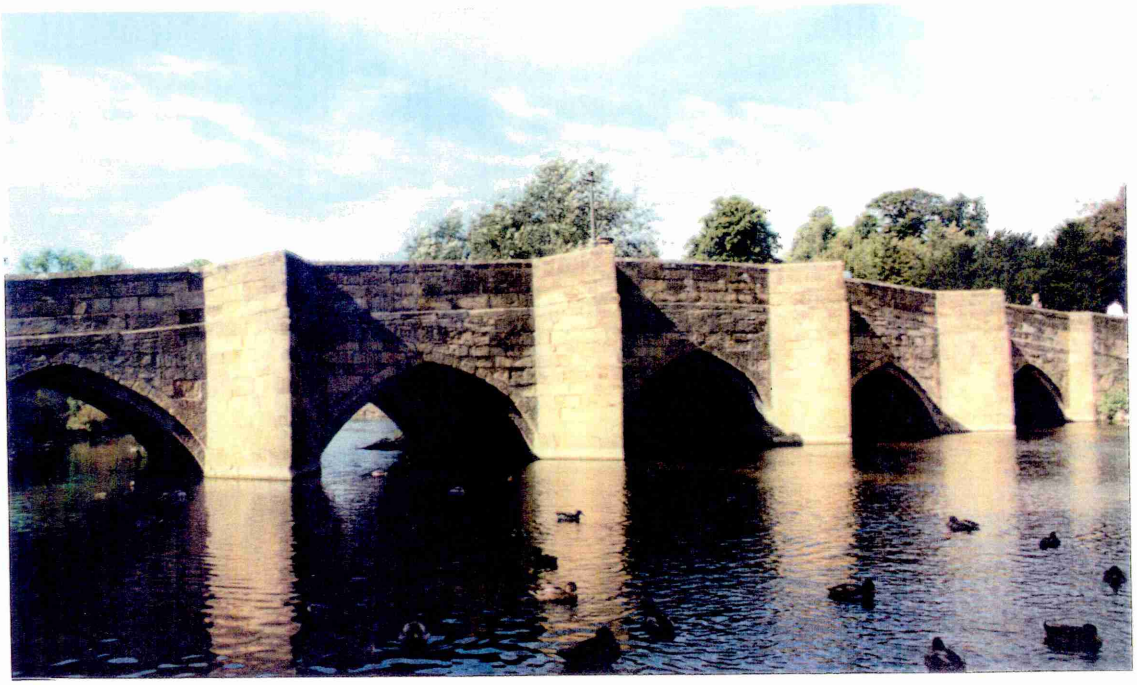

Reputedly the oldest bridge in Derbyshire
(Bakewell, United Kingdom)

PLATE 1.2

Ponte Vecchio (Florence, Italy)

There are two modern schools of thought vis-à-vis arch assessment. The first is termed "plastic", or more specifically mechanism analysis, chronologically at least, attributable to work by Professor Jacques Heyman[10,11,12] of Cambridge University.

This is a limit state approach and deems failure to occur in a doubly encastré single span when the last of four mechanistic "hinges" forms in the arch vault, reducing it to a mechanism and permitting collapse. Heyman's approach was to assume infinite compressive strength for the arch vault material, but others have developed the method (the "modified mechanism method") to allow a more realistic treatment[13].

Some full scale load tests-to-destruction exhibited a four hinge mechanistic failure mode; others do not. Even of those that do, the "prediction" of ultimate loads is often inexact, though factors other than vault strength modelling must have an influence.

The second school of thought is essentially concerned with elastic analysis and takes two forms. One is finite element analysis[14,15] and the second an arch thinning approach[16].

There have been several commercial linear analysis finite element packages available for some time, and a practicing engineer new to the masonry arch analysis field will often turn first to these. Unfortunately, arch behaviour is non-linear and such an approach is inappropriate. Non-linear finite element packages are now also available, but these too have limitations and the creation of a computer model for these one-off structures can be time consuming. Nevertheless, with the advent of cheap computing power, this may be where the future lies.

Observation of full scale and model arches, load tested to collapse, reveals several modes of failure. These include four hinge mechanisms, three hinge snap-throughs, material crushing beneath the live load, punching and even those that are ill-defined. Skewed arches are yet more complex in this respect[17,18]. The influencing factors generally will be geometrical and material as will the load type. Whilst broad categorisation of likely failure modes is possible, this nevertheless remains a difficult area in which to be precise. It is probable, however, that the four hinge mechanism is a common or even the most common mode[9].

It is noteworthy that contemporary arch research has been primarily directed towards the prediction of collapse loads, ie. the ultimate limit state, rather than service loads. It is true to say that the practising bridge engineer is more interested in the loads his

arch bridges *can* safely carry, rather than the loads they *cannot!* The apparently simple remedy of factoring down the collapse live load to arrive at a service load is credible (although the live/dead load ratio questions proportionality), but the appropriate factor is unknown and may vary from structure to structure. Elastic methods can provide a full load path history, but even then the criteria for defining a service level therein are largely unresearched.

Obvious serviceability limit state candidates exist, such as the onset of tension or the first hinge. The former is somewhat out of date but many would find the latter acceptable, assuming that hinge formation is accompanied by material degradation. However, consider what happens when the centering beneath a newly constructed arch is struck - on taking up its self weight for the first time, the arch suffers elastic shortening and its abutments, similarly loaded for the first time, settle and spread slightly. The arch can only accomodate the increased span by forming hinges, say at the springings and around midspan. The scenario that in-service arches may be naturally two or three pinned from new casts doubt on the "first hinge" serviceability limit proposition.

Such is the background to the author's research programme, and the problem is this. The large stock of old arch bridges must be structurally assessed for its ability to carry ever-increasing modern traffic loads. Currently this is done by applying a method - MEXE - which dates from before the second world war, and which may be both nonconservative and uneconomically conservative under certain circumstances[19,20]. Alternative assessment methods are permitted, but these also possess both merits and drawbacks, and none is acceptable in all circumstances. The elastic methods require knowledge of material properties which are difficult to obtain, but do provide a load path history and allow for abutment movement. Plastic methods say nothing of behaviour before failure and need an allowance for arch-fill interaction in deep arches. Thus none of the currently available methods, historical nor contemporary, is universally applicable nor sufficiently dependable.

This thesis aims to contribute to knowledge in the following areas. First, a theoretical study of masonry's fundamental properties has been undertaken; this attempts to minimise the problems associated with (natural) material variability. Second, a refinement of the "plastic" analysis has been developed which obviates the non-conservative infinite compressive strength assumption by employing appropriate masonry properties. Computer software has been developed to automate this procedure and to provide an ultimate load prediction. Third, information technology (IT) techniques have been investigated in the monitoring of laboratory model and field

arch tests to destruction and have cast light on modes of failure, both qualitatively and quantitatively.

The analytical developments have been supported by a variety of model, full scale and computer vision information technology studies, the latter being an innovative technique offering insights into arch behaviour. Throughout, attention is focused upon non-skewed single span forms with non-laminated arch vaults. The intention is to contribute to the ongoing expansion in the database of masonry vault knowledge.

1.2 The Arch Form

The Romans constructed the first proper roads and bridges in the British Isles but of the latter only piers and foundations have survived. The oldest surviving British bridges are mediæval arched river crossings. A few of these date from the 12th century but thereafter increasing numbers of arch bridges survive up to the end of the nineteenth century, and there are some dating from the early twentieth century.

As a construction material, bricks were used by the Romans but were not used again until their re-introduction in the 13th century. The earliest examples of arch bridges in Britain are therefore invariably of stone.

The Romans built semi-circular arches (Plate 1.3) in the mistaken belief that only vertical reactions would occur. However, the most common arch profile is still segmental, though not necessarily semi-circular. Until the 15th century the pointed style was common, a product of the gothic school of architecture and thought to have originated to mimic in stone the even earlier "crucked" timber arch, whereby two curved timbers, or crucks, are leant together. Many fine examples of gothic mediæval architecture still exist. One of the most striking in the U. K. is York Minster - the largest gothic building in Europe and widely considered to be one of the master works of western architecture. As might be expected, the shape of the gothic arch was more æsthetic than structurally efficient, with the result that many arches collapsed on removal of the centering. Figure 1.2 compares some typical arch profiles.

The sheer diversity of the application of the masonry arch form is remarkable, and the plates in this chapter show some disparate examples. Aside from arched bridges carrying vehicular and pedestrian traffic, the form has been employed in a "domestic"

PLATE 1.3

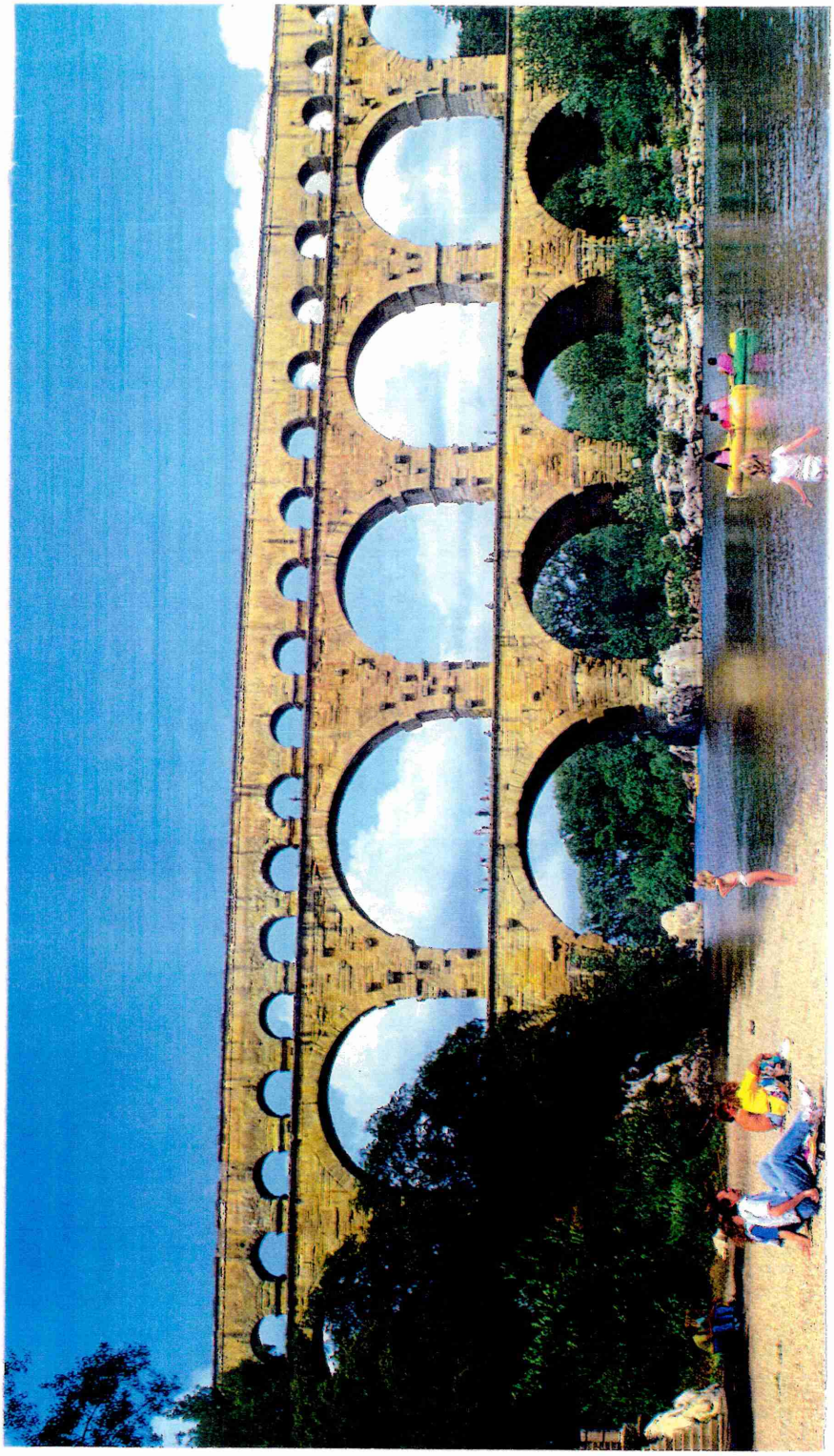

Roman aqueduct (France)

FIGURE 1.2

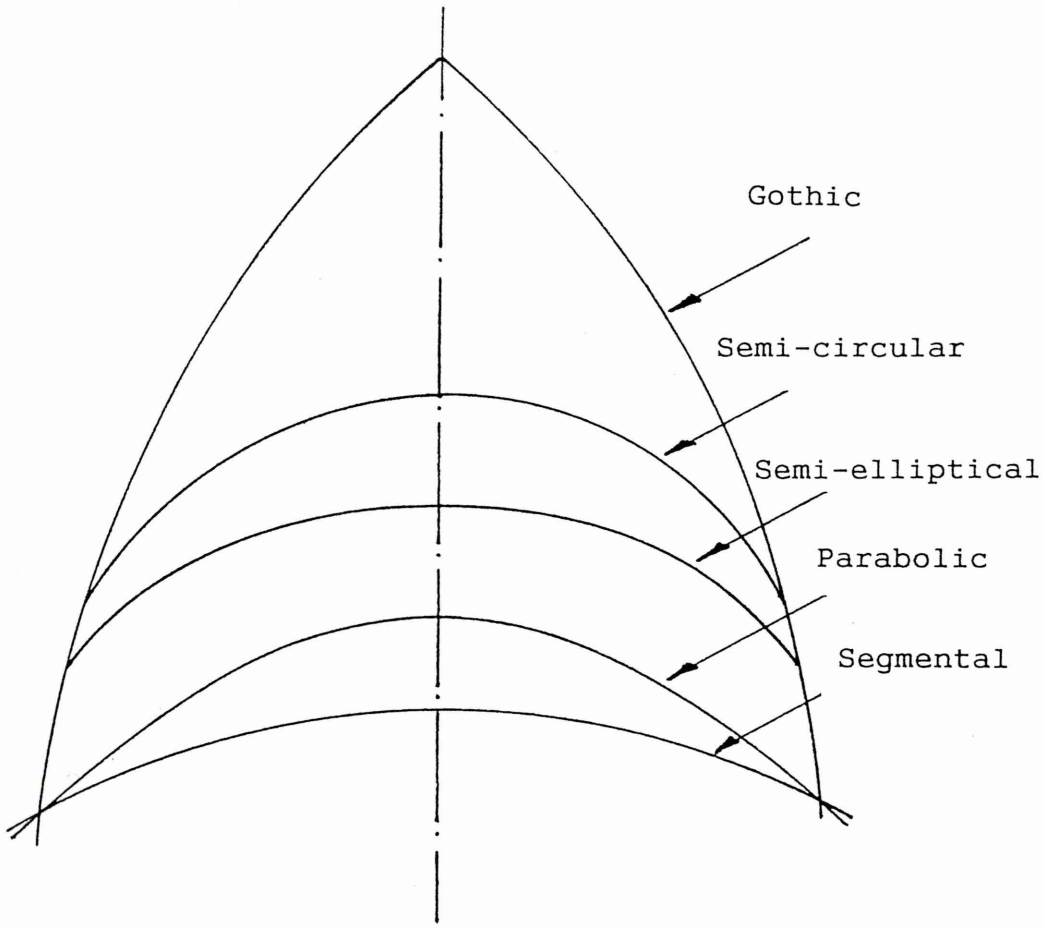

Typical arch profiles

capacity - shown to sublime effect in Plate 1.4, and in contrasting rudimentary fashion in Plate 1.5 It can even be naturally occurring, as two of the plates show. The scale of the task in understanding its behaviour in all its forms is immense - some of the arches illustrated could be regarded as structural types in their own right, only coming under the same generic heading by virtue of being compression only structures with curved thrust lines.

A further development of the arch principle is the dome. This is effectively a three dimensional arch, and rather than needing strong abutments to resist the horizontal thrust, a dome requires a continuous ring beam acting in tension around its base. The object of the present study is, however, to consider arches in their more common form, particularly in their application to bridges.

Figure 1.3 identifies the main structural components of an arch bridge. The fundamental working component is the ring, barrel or vault, composed of discrete masonry blocks called voussoirs, be they of stone or of brick, cemented together in a curved plane. The term "voussoir" is French - many of the early arch studies were conducted by the French and hence many of the terms are of that language. The cement between the voussoirs is not essential for strength, but it does provide a bedding between adjacent members to eliminate point contacts. It also provides a degree of tensile strength, though this may not be reliable and is usually ignored.

Crucially, the arch vault or ring is a *compression only* structural member, and indeed it was the advent of materials possessing tensile strength that heralded the end of the masonry arch.

A layer of fill material is provided over the arch vault giving a level surface for the passage of traffic. There may be, in some instances, a waterproofing membrane at the interface between the arch and the fill. Good fill material is inert and incompressible. In practice it is often of lesser quality. In addition to levelling up the top of the structure, it fulfils a second but vital role in providing permanent dead load to the arch.

To non-engineers, adding more (heavy) fill to increase the arch's strength is counter-intuitive. Up to a point, the more self-weight an arch possesses the better, and the more traffic it can safely carry. This is contrary to the needs of other bridge types. It arises because increasing dead load leads to more pre-compression in the arch vault, in much the same way as steel tendons provide pre-compression in a prestressed or post-tensioned concrete beam, and thus the arch is better able to resist

PLATE 1.4

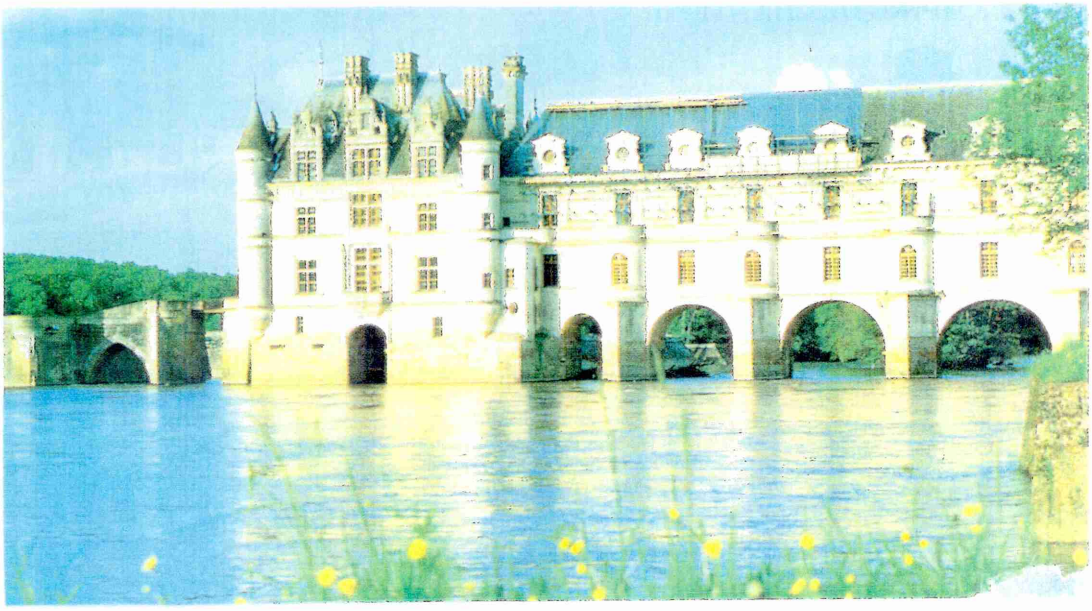

Chateau Chenonceau (Loire, France)

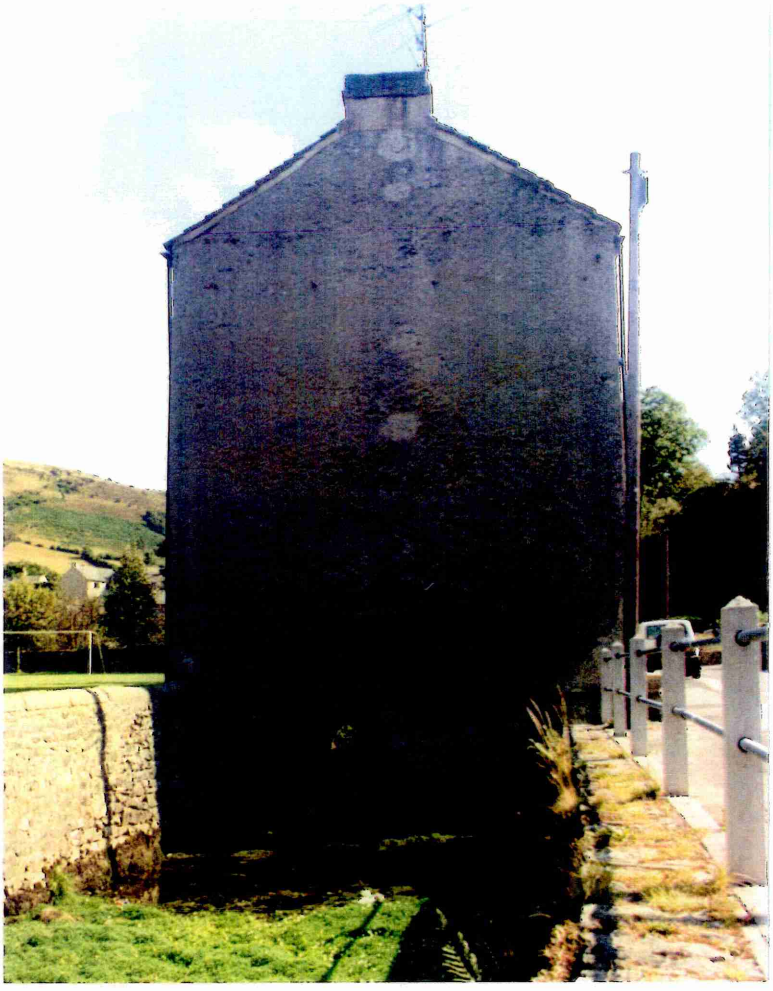

PLATE 1.5

Dwelling built over arch bridge (Derbyshire, United Kingdom)

FIGURE 1.3

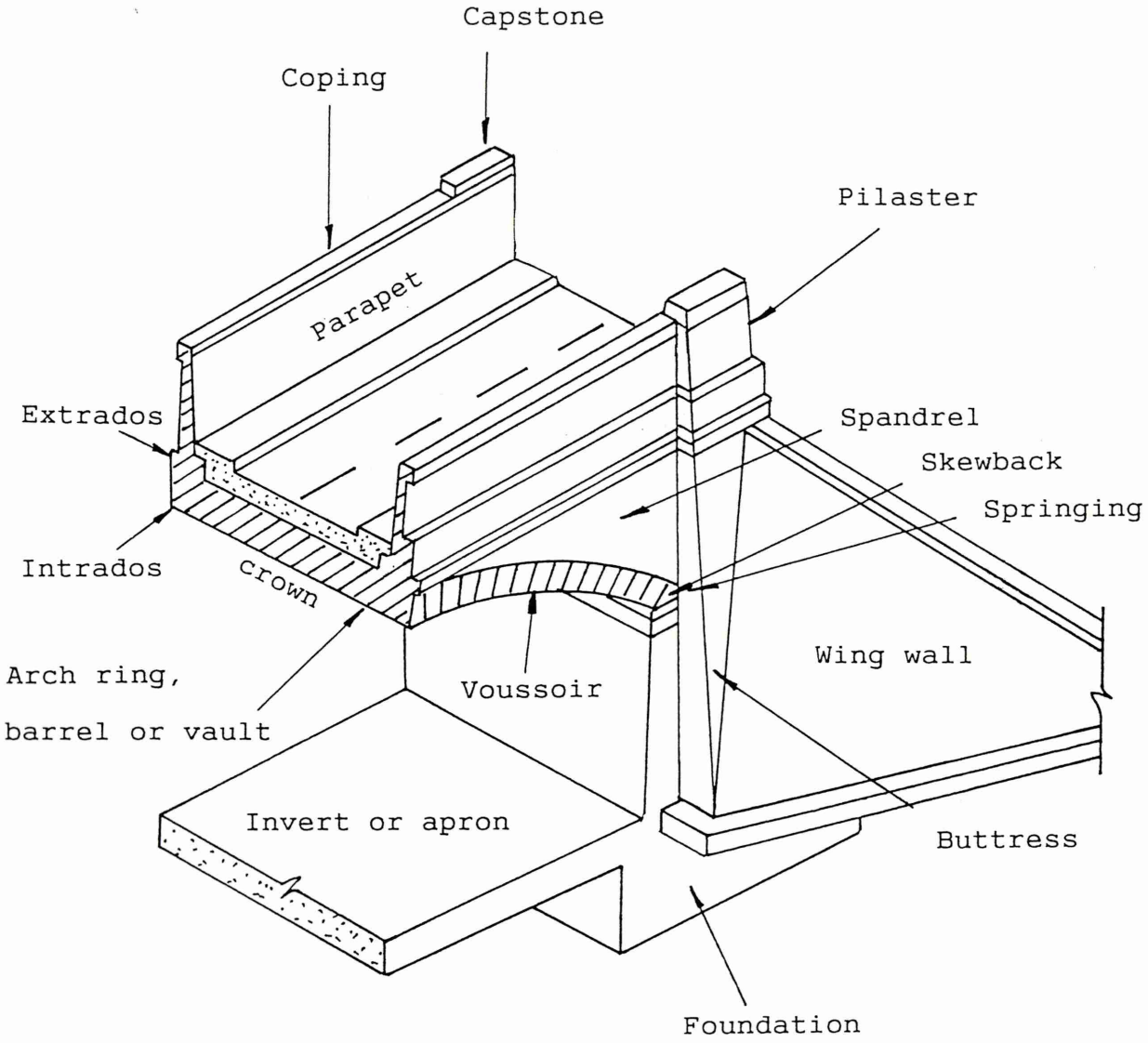

Masonry arch terminology

live load bending. With a prestressed beam, however, limiting compression or tension in the extreme fibres is quickly reached, but the massive cross sectional area of most arches provides comparatively greater scope for pre-compression.

There is yet a third benefit in deep fill. It serves to disperse live loads applied at deck level such that by the time they impinge upon the arch vault, they have become distributed. All structures find point loads more onerous than distributed loads of the same magnitude, and this is especially true of arches, the explanation again being somewhat counter intuitive. For a simple, symmetrical beam, the critical loading position for bending is midspan. Conversely, the critical position for arch bending is around quarter span[12], depending upon the span to rise ratio.

In the case of an arch with deep fill, if a load is applied at one quarter point, distribution through the fill will shed load elsewhere - itself an aid - but in fact load may even be shed to the opposite side of the crown, where it will act as an opposing, restoring force.

To properly fulfil its rôle, the fill material must be contained at the sides of the arch, and this is the function of the spandrel walls which sit astride the edges of the arch vault. They (debatably) also stiffen the edges of the vault, but in practice they can tilt, slide, rotate or split from the vault under the effect of lateral forces (and in doing so allow the fill to rut and settle), and partly as a consequence it may be unwise to rely on any theoretical strength contribution they may provide.

The final key component on an arch bridge is the abutment. All arch vaults (even Roman ones) gain part of their support from large horizontal reactions against the abutments. The flatter the arch, the greater the horizontal component. When constructed on ground that is less than ideal, the abutments may spread on removal of the centering. This gives rise to theories that the natural state of a masonry arch is in fact three pinned, this being the only way the new arch, theoretically encastré, can accommodate the increased span between its abutments.

The basic masonry arch system described may be further complicated by a number of additional factors. One of these is skew, which not only presents problems of setting out for the arch builder but also of analysis. A second problematical subject area is the behaviour of multi-ring brickwork arches[21], which raise their own questions concerning the degree of composite action between the rings (a likely function of the brick bonding adopted) and the practical problem of de-lamination between rings whilst in service.

Plate 1.6 illustrates a further type for the analyst to consider - an arch with pierced spandrels, a rare variant. Plate 1.7 depicts the *flat* arch - the curvature of the main structural member not being necessary, only that of the thrust line.

It is not the intention of this thesis to consider any of the above extensions of the fundamental issue of right, single span, voussoir masonry vaults.

The main structural elements of a masonry arch are simple to describe. They can be designed without calculation, constructed at worst by unskilled labour, and fashioned from apparently unsophisticated materials. Nevertheless, the non-linear behaviour of the resulting deceptively simple structure, and the way in which its basic components interact, gives rise to a system that is extremely complex.

1.3 Historical Overview

1.3.1 Pre-20th century observers

In the year 1676 Hooke propounded the first theory of arch mechanics. He drew an analogy between a flexible hanging catenary and a rigid inverted catenary. It was left to Gregory in 1697 to develop the postulation that an arch would only be "safe" if an inverted catenary could be included within its thickness.

La Hire (1695) was the next to address the problem. By constructing a force polygon for the individual voussoir weights he was able to determine the thrust in an arch. As a result of this he was better able to design adequate abutments to resist this thrust.

Couplet's memoir of 1730 stated that an arch would not collapse if the chord of half the extrados did not cut the intrados but lay within the thickness of the arch. He then examined the semi-circular arch subject to self-weight only and assumed that it collapsed by breaking into four pieces. He developed a cubic equation relating the ratio of arch depth, d, to the mean radius, r, and postulated that the minimum value of the ratio d/r was 0.107. Unfortunately, Couplet's work was forgotten but later much of the same ground was covered by Coulomb.

In the year 1800 Boistard tested a series of model arches featuring dry-jointed voussoirs. One of the models tested was of the very shallow Pont de Nemours, possessing a span to rise ratio of no less than sixteen. Boistard observed models of

PLATE 1.6

Masonry viaduct with pierced spandrels (France)

PLATE 1.7

Flat arch (Split, former Yugoslavia)

failure under various load conditions to determine minimum abutment requirements for resisting horizontal arch thrust, and to obtain an estimate of forces applied to centering during construction. During one of his tests on a semi-circular arch of forty eight voussoirs he observed that it was possible to construct the arch almost up to the quarter span points without the need for centering. This ability of semi-circular arches to support themselves may quite possibly have been used by the Romans and other arch builders of antiquity.

In 1826 Navier was the first to suggest that if the line of thrust lay within the middle third of the voussoirs then none of the arch would be in tension. Following this, Professor Moseley showed in 1835 that, if the arch was unable to resist tension, the line of thrust must lie everywhere within the arch ring. Later, in 1846, Snell was able to raise the question of the possibility of material failure affecting the position of the line of thrust.

Still in 1846, Barlow[22] demonstrated, by means of an ingenious model, that Moseley must be correct. The model employed voussoirs with curved contact faces, such that only one contact point was possible. When loaded, the voussoirs "rolled" against each other until equilibrium was reached whereupon the line of thrust could be observed through the points of contact. Barlow pointed out that, provided the arch was sufficienty deep to contain the thrust line, then many thrust lines were possible. He also raised the important point that, because the assumptions of infinite compressive strength and perfect joints were unrealistic, then the lines of thrust must not be allowed to approach the edges of the arch ring. This latter observation is highly pertinent to the later work of Professor Heyman and mechanism analysis.

In 1845 Villarceau presented a treatise to the Academie des Sciences, France, in which he developed a design method which required the centre of the voussoirs to coincide with one of the possible thrust lines for the load condition, thereby achieving a safe design. By solving the resulting numerical equations, Villarceau produced the first definite design tool. In recent times Professor Heyman has suggested that the work of Villarceau is still valid and would result in an economical and safe design.

In 1879 Castigliano[23] developed the concept of structural analysis by the elastic strain energy method and was to apply this technique to two bridges, one of them the Rialto bridge which still crosses the Grand Canal in that city today.

With the gradual introduction of new materials such as cast and wrought iron during the nineteenth century, however, the era of the masonry arch was drawing to a close

and with it much of the interest in arch mechanics. Interest would eventually be rekindled in the 20th century, but it would initially centre upon the *analysis* of those old arches for modern day loads. Interest in new arch *construction* has only recently emerged[24,25], and this may herald a new era for this durable form of bridge in locations where the headroom limitations it imposes permits its use.

1.3.2 Professor Pippard and the MEXE method

In the 1930's Professor Pippard[26] conducted model experiments and analyses that were to form the basis of arch assessment for the next sixty years. What became known as the "MEXE" method had its origins in this work, and as it has become the Department of Transport's recommended approach[19,20], Pippard will be considered in some detail.

Pippard limited his attention to the case of a two-pinned arch, since, he contended, although constructed as a doubly encastre rib, hinges may form at the abutments very early in its life due to slight spreading under load. Furthermore, he was only to consider arches of a parabolic profile with a quarter point rise to crown rise of 3 to 4. The load considered was a simple central point load. The topology is illustrated in Figure 1.4. Analysis of this singly redundant system was based on strain energy, (remembering Castigliano's "elastic" work) thus:

Let M_X denote the bending moment at abscissa x, then the strain energy, U, may be given as

$$U = 2\int_0^{\frac{1}{2}} \frac{M_X^2 \, ds}{2EI} \tag{1.1}$$

where ds denotes an element of arc length of arch ring, EI refers to flexural rigidity and H denotes the horizontal reaction.

H can be evaluated employing the principle that dU/dH = 0, if H does no work, such that

$$\int_0^{\frac{1}{2}} \frac{M_X \, dM_X \, ds}{EI \, dH} = 0 \tag{1.2}$$

To effect a simplification, Pippard adopted the relationship

$$I = \frac{Io \, ds}{dx} \tag{1.3}$$

FIGURE 1.4

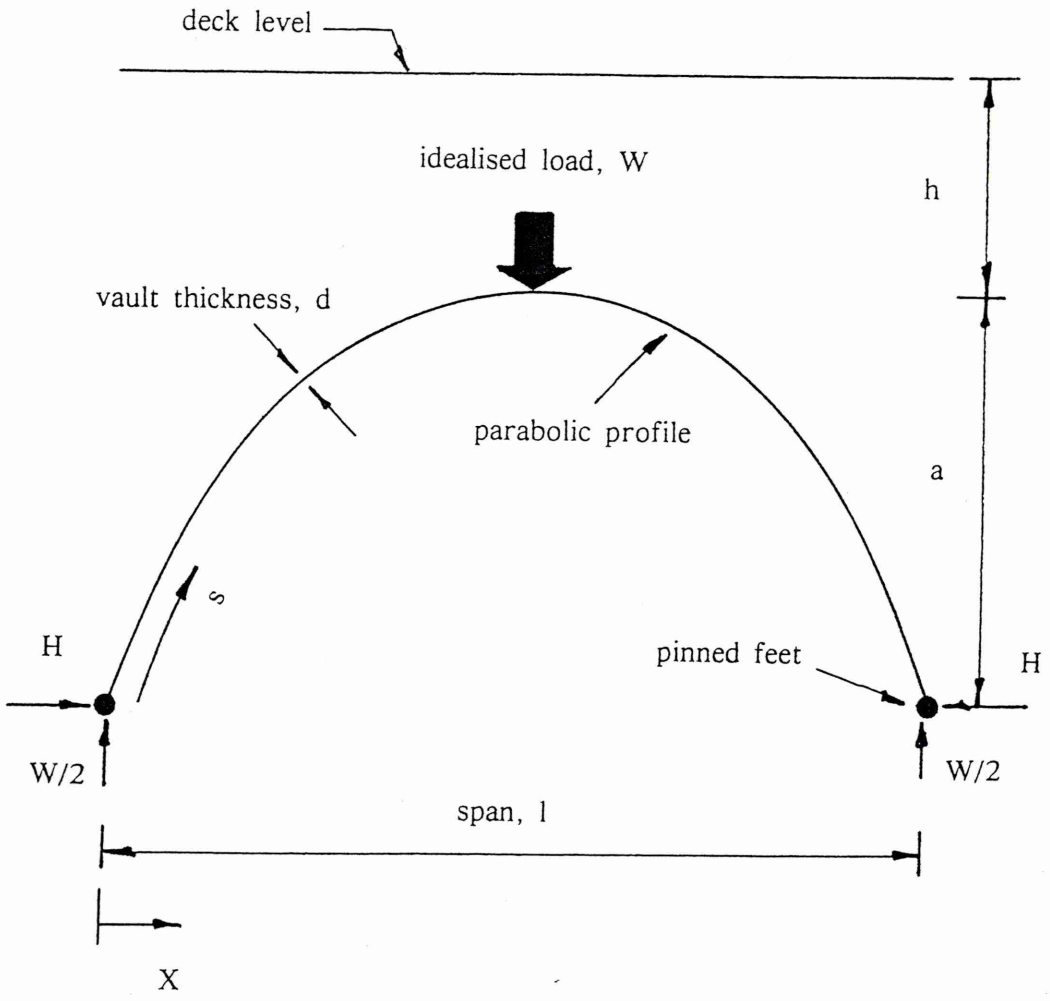

Pippard's elastic analysis

where I represents the second moment of area of the arch ring at x, and Io the same at the crown (Figure 1.4); this implies that the arch ring thickness increases towards the springings.

After manipulation, Pippard showed that the bending moment at the crown due to live load, M_l, became

$$M_l = \frac{-7Wl}{128} \tag{1.4}$$

On to this must be superimposed the corresponding value arising from the dead loads due to the arch ring and its fill. Pippard assumed that the effective width of the bridge was 2h, suggesting a 45° live load dispersal at the crown. He furthermore assumed that the arch ring and fill have equivalent specific weights (denoted by ρ), with the fill possessing zero strength, thereby imposing a purely vertical load on the arch ring. A second strain energy analysis provided the bending moment at the crown, M_d, due to dead load thus

$$M_d = \frac{\rho l^2 ah}{168} \tag{1.5}$$

Live and dead load effects were superimposed and Pippard went on to suggest two possible limiting criteria. As W increases, either,

a) the thrust line at the crown rises and tension develops, this tension being limited by a "middle half" rule such that

$$W_{\text{limiting tension}} = \frac{32\rho lh(2a^2+4ad+2ld(h+d))}{21(28a-25d)} \tag{1.6}$$

b) or it may be instead that a certain limiting value of compressive stress, f, is reached, whereupon

$$W_{\text{limiting compression}} = \frac{256fhd}{l\{\frac{25}{a}+\frac{42}{d}\}} + \frac{128\rho lh\{\frac{a}{28d}-\frac{1}{2l}-\frac{h+d}{4a}\}}{\frac{25}{a}+\frac{42}{d}} \tag{1.7}$$

Pippard then drew upon his experimental work to conclude that the former approach (the "middle half") is most appropriate. Based upon this work, Pippard was later to produce safe load tables for arches. By assuming a parabolic profile with a span to rise ratio of four and knowing the span, the arch ring thickness and the depth of

cover to the crown, together with values for the arch ring and fill specific weights, it was possible to read off the maximum possible safe central point load from the tables.

During World War II it became necessary to route heavy military traffic, such as tanks, over public road bridges. Especially in times of emergency, a simple and quick means of estimating arch bridge carrying capacity was required. The Military Engineering Experimental Establishment (MEXE) consequently developed a technique based on Pippard's work. After the war, the MEXE method, as it has come to be known, was adopted by the Department of Transport and by this stage it had developed into a nomogram, modified by subjective arch condition factors, to evaluate its "mathematical" component. (It is interesting to note its basis on a two pinned, parabolic arch with a central point load. The analysis is elastic, concerned purely with flexure and provides a serviceability limit by applying a factor of safety to stress).

MEXE is quick and simple to apply, a desirable prerequisite considering the large number of arch bridges needing assessment. It initially enables a "provisional axle load" (PAL) to be calculated from data on the span and arch plus fill thickness at the crown. This is then modified by a seies of factors that are intended to compensate for differences between the ideal arch and the one in question. They correct for span to rise ratios other than 4:1; for the shape of the arch; the type of arch; the type of fill; joint condition and overall condition. The resulting "modified axle load" (MAL) now represents a permissible axle load for a two-axled bogie. The permissible axle load for single and tri-axles may also be derived from the MAL, with compensatory allowances made for axle "lift off" in hump back bridge or surface irregularity situations. It cannot deal properly with skew nor with multi-span bridges, unless the individual spans do not interact.

The engineer will compare the MAL with the range of Construction and Use Regulations (1968)[27] vehicle loading configurations currently permitted, plus, possibly, some assessment of the arch's capacity to carry abnormal vehicle (HB) loading. If found wanting, the engineer has a range of both temporary and permanent measures to apply.

The MEXE method was issued to local authorities in various memoranda over the years, the current version being BD 21/93[19] with its accompanying advice note, BA 16/93[20]. They recommended MEXE as suitable for preliminary assessment, and if the arch "passes", no further consideration is necessary. However, if revealed to be inadequate, the result must be confirmed by a more rigorous method.

It will be noted that MEXE has a significant subjective element, although the memoranda do give guidance (including photographs). Nevertheless, in practice anomalous results can emerge, such as the possibility of "failed" bridges being brought back to full a C&U rating by, as MEXE would indicate, repointing the mortar joints or applying a further few millimetres of fill over the crown. In such circumstances engineering judgement must be exercised.

There is debate regarding whether MEXE is conservative or unsafe. It was traditionally regarded as over-conservative and therefore wasteful in terms of repair costs - hence in part the Department of Transport's interest in the subject over the last ten or more years. A relatively recent result of this debate is that if the depth of fill at the crown is greater than the thickness of the arch vault, then the result should again be confirmed by an alternative method, as there is the possibility that MEXE may be unconservative. This is because the vault thickness does not itself enter directly into the calculation, only the sum of vault thickness and cover (ie. d+h). Consequently an extremely thin arch with a great deal of cover, and a thick arch with little cover may be indicated as having similar strength, which is obviously irrational.

Despite its shortcomings and recent reservations regarding its safety, it must be said that as a rudimentary device, originating sixty years ago, MEXE has served remarkably well.

1.4 Modern Practice

1.4.1 Professor Heyman and the mechanism method

Professor Heyman[12] observes that the "plastic" analysis of arches predates elastic methods. The mechanism method is often termed "plastic", and this may seem strange considering that the structural material, masonry, is brittle, does not develop a yield surface and possesses little tensile strength, unlike structural steelwork in which field the term is usually employed. Plastic methods do not provide a load path history. Note that MEXE, with its origins in Pippard's work, is by contrast an elastic method.

Heyman's basic premise is that the arch is doubly encastré (unlike Pippard's two pinned assumption) and that failure occurs upon the formation of a fourth and final plastic hinge. This renders the arch a mechanism, allowing all four hinges to rotate to

collapse. It is thus an ultimate limit state approach, again in contrast to MEXE which provides a serviceability limit state.

Heyman makes the following assumptions:

1. The masonry is infinitely strong in compresssion, or the stress levels are so low that compression failure is unlikely.
2. The masonry has no tensile strength.
3. Shear failure (the sliding of one voussoir past another) is unlikely.
4. Live loads are transmitted from deck level to extrados without dispersal.

Of course, the first asumption is non-conservative, but more reasonable than it might at first appear. It implies that the thrust line can approach the very edge of the voussoirs before failure occurs. The effect will be to overestimate the ultimate strength of the arch by an unquantified amount.

Other commentators in the field make approximations with stress blocks of various shape and permissible stresses. Heyman himself neatly avoids the issue by requiring a "geometrical factor of safety" (GFS) of two - in other words limiting the thrust line to the middle half of the section. This masks the approximation and the true GFS will be rather less than two.

A benefit of the approach is that knowledge of the material's strength is not needed. A drawback is that it says nothing of the load path history. Both points are in contrast to elastic techniques.

Heyman's second assumption of zero tensile strength is also untrue, but a common and conservative one in masonry mechanics[28,29]. Any proponent of utilising masonry tensile strength in analysis should beware, as in-service arches may contain imperfections which would render any tensile capacity most unreliable.

The third asssumption concerning shear failure is borne out by observation of both model and full-scale tests. Local punching shear failure is, however, quite common, but usually only where traffic loads bear upon a large piece of rock fill over the crown or perhaps a public utility pipe or duct bears directly on the extrados. It is certainly quite common for individual pieces of masonry to protrude downwards or to fall out completely[30].

To ignore load dispersal through the fill (the fourth assumption) appears sweeping. However, the behaviour of the fill material, and its interaction with the arch ring, is a complex area in its own right[31] and a categorical contradiction of the assumption is impossible given the present state of knowledge. Research to date is not especially conclusive, and it has been suggested that the amount of dispersal changes with increasing load[32], becoming more focused (ie. less dispersed) towards collapse. Heyman's fourth assumption is conservative.

In the analysis proper, Heyman divides the structure into a series of vertical slices and applies the weight of each slice to the corresponding element of arch ring below. The live loading is applied as one or more point loads directly to the arch, and the thrust line computed using a geometrical method. Failure of the arch is deemed to occur when the thrust line touches the extremities (or factored extremities in the modified method) of the arch ring in four positions. Each position is a potential "plastic" hinge.

It is to be noted that a further, not explicitly stated, assumption is the starting condition of a doubly encastré arch, in marked contrast to Pippard's (and therefore MEXE's) initial two-pinned topology. What is equally noteworthy is that opinion on the matter of the natural state of an arch is still divided today!

Figure 1.5 depicts the salient features of the system topology employed by Heyman, and Figure 1.6 the later so-called "modified" mechanism which crudely allows for finite compressive strength.

The GFS is an unfamiliar concept to most engineers, and is it not the same as the usual "factor of safety". Under limit state design, partial factors of safety are employed but the overall factor for a structure is about two. Foundation design is a less certain science and an overall factor of safety of about three normally applies. Heyman's recommended nominal GFS of two would seem to imply a degree of accuracy but in fact the live load on a typical arch with a GFS of two would need to be approximately quadrupled (not doubled) to cause collapse. Thus the overall factor of safety in a more common sense is about four, and this properly reflects the true level of uncertainty.

Other authorities and individuals have developed their own mechanism-type analyses[13], usually computerised, and with varying details. Generally the method gives good results under appropriate circumstances, but the variety of arch configurations is large and the basic method can be inaccurate or even inapplicable.

FIGURE 1.5

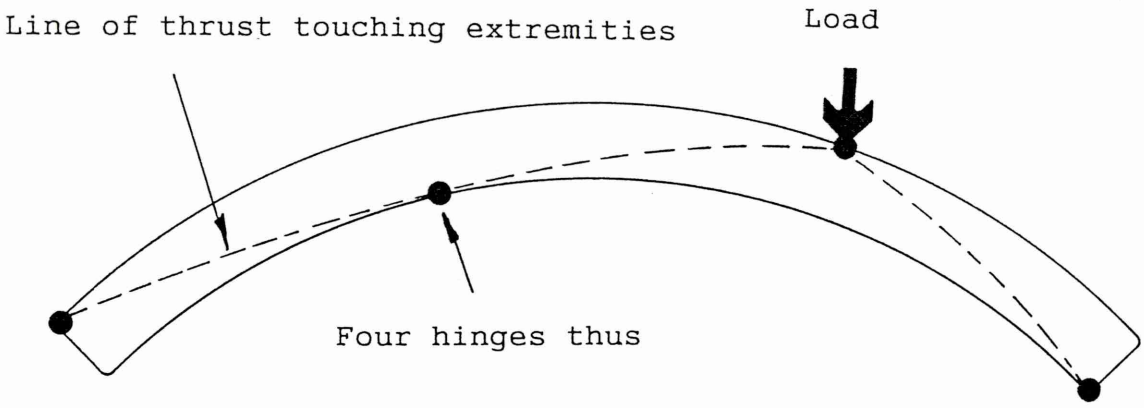

Heyman mechanism

FIGURE 1.6

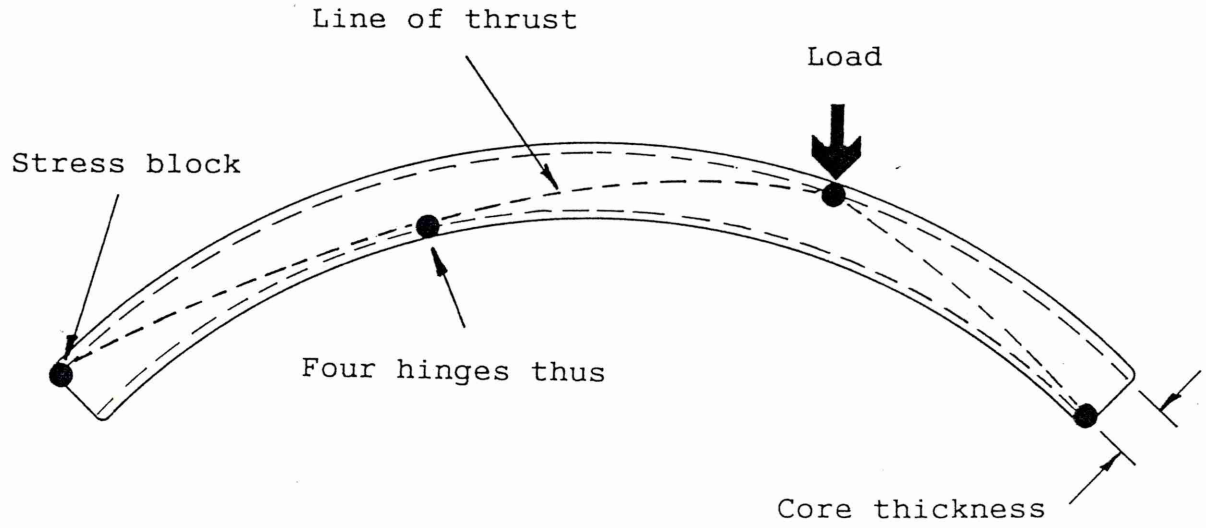

Modified mechanism

For instance, skewed structures are immediately inappropriate; deep fill or low span to rise ratio structures may not fail as a mechanism, and arch-fill interaction, stiff spandrel walls and lumpy fill (ie. boulders) can all lead to large inaccuracies.

Despite the shortcomings, mechanism analysis is often the best currently available but should be seen as one tool in an incomplete kit. Three commercially available mechanism analysis programmes are known to exist; Archie, Assarc and Arch.

1.4.2 Finite element analysis

This modern approach employs a formal non-linear structural analysis procedure applicable throughout the loading regime. It allows for the complexities associated with the lack of tensile strength and crack propagation. Two of the earliest finite element programmes written were by Dr. Crisfield[14] of the Transport Research Laboratory, and Professor Sawko and Mr. Towler[33,34] of Liverpool University and these will be briefly described.

Crisfield's programme was a development of earlier work for the analysis of thin shells. He validated the programme against a published theoretical study due to the aforementioned Sawko and Towler. The study took the form of the application of various alternative analytical techniques (MEXE, Pippard, Heyman and Sawko/Towler) to a series of hypothetical arch bridges. Crisfield adds both his 10 and 20 element model results to the others. A striking observation is the very wide scatter of ultimate loads, ranging from 63 kN by Heyman to 119 kN by Sawko and Towler, with Crisfield between. As the structure under study was purely theoretical, however, little can be said of the programme's accuracy other than it gave a broadly similar result to that of other analyses.

Crisfield also applied his programme to the full scale arch bridge test at Bridgemill, Girvan. It gave ultimate load values ranging from 1500 to 2700 kN, against a true figure in excess of 3100 kN. These are fair results, but the method offered no advantage over others that are simpler to apply.

The second finite element programme, due to Sawko and Towler, was novel in so far as it incorporated parabolic modelling for the stress strain characteristic of the arch vault material. This non-linear relationship was becoming accepted at the time largely due to the work of Hodgkinson and Powell who were working in the field of brickwork. Further development of the non-linear material response forms a later part of this thesis.

Sawko and Towler constructed four, four metre span brick arches in the Laboratories of Liverpool University and loaded these both to "serviceability" and to destruction. A résumé of the results was published in the Proceedings of the 6th International Brick Masonry Conference, Rome, 1982. The finite element programme appears to give quite good results for the two model arches tested to collapse, giving results within -13% and +21% of the actual collapse values. However, the results quoted are very wide of the mark in respect of the serviceability tests, although the nature and criteria for these tests are not described.

A final point regarding Sawko and Towler's series of model tests is that the arch vaults were tested in a "pure" form, uncomplicated by load dispersal through fill, arch-fill interaction or edge stiffening effects due to spandrel walls. The results are therefore useful in assessing software which takes no account of the latter effects and because of this their data is used later in this thesis.

Over recent years other finite element programmes have been written, but to date only one is commercially available, MAFEA, which has been written by British Rail Research. This programme is non-linear with automatic mesh generation, and defects and haunching can be modelled.

Recent non-commercially available programmes include those written by Nottingham University. One of these is three dimensional and employs 8-noded shell elements. It has been used, rather ironically, to provide guidance to practicing engineers on the effects of cracking in the arch vault, thus enabling the engineer choose a more rational condition factor for input to MEXE!

1.4.3 Thinning elastic method

Castigliano[23] derived an elastic analysis which permitted no tension in the arch vault. A similarly based computer programme has been developed by Hughes, Bridle and Vilnay[16] at the University of Cardiff, Wales. It utilises a strain energy elastic analysis coupled to a no-tension model of the section. The model idealises the arch as a curved beam, simulating the effects of arch cracking, soil pressures and geometry changes. The programme proceeds to remove or "thin" the arch vault on successive iterations, removing those portions in tension. The load is carried in compression by the remaining masonry.

It claims to provide information on cracking, stresses, shear and axial forces, and deflections at design or ultimate load.

In 1989 the TRL awarded a contract to Cardiff to develop an assessment tool. Uniquely, the product which emerged (called CTAP, and is commercially available) uses a mechanism analysis to quickly determine the critical loading configuration which is then analysed by the above elastic procedure to give the detailed assessment data.

1.4.4 Computerised Pippard/MEXE method

Chapter four of BA16/93[20] describes a computerised version of the Pippard/MEXE method which is said to offer greater flexibility than does MEXE with respect to geometrical, material and loading parameters. It goes on to recommend that it is used as an additional tool following a MEXE analysis, especially in marginal cases.

1.4.5 Fuller's construction

A venerable technique still of value is Fuller's[35,36] construction, a graphical method for calculating the line of thrust in an arch. It is easy to use and is claimed to give an insight into arch behaviour, being of especial use in the assessment of hump-backed bridges. The fact that such a technique is still in use is testimony to the state of the art.

1.5 Summary

Stone imposes severe limitations on the distance it can span as a beam. *Perhaps by observing nature* (Plates 1.8, 1.9), this was overcome in antiquity with the development of the arch. Ancient examples of the utilisation of the arch principle abound in diverse applications (Plates 1.10, 1.11).

The principal application with which this thesis is concerned is the masonry arch bridge. This was uniquely and universally employed until the last century, and only in the early part of the present century was it eventually replaced. Despite being a long obsolete form, its great durability has ensured that today it is still the most numerous type of public road bridge in the United Kingdom.

Over the years traffic loads have increased enormously both in magnitude and frequency. The current maximum vehicle weight permitted in the United Kingdom under the Construction and Use Regulations[27] is 38 tonnes. This will be increased to 40 tonnes before the end of the century, and 55 tonne vehicles are already permitted

PLATE 1.8

Naturally occurring masonry arch

PLATE 1.9

"Naturally" occurring masonry arch

PLATE 1.10

Arched strutting between dwellings to give earthquake resistance (Rhodes, Greece)

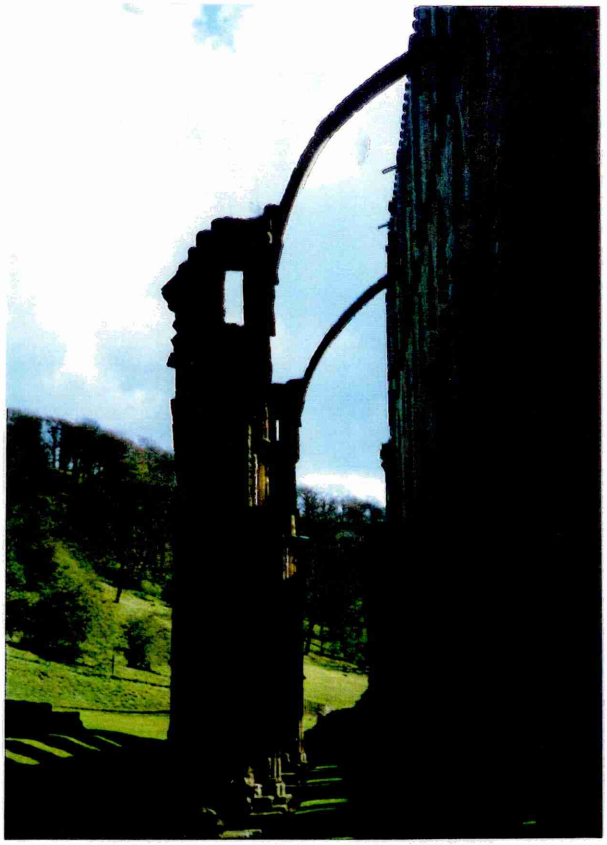

PLATE 1.11

Remarkably slender flying buttresses (Rivaulx Abbey, United Kingdom)

in The Netherlands, underlining the probable future course of events. In order to ensure continuing public safety, the existing stock of these old bridges must be structurally assessed for these new loads.

The current first choice assessment tool, MEXE, dates from before the second world war. It was developed for military use but appears in modified civil form in BD21/93 and BA16/93. It is an elastic method based on a two pinned parabolic arch with a central point load and yields a serviceability limit state permissible axle load, based upon a limiting stress. It is inapplicable if:

a) The depth of fill at the crown is more than the vault thickness at the crown (in which case it may be unconservative).
b) The arch is distorted.
c) The arch is multi span - unless the piers are sufficiently stocky to enable each span to act independently, though no advice is given on what constitutes a sufficiently stocky pier.
d) The arch is appreciably skewed.
e) The span is more than 18 metres.

Current Department of Transport policy, laid down in the above documents, is that if the application of MEXE provides adequate arch capacity (a "pass"), then the result is to be accepted. If MEXE suggests insufficient capacity, then the result must be confirmed by a more rigorous method.

Clearly it is undesirable from a bridge owner's point of view to have to rely upon a technique that may be either unsafe or uneconomically conservative (or in fact inapplicable by one or more of the above criteria), and this is the impetus behind the current research in many quarters to derive a more rational and precise alternative assessment method.

All the present alternative methods possess both merits and drawbacks, and none is acceptable in all circumstances. The elastic methods require knowledge of material properties which are difficult to obtain, and particularly with stone arches these may vary considerably within a given structure. Elastic methods can, however provide a load path history and allow for abutment movement. Set against this, they can be capable of "proving" that an arch fails under temperature loading alone, which we know to be false. Furthermore, the TRL full scale tests have revealed that masonry arches do not always behave elastically under load, and certainly not linearly. Computer programmes in this category are relatively demanding of the hardware.

The so called plastic methods tell us nothing of behaviour before failure and need an allowance for the interaction between the arch and the fill if they are to give reasonable results for deep arches. The contribution of the fill should not be underestimated - the TRL reports[37] that the response of one bridge was found to change by a factor of two between warm and freezing temperatures, the freezing of the water in the fill adding substantially to its strength. Furthermore, not all arches fail as a four hinge mechanism and a variety of failure modes have been observed in tests. Mechanism computer programmes are, however, simple and quick to use and are undemanding of the hardware.

It is true to say that the ideal alternative to MEXE has not yet been found. The aim of this research programme is to study just one of the contenders - the four hinge arch vault mechanism and specifically the mechanics of masonry hinges, both analytically and experimentally.

The theoretrical work is supported by a variety of model, full scale and computer vision information technology studies, the latter being an innovative technique offering insights into arch behaviour.

It is hoped that a novel and useful contribution can be made in the broad and complex masonry arch mechanics debate. The ultimate aim of this and related studies in the field is to expand the knowledge database to a point where a rational, scientific alternative to current arch bridge assessment techniques may be developed.

CHAPTER TWO

The Constitutive Properties of Masonry

2.1 Synopsis

Masonry materials have traditionally been regarded as either having linear stress-strain characteristics[28,29] or alternatively (and non-conservatively) infinite stiffness and compressive strength, the latter having become especially associated with the work of Professor Heyman[10,11,12].

Relatively recent research[38] has, however, provided ample evidence that masonry exhibits softening under increasing stress and a second order parabolic expression has gained acceptance by providing a basic modelling of this property.

In this chapter a new, unified masonry constitutive theory is put forward which supersedes all previous models and enables the accurate modelling of any load-deflection characteristic.

The new expression can model the range of characteristics from infinite stiffness and compressive strength, through second order parabolic to a linear response, including an infinite variety between, simply by varying one parameter. The analyst is thereby able to dispense with the earlier non-conservative or inaccurate assumptions and indeed to tailor an individual mathematical model to the particular masonry material under consideration.

The theoretical studies are supported by two series of laboratory tests; ten ultimate load compression tests on full calcium silicate bricks to BS 187:1978 and ten load-deflection tests on cores obtained from calcium silicate bricks.

2.2 Full Brick Compression Tests

The purpose of this initial test series was to explore the suitability, and to gain experience of, a material for use in later practical and theoretical vault studies. In particular, a medium with predictable and repeatable physical properties was required, and hence a class 4 calcium silicate (sand lime) brick to B.S. 187:1978 was chosen.

The merits of this brick type included a reported uniformity both in terms of dimensions (since it is a cast brick) and also, being synthetic, its composition and engineering properties.

The actual bricks used were solid commons, without a frog, of nominal size 215x102.5x65 mm. Class 4 bricks (there are seven classes in all) are required to have a mean compressive strength of not less than 27.5 N/mm^2 from a sample of ten bricks, and a predicted lower limit of not less than 21.5 N/mm^2, the predicted lower limit being defined as the mean strength less the standard deviation.

The standard compressive strength test employed[39] (the "Flower Test") consists of taking ten bricks and immersing them in water at 20±5° for 18±2 hours prior to testing. The bricks are then sandwiched between 4mm plywood sub platens and loaded at a rate of 36 N/mm^2 per minute for the first half of the expected load, then at 18 N/mm^2 per minute for the remainder. The area of loading is taken to be 22000 mm^2 (ie. $\simeq$ 215x102.5mm) and the strength is reported to the nearest 0.1 N/mm^2.

The mean stress at failure is reported, as is the standard deviation on peak stress which is calculated as

$$\sqrt{\frac{\sum_{i=1}^{n} [x_i - x_{mean}]^2}{n-1}} \qquad (2.1)$$

and the coefficient of variation, defined as standard deviation/meanx100%, is also computed.

The results of the ten test series carried out thus in Sheffield Hallam University's Structures Laboratory, using a standard concrete cube crushing machine, are shown in Table 2.1 overleaf.

Sample Number	Peak Load (kN)	Peak Stress (N/mm^2)
1	625	28.4
2	615	27.9
3	622	28.2
4	606	27.5
5	617	28.0
6	575	26.1
7	616	27.9
8	606	27.5
9	613	27.8
10	613	27.8

Table 2.1 Full brick load test results

The mean stress at failure was computed to be 27.7 N/mm^2; the standard deviation on peak stress was 0.632 N/mm^2 and the coefficient of variation ±2.280%.

This basic series of tests revealed that the bricks exceeded the requirements of the British Standard and possessed a very low standard deviation, confirming the suitability of this medium to the further testing and theoretical studies envisaged.

2.3 Brick Core, Stroke-controlled Compression Tests

The object of this series of tests was to obtain a set of masonry load-deflection curves to assist in the development of a theoretical study of the constitutive properties of masonry.

The cores, cut from whole bricks, were of 50 mm diameter and 125 mm long giving the desired aspect ratio[40] of 2.5:1. Coring the bricks proved to be difficult and resulted in samples that were less than perfect cylinders. The consequences of these imperfections may well manifest themselves in the slightly greater standard deviation for the core test series than for the brick test series, albeit in the same material. The loading was applied in a stiff, servo-controlled testing machine[41] at a rate of 0.0023mm/second.

A core was loaded by mounting its uncapped base directly on the lower machine platen, with its top separated from the upper platen by a sandwich of (from top to bottom) greaseproof paper, plastic padding (an epoxy-type resin), and a sub-platen. Displacement was measured by a transducer reading from the underside of the top sub-platen and was plotted automatically against load on an X-Y flat-bed plotter.

Plate 2.1(a) depicts a typical core before loading under this regime; Plate 2.1(b) shows the same core after failure and Plate 2.1(c) illustrates a typical failure mode (of another sample) in greater detail.

Capping the core ends, for example with sulphur, was considered but rejected as earlier experience with sandstone cores[30] had produced an undesirable reverse curve near the load-deflection plot origin as the caps bedded in. Whilst correction for the reverse curve by projecting a line back to give an effective origin is reasonable for a *linear* plot, it was not considered acceptable for the non-linear plot expected here.

The earlier work with sandstone cores, incidentally, had demonstrated that sandstone possesses a non-linear stress-strain relationship[30].

The response of each of the ten cores tested was essentially similar and the load-deflection trace was, as expected, distinctly non-linear from the outset. Figure 2.1 reproduces a typical example of the raw X-Y output. Peak load is just under 70 kN at a corresponding displacement of about 0.5mm. A small degree of bedding-in is evident at the origin, as revealed by the slight reverse curve, but it is considered to be trivial. It was taken out by projecting a short straight line back to the abscissa and shifting the origin to that point.

An immediate impression was that the curve shape might obey some parabolic power law to at least maximum load. The great difference in relative stiffness between the massive stroke-controlled testing machine and the small masonry sample has enabled a smooth falling branch to be easily traced to a deflection of 1.5 mm and beyond. In practice the falling branch could be followed as far as desired, and so the tests were terminated by manual intervention. The smoothness of the rising curve is continued beyond peak load and down the falling branch for some distance before it is disrupted by macro cracking in the sample. The possibility of fitting a mathematical model to the curve to well beyond peak load, ie. to the breakup point, is therefore credible. The detailed results of the ten core tests are summarised in Table 2.2.

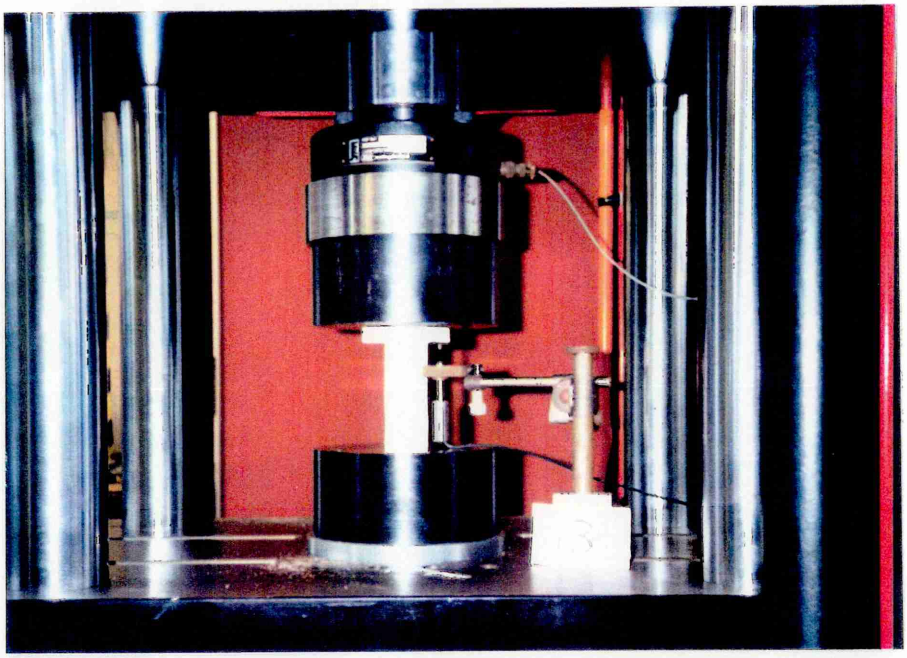

(a)

Typical core sample prior to loading

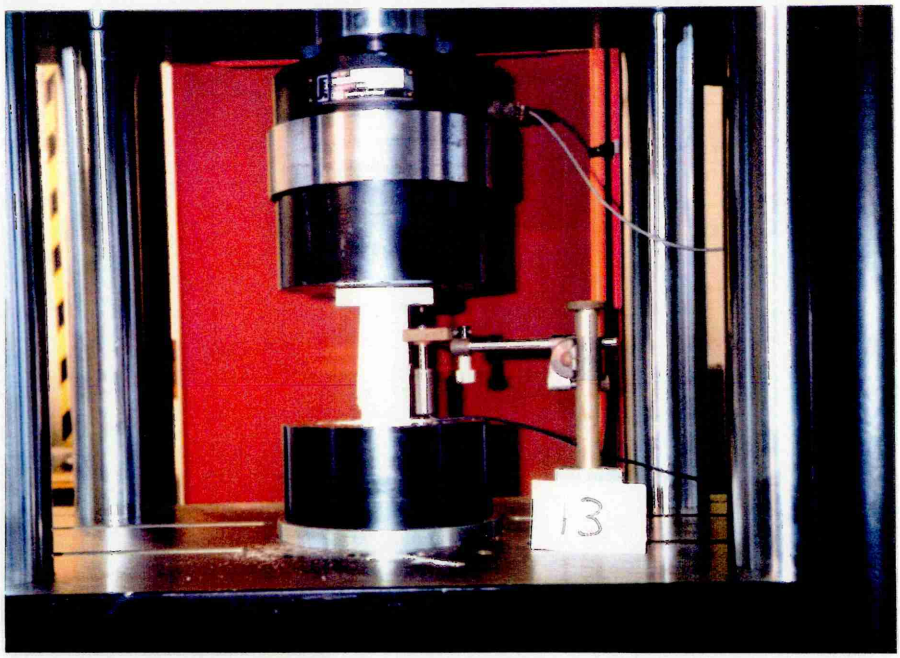

(b)

Same core after failure

(c)

Typical core sample showing failure mode in greater detail

PLATE 2.1

Brick core tests

FIGURE 2.1

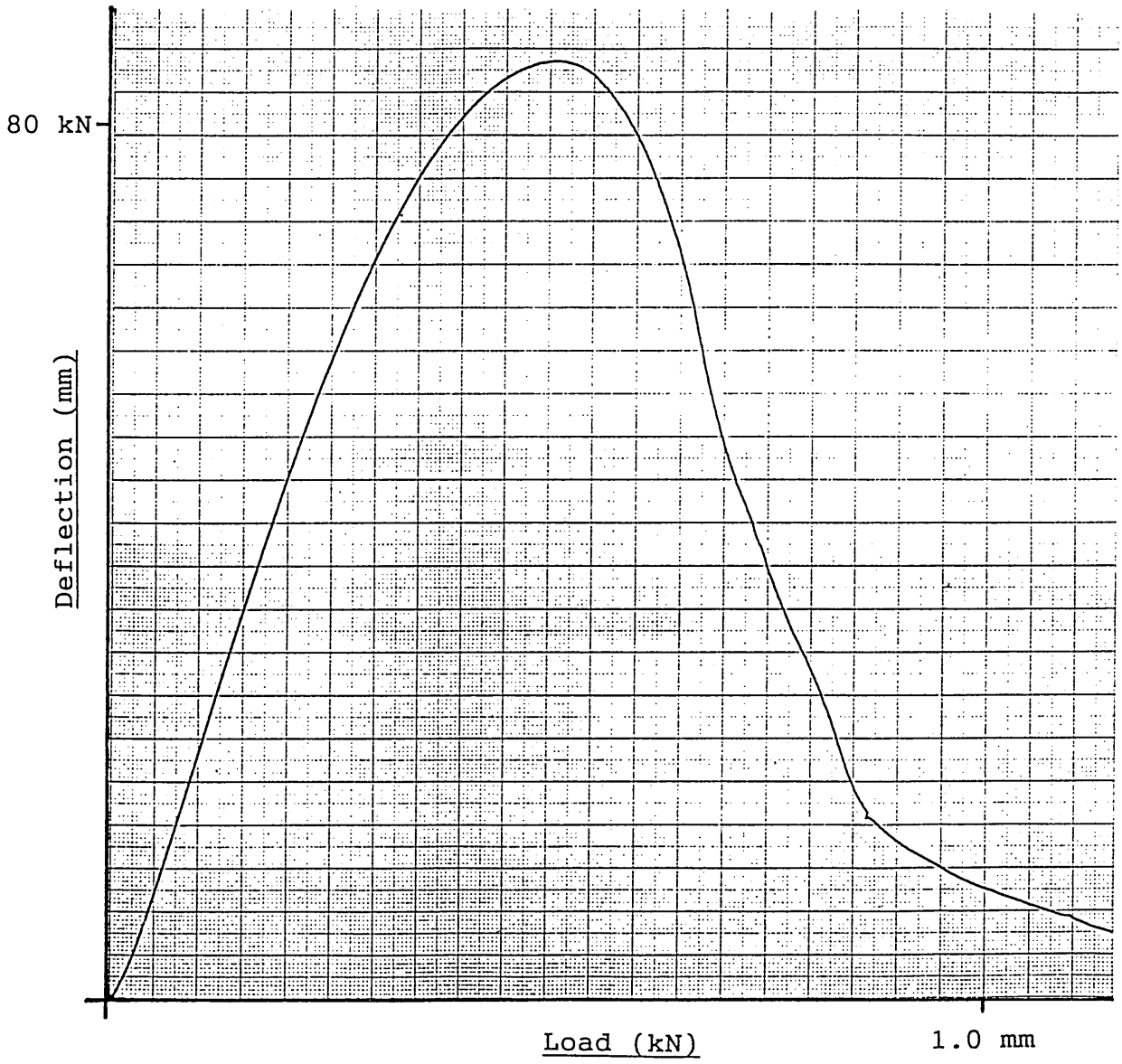

Raw X-Y plotter trace for a brick core sample

Errata: Axes labels require transposition.

Sample Number	Peak Load (kN)	Peak Stress (N/mm^2)	Peak Strain
1	60.00	34.63	0.00480
2	68.80	35.04	0.00406
3	69.40	35.34	0.00408
4	67.60	34.43	0.00400
5	72.27	36.81	0.00344
6	69.69	35.49	0.00412
7	70.41	35.86	0.00400
8	69.28	35.28	0.00404
9	69.28	35.28	0.00344
10	70.40	35.85	0.00396

Table 2.2 Core load test results

The mean peak stress was 35.4 N/mm^2 (based on the nominal diameter of 50 mm) and the corresponding mean strain was 0.003994.

For comparison with the earlier whole brick load tests, the standard deviation on stress was computed at 0.675 N/mm^2, with a coefficient of variation of ±1.907%.

A primary purpose of the core load tests was to study the *shape* of the curve and so the ten load-deflection curves were non-dimensionalised. At the same time as the plots were being manually digitised, scaled and replotted in a non-dimensional form, the minor bedding-in reverse curves were eliminated as previously described. By way of example, four of the non-dimensionalised curves thus produced are shown in Figure 2.2, corresponding to samples 4 to 7.

The final task in this practical exercise was to superimpose all the non-dimensional curves to give the result depicted in Figure 2.3. Superposition allows direct comparison of the individual shapes, their scatter and ultimately some engineering judgement as to a "mean" curve shape for this material. In fact, the curves exhibit a very similar profile up to failure, with an increasingly widespread scatter beyond. Reference to this work and the "mean" shape of this load-deflection locus will be made in the ensuing which deals with the theoretical aspects of masonry constitutive properties. Further reference will be made in Chapter Three when calcium silicate bricks are used again in model masonry hinge experiments in validation of further theoretical studies concerning moment-thrust interaction and the limit state.

FIGURE 2.2

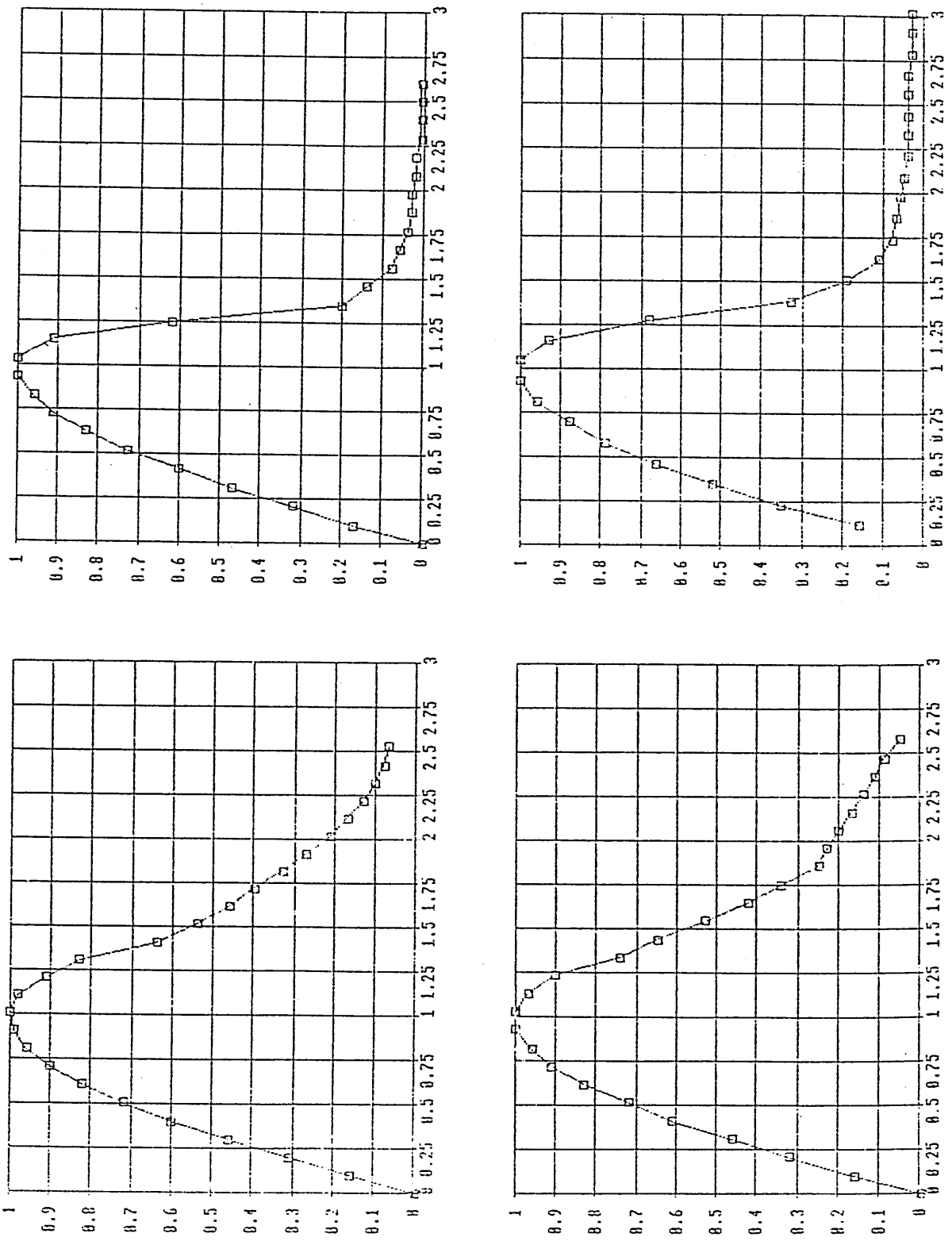

Specimen non-dimensionalised brick core
load-deflection plots (samples number 4, top left, to 7, bottom right)

FIGURE 2.3

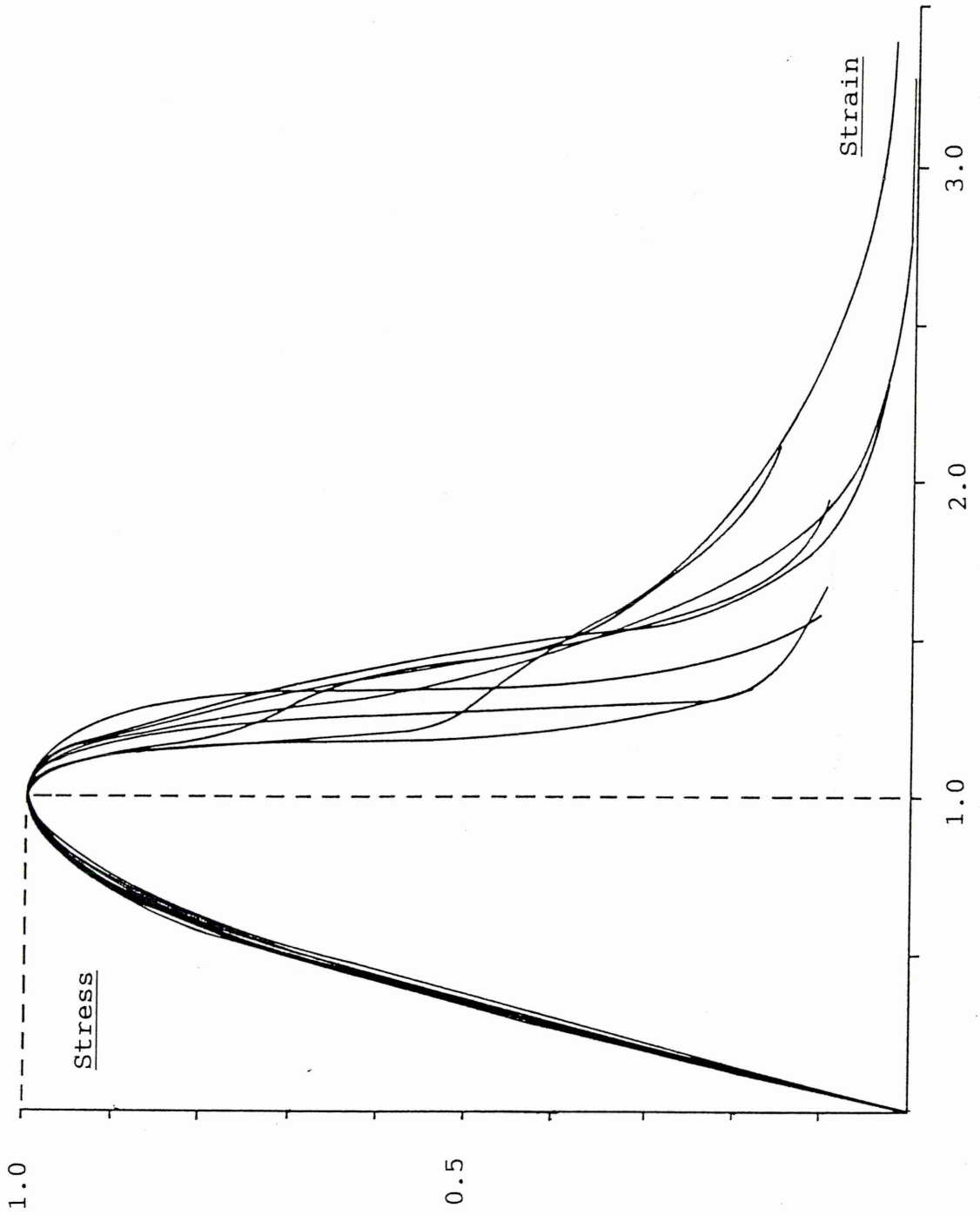

Superimposed non-dimensionalised load-deflection plots for brick cores (with k=3 transparent overlay - see later text)

2.4 A Theoretical Non-linear Constitutive Model

The initial parabolic non-linear load-deflection expression of recent times takes the form

$$\frac{\sigma}{\sigma_m} = \frac{2\varepsilon}{\varepsilon_m} - \left(\frac{\varepsilon}{\varepsilon_m}\right)^2 \qquad (2.2)$$

where σ_m and ε_m denote the peak stress and corresponding strain, respectively. It is to be noted that tensile strength is considered to be negligible. Figure 2.4a) shows the form of this expression, and it has been reported[42,43] that the profile fits well experimentally with four brick types. However, a *novel*, alternative and more sophisticated modelling equation is now introduced[44]:

$$\frac{\sigma}{\sigma_m} = \frac{1}{k-1}\left[\frac{k\varepsilon}{\varepsilon_m} - \left(\frac{\varepsilon}{\varepsilon_m}\right)^k\right] \qquad (2.3)$$

The significance of the introduction of the novel curve shape constant 'k' is that by varying its value, a family of curves may be produced to mimic load-deflection curves, ranging from a 'Heyman' material (k=0) which possesses infinite compressive strength and stiffness, through to a linear response material with k=∞ (whilst noting the singularity at k=1, ie. $0 \le k < 1$; $1 < k \le \infty$). It will be later shown that 'k' is in fact a parameter related to stiffness.

It is apparent that the generally accepted equation 2.2 is in fact a special case of the above new equation with k=2.

Typical 'real' masonry materials possess values of k in the range 2 to about 12[44]. It is a simple matter to produce a set of k curves on transparencies and to overlay each in turn upon real masonry stress-strain plots to determine an appropriate k value for that material. Figure 2.4b) depicts such a set of k curves in the range 0 to 12, plus ∞.

The significance of the new masonry modelling equation is this. Formerly, either a non-conservative infinite stiffness, infinite compressive strength model, or a linear model, had been employed. Latterly, a second order parabolic equation has also become accepted. All of these approaches possess drawbacks and none are able to represent the full range of masonry material load-deflection responses encountered in practice.

FIGURE 2.4

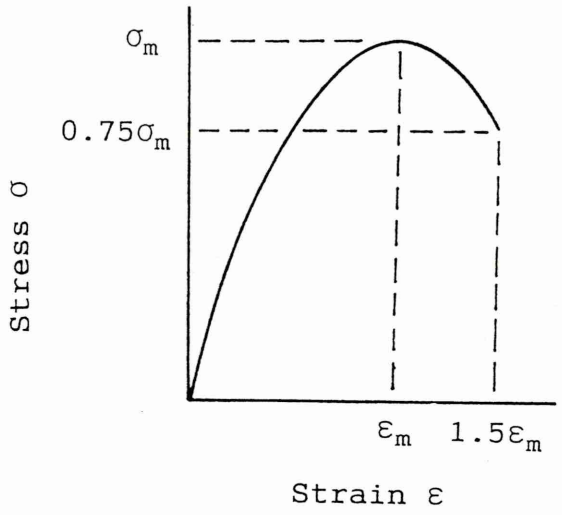

a) Existing constitutive locus

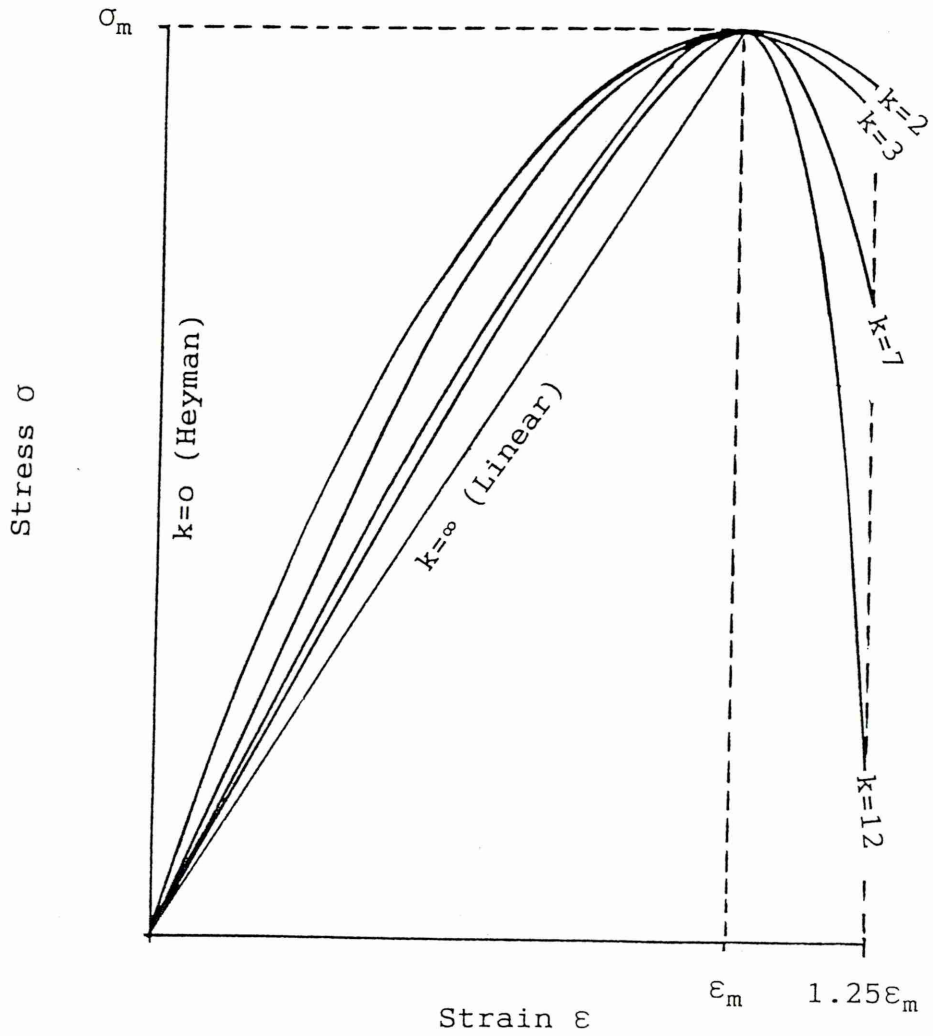

b) Proposed constitutive locus employing $\frac{\sigma}{\sigma_m} = \frac{1}{k-1}\left[\frac{k\varepsilon}{\varepsilon_m} - \left(\frac{\varepsilon}{\varepsilon_m}\right)^k\right]$

The new equation can practically 'mimic' all the above approximations, and any response between, by manipulating one parameter. For real masonry materials, the range is $k>1$ and finite.

Referring back to the 'mean' shape of the load-deflection characteristic for calcium silicate bricks suggested by Figure 2.3, it will be seen that overlaying a $k=3$ locus provides a very acceptable fit. Thus it is suggested that substitution of $k=3$ in equation 2.3 provides a mathematical expression for modelling this material's response more accurately than has hitherto been possible. The value of this form of modelling will become apparent in the next chapter when the concept will be developed further to derive moment-thrust data, together with *limit state characteristics*, for masonry materials possessing any practical load-deflection response. This work will then bear directly on the study of masonry vault mechanism hinges.

Figure 2.5 illustrates a complete stress-strain locus for a damaged voussoir taken from Rivelin Mill bridge, Sheffield. The test was undertaken, as before, in a modern, stiff, servohydraulic testing machine. As with the earlier curves obtained from calcium silicate bricks, this plot for a sandstone voussoir is non-linear throughout and exhibits a definitive falling branch and, importantly, is indistinguishable from

$$\frac{\sigma}{\sigma_m} = \frac{1}{k-1}\left[\frac{k\varepsilon}{\varepsilon_m} - \left(\frac{\varepsilon}{\varepsilon_m}\right)^k\right] \text{ (eqn. 2.3) with } k=7,\ \sigma_m=33 \text{ N/mm}^2 \text{ and } \varepsilon_m=0.00378$$

Experimentally, fracture does not occur until $\varepsilon=\gamma\varepsilon_m$, while $\varepsilon=\lambda\varepsilon_m$ relates to the maximum strain occurring at the static limit state, termed the *hinge limit coefficient*; this latter parameter is of significance and is discussed in the following. In Figure 2.5, $\gamma=1.47$ and $\lambda=1.16$.

Recalling the calcium silicate brick core tests affords interpretations of γ and λ as shown in Figure 2.6. As indicated, nine of the ten constitutive loci are indistinguishable from equation 2.3 with $k=3$ for $\varepsilon/\varepsilon_m \leq \lambda$ ($\lambda>1$). It is considered that Figure 2.6 provides excellent data characteristics for $\varepsilon/\varepsilon_m \leq \lambda=1.227$ with experimental fracture not being completed prior to $\gamma=2.5$. Further experimental masonry constitutive data are available elsewhere[33,46], relating, for example, to brick *pier* testing, and are illustrated in Figure 2.7. A key observation in this instance is that, practically, for one locus material breakup occurred before the hinge limit coefficient was reached, ie. $\gamma<\lambda$.

Finally, Figure 2.8 summarises the key constitutive factors entailed.

FIGURE 2.5

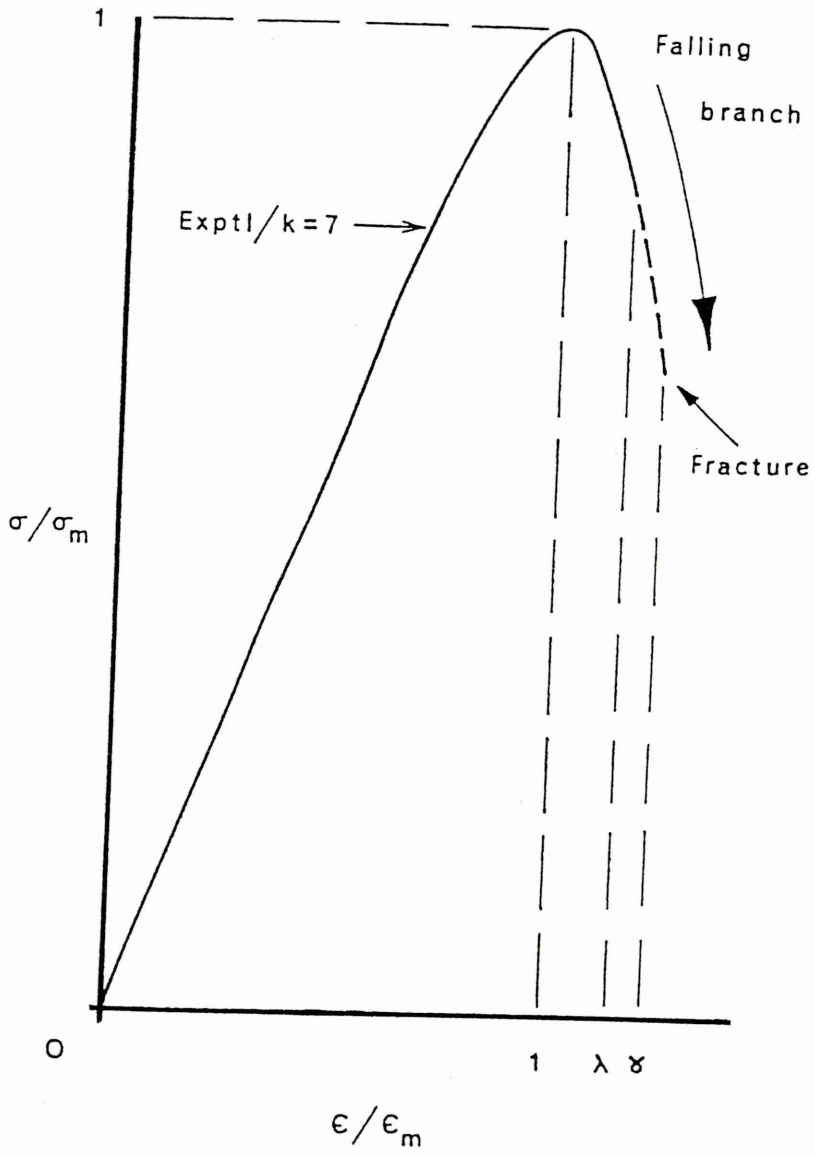

The constitutive locus for a Rivelin Mill Bridge voussoir masonry core provides a good fit to $\frac{\sigma}{\sigma_m} = \frac{1}{k-1}\left[\frac{k\varepsilon}{\varepsilon_m} - \left(\frac{\varepsilon}{\varepsilon_m}\right)^k\right]$ with k=7, σ_m=33 N/mm2 and ε_m=0.00378

FIGURE 2.6

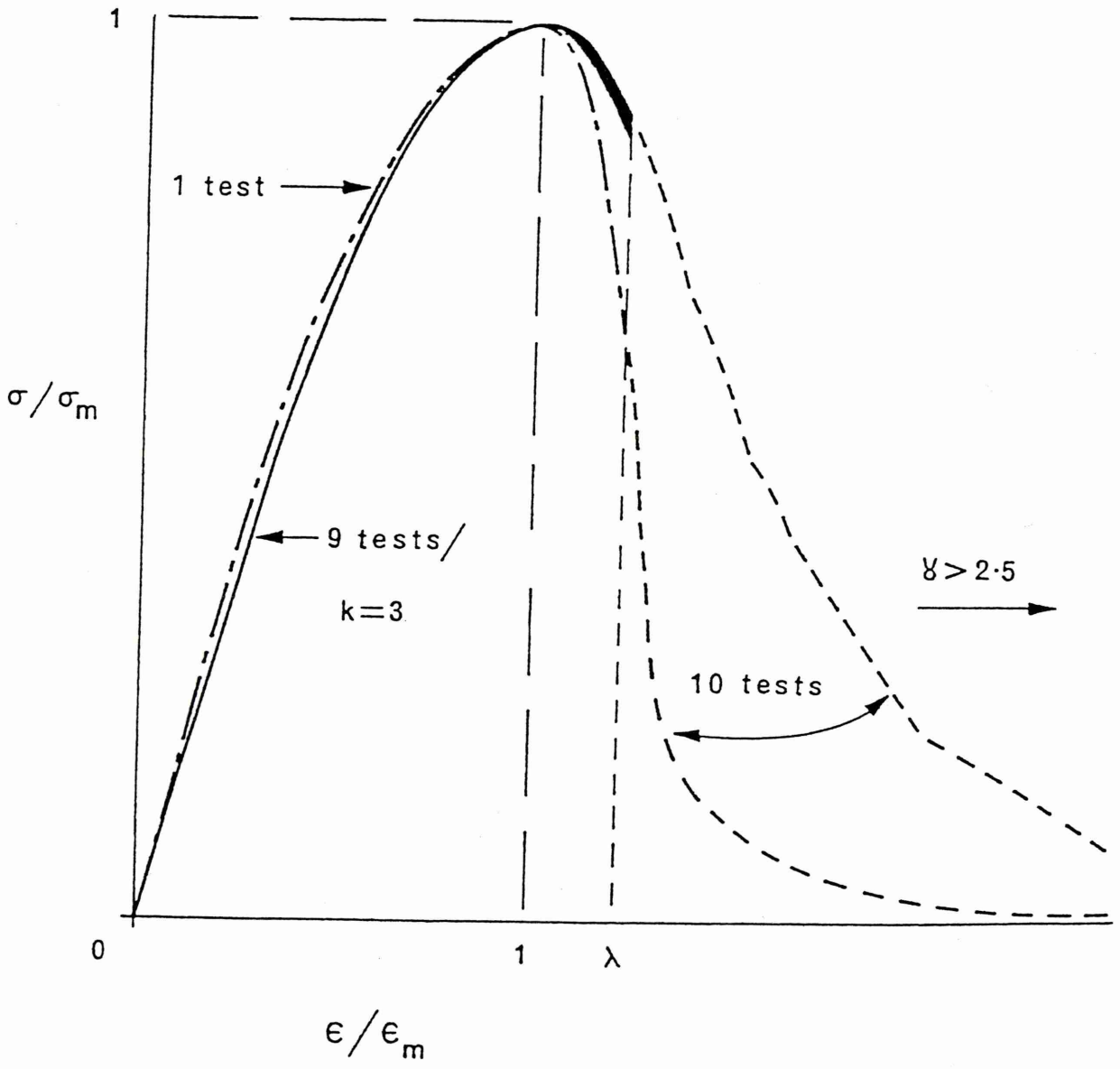

Calcium silicate brick core constitutive loci

FIGURE 2.7

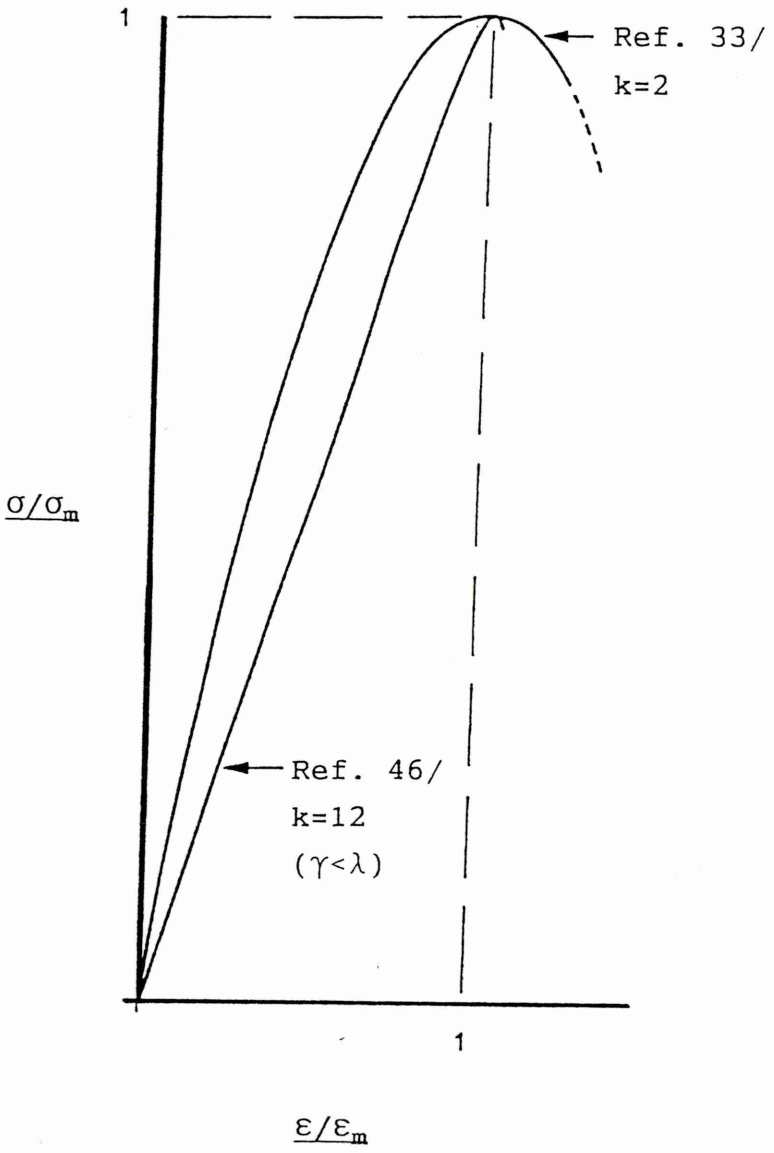

Interpretation of brick pier constitutive loci

FIGURE 2.8

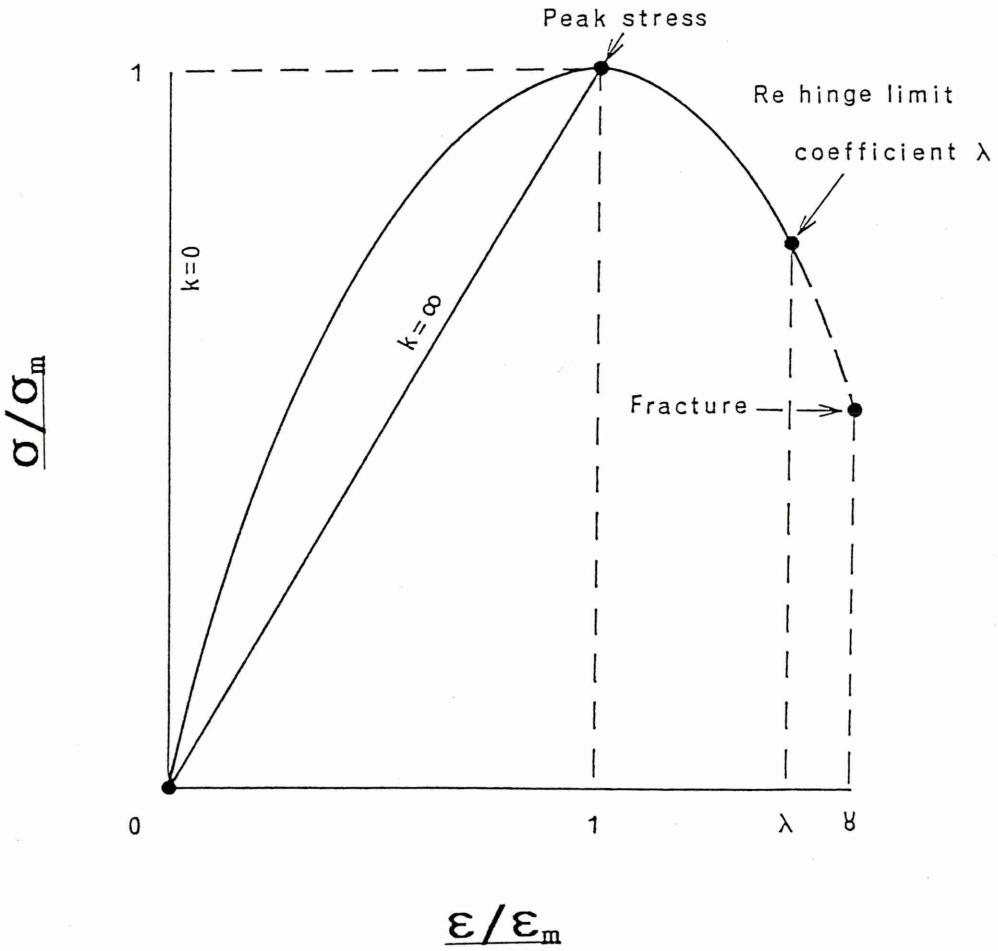

Idealised constitutive locus

2.5 Conclusions

The universality of non-linear stress-strain laws for *all* masonry materials is considered probable; viz the well known shape of the curve for concrete, the parabolic shape for sandstone[30] and the similar result for calcium silicate brick from the laboratory tests reported here are all strong evidence in addition to a large volume of material by others[37,38,42,45].

As a response, a novel equation capable of modelling the stress-strain law for *all* such material characteristics has been presented.

The previous simplistic approaches of assuming infinite compressive strength and the use of either an unrepresentative linear, or second order parabolic stress-strain relationship have been rendered unnecessary by these studies.

The ability to determine *limit state characteristics* using the above approach will be explored in the next chapter.

CHAPTER THREE

The Brittle Hinge

3.1 Synopsis

The non-linear constitutive studies of Chapter Two are developed further[44] and equations employing the novel 'k' modelling are derived for a rectangular masonry section under combined bending and thrust. Numerical solution routines are developed to solve these expressions and the results are discussed. Graphical interpretation of the equations provides two axial thrust-bending moment limit state interaction diagrams, one for the ultimate limit state and the other for a crack-prevention serviceability limit state.

The work is extended to consider static limit state properties for a masonry vault and further novel equations are synthesized which also require recourse to numerical techniques for their solution. The overall findings support the development of a masonry arch bridge mechanism model based on proposed, novel finite 'k' hinge formulations.

Key inferences are drawn from the interaction diagrams, particularly with respect to the superiority of the 'k' modelling over traditional methods and the hypothesis that masonry hinges must be located at the edge of the derived ultimate limit state envelope. The negation of the traditional middle third rule for crack prevention, and the development of a 'middle half rule' for bending capacity maximisation, are both postulated by these non-linear methods.

Model hinge experimentation is undertaken in the laboratory to test the theoretical studies, and it is considered that overall experimental consistency and good experimental correlation with the theoretical studies is obtained. Qualitative conclusions are also drawn from the laboratory tests enabling speculation in the wider context of masonry arch bridge analysis.

3.2 Moment and Thrust

3.2.1 The effect of 'k' modelling on moment and thrust

With reference to Figures 3.1a) and 3.1b), for either condition axial thrust P is given by

$$P = \int_{-d/2}^{d/2} \sigma b dy \tag{3.1}$$

where d denotes the section's depth and b its width, and bending moment M is given by

$$M = \int_{-d/2}^{d/2} \sigma b y dy \tag{3.2}$$

Recalling $\frac{\sigma}{\sigma_m} = \frac{1}{k-1}\left[\frac{k\varepsilon}{\varepsilon_m} - \left(\frac{\varepsilon}{\varepsilon_m}\right)^k\right]$ from equation (2.3) and that for plane sections

$$\varepsilon = k_1 + k_2 y \tag{3.3}$$

it can be shown that

$$\varepsilon = \left(\frac{\varepsilon_1+\varepsilon_2}{2}\right) + \frac{y}{d}(\varepsilon_1-\varepsilon_2) \tag{3.4}$$

for the uncracked condition and

$$\varepsilon = \frac{\varepsilon_1}{2} + \frac{\varepsilon_1 y}{d'} \tag{3.5}$$

for the cracked condition.

Substitution of these expressions, respectively, into equation 2.3 yields,

$$\sigma = \frac{\sigma_m}{k-1}\left(\frac{k}{\epsilon_m}\left[\left(\frac{\varepsilon_1+\varepsilon_2}{2}\right) + \frac{y}{d}\left(\varepsilon_1-\varepsilon_2\right)\right] - \left[\frac{1}{\varepsilon_m}\left(\left(\frac{\varepsilon_1+\varepsilon_2}{2}\right) + \frac{y}{d}\left(\varepsilon_1-\varepsilon_2\right)\right)\right]^k\right) \tag{3.6}$$

for the uncracked section and

FIGURE 3.1

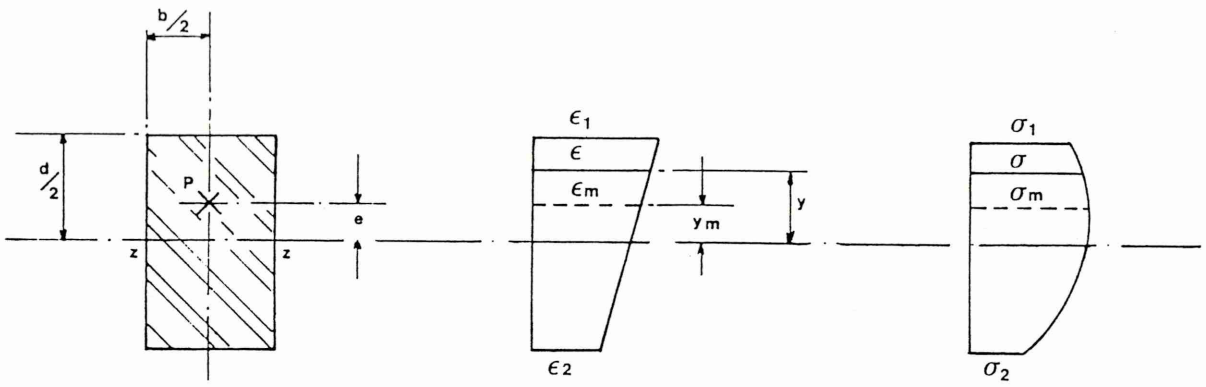

Section Strain Stress

a) uncracked section

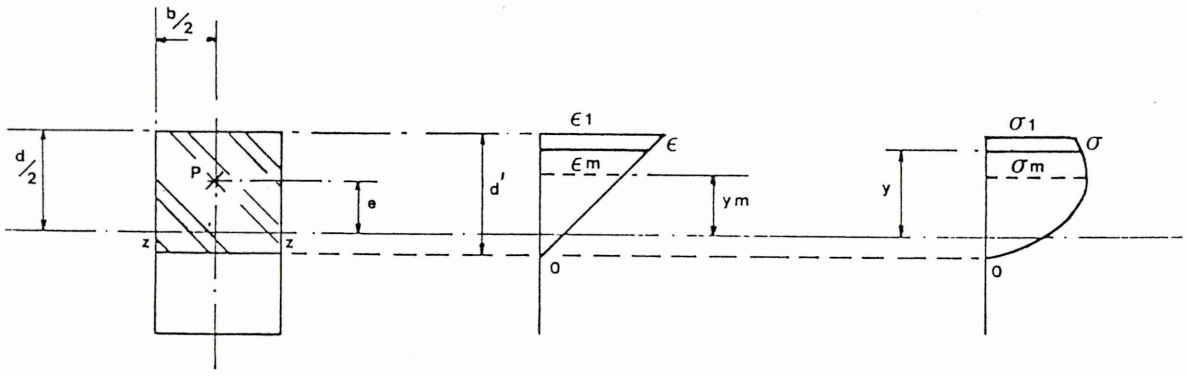

Section Strain Stress

b) cracked section

Section topology for combined bending and thrust study

$$\sigma = \frac{\sigma_m}{k-1}\left(\frac{k\epsilon_1}{\epsilon_m}\left[\frac{1}{2}+\frac{y}{d'}\right] - \left(\frac{\varepsilon_1}{\varepsilon_m}\right)\left[\frac{1}{2}+\frac{y}{d'}\right]\right) \qquad (3.7)$$

for the cracked section.

After extensive further manipulation

$$M = \frac{\sigma_m b d^2}{(k-1)\varepsilon_m}\left[\frac{k(\varepsilon_1-\varepsilon_2)}{12} - \frac{(\varepsilon_1^{k+1}+\varepsilon_2^{k+1})}{2(k+1)\varepsilon_m^{k-1}\ (\varepsilon_1-\varepsilon_2)}\right.$$

$$\left. + \frac{(\varepsilon_1^{k+2}-\varepsilon_2^{k+2})}{\varepsilon_m^{k-1}(k+1)(k+2)\ (\varepsilon_1-\varepsilon_2)^2}\right] \qquad (3.8)$$

and

$$P = \frac{\sigma_m b d}{(k-1)\varepsilon_m}\left[\frac{k(\varepsilon_1+\varepsilon_2)}{2} + \frac{(\varepsilon_2^{k+1}-\varepsilon_1^{k+1})}{(\varepsilon_1-\varepsilon_2)\quad \varepsilon_m^{k-1}(k+1)}\right] \qquad (3.9)$$

for the uncracked condition, and,

$$M = \frac{\sigma_m b d'}{2(k-1)}\left[\frac{k}{6}(3d-2d')\left(\frac{\varepsilon_1}{\varepsilon_m}\right) - \frac{1}{(k+1)}\left(d-\frac{2d'}{(k+2)}\right)\left(\frac{\varepsilon_1}{\varepsilon_m}\right)^k\right] \qquad (3.10)$$

and

$$P = \frac{\sigma_m b d'}{k-1}\left[\frac{k}{2}\left(\frac{\varepsilon_1}{\varepsilon_m}\right) - \frac{1}{(k+1)}\left(\frac{\varepsilon_1}{\varepsilon_m}\right)^k\right] \qquad (3.11)$$

for the cracked condition.

Equations 3.8 and 3.9, and 3.10 and 3.11, are key paired relationships. They may be employed to solve *any* rectangular masonry section under combined bending moment and thrust.

By varying the parameter 'k', such solutions may be obtained for the practical range of masonry materials ($k>1$ and finite), together with a theoretical linear ($k=\infty$) response, and a 'Heyman'[12] infinitely strong, infinitely stiff ($k=0$) theoretical response.

Furthermore, these solutions give access to limit state moment-thrust interaction behaviour, again for the full range of 'k', and hence masonry, types.

3.2.2 Solution of the bending moment and thrust equations

For specified parameters P and M, equations 3.8 to 3.11 must be solved simultaneously to provide a solution for ε_1 and ε_2 in the case of an uncracked section, and for ε_1 and d' in the case of a cracked section.

In both cases further manipulation affords a polynomial of degree four in ε_1. Solution for ε_1 then readily results in the evaluation of ε_2 or d' by back substitution.

Standard polynomial solution routines were considered for this purpose - for example those attributable to Bairstow and Newton Raphson - but instead it was decided to purpose-write software. This brought benefits by helping to develop a feel for the problem, and it also gave a better understanding of data trends through the use of graphical output. In addition, non-linear expressions can be sensitive and this was a further reason for the development of dedicated software.

A pair of software routines was thus developed, one each for the uncracked and cracked section cases, written in BASIC language and packaged together under the title PSTRESS1. Appendix 'A' provides a full programme listing. These half interval search routines output simple graphical representations to the computer monitor enabling all roots to be seen, considered and evaluated if required. After evaluating the appropriate root, the routine goes on to plot the stress and strain distributions for the section in question. The process is properly illustrated by reference to an example.

3.2.3 Computer programme PSTRESS1

Consider the example of a typical masonry section 0.3 m deep (unit, or one metre, width assumed) possessing a peak failure stress (σ_m) of 16 N/mm^2 at a corresponding strain (ε_m) of 0.0024. A stroke-controlled load test of a sample has shown the load-deflection response to be non-linear, and overlaying a set of 'k' curve tranparencies has revealed that k=2 is most appropriate modelling for this material.

Imagine the section is subjected to an axially applied compressive load of, say, 1200 kN acting in conjunction with a bending moment of 110 kNm.

Figure 3.2 depicts PSTRESS1's uncracked section analysis graphical output for this example. Clearly there is more than one root, as might be expected, but the leftmost

FIGURE 3.2

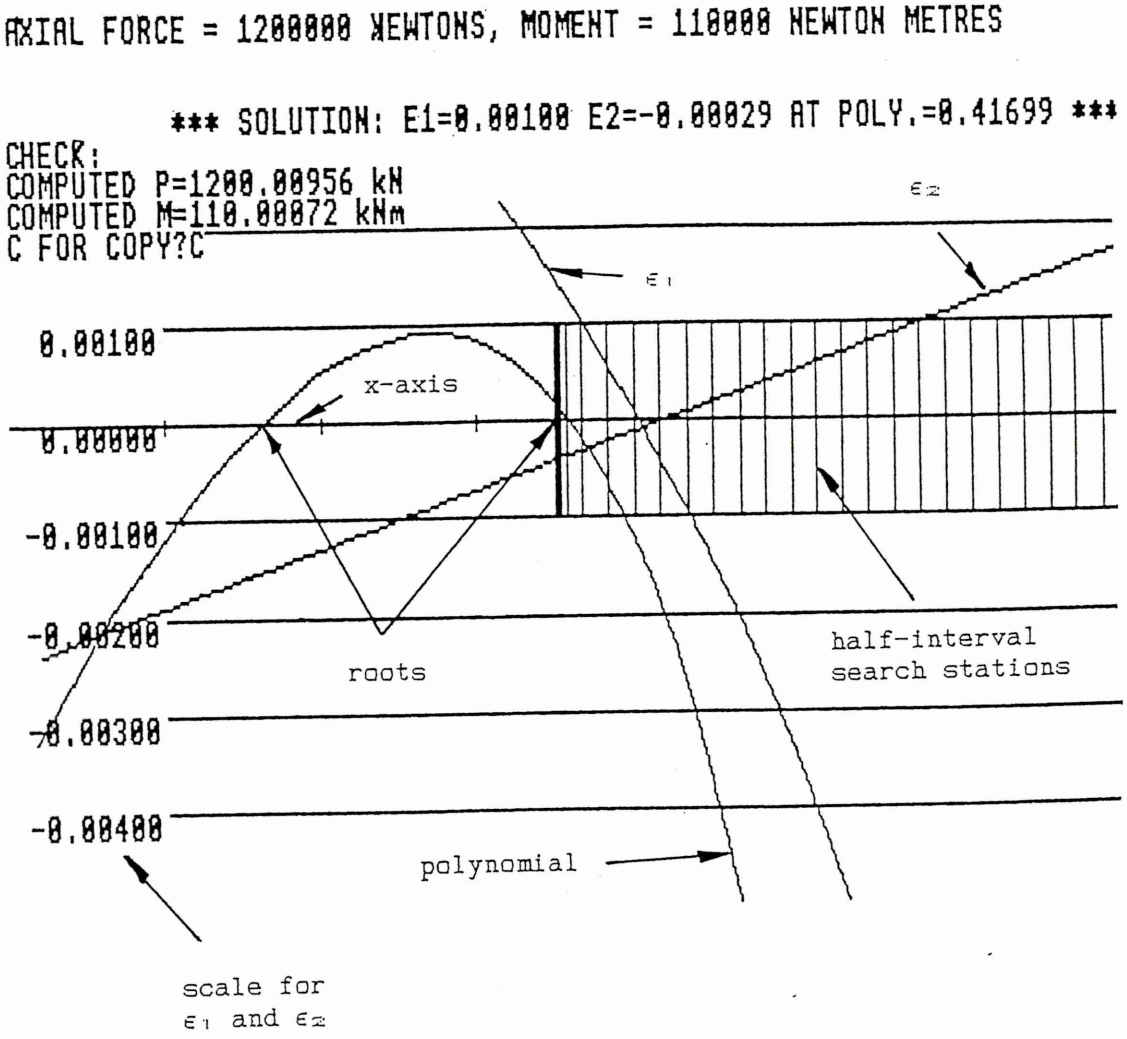

PSTRESS1 graphical output for the example in the text (uncracked section). The two polynomial roots are indicated; the root on the right is 'correct'.

Please note: excessive decimal detail employed to show mathematical rigour only.

is trivial in that ε_1 is massively positive, and ε_2 is negative. Considering the rightmost root, then, it is apparent that whilst both ε_1 and ε_2 have credible absolute values, ε_2 is slightly negative. This indicates that the section is in fact cracked and so PSTRESS1 automatically proceeds to its cracked section analysis.

Figure 3.3 is similar to before but is the result of the cracked section analysis. Once more the left root provides a trivial solution (ε_1=0), but the right root finally affords the required answer:

ε_1=0.00133
d'(uncracked section depth) = 0.165 m.

PSTRESS1 completes its run by plotting the resulting stress and strain distributions across the masonry section and these are shown in Figure 3.4. One will observe the curved boundary to the stress plot - a direct consequence of the non-linear, k=2 constitutive property.

It is interesting to note that the section is cracked through 45% of its depth and yet is well below failure in bending. Maintaining the axial thrust constant but increasing the bending moment eventually produces a bending "failure" at 131.5 kNm for this particular example. Failure is deemed to occur when no viable polynomial solutions remain, and in practical terms this means that increasing the externally-applied moment beyond that point will result in the masonry being unable to internally generate an equal and opposite reaction. In other words, a limit state has been reached.

Figure 3.5a) depicts the polynomial *just beyond* failure (ie. no viable solutions are depicted), and Figure 3.5b) the stress and strain plots *at* the limit state condition showing cracking extending through almost two thirds of the section. A point of interest is the separation of maximum effects - the peak stress occurs within the section whereas the peak strain is at the extreme fibre.

Crucially, since increasing the applied bending moment beyond the limit state condition (131.5 kNm in this example) would be unopposed by an internal reaction, the masonry section would rotate uncontrollably It is therefore concluded that *the limit state condition now reached represents a masonry hinge*. This interpretation will be developed in the ensuing.

FIGURE 3.3

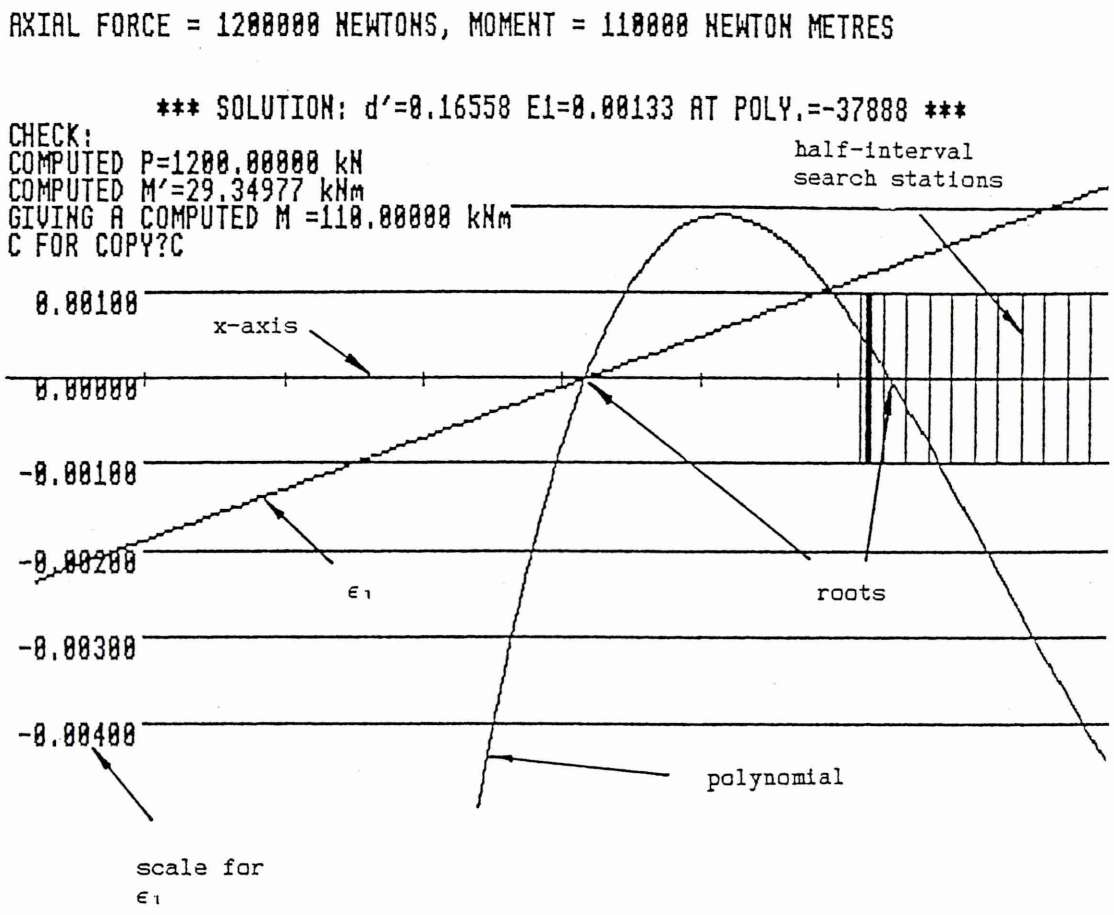

PSTRESS1 graphical output for the example in the text (cracked section).
The two polynomial roots are again indicated; the root on the right is 'correct'.
(note that the search routine graphical display is inaccurate;
the root has in fact been properly located numerically)

FIGURE 3.4

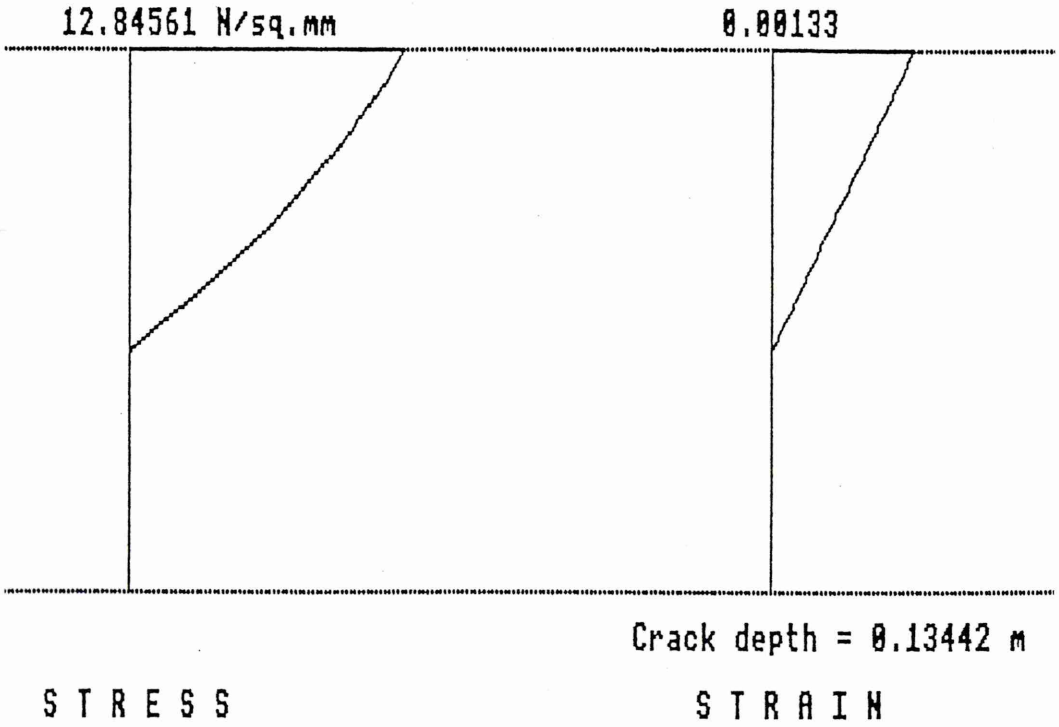

Computer programme PSTRESS1 graphical output for the example in the text showing stress and strain plots across the section.

FIGURE 3.5a)

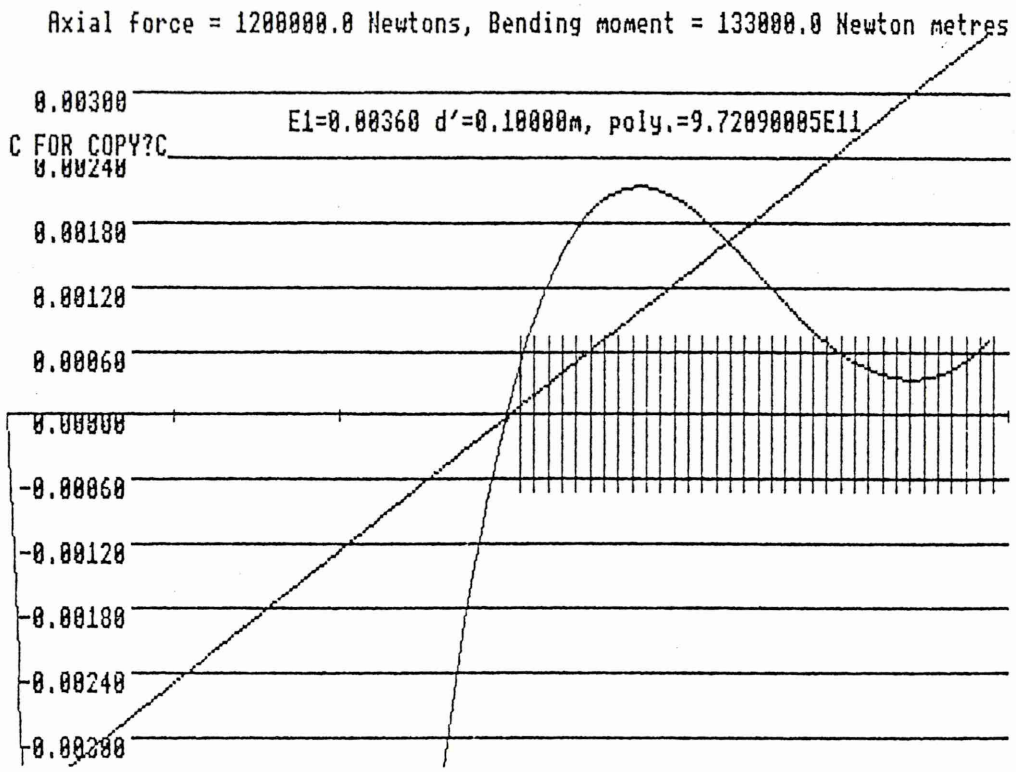

PSTRESS1 graphical output for the example in the text showing a cracked section analysis post failure (ie. no viable roots exist).

FIGURE 3.5b)

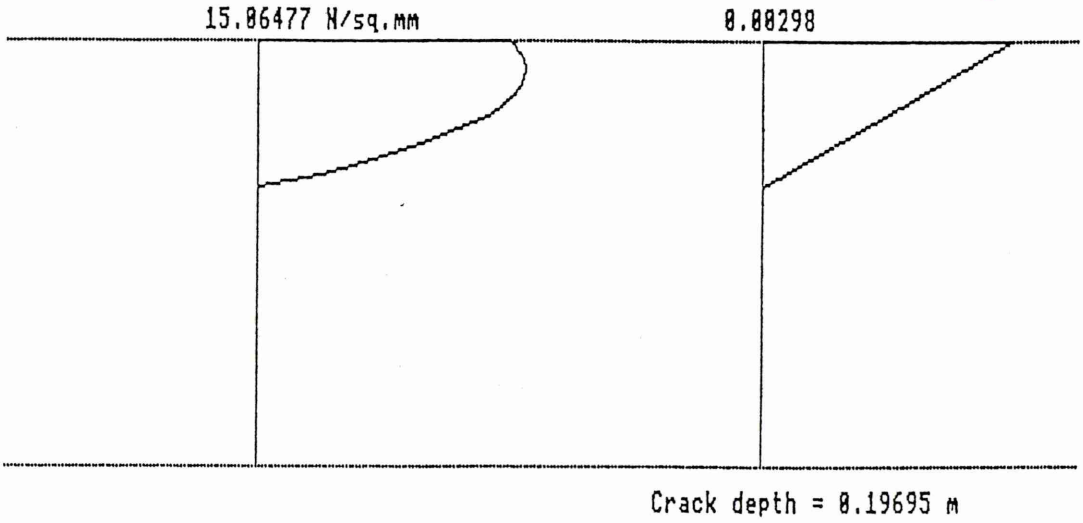

PSTRESS1 graphical output for the example in the text showing stress and strain plots across the section at the ultimate limit state.

As would be expected from a fourth order polynomial, there may be up to four roots but under most circumstances only one of these provides a physically sensible result. It is interesting to note, however, that close to failure one of the other three roots may briefly provide an alternative credible answer. This second solution is based upon different stress and strain blocks and a different crack depth. This implies that, near failure, the section can theoretically mobilise two alternative internal force regimes to balance the external one. It is a matter of engineering judgement to assess these two states; the effect is due to the falling branch providing two strain states for any given stress level for stresses 'above' σ^* (see Figure 2.8).

3.3 Static Limit State Considerations

3.3.1 The static limit state

Static limit states are determined by obtaining the maximum bending moment that the section can withstand at any given value of axial compression. The numerical maximisation procedure, in practice performed by computer, is depicted in Figure 3.6.

An essential outcome is that static limit states occur for $\varepsilon_1=\lambda\varepsilon_m$, and $\varepsilon_1=\lambda\varepsilon_m-(\lambda-1)\varepsilon_2$ for the cracked and uncracked configurations, respectively, with $\lambda>1$ being a constant for any specified k. Given that $0\leq\varepsilon_2\leq\varepsilon_m$, and $\lambda\varepsilon_m\leq\varepsilon_{1\leq}\leq\varepsilon_m$, then the cracked/uncracked interface will occur when $d'=d$ as $\varepsilon_2=0$ at $\varepsilon_1=\lambda\varepsilon_m$.

In other words, for $0\leq k\leq\infty$ $(k\neq1)$, static limit states for the cracked configuration coincide with the maximum compressive strain obeying

$$\varepsilon_1 = \lambda\varepsilon_m \qquad (3.12)$$

whilst for the uncracked configuration they coincide with

$$\varepsilon_1 = \lambda\varepsilon_m-(\lambda-1)\varepsilon_2 \qquad (3.13)$$

with the previously noted hinge limit coefficient, λ, a constant for any specified 'k'. Equations 3.12 and 3.13 represent *simulated* algebraic expressions deduced from a considerable numerical database in 'k'. Typical values for 'k' and λ are given in Table 3.1 which follows.

FIGURE 3.6

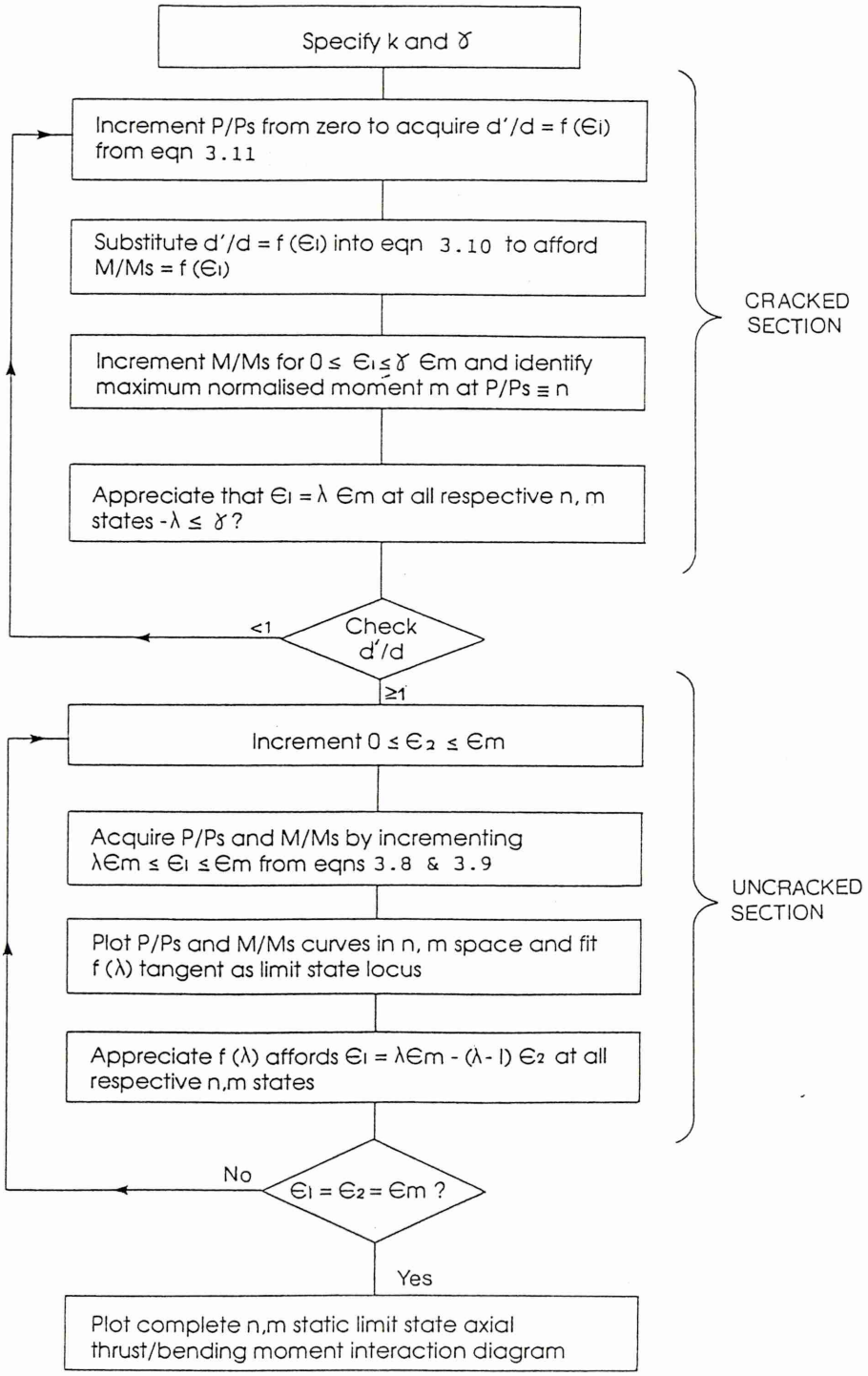

Maximisation procedure

Material Specimen/Data Source	k	λ	γ
Calcium Silicate Brick	3	1.227	>2.5
Rivelin Mill Bridge Sandstone[30]	7	1.16	1.23
Hodgkinson & Davies[46]	12	1.13$^{\triangledown}$	1.03$^{\triangledown}$
Sawko & Towler[33]	2	1.25	1.34

Table 3.1 Limit state parameters

$^{\triangledown}$Note: $\gamma<\lambda$

Static limit state values for structural masonry are therefore available from the key equations 3.8 to 3.11 subject to the conditions given above with, in normalised terms,

$$n = \frac{P}{P_s}\Bigg|_{\varepsilon_1=\lambda\varepsilon_m} \quad \text{and } m = \frac{M}{M_s}\Bigg|_{\varepsilon_1=\lambda\varepsilon_m} \tag{3.14}$$

(where P_s is the squash load and M_s is the maximum bending moment available from the section, equal to $P_s d/4$ - see note (ii) below regarding the middle half rule) for the cracked configuration $0\le n\le n_i$, as $0\le d'\le d$ and

$$n = \frac{P}{P_s}\Bigg|_{\varepsilon_1=\lambda\varepsilon_m-(\lambda-1)\varepsilon_2} \quad \text{and } m = \frac{M}{M_s}\Bigg|_{\varepsilon_1=\lambda\varepsilon_m-(\lambda-1)\varepsilon_2} \tag{3.15}$$

for the uncracked configuration $n_i\le n\le 1$, as $0\le d\varepsilon_m\le\varepsilon_m$.

3.3.2 A static limit state interaction diagram: cracked masonry sections

Equations 3.14 and 3.15 are represented most conveniently by means of a static limit state axial thrust/bending moment interaction diagram, and the result is depicted in Figure 3.7. This illustrates the static limit state interaction loci for k=2,3,7 and 12 with the k=2 locus representing the most enveloping or most resistant case concerned.

Safe combinations of axial compression and bending moment (sagging, $0\le e\le d/2$) lie between the respective 'k' locus and the abscissa. For hogging moments, $-d/2\le e\le 0$, the interaction loci adopt a mirror image about the abscissa.

FIGURE 3.7

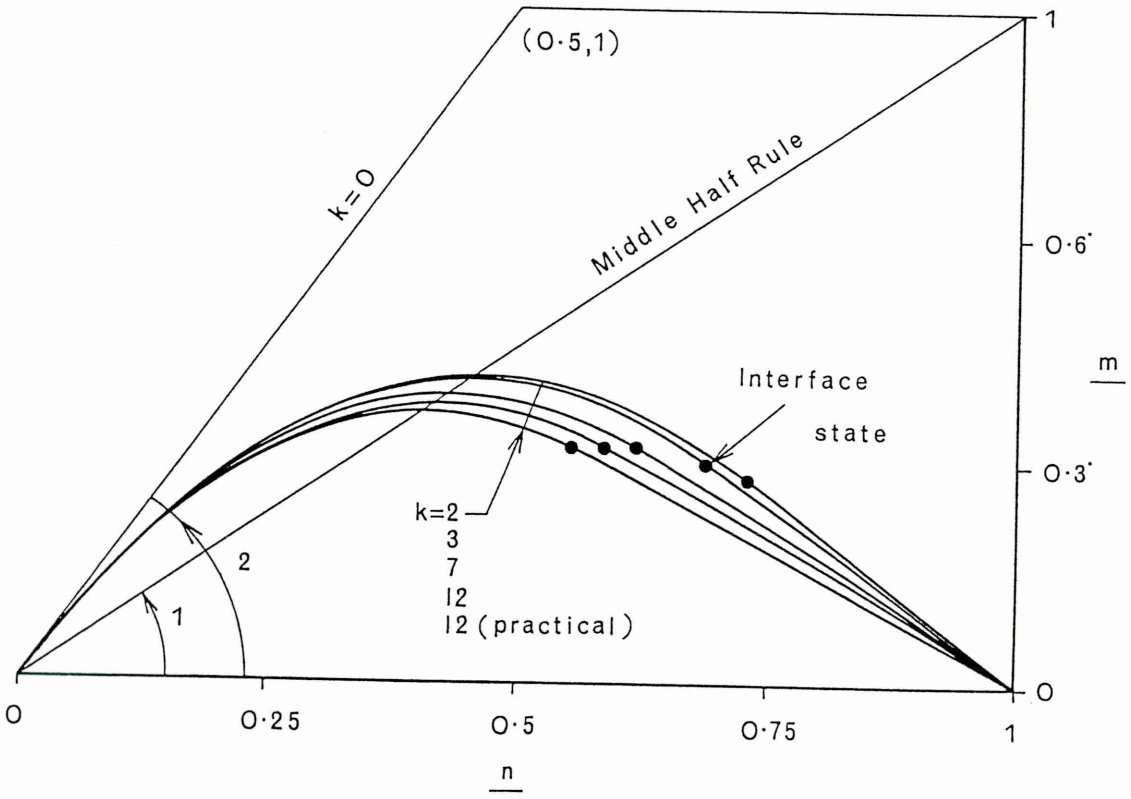

Static limit state axial thrust–bending moment interaction diagram

Key features to note are:

i) That the sectional resistance is enhanced as the constant 'k' decreases for $k>1$.

ii) That all loci maxima lie on the *middle half rule* - this can be demonstrated numerically by employing PSTRESS1 with typical output given in Table 3.2.

iii) That all 'real' material loci are inferior to a 'Heyman' idealised material locus ($k=0$), and thus a 'Heyman' material is non-conservative.

iv) That any point on a 'k' locus is taken to represent a masonry hinge for that material.

It should also be observed that since $\lambda>1$ in all cases, (as shown in Table 3.1) the falling branch of the load-deflection curve is as a direct consequence *crucial* to limit state definition.

By way of an example, consider the following. Let $k=2$ and $n,m=0.464$. The effective depth d' is 0.638d, and not zero as would be the case for an idealised Heyman material. Remembering that the maximum stress may not occur at the extreme fibre, then in this example, which corresponds with the middle half rule (see Table 3.2 below), maximum stress occurs at $y=0.372d \neq d/2 \neq d/4$.

k	Middle half rule moment maxima co-ordinates (n,m)	Cracked/uncracked interface state co-ordinates (n,m)
2	0.464, 0.464	0.729, 0.312
3	0.456, 0.456	0.689, 0.336
7	0.436, 0.436	0.618, 0.360
12	0.422, 0.422	0.586, 0.359
12$^{\heartsuit}$	0.408, 0.408	0.552, 0.358

Table 3.2 Key limit state interaction loci data

$^{\heartsuit}$Note: γ-restricted values for $\gamma<\lambda$ as Table 3.1

The foregoing presumes material integrity is available for strains up to at least $\lambda\varepsilon_m$, ie. $\lambda\varepsilon_m$ must not exceed fracture strain. The procedure in Figure 3.1 checks for this. Being a physical parameter, γ varies independently of 'k' so that masonry materials sharing a common 'k' value may readily possess individual values of fracture

strain $\gamma\varepsilon_m$. The k=12 example in Table 3.1 involves the corresponding mathematical parameter λ=1.13, in excess of the physical parameter γ=1.03 for the particular material under consideration. In such cases, the theoretical static limit state as set out above is unachievable, and the maximisation procedure must be modified - data runs show this is achieved simply by replacing λ with γ to force a lower practical hinge coefficient limit, this effectively results in a more restricted or less competent moment-thrust envelope.

To illustrate the point, two k=12 loci are shown in Figure 3.7; one corresponding to cases where λ=1.13$\leq\gamma$, the other to the particular case where practical fracture restrictions apply to the static limit state with γ=1.03$\leq\gamma$.

3.3.3 A static limit state interaction diagram: uncracked masonry sections

The traditional model for prevention of cracking (a defensible serviceability criterion), based upon a linear stress-strain law, is the middle third rule. This states that while ever the line of thrust remains within the middle third, or kern, of the section, then cracking will not occur. An alternative formulation is however obtainable based upon the more probable non-linear stress-strain law appropriate to most if not all masonry materials.

Static limit state values in prevention of cracking are available from the key equations 3.10 and 3.11 by substitution of d'=d and normalising as previously,

$$n = \frac{P}{P_s}\Bigg|_{d'=d} \qquad \text{and } m_{mc} = \frac{M}{M_s}\Bigg|_{d'=d} \qquad 0\leq n_{nc}\leq n_i \tag{3.16}$$

a non-linear formulation is available which defines the onset of cracking. Figure 3.8 once more represents the result in n, m space.

It will be noted that Figure 3.8, again depicting k=2,3,7 and 12 loci, is similar to Figure 3.7 but the areas between the locus and the abscissa in this case denote safe axial thrust-bending moment pairs *without cracking* the section. The loci themselves, therefore, represent the onset of cracking and each is consequently analogous to the middle third rule for its respective material. It is a key finding that, for any masonry material possessing a non-linear stress-strain characteristic, the traditional middle third rule strictly *does not apply*[43], and furthermore is *non-conservative* in respect of prevention of cracking.

FIGURE 3.8

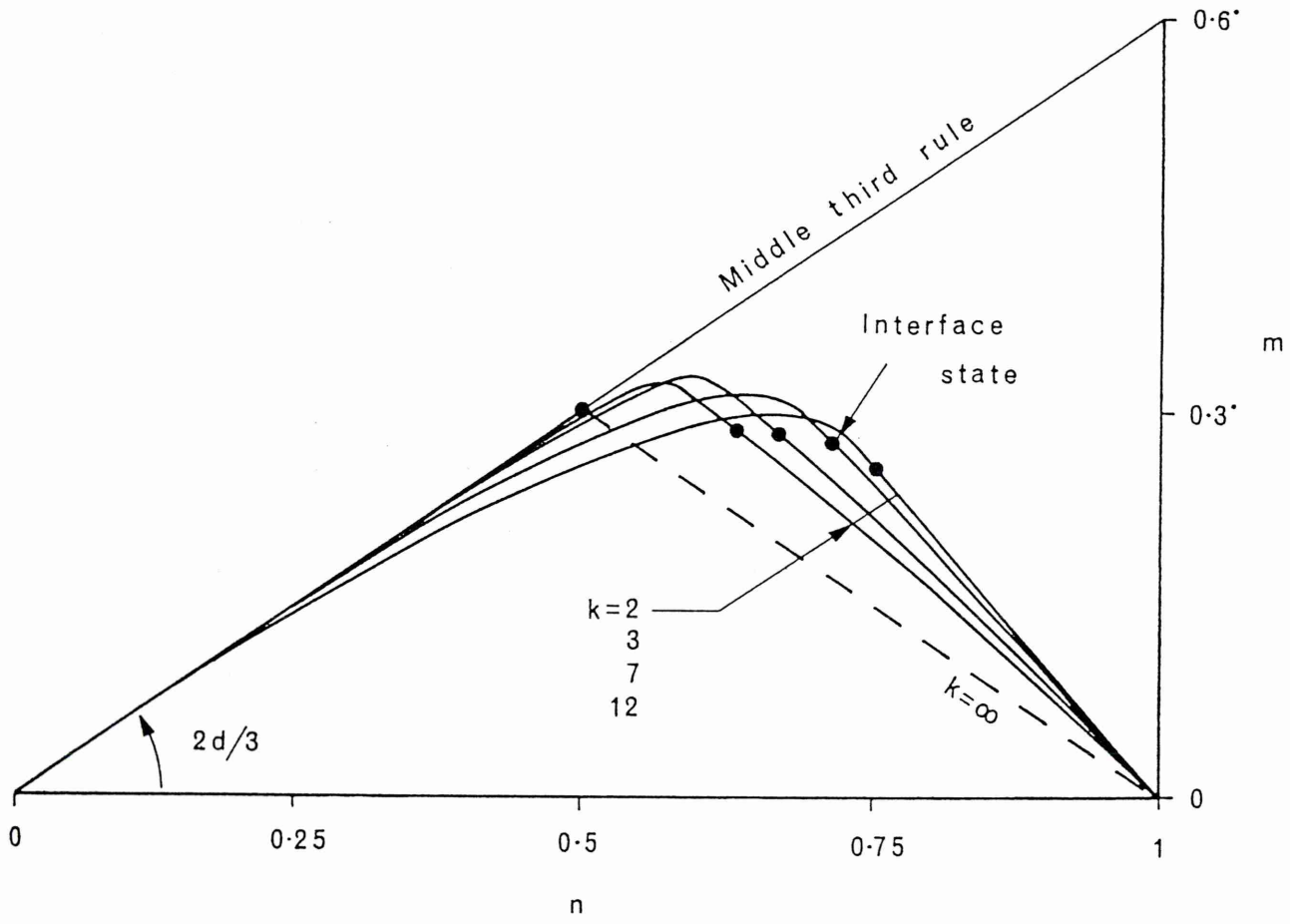

Static limit state axial thrust–bending moment interaction diagram for prevention of cracking

Figure 3.8 also depicts the middle third rule itself, which, as would be expected, corresponds precisely with the $k=\infty$ locus since this represents a linear stress-strain characteristic which is the basis for the middle third rule itself.

The divergence between the middle third rule and the "real" material 'k' loci can be seen to become progressively more significant at higher values of 'n'. The consequence of this is that the degree of non-conservatism of the middle third rule becomes progressively greater at increasing strains.

At high values of 'n', dependence upon the middle third rule would result in premature cracking for a "real" material possessing a non-linear stress-strain law.

In circumstances where a no-tension serviceability criteria is appropriate (questionable in the case of masonry vaults) the usefulness of the figure should be noted.

Finally, it must be said that the loci corresponding to equation 3.16 theoretically continue beyond the interface states shown in Figure 3.8. Each locus decays rapidly 'below' the respective uncracked static limit state locus, with each terminating at an unshown intersection (eg. 0.75, 0.25 for k=2) with a corresponding kinematic *physical breakdown* limit state locus. This latter locus can be derived for any $0<k<\infty$, $0\leq n\leq 1$, from the key equations given previously with, typically, λ replaced by γ in equations 3.14 and 3.15.

These kinematic physical breakdown loci typified by the k=12 (practical) locus in Figure 3.7 lie wholly within their static equivalents' envelopes and represent the states to which the static limit states degenerate as collapse, preceded by local crushing, finally occurs.

Computer programme PSTRESS1 may be used to derive stress and strain distributions for various points of interest on an interaction diagram, for example those depicted in Figures 3.7 and 3.8. Such exemplification serves to cross check between the two procedures and hence assists in verifying both, but is also helpful in the visualisation of the physical phenomena involved.

Figures 3.9 and 3.10 reproduce the two aforementioned interaction diagrams but this time with typical PSTRESS1-produced stress and strain plots (for k=2) superimposed.

FIGURE 3.9

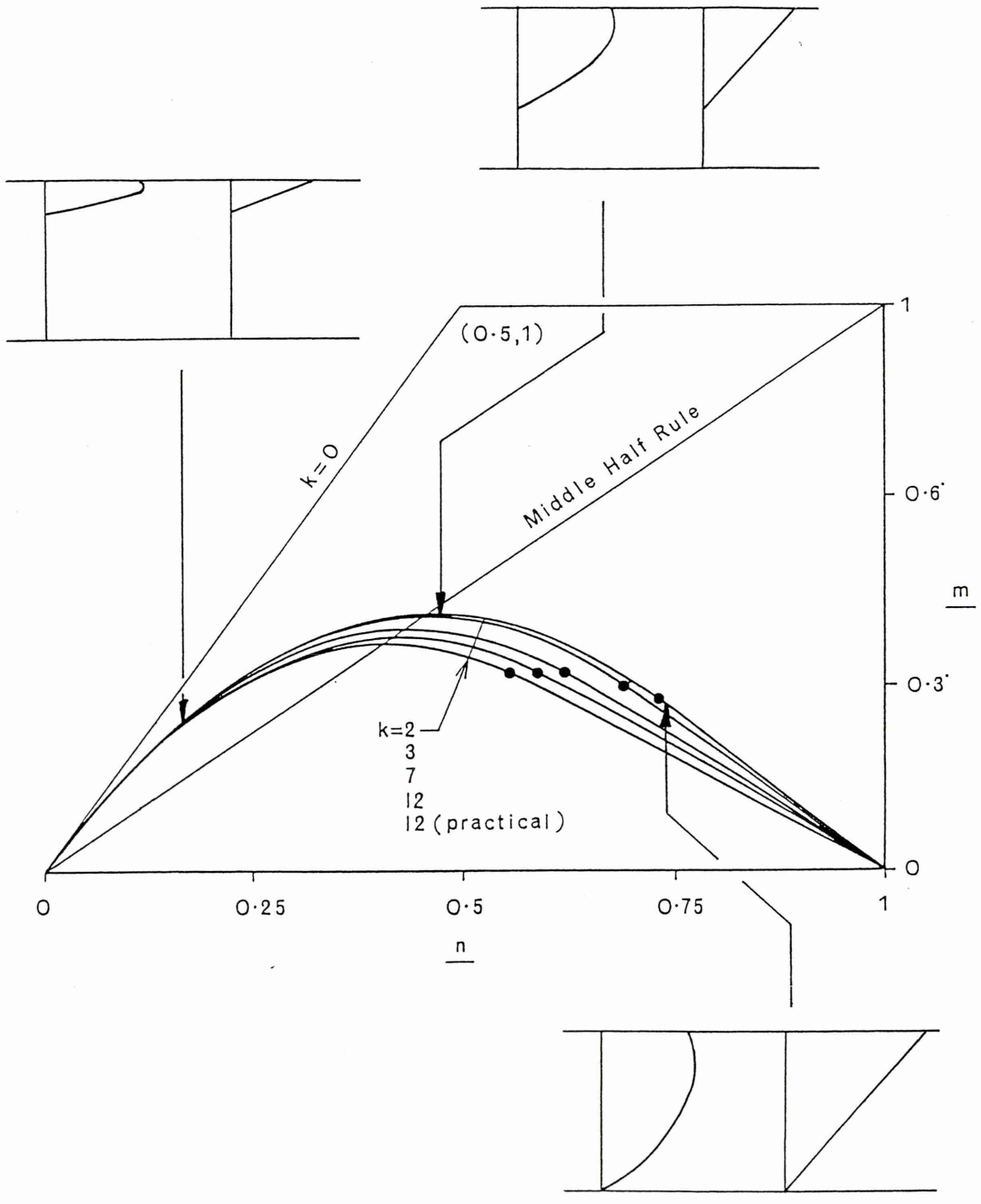

Static limit state interaction diagram with PSTRESS1-produced stress and strain distributions superimposed (k=2).

FIGURE 3.10

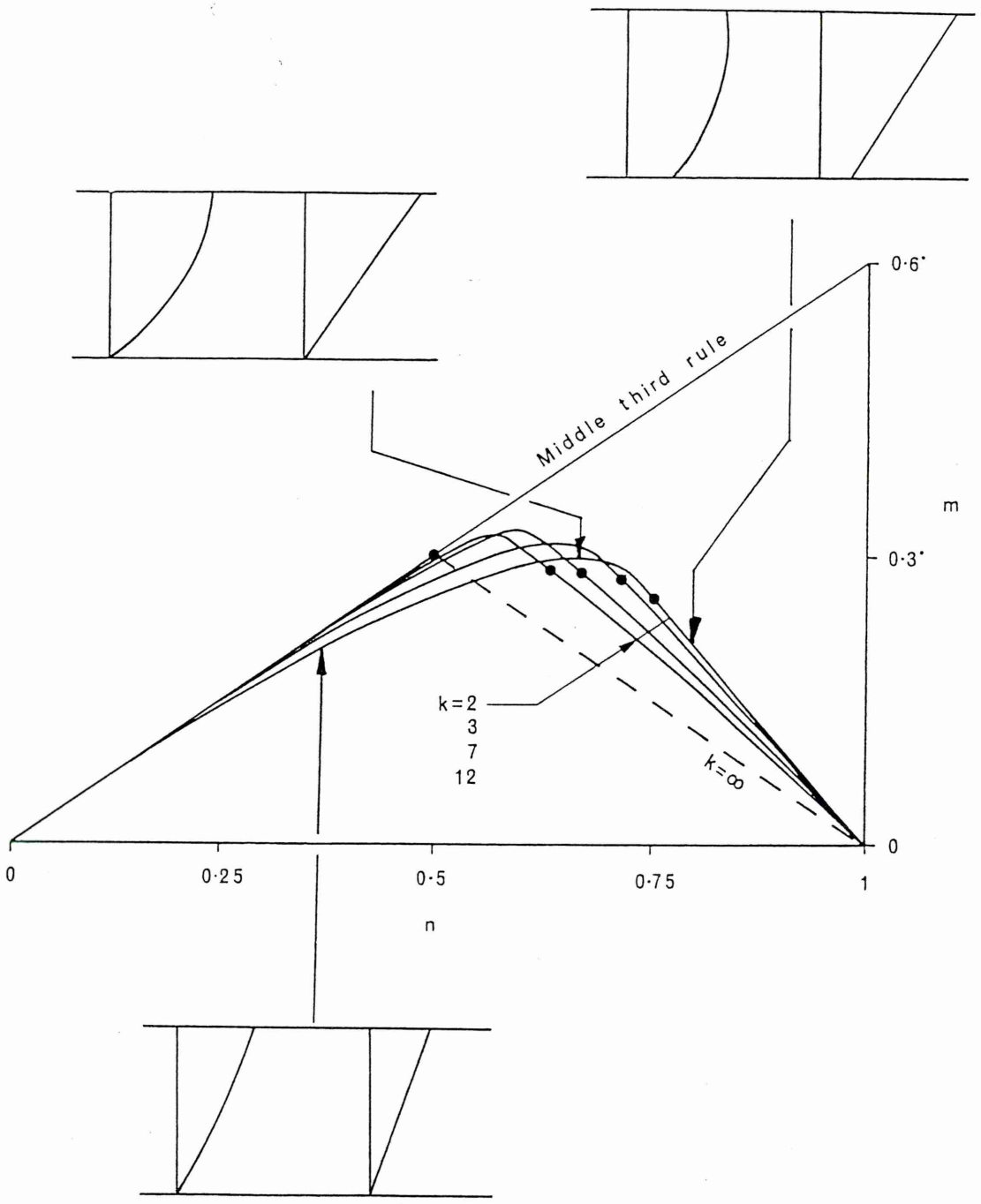

No-cracking static limit state interaction diagram with PSTRESS1-produced stress and strain distributions superimposed (k=2)

3.4 Experimental Masonry Hinge Models

The purpose of this work is to test the foregoing limit state studies in a context of some relevance to masonry arch vaults. It was therefore decided to attempt to model masonry hinges of the kind that might occur in an arch bridge four hinge mechanism failure. The calcium silicate bricks, for which a good deal of background data had already been gathered, were clearly ideal in both providing a known material and in a format that could be found in in-service brick barrelled arch bridges. Dry-jointing of the bricks was chosen to avoid composite material complications.

3.4.1 The testing regime

The loading was applied using the same in-house stroke-controlled rig as before. The object was to achieve a rotational failure in an eccentrically loaded pair of class 4 calcium silicate bricks, the pair being sandwiched between a further pair of bricks to minimise end effects. The arrangement was mounted in the testing machine between a pinned ram at the top and a pin joint at the bottom. The end conditions may not have been truly symmetrical since a preponderance for lower brick fractures was observed. Figure 3.11 depicts the arrangement.

Rotation was measured by two pairs of transducers reading from aluminium plates mounted on and projecting laterally from the brick pair under test. The angle of rotation for each brick was computed from the transducer pair displacement difference over the known gauge length. Plate 3.1 shows the transducer set-up from the side of the rig. Load data was taken directly from the loading machine.

It is generally accepted that stresses are low in traditional masonry structures and thus it was conjectured that hinges in masonry vaults were most likely to exist in the low 'n' region of n, m space (this is demonstrated in Chapter Five). Thus it was decided to bracket this range and to divide the hinge tests into three series of five, each at a different loading eccentricity, corresponding to three fairly low values of n. The values chosen were n=0.1, n=0.2 and n=0.3. The notation used was Na/b, denoting test number 'b' at n=0.'a'. The necessary offsets for the central brick pair were calculated and specified as 'e', as shown in Figure 3.11. All brick interfaces were rubbed together before mounting in the rig and the loading topology was then carefully set up.

FIGURE 3.11

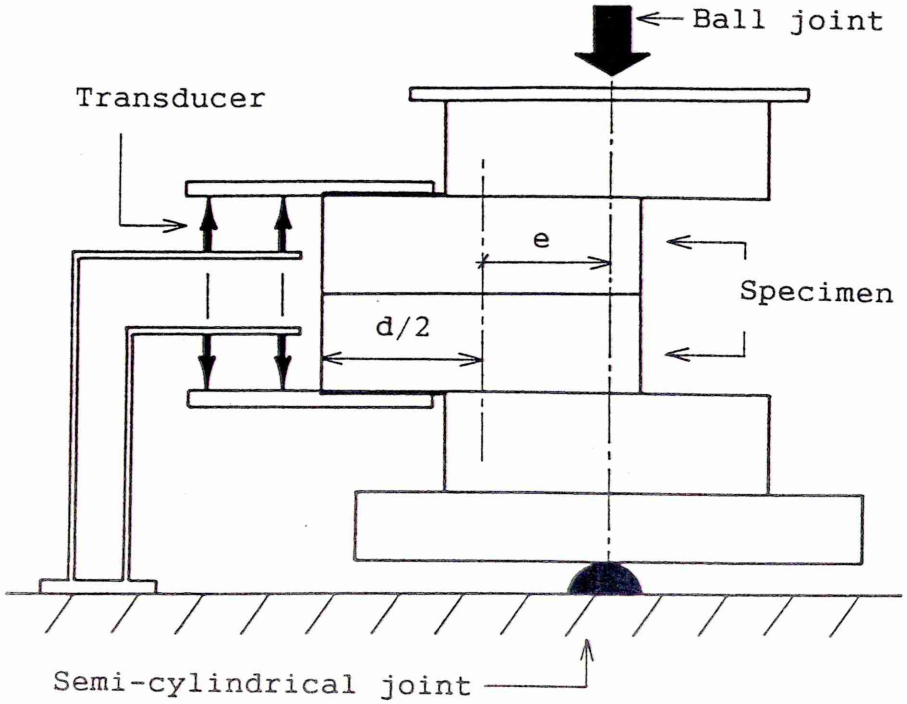

Experimental masonry model hinge test topology

PLATE 3.1

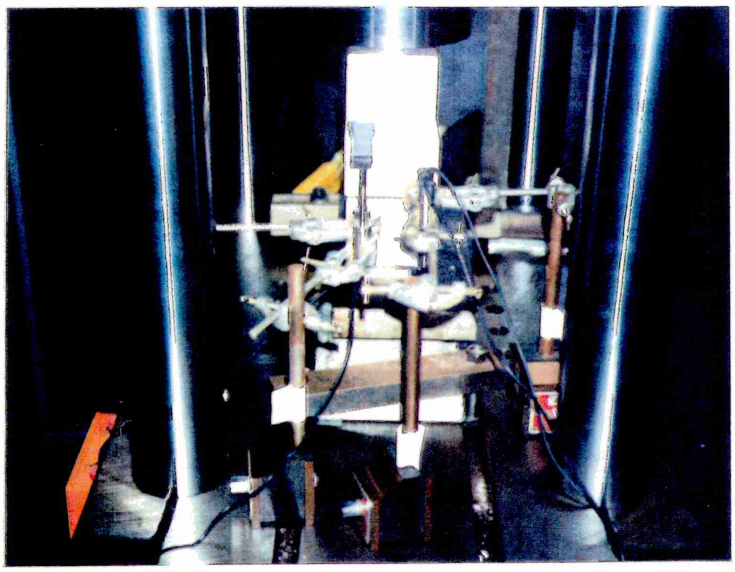

Detail of arrangement for model hinge rotation measurement

Despite fears that the loading arrangement was potentially unstable, the tests proceeded well and hinge-type failures were produced in a progressive and predictable manner. In practice the tests could have been taken as far as required, but were in fact terminated a reasonable period after peak load.

Appendix 'B' contains Plates B1 to B5 which the five samples tested at n=0.1 either before or after testing; Plates B6 to B10 similarly show the n=0.2 set, and Plates B11 to B15 the n=0.3 set. Accompanying each plate a corresponding Figure (B1 to B15) traces the force-rotation curve, respectively, for each test. Note that only the data points in the figures relate to measured information.

For purity at least, one would wish to produce true moment-rotation curves. The lack of a simple means to measure the changing 'e' as deflections became significant, however, results in the production of the force-rotation curves presented instead. Despite this, rotation proved to be slight before peak load and thus the curves may in practice be regarded as effectively moment-rotation to at least that point.

Table 3.3 which follows gives primary data relating to the hinge tests.

Ecc. e (n)	Peak Loads -------- Test number --------- 1/	/2	/3	/4	/5	Mean peak load (kN)	Std. dev. (+/-)	Coeff var. (%)	Theo. peak load$^{\nabla}$ (kN)
0.1	84.2	91.9	80.2	89.7	81.5	85.5	5.108	5.97	70
0.2	137.9	140.2	137.2	143.9	161.1^{R}	144.1	9.878	6.85	139
0.3	200.1	221.1^{R}	214.7	211.8	218.2	213.2	8.112	3.80	209

Table 3.3 Model hinge test data

$^{\nabla}$Note: The theoretical peak load employs average σ_m from corresponding whole brick and core tests.

^{R}Note: Replacement test after an originally anomalous result (thought to have arisen from a defective brick).

3.4.2 Model hinge test results

The theoretical peak load values given in Table 3.3 employ the average of the mean peak stress data as noted in Chapter Two (ie. σ_m=31.6 N/mm^2) in conjunction with equation 3.14 for k=3 and λ=1.227 as stipulated in Table 3.1; it is considered that experimental consistency and good experimental/theoretical correlation are exhibited.

The validity of averaging the mean full brick and core values for σ_m for use with the hinge experiments lies with the fact that, while full brick constitutive testing effectively corresponds to the use of the same prototype model voussoirs as employed in the hinges, the cores, with their smaller cross-section, are more representative of the corresponding voussoir strain gradient topology encountered therein.

A graphical interpretation that enables theoretical/experimental correlation to be put in the context of *both* flexural and compressive actions is to be seen in Figure 3.12 which superposes experimental data on the appropriate portion of the k=3 interaction diagram. Good overall experimental/theoretical correlation is again displayed.

Figure 3.12 also includes the corresponding limit state locus based on the linear elastic constitutive model ('Heyman', $k=\infty$). The superiority of the proposed non-linear k=3 modelling over the traditional linear model can be seen.

Such findings support the development of a masonry arch bridge mechanism model based on the proposed non-zero but finite 'k' hinge formulations, and this is undertaken in the next Chapter.

3.4.3 Discussion

It was observed during the laboratory hinge testing that very little distress would normally occur before maximum load was attained. This was supported by the smooth nature of the load-deflection response to beyond peak load, and its breakup, accompanied by cracking sounds, as macro-cracking occurred later. Equally, visible signs of rotation of the samples were difficult to detect before the peak load.

It is concluded that *in-service masonry arch bridges may embody visually undetectable hinges*.

The point is well illustrated in Plate 3.2 which time-lapse traces a complete hinge test.

The mode of failure of the hinges appears to be a function of 'n'.

Plate 3.3 depicts a typical failure at n=0.1, Plate 3.4 one at n=0.2 and Plate 3.5 one at n=0.3. Plates 3.6 and 3.7 depict n=0.3 failures viewed from the end.

FIGURE 3.12

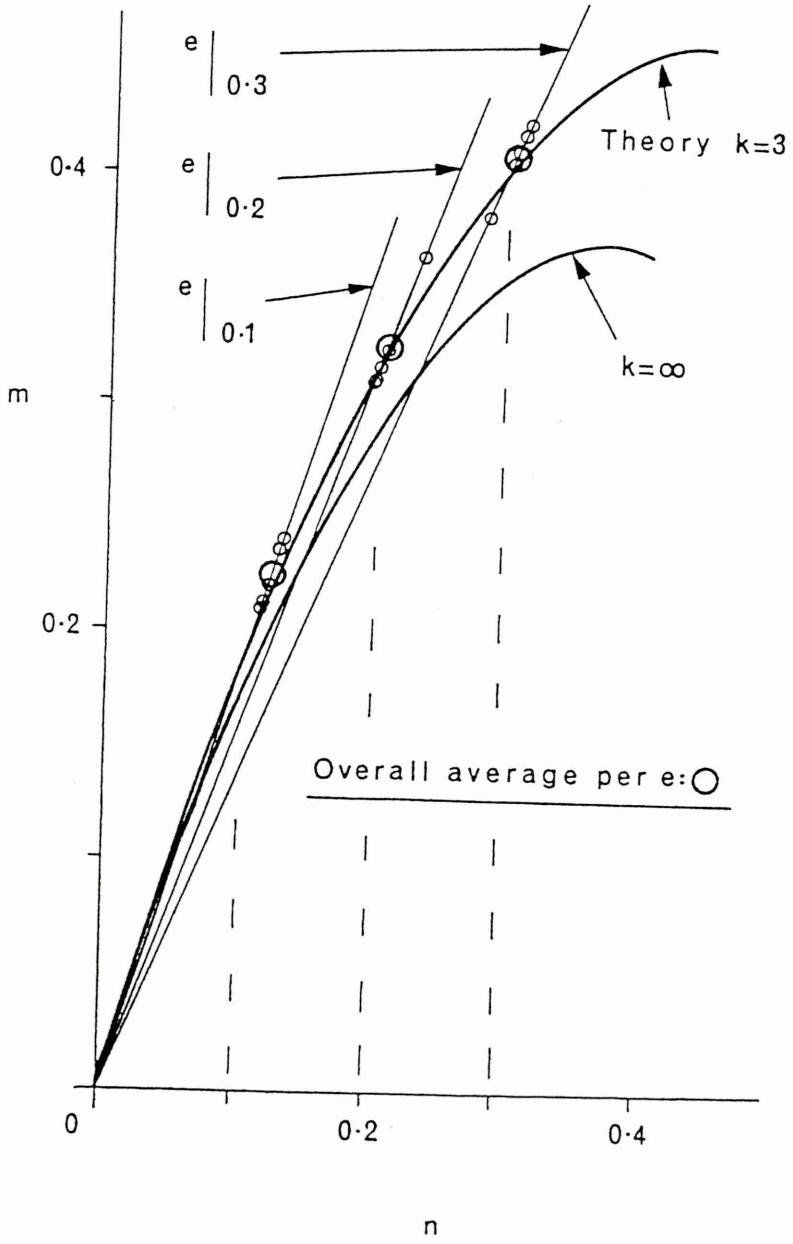

Experimental interaction data

PLATE 3.2

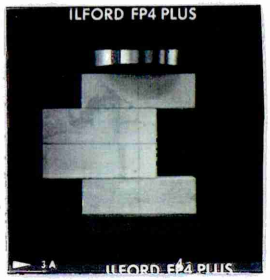

Start 150kN

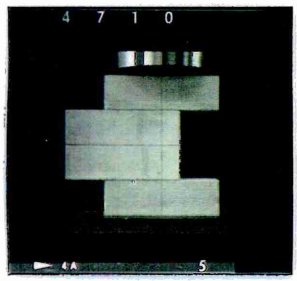

160kN

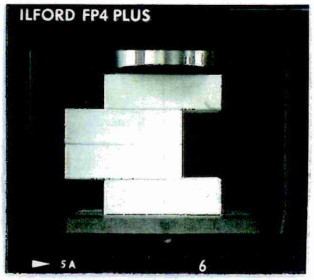

180kN

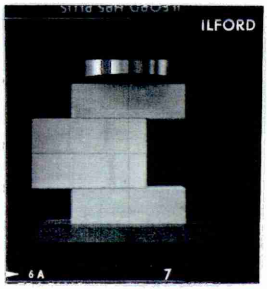

190kN

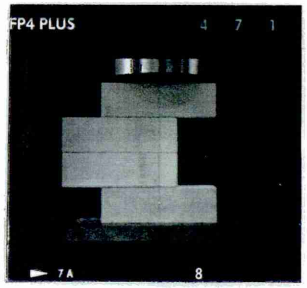

193kN (Peak)

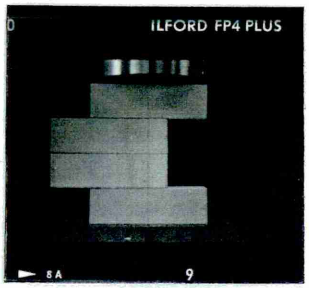

180kN

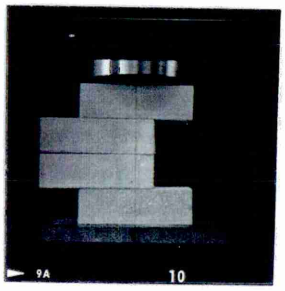

120kN

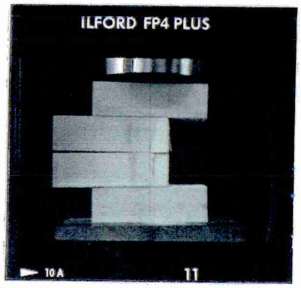

100kN

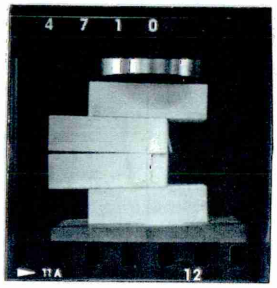

80kN

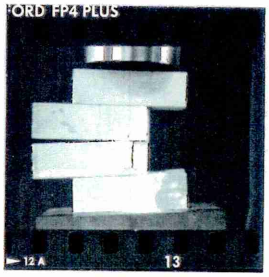

50kN End

This sequence of ten time-lapse photographs traces a masonry model hinge test under stroke-controlled loading. Note the absence of distress (and rotation) visible before the peak load is reached.

PLATE 3.3

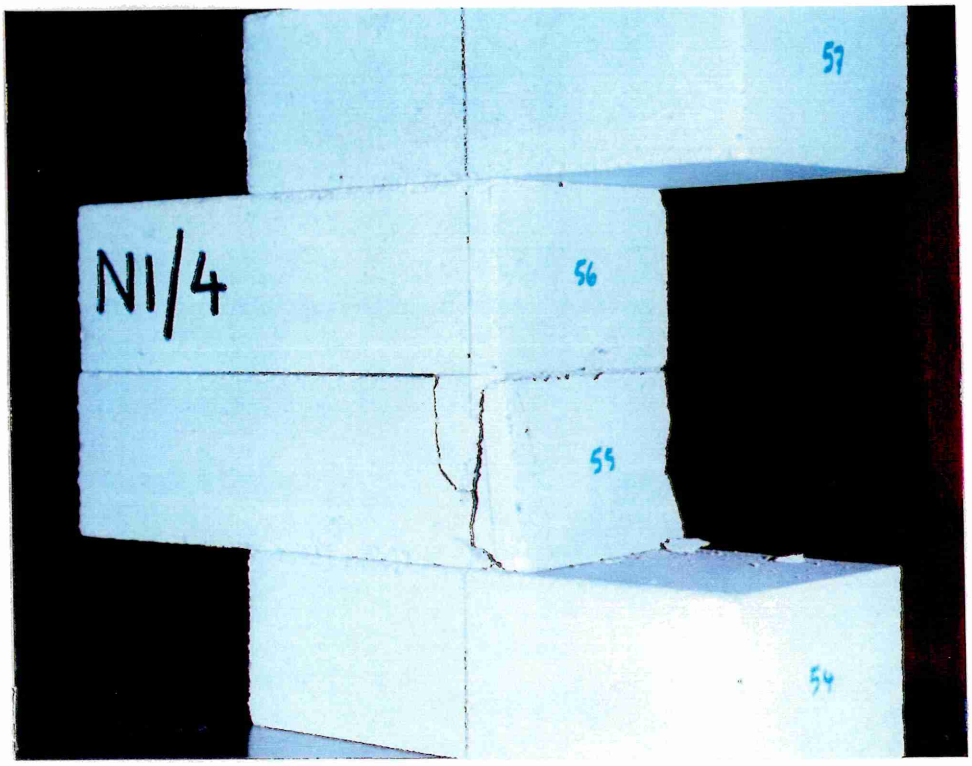

Typical model hinge failure mode for n=0.1 (compare with Plates 3.4 and 3.5)

PLATE 3.4

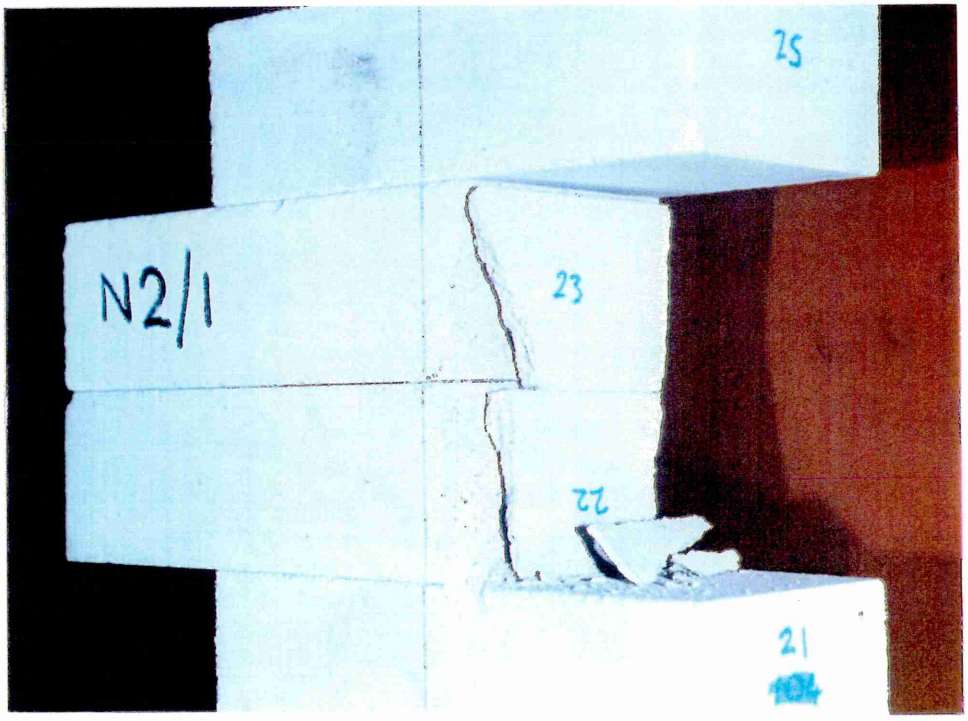

Typical model hinge failure mode for n=0.2 (compare with Plates 3.3 and 3.5)

PLATE 3.5

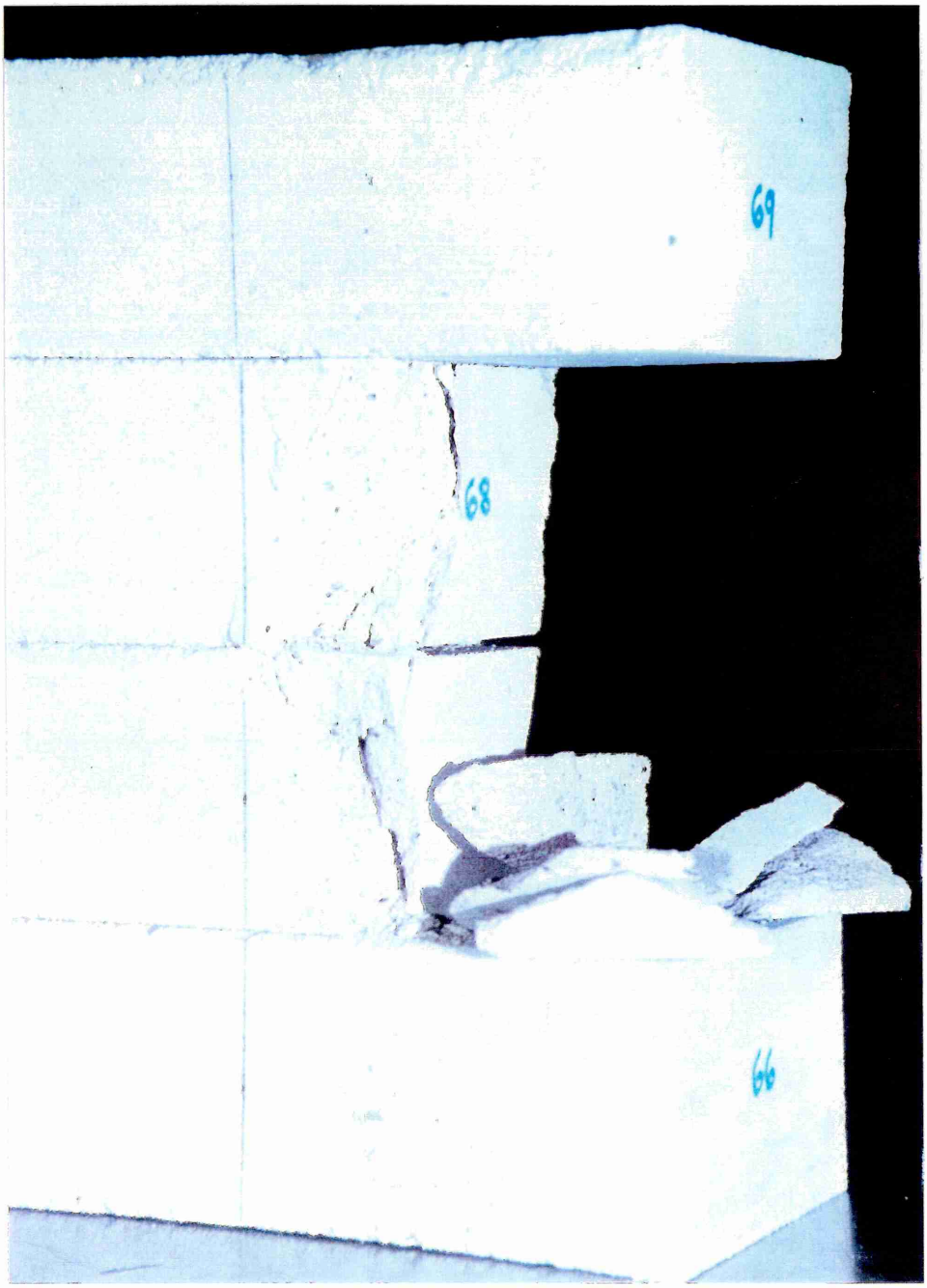

Typical model hinge failure mode for n=0.3 (compare with Plates 3.3 and 3.4)

PLATE 3.6

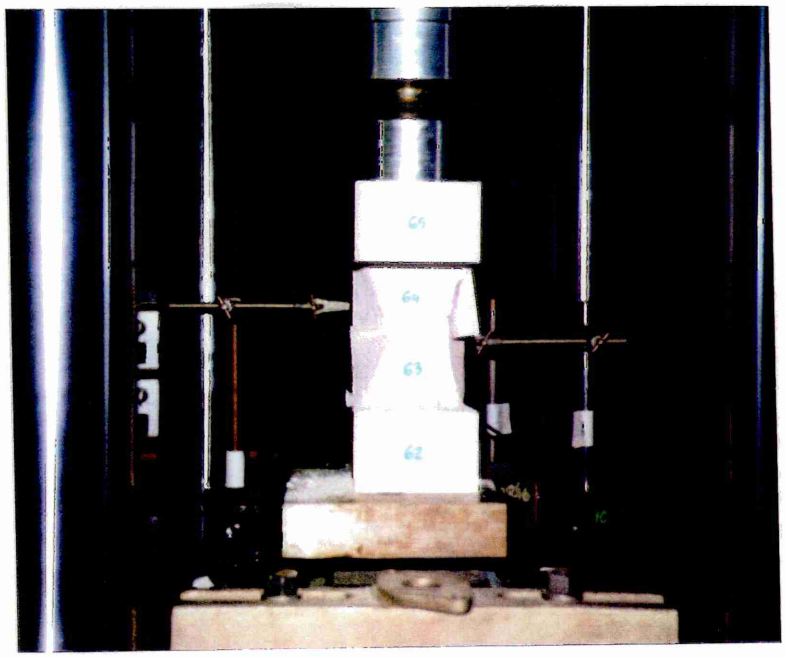

End view of mode of failure for test N3/1

PLATE 3.7

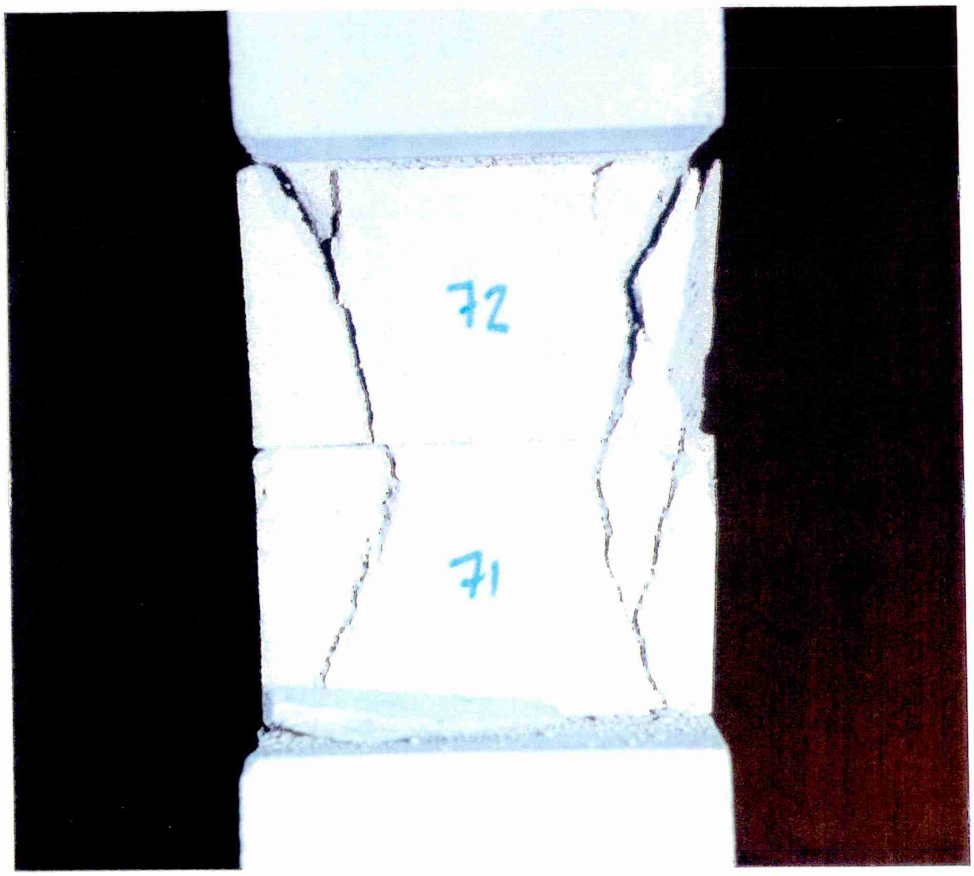

End view of mode of failure for test N3/3

As noted previously, only the data points in the force-rotation plots (Appendix 'B') relate to measured information. The smooth curve also portrayed is a mathematical idealisation for that data set. The form of equation employed is

$$y = C_1 - C_2\sqrt{x - C_3 e^{-C4x}} \qquad (3.17)$$

where C_1 to C_4 are constants influencing influencing rate of attack (initial stiffness), peak value and rate of decay. They were varied by trial and error for each of the fifteen hinge tests until a good fit was achieved for each. The coefficients were then averaged for the n=0.1, 0.2 and 0.3 sets to produce an 'average' curve for each data set. The resulting three curves are superimposed and plotted as Figure 3.13a). It may be noted from this figure that:

i) The peak loads occur at lower rotations with increasing 'n'.

ii) The rate of attack (rotational stiffness) increases with increasing 'n'.

iii) As a consequence of i) and ii) above, the hinge becomes more brittle with increasing 'n'.

A conclusion is that, if "large" arch vaults do occupy regions of n, m space further from the origin than "small" arch vaults, then larger arch vaults may exhibit a more brittle onset of hinge formation.

Figure 3.13b) shows where on a k=3 interaction diagram the three sets of hinge tests lie.

It should also be noted that the derived thrust-rotation loci are quite distinct from their familiar *ductile* steel counterparts; this is not surprising in view of their lack of a constitutive yield surface in accordance with Figure 2.8 in the previous chapter.

A key implication with regard to masonry arch bridge mechanism analysis is that deformations are unlikely to be significant until hinge formation is well advanced and that any early formed hinge in a four hinge collapse mechanism undergoes fluctuations in resistance while awaiting development of the fourth, mechanism completing hinge. Figure 3.13a) is not to suggest, however, that eccentricity would remain constant in the process. Load/deformation path history is not essential to a four hinge mechanism limit state model; the primary requirement is that, for any particular case study, the proposed mechanism must be statically admissible.

FIGURE 3.13

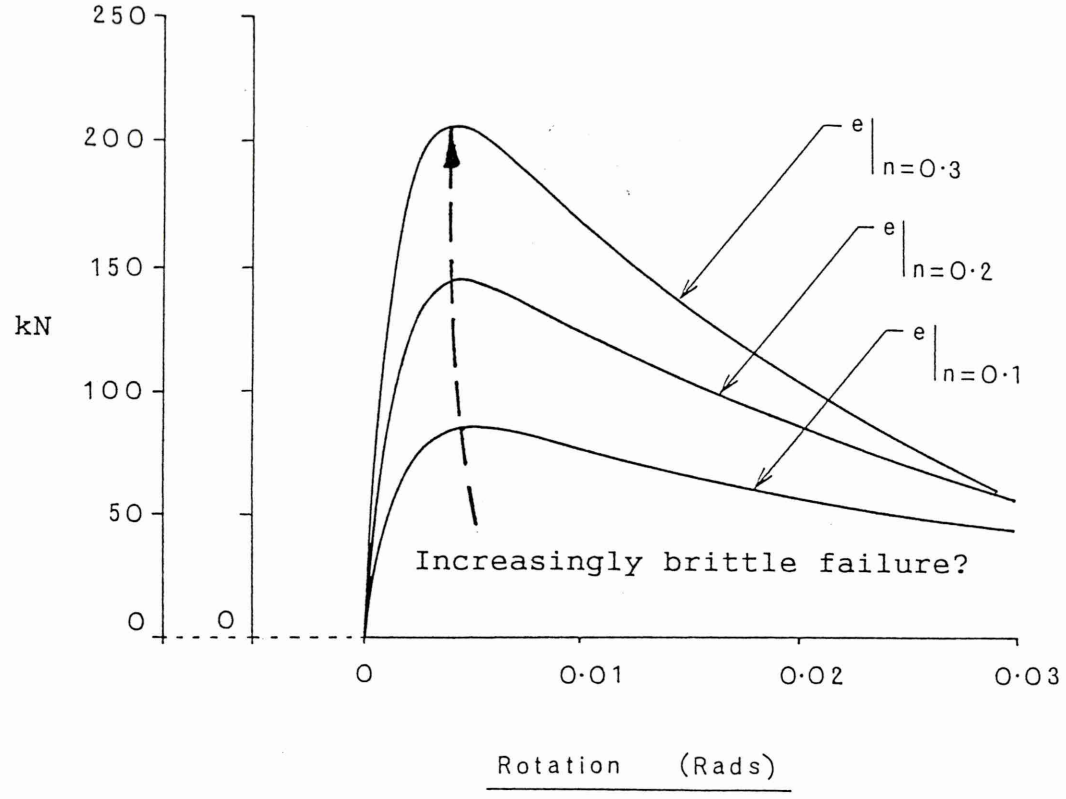

a) Force-rotation diagram

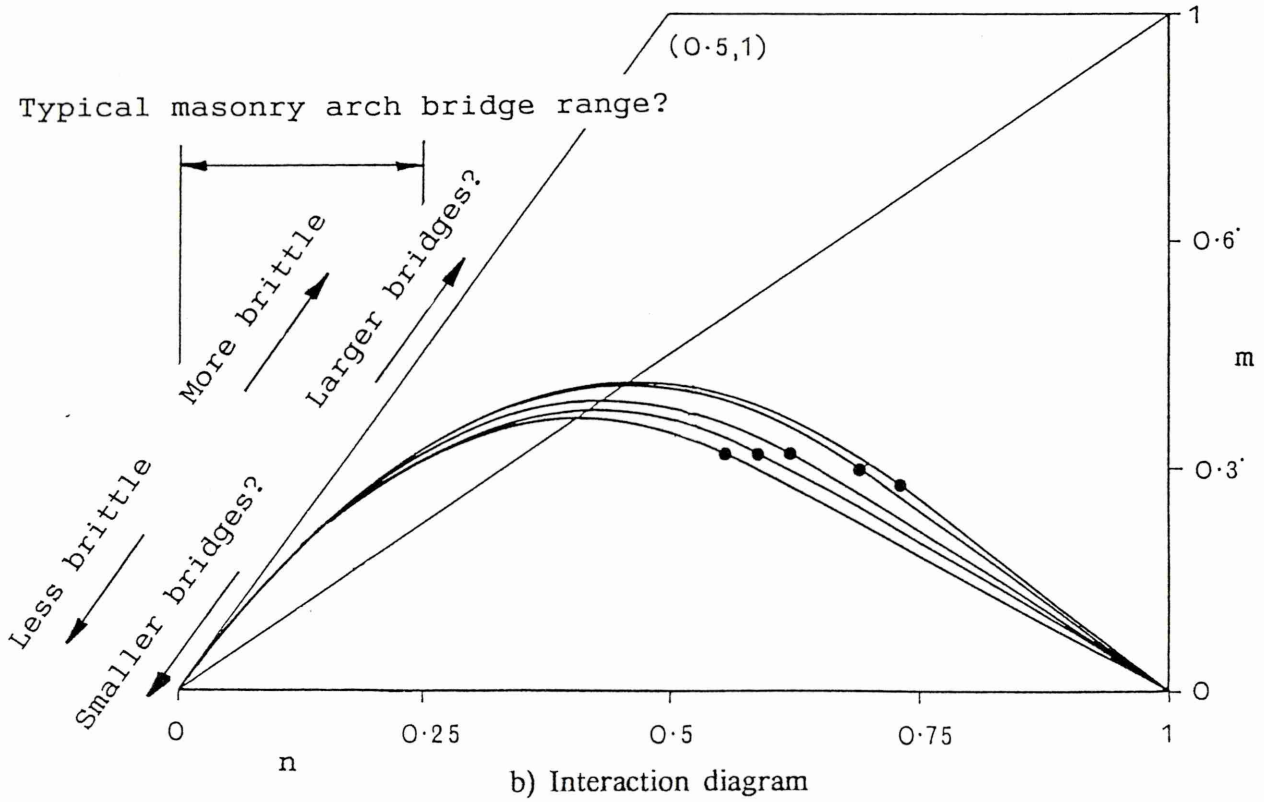

b) Interaction diagram

Speculation on the relative brittleness of the onset of hinge formation for mechanism failures for varying sizes of arch vault.

3.5 Conclusions

The non-linear 'k'-based formulations of the previous chapter have been developed to provide a set of equations, unamenable to formal computational manipulation, which have been solved numerically to enable the solution of the state of stress in a masonry section; to furnish both a static limit state axial thrust/bending moment interaction diagram, and also a corresponding serviceability limit state, prevention of cracking interaction diagram.

A key conclusion stemming from the diagrams is that sectional resistance is enhanced as the constant 'k' decreases. Differentiation is thus now possible between hitherto identically-treated natural materials, and equally one may now dispense with the incongruous and non-conservative infinite stiffness/strength model often employed in the masonry arch field.

A second key finding, of wider "rule-of-thumb" value in its own right, is that all 'k'-loci maxima lie on the middle half rule. Thus a masonry section's maximum bending resistance occurs when the thrust line lies at the middle half position. Furthermore, this is true irrespective of the material's constitutive properties.

A related key implication is that, for any masonry material possessing a non-linear stress-strain characteristic (possibly all such materials), the traditional middle third rule strictly *does not apply*, and additionally is *non-conservative* in respect of prevention of cracking.

It is postulated that any point on a static limit state interaction diagram 'k' locus represents a masonry hinge for that material. A more sophisticated prediction and modelling of hinge formation than is presently the norm should be possible, of especial use in masonry arch mechanism analysis.

An extensive series of model hinge tests has been undertaken in the laboratory to test the 'k'-hypothsis, and it is considered that overall experimental consistency and good experimental correlation with the theoretical studies have been obtained. The claim that masonry hinges are located on the edges of the appropriate 'k' interaction envelope has been supported, paving the way for its application in masonry arch mechanism applications.

CHAPTER FOUR

A Masonry Arch Mechanism Analysis Computer Programme

4.1 Synopsis

The findings of Chapters Two and Three are applied practically in purpose-written computer software, SMARTMEC, which analyses masonry arch vault mechanisms at the ultimate limit state *with allowance for material properties at the hinges*.

Briefly, SMARTMEC solves for the value of an external point load, applied at deck level, by numerical analysis of a metre strip, single span, unskewed masonry vault with its abutments at the same level and with no allowance for spandrel wall edge stiffening. The arch profile is described by a quartic equation fitted through five points symmetrical about the crown. The live load may be distributed down through the fill and allowance made for lateral earth pressures. An animated computer monitor display continually updates data for each hinge. When the numerical solution routine non-closure falls below a small predetermined figure, the programme terminates and the final value of the external live point load is displayed.

4.2 A Computer Programme: SMARTMEC

4.2.1 Introduction

SMARTMEC, a P.C.-based software package, was written to perform a masonry arch mechanism analysis of the generic type described in Chapter One. As noted therein, mechanism analyses have hitherto employed either infinite stiffness/strength

constitutive properties, or alternatively a finite strength leading to approximate, linear, compressive stress distributions through reduced sections at the hinge positions.

SMARTMEC instead employs the ultimate limit state interaction curve studies of Chapter Three to provide a more refined hinge modelling.

Figure 4.1 depicts the salient differences between the traditional hinge model (Figure 4.1c) against the proposed model (Figure 4.1b) in the context of a four hinge mechanism arch failure (Figure 4.1a).

4.2.2 SMARTMEC: preliminaries

SMARTMEC evolved substantially during these studies but only the final version will be described here. As essentially a vehicle for the proposed interaction curve-based hinge theory, even in its final form it makes no claim to fully cater for other parameters, eg. differences in horizontal earth pressures for vault segments moving into and away from the fill, particularly in comparison with commercially available equivalents, eg. "Archie".

The incorporation of the interaction curve-based hinge theory was crucially dependent on the hypothesis that hinges lie on the relevant (to that particular masonry type) static limit state interaction locus.

To simplify programming it was desirable to have available a closed-form expression for the interaction loci. This was obtained by rearranging equation 3.11 for d' and substituting into equation 3.10 to yield a closed-form equation between bending moment (M) and thrust (P). This equation is employed within SMARTMEC.

By expressing M and P in terms of their respective maxima, the closed-form equation may be further rearranged to afford a general purpose, closed-form equation for a cracked section in terms of m and n thus

$$m = 2n\left[1-\left\{\frac{[1-k]}{3[k+1][k+2]}\,\frac{[6\lambda^k-k\lambda(k+1)(k+2)]}{[k\lambda/2-\lambda^k/(k+1)]^2}\right\}n\right] \qquad (4.1)$$

This equation is valuable since it relates 'm' and 'n' directly, *enabling the solution of moment and thrust at a cracked masonry hinge with any characteristic 'k' value.*

FIGURE 4.1

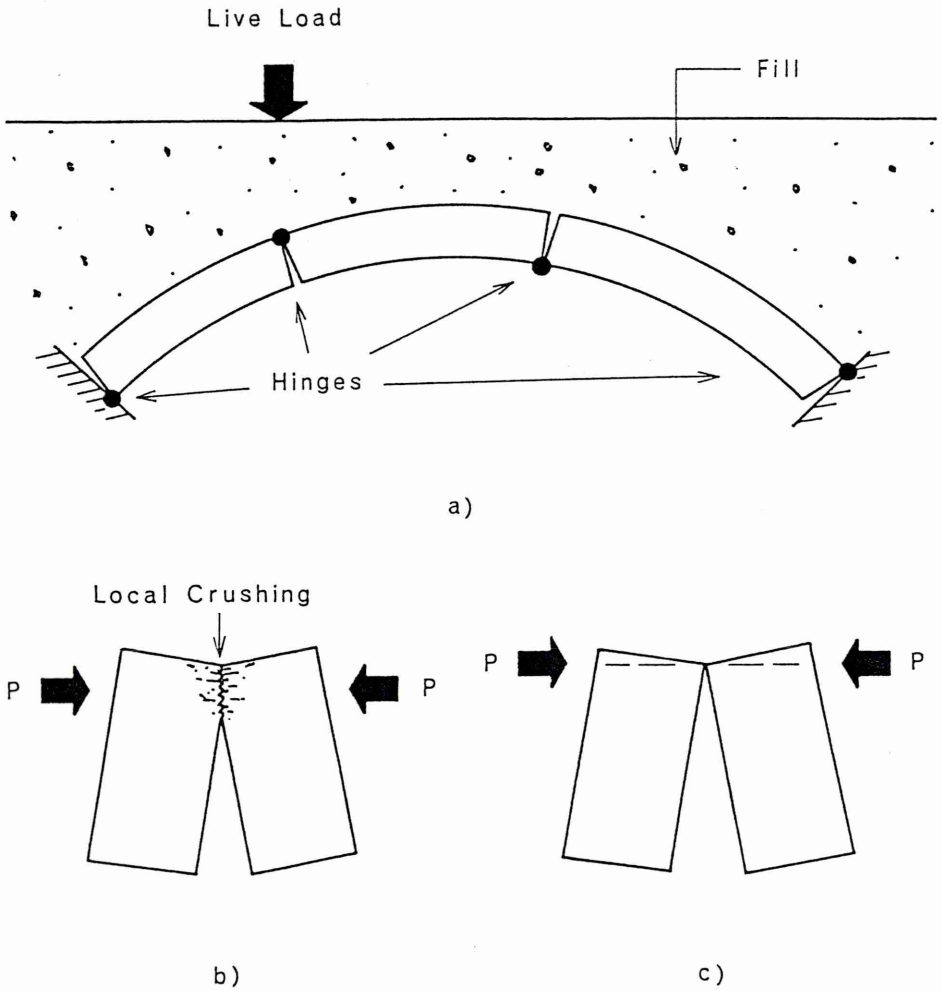

Four hinge masonry arch collapse mechanism

a) Topology b) Proposed hinge model c) Existing hinge model

Limiting the scope solely to cracked sections is considered justified since, as later work will show, masonry vault hinges typically form at relatively low values of 'n' in n, m space. As a consequence, the cracked equations of the last chapter alone suffice for all practical purposes.

4.2.3 SMARTMEC: assumptions and features

The basic features of SMARTMEC are:

1. The analysis is limited to a metre strip of a single span, unskewed masonry vault with its abutments at the same level, making no allowance for stiffening effects due to spandrel or parapet walls.

2. The arch profile is described by a quartic equation fitted through five points symmetrical about the crown, so various (symmetrical) profiles can be approximately modelled. Alternatively, a segmental profile can be declared at the outset and just the span and rise input.

3. Different barrel thicknesses may be specified at the springing and the crown, with the programme linearly interpolating the thickness between. This feature is needed to analyse Shinafoot full-scale arch test, to be described in the next chapter.

4. Loading is limited to a single point load (or knife edge load (KEL)) applied in any position on a half span. In practice the load is usually applied at the quarter point, being approximately the critical position.

5. The single point load may be transmitted from deck level down through the fill by any one of four, user-specified, means:

    a) A Boussinesq distribution.
    b) A 2:1 (vertical to horizontal) distribution applied as a triangular load at extrados level.
    c) A 2:1 distribution applied as a uniformly distributed load at extrados level.
    d) With no distribution at all and the point load applied directly to the extrados.

6. The vault is divided into fifty elements of equal length when projected onto the horizontal chord. The weight of the strip of fill above each element is applied as a

point load to the element of vault below it.

7. Horizontal forces may be applied to allow for lateral earth pressures by multiplying each of the fifty vertical loads by a specified earth pressure coefficient to give a horizontal component. The coefficient is a single value for the entire arch and no distinction is made between areas of barrel tending to move into the fill and those tending to move away. An empirical enhancement factor (typical values 1 to 2) may also be used and is applied to the coefficient linearly from its specified maximum value at the springings to unity at the crown.

After data input a graphic depiction of the structure and its loading are output to the computer monitor - see Plate 4.1. An animated display of the load vectors (a combination of vertical and lateral force components) is shown at the top of the screen together with continually updated data for each hinge displayed towards the bottom. The hinge positions are marked by small circles. External reaction values and the solution routine current measure of closure are also portrayed.

When the numerical solution routine non-closure falls below a small predetermined figure, the programme terminates and the final value of W is displayed. This will typically take tens of minutes, depending upon the computer available.

4.2.4 SMARTMEC: algorithm

The aim is to solve for the value of W, the external point load, for which eleven equations are required (it is implicit in the method that the structure is in horizontal equilibrium if lateral earth pressures are invoked). The main algorithm is:

1. Define span, rise and quarter point rise. Fit a quartic equation through these five points (Figure 4.2a).

2. Divide the span into fifty vertical strips based upon equal horizontal projections (Figure 4.2b).

3. Compute the x and y coordinates at each of the resulting 51 nodes. Analysis henceforth relates to this structural centreline skeleton.

4. Define the vault thickness at the springings and at the crown. These are usually the same, but linear interpolation between the two can provide for a varying vault thickness.

PLATE 4.1

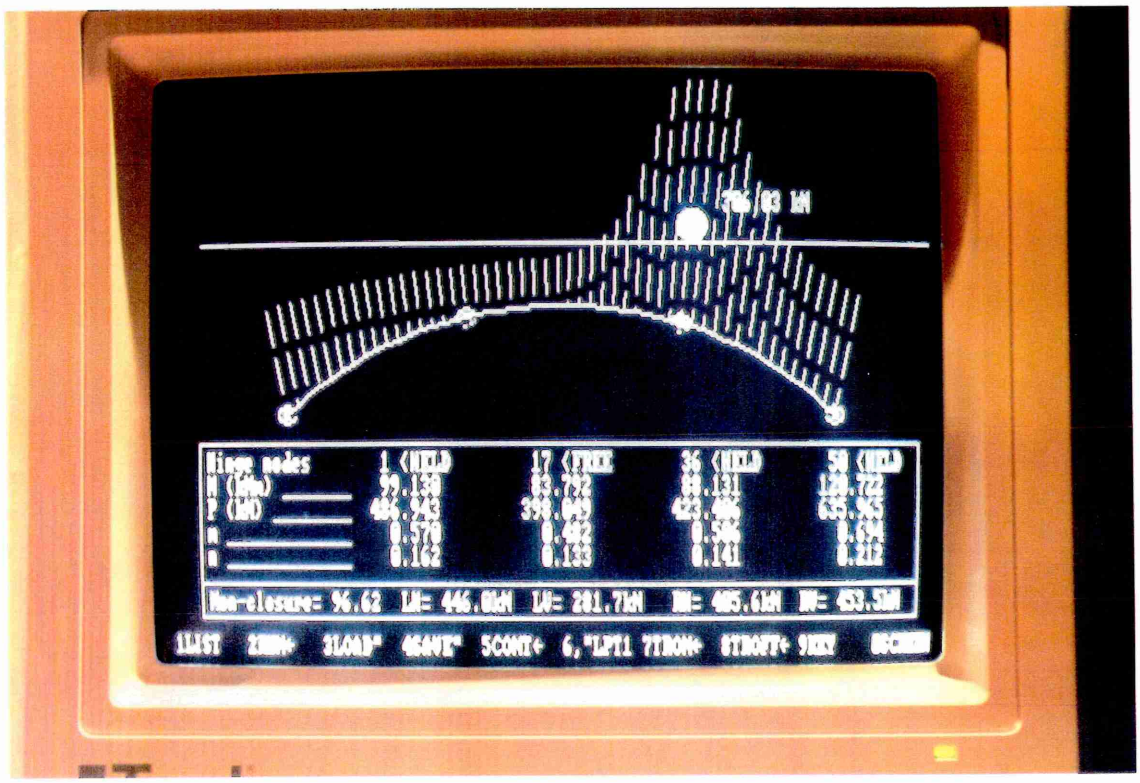

Typical SMARTMEC computer programme monitor display

The single wheel live load is depicted at deck level and its weight, together with the dead load due to the arch and fill, are transmitted to the vault by the point load vectors shown. Their inclination is due to the horizontal earch pressure component. The current positions of the (moveable) hinges are depicted by the small circles on the arch. The table at the foot of the display gives data (moment, thrust, n and m) for each hinge together with the external reactions and the current state of closure of the numerical routine. The display is refreshed on each cycle of the numerical analysis until convergence is reached.

FIGURE 4.2

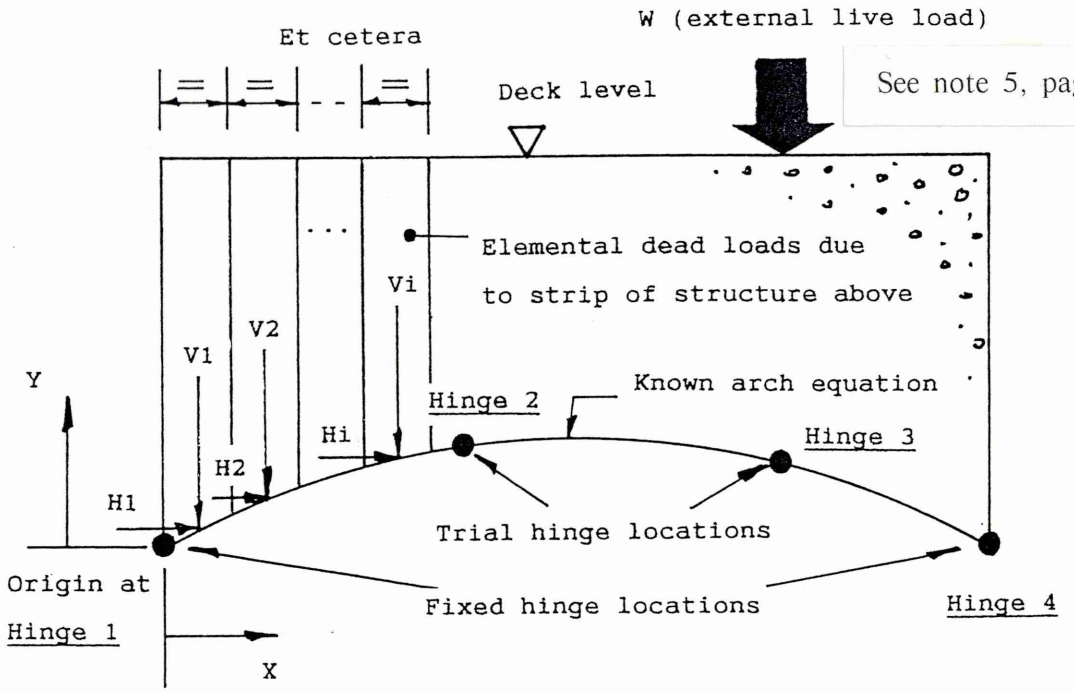

	Hinge number			
	1	2	3	4
X	X_d	X_c	X_b	X_a
Y	Y_d	Y_c	Y_b	Y_a

Hinge coordinates

Note: Elemental forces V_i, H_i act at coordinates X_i, Y_i.

a) Topology

Equation 4.1 relating moment and thrust at hinge 1
Equation 4.1 relating moment and thrust at hinge 2
Equation 4.1 relating moment and thrust at hinge 3
Equation 4.1 relating moment and thrust at hinge 4

b) Equations SM1 to SM4

SMARTMEC main algorithm (1)

5. Define various physical parameters; depth of fill over crown, a weighted specific weight value encompassing both fill and masonry, a coefficient of horizontal earth pressure, an empirical enhancement coefficient to apply to the latter near the springings, a mode of load dispersal through the fill, and finally the position of the single point (knife edge) vertical load. The critical position for the load varies from the third to the fifth span positions (depending on the vault's span to rise ratio), but commonly a quarter point load is employed and a hinge will typically form beneath it.

6. Apply the values from step 5 to obtain vertical and horizontal forces at each node (Figure 4.2a).

7. Define the arch vault material parameters σ_m, k and λ.

8. Fix the two outer hinges (hinges 1 and 4) at the springings (nodes 1 and 51). Select trial initial hinge positions for the other two hinges (hinges 2 and 3). See Figure 4.2a.

9. At hinge 1, apply the moment and axial thrust (M and P) version of equation 4.1 yielding equation SM1. Repeat for the remaining three hinges giving equations SM2, SM3 and SM4 (Figure 4.2b).

10. Resolve vertically and horizontally to yield equations SM5 and SM6 in Vd and H4. (Figure 4.3a).

11. Take moments about hinge 1 to yield equation SM7 in Va (Figure 4.3a).

12. For the left substructure, take moments about hinge 2 to yield equation SM8 in H_1 (Figure 4.3b).

13. Resolve forces at hinge 1 to yield equation SM9 for Pd (the axial component of thrust) in terms of H_1 and Vd (Figure 4.3c).

14. For the right substructure, take moments about hinge 3 to yield equation SM10 in Va (Figure 4.3d).

15. Resolve forces at hinge 4 to yield equation SM11 for Pa (the axial component of thrust) in terms of H_4 and Va (Figure 4.4a).

FIGURE 4.3

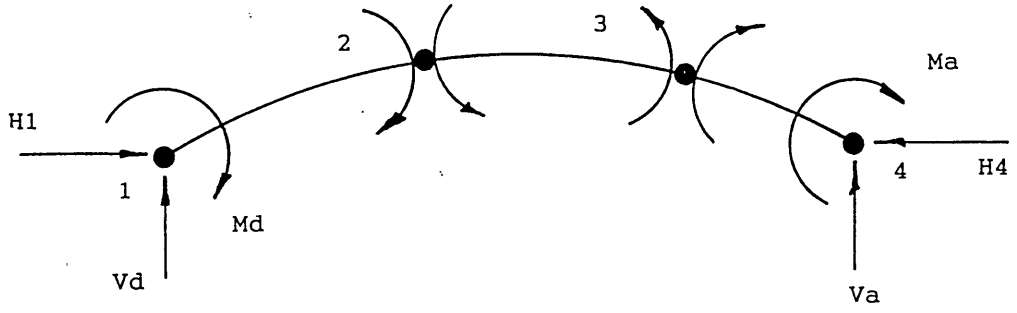

Resolving vertically: $Vd = \sum_{1}^{4} Vi - Va$

Resolving horizontally: $H4 = H1 - \sum_{1}^{4} Hi$

Taking moments about hinge 1: $Va = \dfrac{Md + Ma + \sum_{1}^{4} ViXi + \sum_{1}^{4} HiYi}{Xa - Xd}$

a) Whole structure: equations SM5, SM6 & SM7

Taking moments about hinge 2:

$$H1 = \frac{Mc + Md - \sum_{1}^{2} HiYi - \sum_{1}^{2} ViXi + Vd(Xc - Xd)}{Yc - Yd}$$

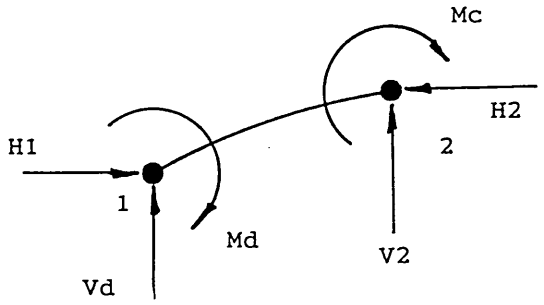

b) Substructure 1-2: equation SM8

Resolving forces at hinge 1:

$Pd = \sqrt{Vd^2 + H1^2}\ \cos\Theta_1$

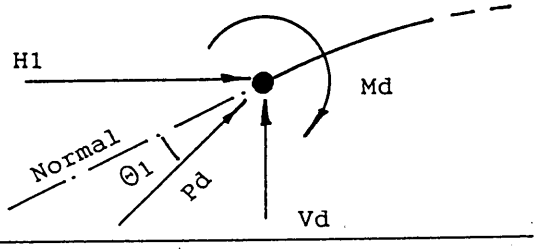

c) Substructure 1-2: equation SM9

Taking moments about hinge 3:

$$Va = \frac{Ma + Mb + \sum_{3}^{4} HiYi + \sum_{3}^{4} ViXi + H4(Yb - Ya)}{Xa - Xb}$$

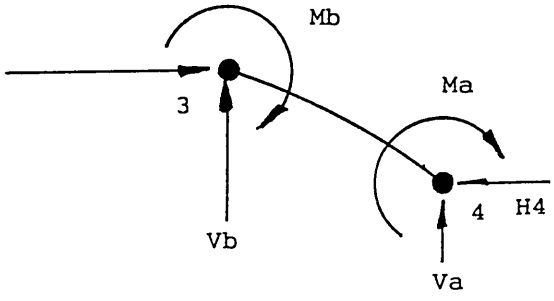

d) Substructure 3-4: equation SM10

SMARTMEC main algorithm (2)

FIGURE 4.4

Resolving forces at hinge 4:

$Pa = \sqrt{Va^2+H4^2}\ \cos\Theta_4$

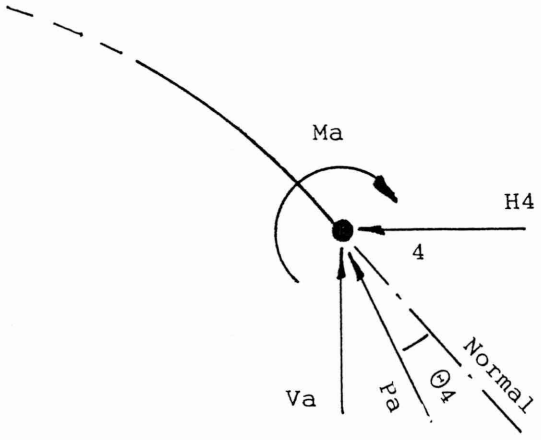

a) Substructure 3-4: equation SM11

Resolving forces at hinge 3:

$Pb = \sqrt{Hb^2+Vb^2}\ \cos\Theta_3$

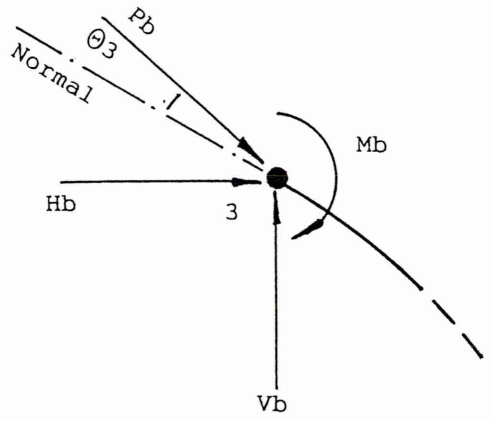

b) Substructure 3-4: equation SM12

Resolving forces at hinge 2:

$Pc = \sqrt{Hc^2+Vc^2}\ \cos\Theta_2$

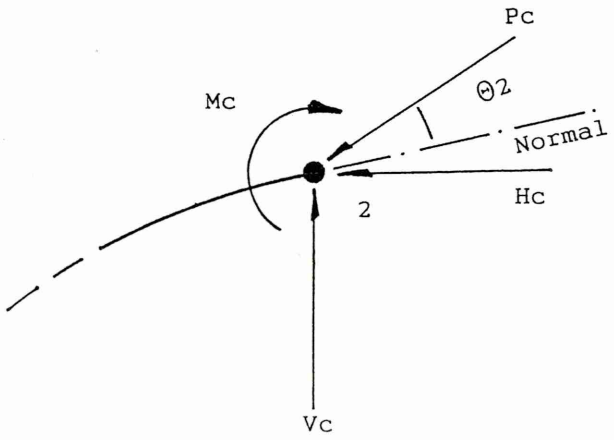

c) Substructure 1-2: equation SM13

SMARTMEC main algorithm (3)

16. For the right substructure, resolve forces at hinge 3, and hence obtain equation SM12 in Pb (the axial component of thrust at hinge 3). See Figure 4.4b.

17. For the left substructure, resolve forces at hinge 2. This yields equation SM13 for Pc, the axial component of thrust at hinge 2. Refer to Figure 4.4c.

18. Solve equations SM1 to SM13, noting that some are non-linear, by a purpose-written numerical routine and hence derive a solution for W, the externally-applied knife edge point load, for this system of hinge positions.

19. Repeat the process for other positions of hinges numbers 2 and 3 to find the lowest bound value of W and hence the overall solution for the structure.

4.2.5 SMARTMEC: limitations of model

Known deficiencies of the SMARTMEC model include the rudimentary treatment of soil-arch interaction. The behaviour is not yet well understood and its effect on the result can be considerable, sometimes leading to mechanism methods yielding significant underestimates, especially in cases of low span to rise ratio arches with substantial cover at the crown.

The distribution of live load through the fill is also a process that is not well understood, and indeed it may vary during the loading regime and from structure to structure. It has been observed that SMARTMEC often gives results more faithful to the prototype when the single point load is taken down through the fill without any distribution at all (SMARTMEC provides this option). It is also to be noted that SMARTMEC has difficulty in converging with semi-circular arches and those approaching these proportions, perhaps due to ill-conditioning of the equations in such circumstances. This aspect requires further study.

Finally, fixing the two end hinges to the springing points in many instances results in the hinge positions at variance to those in the prototype under study. A 'bare' arch with no fill will always form hinges at the springings, but the influence of fill, especially in deep arches, will tend to displace the springing hinges into the span.

4.2.6 SMARTMEC: "validation"

SMARTMEC was assessed against prototype arch test data from three sources in order to test the proposed hinge modelling:

Data Set 1 A series of *full-scale arch bridge tests* commissioned by the Transport Research Laboratory (TRL). These have the advantage of being full scale, real structures, but suffer from the disadvantage of being very highly variable in form, sometimes with features (for example skew) which are difficult for SMARTMEC to deal with.

Data Set 2 *Arch model tests by others.* These structures are, by definition, small, and are therefore less representative of 'real' bridges. Conversely, details of their construction, properties and materials are more tightly controlled and are generally quantified and thus fewer assumptions are necessary than for the case studies in Data Set 1 above.

Data Set 3 A series of *in-house model tests.* Again small scale, but in other respects they are tailored to the needs of this research programme.

Each of the above will be described at length in the next chapter.

CHAPTER FIVE

The Application of a Masonry Arch Mechanism Analysis Computer Programme

5.1 Synopsis

The masonry arch mechanism analysis computer programme SMARTMEC is applied to arch collapse test data from three sources; full-scale bridges tested by the Transport Research Laboratory (TRL) as part of a national programme, to laboratory model tests by various other bodies, and finally to further models constructed and tested in the laboratories of Sheffield Hallam University. The results obtained are encouraging overall.

Parametric studies utilising SMARTMEC enable the effects of both material strength and 'k' value to be examined and conclusions drawn as to their relevance to arch analysis.

5.2 Data Set 1 Tests: Against Full Scale Prototypes

5.2.1 Intruduction

The Transport and Road Research Laboratory is conducting research[9] to improve the present method of assessing the load carrying capacity of masonry arch bridges. This involves a series of full scale load tests to destruction[9].

Each bridge in the programme is unique (they were chosen to represent the range of types encountered) and none is ideally suited to these studies. Attention will thus be

limited to those that failed as four hinge mechanisms, and those with features that the software does not model (such as skew), as previously noted, will also be excluded. It must nevertheless be emphasised that this data set is difficult to make use of as there is a lack of detailed data relevant to the exercise proposed.

Those TRL tests most nearly meeting the acceptance criteria are the Bridgemill, Prestwood and Shinafoot bridges.

Since some parameters pertaining to these structures must, of necessity, be estimated here (having not been measured by TRL), it is proposed to choose highest and lowest credible values for these. Two SMARTMEC runs will then be made; one combining the 'high' values (ie. those tending to make the structure stonger), and one combining the 'low' values (ie. those tending to make the structure weaker). The result will thus be a predicted collapse load spectrum for each structure.

This approach is similar to the one often followed in practice, where one gains a feel for the structure's sensitivity to the various input parameters, many (if not more) of which would be similarly unknown. Clearly, results close to the upper and lower bound are less probable.

In order to provide an "optimum" SMARTMEC result within the above range, a third computer run has been made using a combination of the "most probable" input parameter values. Finally, to set these results in context, an equivalent result derived from commercial arch mechanism analysis software, called "Archie", is also presented. The comparison is approximate, however, since the two computer programmes are somewhat different and some of their features are not comparable. Consequently, the "most probable" values used for input to SMARTMEC do not necessarily employ Archie at its best; Archie is not under test. For example, Archie features a "factor on passive pressure" parameter (set at its default value of 0.1 in this study), which is not directly equivalent to SMARTMEC's earth pressure enhancement factor. Furthermore, Archie positions the load at set incremental positions traversing the span, and so the quarter point load result has been derived in many cases by averaging two results just to either side of the quarter point. A major difference is also that Archie always distributes the load through the fill, whereas SMARTMEC has invariably been used without this feature for its optimum runs.

Despite all these difficulties the comparison is considered worthwhile, but it is emphasised that it is not claimed that the differences in output arise purely from the hinge modelling employed by SMARTMEC.

5.2.2 Bridgemill Bridge

This test was carried out by the University of Edinburgh on behalf of the TRL[47]. Bridgemill bridge was built in 1869 with a shape close to parabolic and a span to rise ratio of 6.4. The topology is illustrated in Figure 5.1.

Under quarter point KEL loading the bridge failed partly as a four hinge mechanism and partly due to snap through at a load of 3100 kN. The TRL test report shows stress-strain plots for two stone samples which are rather strange and appear to show *increasing* stiffness under load. However, this bridge remains a fair candidate for the present purposes. The SMARTMEC input parameters relating to this arch are given in Table 5.1 below.

No.	Data Item	Value(s)	Note
1.	Span (m)	18.29	
2.	Rise (m)	2.84	
3.	Quarter point rise (m)	2.16	
4.	Barrel thickness at springing (m)	0.711	
5.	Barrel thickness at crown (m)	0.711	
6.	Cover at crown (m)	0.203	
7.	Mean material specific weight (kN/m^3)	21	
8.	Earth pressure coefficient	0.271	(I)
9.	Earth pressure enhancement factor	1-1.1	(II)
10.	σ_m (N/mm^2)	5-8	(III)
11.	k	2	(IV)
12.	λ	1.25	
13.	Distance of load from RHS (m)	4.572	
14.	UDL over whole span (kN, total)	0	
15.	Live load distribution type	KEL-Bous.	(V)

Table 5.1 SMARTMEC input data: Bridgemill Bridge

(I) A typical Φ value of 35° has been assumed and a coefficient of active earth pressure employed.

(II) Experience has shown that a low figure yields best results for shallow arches.

(III) This range is quoted in the TRL test report.

(IV) Assumed figure for sandstone. It will be shown in later in this chapter that the result is insensitive to the actual value chosen provided it is finite and greater than unity.

(V) These are the two extremes with respect to distibution through the fill, but experience shows that no distribution (the KEL option) often yields the best results.

FIGURE 5.1

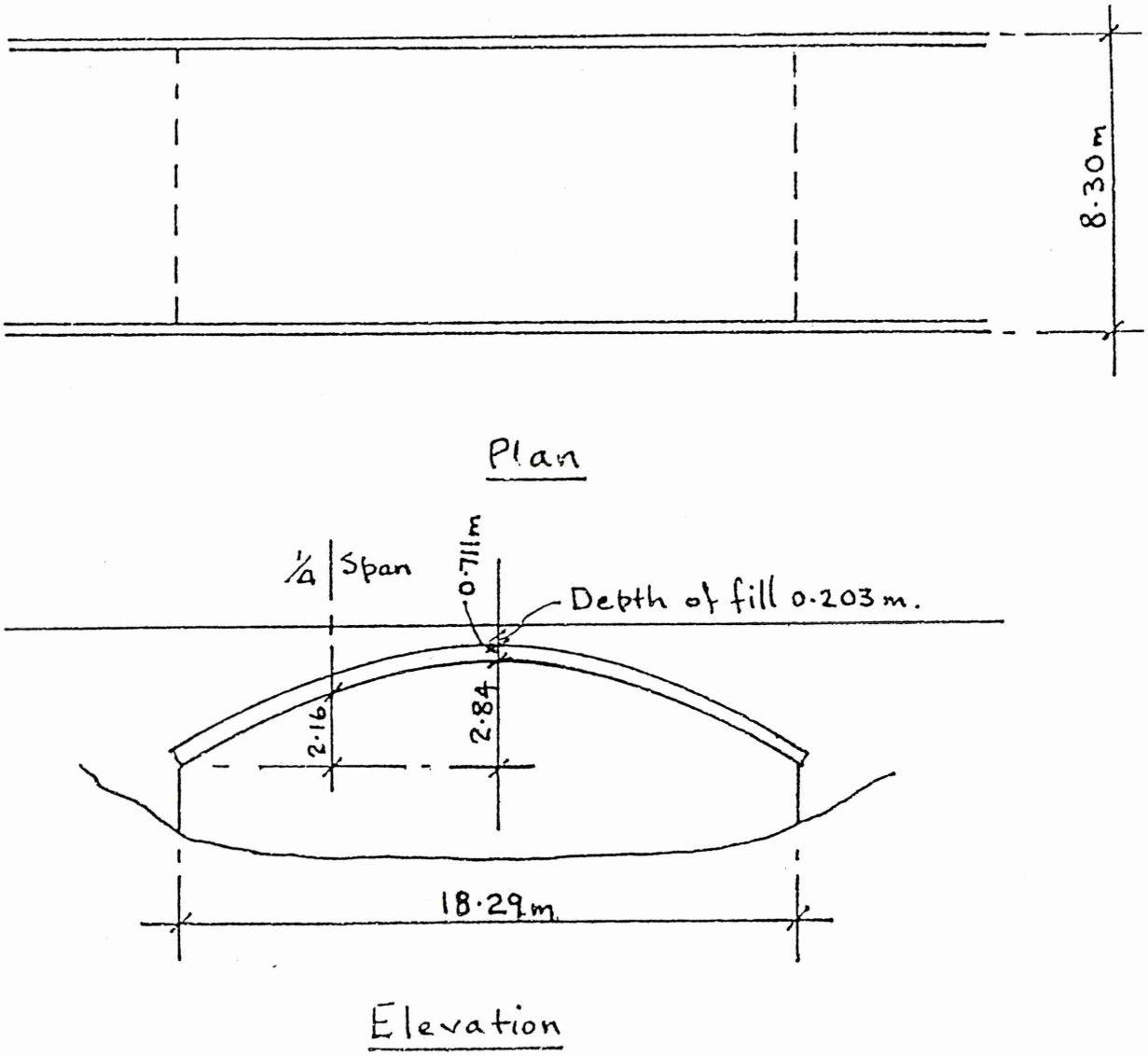

Bridgemill Bridge load test topology

This data provides three SMARTMEC runs; an upper bound (Table 5.1 'high' values), a lower bound (Table 5.1 'low' values) and an 'optimum' (using values noted below):

Prototype collapse load 3100 kN		
No.	Output Item	Value
1.	Upper bound collapse load, kN, (% of prototype)	4408 (142.2)
2.	Optimum collapse load, kN, (% of prototype)	2990 (96.5)
3.	Lower bound collapse load, kN, (% of prototype)	2763 (89.1)
4.	'n' for hinge under load position at optimum	0.179
5.	Archie analysis, kN, (% of prototype)	2071 (66.8)

Table 5.2 SMARTMEC output: Bridgemill Bridge

Note: SMARTMEC optimum run is based on σ_m = 6 N/mm^2, no earth pressure enhancement and K.E. loading. Note the comparatively high 'n' value.

5.2.3 Prestwood Bridge

The SMARTMEC input parameters are given in Table 5.3 below.

No.	Data Item	Value	Note
1.	Span (m)	6.550	
2.	Rise (m)	1.428	
3.	Quarter point rise (m)	-	
4.	Shape	segmental	(I)
5.	Barrel thickness at springing (m)	0.220	
6.	Barrel thickness at crown (m)	0.220	
7.	Cover at crown (m)	0.165	
8.	Mean material specific weight (kN/m^3)	21	
9.	Earth pressure coefficient	0.271	
10.	Earth pressure enhancement	1-1.5	(II)
11.	σ_m (N/mm^2)	4.5	(III)
12.	k	2	(IV)
13.	λ	1.25	
14.	Distance of load from RHS (m)	1.637	
15.	UDL over whole span (kN, total)	0	
16.	Live load distribution type	KEL-Bous.	(V)

Table 5.3 SMARTMEC input data: Prestwood Bridge

(I) The (asymmetric) deformation cannot be taken into account by SMARTMEC and a segmental shape is assumed.

(II) A similar reasoning to Bridgemill applies.

(III) Quoted in the TRL test report for the brick and mortar together.

(IV) The TRL test report quotes a compressive strength plus a secant modulus. It is not therefore possible to arrive at a 'k' value and a typical k=2, λ=1.25 has been assumed.

(V) A similar reasoning to Bridgemill again applies.

Prestwood Bridge did in fact fail as the required classic four hinge mechanism[48].

Figure 5.2 depicts a front elevation of the bridge (a plan view is not available). The bridge is not skewed. It is, however, quite deformed from its original segmental shape but in other respects remains a fair candidate for these studies, particularly given its clear four hinge failure.

The results are again presented in the form of a table, once more with a comparable Archie analysis to set it in context:

Prototype collapse load 228 kN		
No.	**Output Item**	**Value**
1.	Upper bound collapse load, kN, (% of prototype)	244.4 (107.9)
2.	Optimum collapse load, kN, (% of prototype)	137.0 (60.1)
3.	Lower bound collapse load, kN, (% of prototype)	127.9 (56.1)
4.	'n' for hinge under load position at optimum	0.067
5.	Archie analysis, kN, (% of prototype)	104.5 (45.8)

Table 5.4 SMARTMEC output: Prestwood Bridge

Note: SMARTEMEC optimum run is based on an earth pressure enhancement of 1.2 and a knife edge load.

5.2.4 Shinafoot Bridge

Shinafoot bridge is also reported[49] as failing as a four hinge mechanism and is a good candidate. Its voussoirs tapered towards the crown, and this feature was specifically incorporated within SMARTMEC to deal with Shinafoot bridge.

The layout of Shinafoot Bridge is shown in Figure 5.3.

The input parameters relating to Shinafoot are given in the following Table 5.5.

FIGURE 5.2

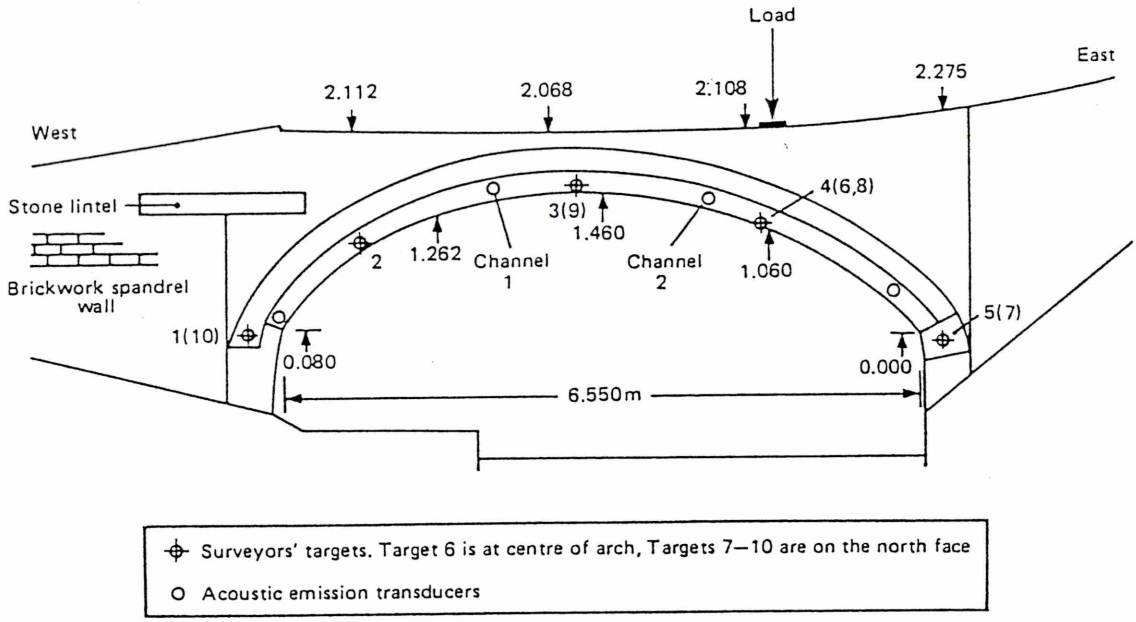

Prestwood Bridge load test topology

FIGURE 5.3

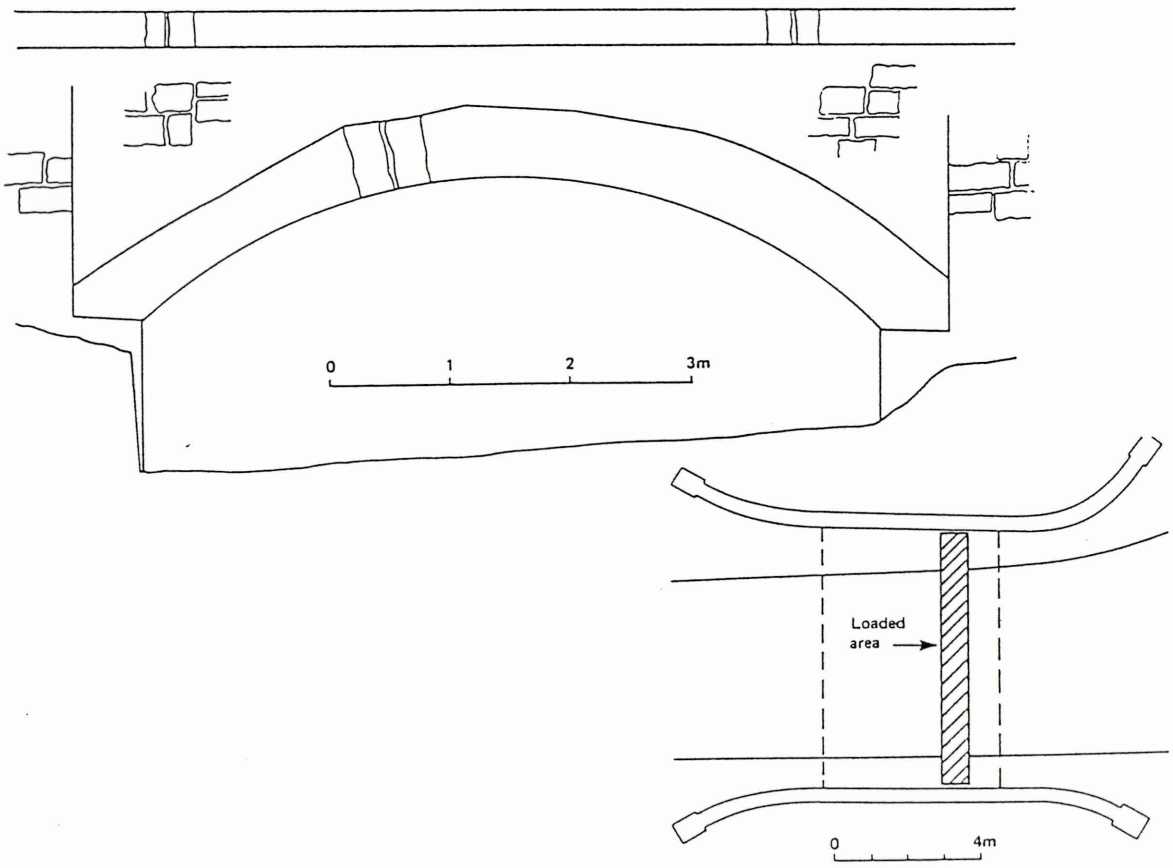

Shinafoot Bridge load test topology

No.	Data Item	Value	Note
1.	Span (m)	6.160	
2.	Rise (m)	1.185	
3,	Quarter point rise (m)	-	
4,	Shape	Segmental	
5,	Barrel thickness at springing (m)	0.770	
6.	Barrel thickness at crown (m)	0.390	
7.	Cover at crown (m)	0.215	
8.	Mean material specific weight (kN/m^3)	21	
9.	Earth pressure coefficient	0-0.271	(I)
10.	Earth pressure enhancement	1	(II)
11.	σ_m (N/mm^2)	2.5-5.0	(III)
12.	k	2	(IV)
13.	λ	1.25	
14.	Distance of load from RHS (m)	1.54	
15.	UDL over whole span (kN, total)	0	
16.	Live load distribution type	KEL-Bous.	(V)

Table 5.5 SMARTMEC input data: Shinafoot Bridge

(I) An earth pressure coefficient as low as zero is credible since the arch is reported to have been haunched with rubble fill.

(II) Due to (I) above.

(III) The range quoted in the TRL report, although the yield stress used in the report's mechanism analysis is 5 N/mm^2.

(IV) In the absence of data a k value of 2 has been assumed with λ=1.25.

(V) The full range is again applied for completeness.

Uniquely in these case studies, but notoriously for non-linear studies, a second solution was found to exist at a KEL of over 7000 kN. This may be a consequence of the varying vault thickness.

Another consequence appeared to manifest itself in that SMARTMEC's solution routine had a great deal of difficulty in converging, and some manual intervention proved necessary. This was done by choosing different starting values for the numerical solution routine.

The output for the "correct" solution is given in Table 5.6 together with an Archie analysis for comparison.

Prototype collapse load 2524 kN		
No.	Output Item	Value
1.	Upper bound collapse load, kN, (% of prototype)	4678 (185.3)
2.	Optimum collapse load, kN, (% of prototype)	2362 (93.6)
3.	Lower bound collapse load, kN, (% of prototype)	1548 (61.3)
4.	'n' for hinge under load position at optimum	0.213
5.	Archie analysis, kN, (% of prototype)	1905 (75.5)

Table 5.6 SMARTMEC output: Shinafoot Bridge

Note: SMARTMEC optimum run is based on an earth pressure coefficient of 0.15, a σ_m of 3 N/mm^2 and a knife edge load.

5.2.5 Discussion on Data Set 1 results

The SMARTMEC results bracket the prototype collapse loads for all three bridges. This is considered to be a reasonable outcome, and with a realistic choice of input data - the "optimum" values presented - the programme is capable of giving answers acceptably close to the prototypes and as such is viable as a basic analytical tool in its present form. The results compare well with those of Archie, but the latter's somewhat low results may be due to the aforementioned factors.

It is contended that the hypothesis that hinges lie on interaction loci is justified, and the general correctness of the interaction data itself is considered to be reasonably well demonstrated, given the significant assumptions made.

What these results fail to do, however, is to provide a basis for drawing inferences about the effect of 'k' modelling or employing finite material strength in the place of an infinite value.

This is partly because the TRL did not require, nor collect, detailed constitutive data, since current methods do not need it, and so assumptions have been made herein. In addition, the complexities of these real bridges, many aspects of which are not modelled by SMARTMEC, may have masked any gains made in refining the hinge modelling.

Some of these shortcomings will be addressed in the Sheffield Hallam University in-house series of model arch tests to be described in Section 5.5.

5.3 Data Set 2 Tests: Against Laboratory Scale Models by Others

5.3.1 Dundee. University model arch bridge

This bridge was constructed in the laboratories of Dundee University on behalf of the TRL[50] to effectively full-size proportions. Figure 5.4 shows this large model. Noting the limitations of SMARTMEC set out in the last chapter, it is unsurprising that this model's semi circular profile makes analysis difficult. Otherwise this bridge is useable for this study and, in spite of problems with the test configuration, it did in fact nominally fail as a four hinge mechanism.

The SMARTMEC input parameters are given in Table 5.7 below.

No.	Data Item	Value	Note
1.	Span (m)	4.000	
2.	Rise (m)	2.000	
3.	Quarter point rise (m)	-	
4.	Shape	Semi-circ.	
5.	Barrel thickness at springing (m)	0.250	
6.	Barrel thickness at crown (m)	0.250	
7.	Cover at crown (m)	0.250	
8.	Mean material specific weight (kN/m^3)	22	(I)
9.	Earth pressure coefficient	0.172	(II)
10.	Earth pressure enhancement	1-2	(III)
11.	σ_m (N/mm^2)	8-30	(IV)
12.	k	2	(V)
13.	λ	1.25	
14.	Distance of load from RHS (m)	1.382	(VI)
15.	UDL over whole span (kN, total)	0	
16.	Live load distribution type	KEL-Bous.	(VII)

Table 5.7 SMARTMEC input data: Dundee University model

(I) The measured fill density was a well compacted 21 kN/m^3, so a higher overall weighted value of 22 kN/m^3 has been chosen to include masonry.

(II) Based on the measured Φ of 45° and employing active earth pressure.

(III) The deep nature of the arch suggests a high value may be appropriate.

(IV) This range is based on the separate measured values of concrete voussoir and mortar strengths of 30 and 8 N/mm^2 respectively.

FIGURE 5.4

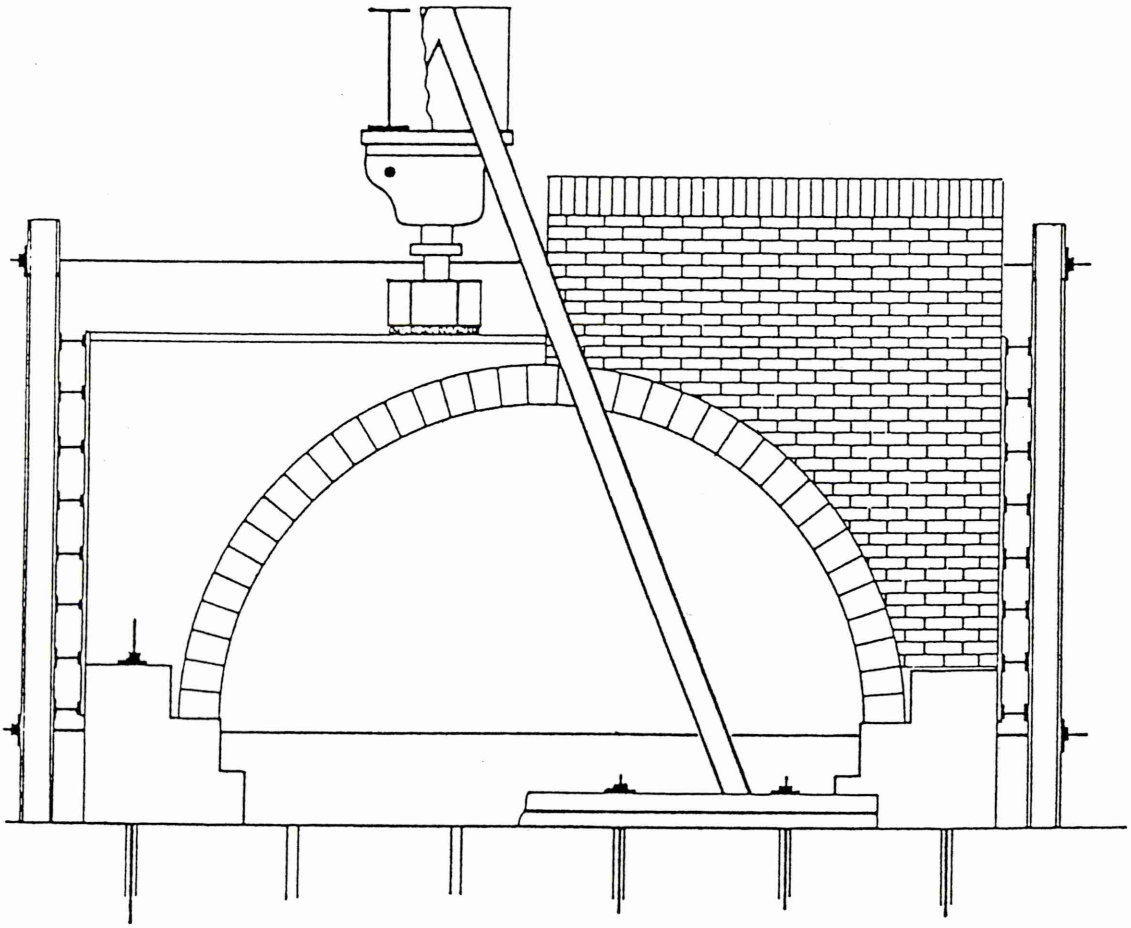

Dundee University model arch load test topology

(V) Assumed - though may be reasonable for the concrete voussoirs.

(VI) The contractor's report does not quote a figure. The figure used here was obtained from a personal enquiry to Dr. Fraser Smith of Dundee University.

(VII) Chosen to cover the full range of possibilities.

As with the TRL tests previously, the above data provides both upper and lower bound computer runs. However, possibly due to the arch's semicircular profile giving rise to ill-conditioning of the equations, SMARTMEC will not converge to provide the upper bound and optimum solutions, and only the lower bound is therefore presented here, together with the Archie result, this programme having experienced no difficulties.

Prototype collapse load 1020-1060 kN		
No.	**Output Item**	**Value**
1.	Lower bound collapse load, kN, (% of prototype)	356.6 (34.3)
2.	Archie analysis, kN, (% of prototype)	258.0 (24.8)

Table 5.8 SMARTMEC output: Dundee University model

5.3.2 Liverpool University scale model arches

Several models were constructed by Dr. Sawko and Mr. Towler at Liverpool[34,51], but only one test was performed that is of use here, the others being loaded at the crown or not to collapse. Again with reference to the aforementioned limitations of SMARTMEC, loading at the crown cannot be accommodated since it leads to a theoretical *five* hinge failure.

Figure 5.5 depicts Liverpool University's model arch overall topology. The tests were unique in that a common philosophy is shared concerning the parabolic stress-strain relationship for masonry, and indeed reference to Towler was made in Chapter Two. It is Towler's supposition that masonry exhibits a second order parabolic load deflection characteristic, ie. in the light of the present studies that k=2.

That the model was constructed without spandrel walls, in the absence of load distribution through the fill, and fill interaction, all make this test most useful in eliminating unwanted variables such as stiffening by spandrel walls and arch-fill interaction.

The input data to SMARTMEC is depicted in Table 5.9 which follows.

FIGURE 5.5

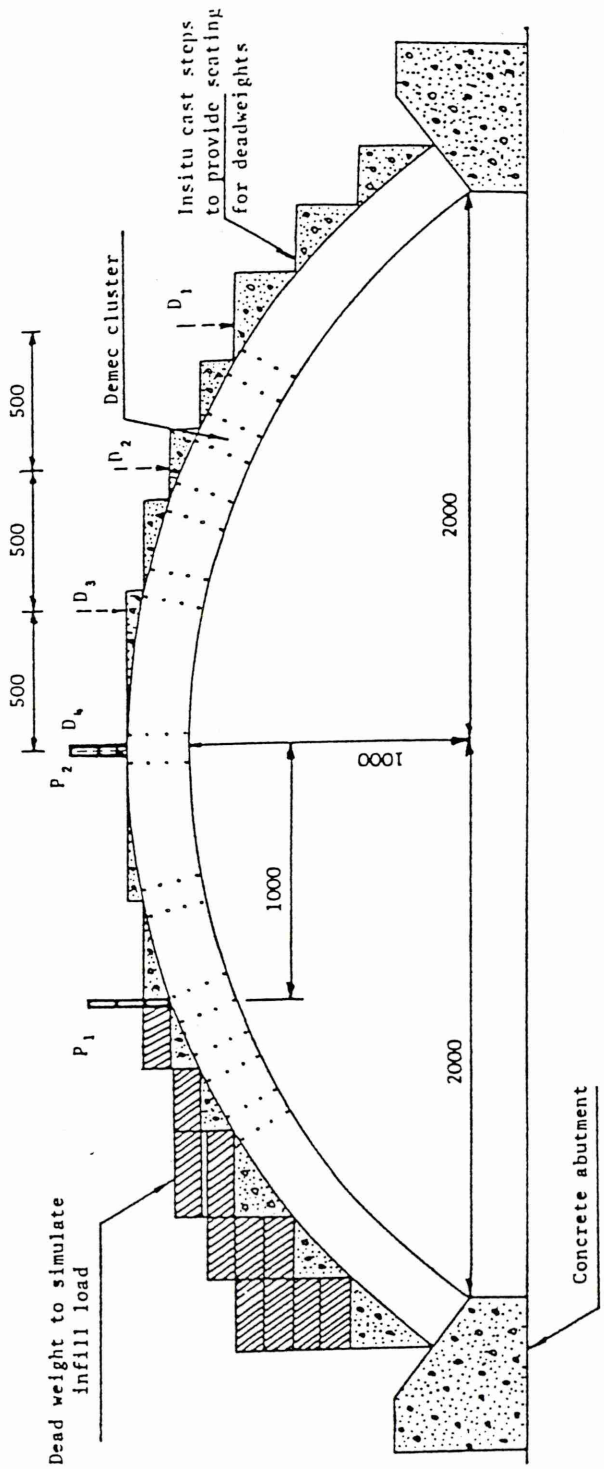

Liverpool University model arch load test topology

No.	Data Item	Value	Note
1.	Span (m)	4.000	
2.	Rise (m)	1.000	
3.	Quarter point rise (m)	-	
4.	Shape	Segmental	
5.	Barrel thickness at springing (m)	0.335	
6.	Barrel thickness at crown (m)	0.335	
7.	Cover at crown (m)	0.250	
8.	Mean material specific weight (kN/m^3)	21	(I)
9.	Earth pressure coefficient	0	(II)
10.	Earth pressure enhancement	1	(III)
11.	σ_m (N/mm^2)	65, 16, 10	(IV)
12.	k	2	(V)
13.	λ	1.25	
14.	Distance of load from RHS (m)	1	
15.	UDL over whole span (kN, total)	0	
16.	Live load distribution type	KEL	(VI)

Table 5.9 SMARTMEC input data: Liverpool University model

(I) Assumed typical earth fill value.
(II) No earth pressures present.
(III) As (II).
(IV) Reported measured values for brick alone, mortar and brick combination, and mortar alone, respectively.
(V) Reported value.
(VI) True knife edge loading

Unlike the full scale tests and the Dundee model, removal of many of the uncertainties means that only SMARTMEC runs with varying material strengths are needed, ie. σ_m = 10, 16 (the "optimum" here) and 65 N/mm^2. The results are given below.

Prototype collapse load 117 kN		
No.	Output Item	Value
1.	Upper bound collapse load, kN, (% of prototype)	89.5 (76.5)
2.	Optimum collapse load, kN, (% of prototype)	86.9 (74.3)
3.	Lower bound collapse load, kN, (% of prototype)	85.0 (72.6)
4.	'n' for hinge under load position at optimum	0.013
5.	Archie analysis, kN, (% of prototype)	181.5 (155.1)

Table 5.10 SMARTMEC output: Liverpool University model

These collapse loads are surprisingly low and, given that the test configuration was favourable to SMARTMEC, it is difficult to provide a satisfactory explanation. However, Sawko and Towler, using their own finite element software, obtained a theoretical value of 102 kN, also low at 87.2% of the prototype. It may be that the concrete steps provided to support the dead load (Figure 5.5) inadvertently strengthened the vault. A similar problem was encountered during the Sheffield Hallam University pilot model arch test to be described in section 5.4. Archie's high result may be due to its use of load dispersal through the fill (this feature cannot be switched off), something that was not present in the prototype test.

5.3.3 Edinburgh University scale model arches

Professor Hendry of Edinburgh University conducted an extensive series of 24 model arch tests[52]. His primary aim was to study the effects of spandrel walls and arch fill and thus only the small number of tests relevant to this thesis are described below.

5.3.3.1 Bridgemill Bridge

The first models to be of interest were scaled from the Bridgemill prototype thus:

No.	Data Item	Value	Note
1.	Span (m)	1.000	
2.	Rise (m)	0.158	
3.	Quarter point rise (m)	-	
4.	Shape	Segmental	
5.	Barrel thickness at springing (m)	0.038	
6.	Barrel thickness at crown (m)	0.038	
7.	Cover at crown (m)	0.012	
8.	Mean material specific weight (kN/m^3)	15	(I)
9.	Earth pressure coefficient	0.271	(II)
10.	Earth pressure enhancement	1	(III)
11.	σ_m (N/mm^2)	19.5, 1.47	(IV)
12.	k	2	(V)
13.	λ	1.25	
14.	Distance of load from RHS (m)	0.25	
15.	UDL over whole span (kN, total)	6.437	
16.	Live load distribution type	KEL-Bous.	(VI)

Table 5.11 SMARTMEC input data: Edinburgh University Bridgemill Bridge models

(I) The measured fill density was a low 14 kN/m^3, so an overall weighted value of 15 kN/m^3 has been chosen to include masonry.
(II) Based on the measured Φ of 35° and employing active earth pressure.
(III) Considered unlikely in a shallow model.
(IV) Measured values of voussoir and mortar strengths at 19.5 and 1.47 N/mm^2.
(V) No information available, so k=2 assumed.
(VI) To cover the full range of possibilities.

Figure 5.6 sets out the leading dimensions and form of construction of these (identical) models. Models numbers 4, 5 and 6 were constructed at one metre span from clay bricks and, of value here, tested without the complication of spandrel walls.

The results are again presented by means of an output table, and this is depicted below. No Archie result is presented, since the programme cannot model the uniformly distributed load employed in the prototype test.

Prototype collapse load range 2.15 kN to 2.5 kN, mean 2.3 kN		
No.	Output Item	Value
1.	Upper bound collapse load, kN, (% of prototype)	3.11 (135.2)
2.	Optimum collapse load, kN, (% of prototype)	2.25 (97.8)
3.	Lower bound collapse load, kN, (% of prototype)	1.82 (79.1)
4.	'n' for hinge under load position at optimum	0.049

Table 5.12 SMARTMEC output: Edinburgh University Bridgemill Bridge models
Note: optimum run is based on σ_m = 5 N/mm^2 and a distribution option of knife edge load (ie. nil distribution).

5.3.3.2 Carron River Bridge

The second type of model to be of interest were scale models of the Carron River Bridge in the Highland Region. The prototype structure had not been the subject of a load test but it was chosen by Hendry so as to obtain models of realistic proportions.

As with the Bridgemill models, two (numbers 4 and 5) were constructed and tested without spandrel walls, again of value here. Only these two, nominally identical, tests will be considered. Figure 5.7 depicts the Carron Bridge dimensions. The mean result of the two tests is quoted here.

FIGURE 5.6

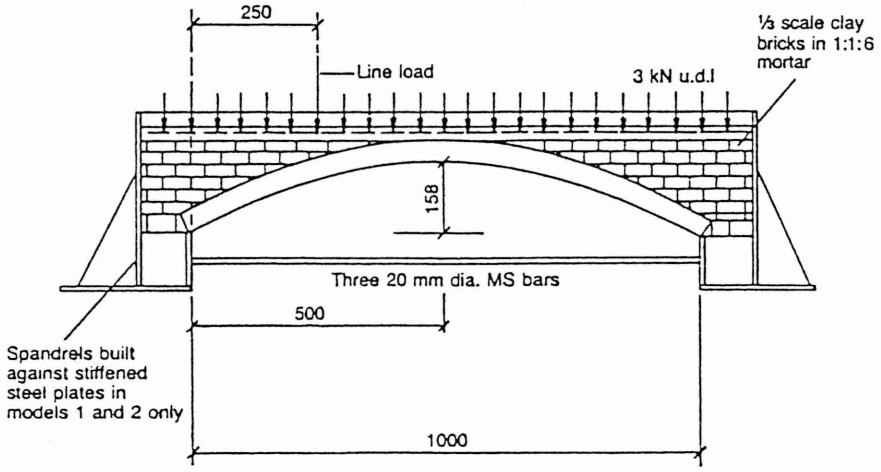

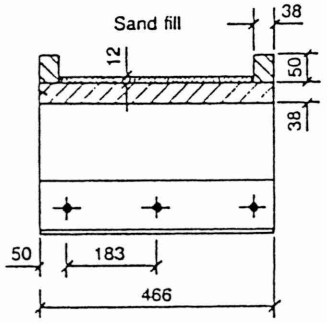

Edinburgh University's Bridgemill Bridge model arch load test topology

FIGURE 5.7

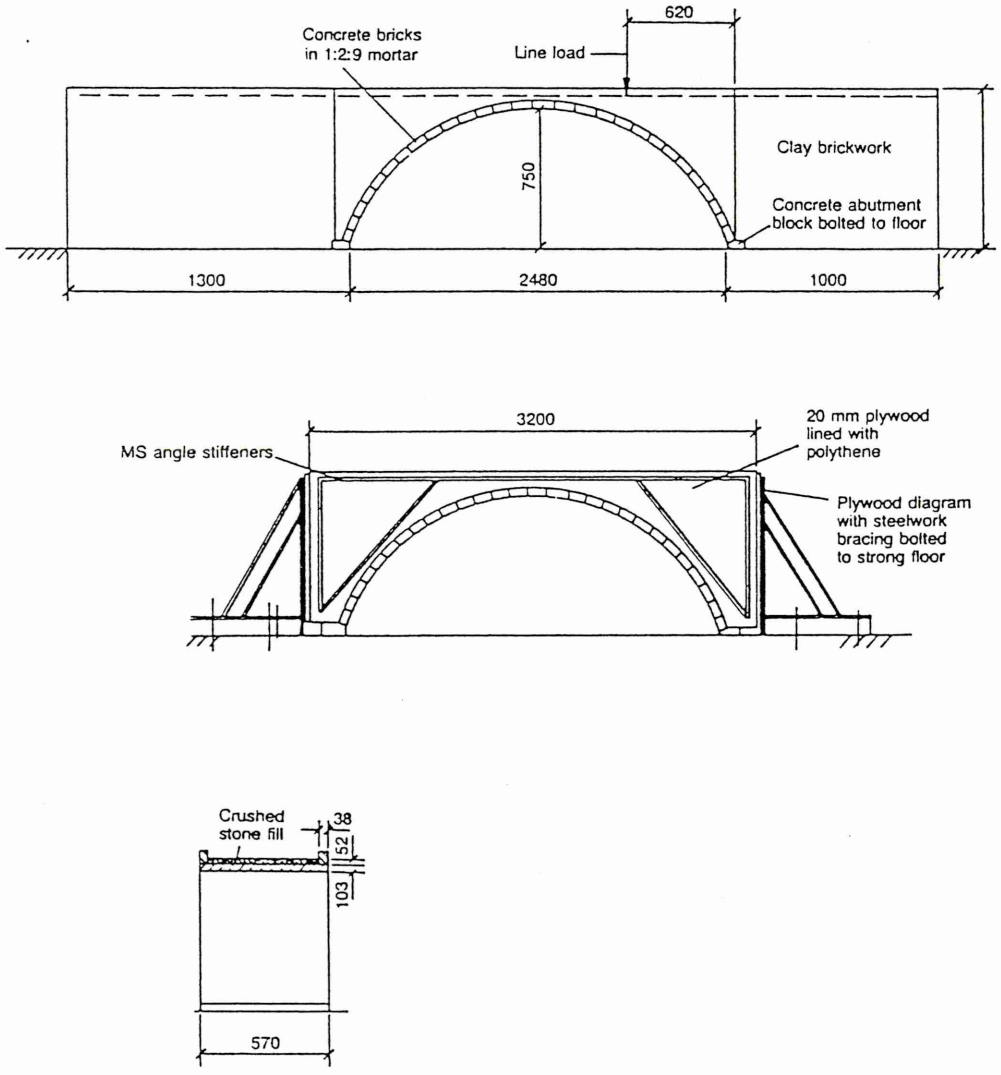

Edinburgh University's Carron River Bridge model arch load test topology

No.	Data Item	Value	Note
1.	Span (m)	2.480	
2.	Rise (m)	0.750	
3.	Quarter point rise (m)	-	
4.	Shape	Segmental	
5.	Barrel thickness at springing (m)	0.103	
6.	Barrel thickness at crown (m)	0.103	
7.	Cover at crown (m)	0.052	
8.	Mean material specific weight (kN/m^3)	15	(I)
9.	Earth pressure coefficient	0.271	(II)
10.	Earth pressure enhancement	1	(III)
11.	σ_m (N/mm^2)	30.0, 1.47	(IV)
12.	k	2	(V)
13.	λ	1.25	
14.	Distance of load from RHS (m)	0.620	
15.	UDL over whole span (kN, total)	0	
16.	Live load distribution type	KEL-Bous.	(VI)

Table 5.13 SMARTMEC input data: Edinburgh University Carron River Bridge models

(I) The measured fill density was a low 14 kN/m^3, so a higher overall weighted value of 15 kN/m^3 has again been chosen to include for masonry.
(II) Based on the measured Φ of 35° and employing active earth pressure.
(III) Considered unlikely to be developed in a model.
(IV) Measured values of voussoir and mortar strengths at 30.0 and 1.47 N/mm^2, respectively.
(V) In the absence of data k=2 has been assumed.
(VI) To cover the full range of possibilities.

The corresponding output table is depicted below.

Prototype collapse load range 3.5 kN to 4.0 kN, mean 3.75 kN		
No.	Output Item	Value
1.	Upper bound collapse load, kN, (% of prototype)	4.80 (128.0)
2.	Optimum collapse load, kN, (% of prototype)	4.02 (107.2)
3.	Lower bound collapse load, kN, (% of prototype)	2.83 (75.5)
4.	'n' for hinge under load position at optimum	0.008
5.	Archie analysis, kN, (% of prototype)	2.56 (68.3)

Table 5.14 SMARTMEC output: Edinburgh University Carron River Bridge models

Note: SMARTMEC optimum run is based on σ_m = 6 N/mm^2 and a distribution option of knife edge load (ie. nil).

5.3.4 Discussion on Data Set 2 results

These results are mixed in accuracy, with the Edinburgh University small scale models the most encouraging with SMARTMEC bracketting the prototype results and the optimum values being very close indeed. The absence of spandrel walls in these tests is a feature which has contributed to the good correlation between theory and practice. It should be noted also that the model prototypes themselves exhibited a scatter of collapse load results of up to 15.2% for supposedly identical models, highlighting the difficulty of repeatable construction.

The easy conclusion that SMARTMEC provides its best results in controlled, laboratory model situations, with extraneous features excluded is, however, detracted from by the Liverpool University model results which are significantly lower than those of the prototype. The explanation for this is not known, but it has been suggested that the prototype vault was strengthened by concrete bedding to the dead loading.

The Dundee University results are questionable given the semi-circular profile of the prototype which SMARTMEC finds problematical.

The variation in 'n' value between these model tests and the earlier full scale tests is noteworthy and supports the scale effect hypothesis. Overall, the results for this data set are considered to be reasonable.

5.4 Data Set 3 Tests: Against In-house Scale Models

5.4.1 Initial considerations

A series of in-house model arch tests was proposed at Sheffield Hallam University in order to provide scientific test data more appropriate to the theoretical studies. The main drawback of the external case studies so far presented is that material constitutive considerations have usually been give a low priority and description of the

mode of *material* failure is often brief. Was there, for instance, evidence of local crushing along the edges of voussoirs in the vicinity of hinges?

The objectives of the in-house series were therefore:

1. To extend the data set so far available.
2. To eliminate some of the independent variables present in tests by others.
3. To observe material failure modes at first hand.
4. To correlate with the masonry hinge tests described in Chapter Three.
5. To provide an initial vehicle for studies in computer vision (see later), with particular reference to edge detection and its application in the study of arch failure.

Given that the primary purpose was to study masonry hinges in vaults, all other variables needed to be eliminated as far as possible, and the additional complexities introduced by fill interaction, load dispersal through the fill and spandrel wall edge stiffening were all preferably to be avoided.

Further, in order to maximise and demonstrate any difference between 'k' hinge modelling and traditional approaches it would be beneficial to work at as high an 'n' as possible in n,m space since the divergence between proposed and current theory increases with increasing 'n' (refer to Figure 3.2). Theory suggests, however, that this may be difficult to achieve at small scale and therefore the mitigating measure of making the arch barrel material as soft as possible in an attempt to induce some demonstrable compressive yielding was adopted. To obtain as high a dead load axial arch thrust component as possible would require the test to be undertaken in a centrifuge, thereby enhancing gravity. Such a facility was not available and instead a pilot model test relying on more accessible technology was set up to examine some of the practical aspects.

5.4.2 Pilot model test

One configuration that offered promise was to hang large weights from the voussoirs to simulate dead load and to apply live load directly to the arch extrados via a knife edge, rather like the Liverpool University arrangement. The senior concrete laboratory technician, who had many years experience, was therefore asked to mould concrete voussoirs in as weak a mix as he was able, consistent with handleability and the rigours of construction. The resulting one metre span model arch, shown in Plate 5.1, was successfully load tested (Plate 5.2) in a stiff, servo-controlled Schenck rig.

PLATE 5.1

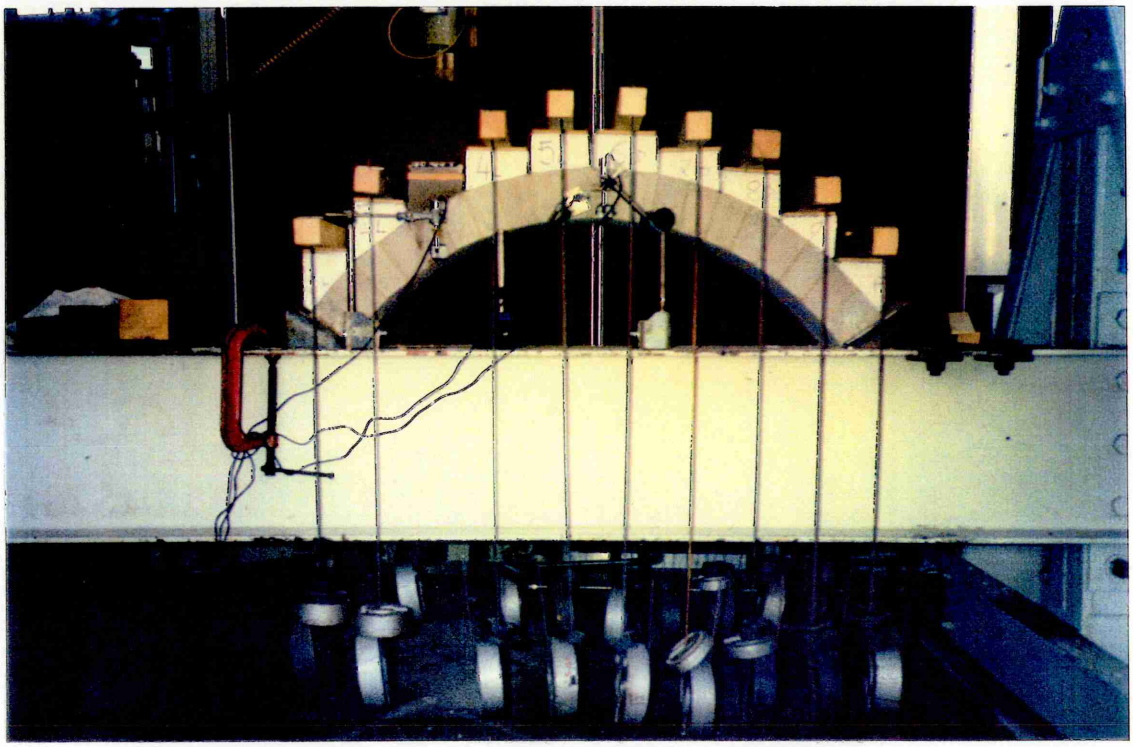

Pilot model arch

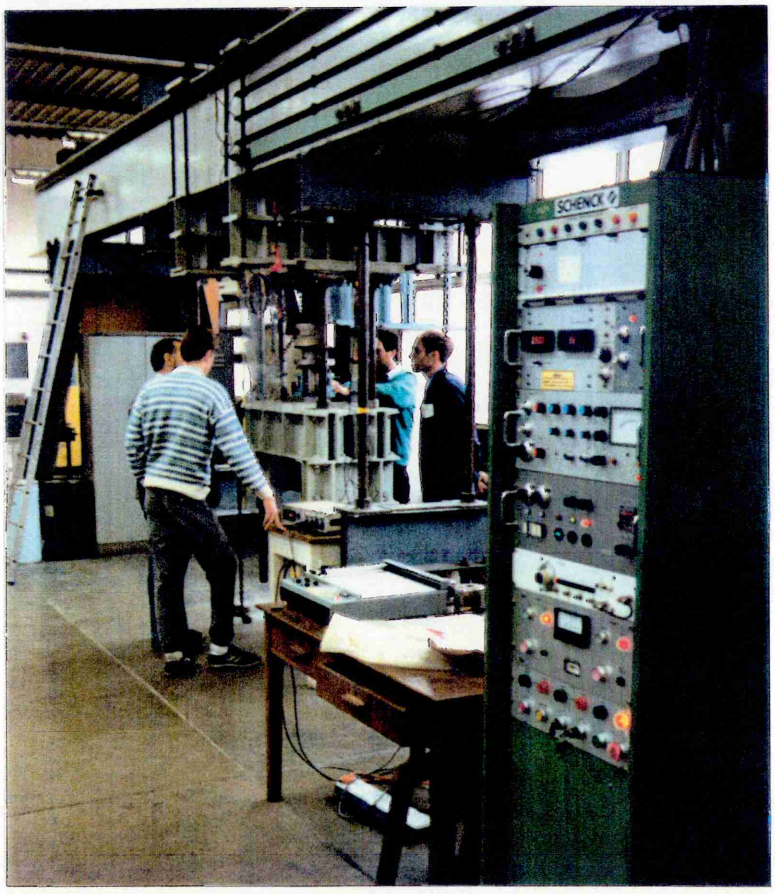

PLATE 5.2

Arch testing rig (Schenck)

A four hinge mechanism failure was produced, as expected. However, the configuration was not ideal, especially with regard to maximising dead load. The polystyrene levelling blocks (Plate 5.1), each astride two voussoirs, had an inhibiting effect on the vault joints (supporting the concern that the Liverpool model had suffered similarly) and concerns were expressed over the safety of allowing the steel weights to drop to the floor at failure. An alternative arrangement for simulation of spandrel fill dead load was therefore sought.

5.4.3 First model arch series

The revised configuration chosen was similar to the pilot study model in terms of primary dimensions, except the barrel thickness was reduced, producing a more slender span enhancing flexural deformation whilst reducing squash load resistance.

A further difference was to simulate fill dead load by means of 250mm long, 5mm diameter mild steel rods, stacked on the extrados up to a level "deck" surface 100mm above the crown (Plate 5.3 - note centering is still in place). To contain the rods beyond the span, rigid steel stop ends were positioned above the steel skewbacks.

Plate 5.4 shows a typical model from the opposite side.

The density of steel rod fill is almost four times that of soil, and in fact the one metre span model supported over a quarter of a tonne of rods. Like soil, however, the steel rod fill could deform to accommodate arch deflections and was expected to generally behave in a soil-like fashion.

A further advantage of the steel rod fill was that a soil-like medium could be obtained that needed no lateral containment, and the deformation of the fill as well as the arch could be directly observed. In effect, the rod fill was thought to be a super-dense two-dimensional soil. This rather naïve assumption lead to a parallel set of experiments to study live load dispersal through the rod fill, but these proved to be fundamentally flawed.

When patch loaded at "deck" level, the load tended to displace rods and punch into the fill. As a load test progressed, the effect was so great that the load point approached the extrados and no meaningful results could be obtained.

Further investigation (ref Lambe & Whitman), too late in the series to abort the studies, revealed the several sources of the problem:

PLATE 5.3

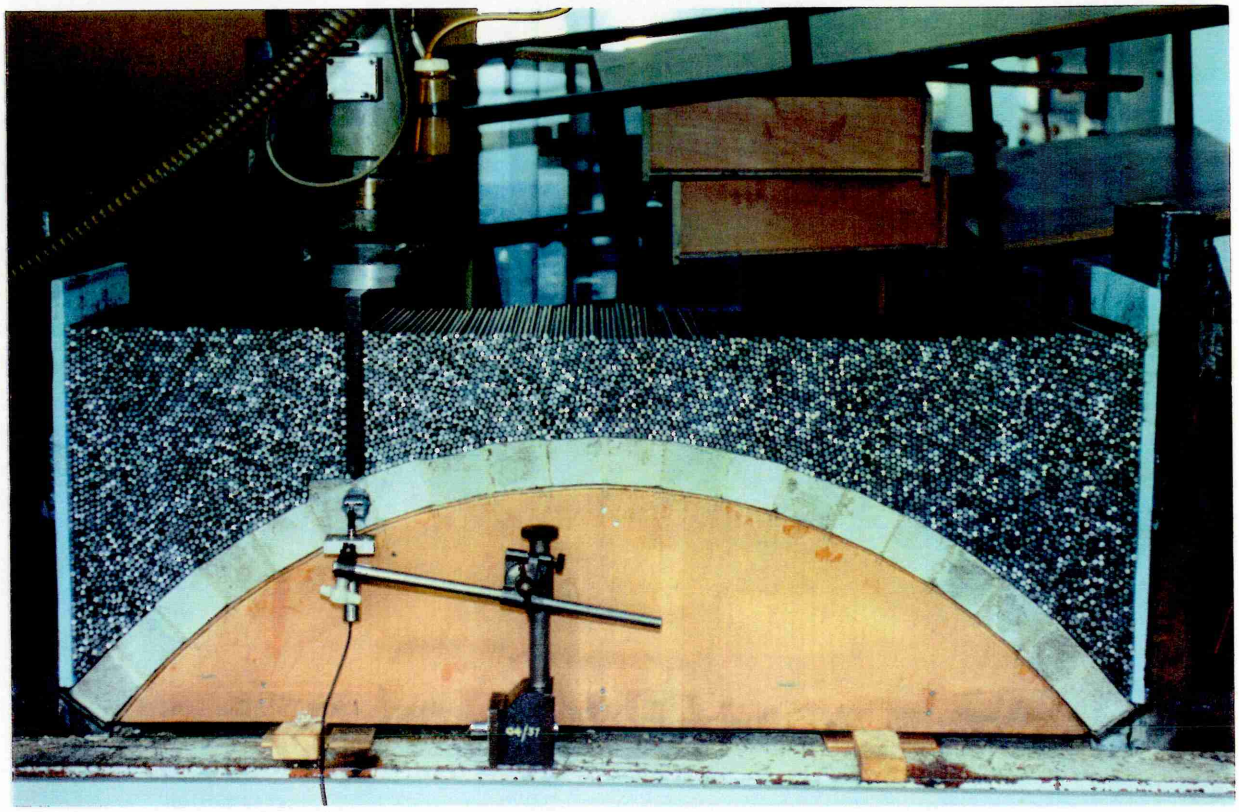

First model arch series

PLATE 5.4

View from far side of an in-house model arch

1. Friction between the patch load and the rod fill was very low - for a real structure this would be significant.
2. The void ratio of the rod fill was too low at about 0.3. A typical soil would possess a much higher value, say 0.6.
3. The rod fill could only develop *linear* internal shear planes (an example can be seen in Plate 5.5 above the crown). The ability to develop *curved* shear planes is an essential prerequisite of soil modelling and in particular necessary to mimic the classical soil failure mode.
4. Bearing capacity is also a function of overburden (surcharge), but the modelling has none.
5. The rods are all smooth and homogeneous. True soil particles range in shape from rounded to angular resulting in greater internal friction.

The solution would have been to mix the rods with a proportion of rods of other diameters, together with ones of different cross section such as square and hexagonal. This would have disrupted the regular packing and increased the void ratio, whilst at the same time increasing internal friction and permitting the development of curved shear planes. It was, however, decided instead to concentrate attention on the main purpose of the arch load tests and revert to regarding the rod fill as simply a convenient, flexible and very dense dead loading.

With regard to the mainstream studies, a steel knife edge plate was fabricated to transmit the load from the actuator directly down to the extrados (Plate 5.6) to avoid live load dispersal through the rods. Deflection measurement was initially extensive via several transducers, but was later limited to vertical displacement at the live load position only.

Generally, cores were cast from the weak concrete used to form the voussoirs and were tested on the day of the arch load test. Plate 5.7 shows a core after test. Mortar cubes were also taken and similarly tested. A 'k' value of 2 was assumed for both the concrete and mortar.

The revised configuration worked well in practice and so a series of five such tests was undertaken.

All tests were nominally identical, but there were some variations. For example, the material strengths of both the voussoir "concrete" and the jointing "mortar" varied between tests since the time between casting and testing varied.

PLATE 5.5

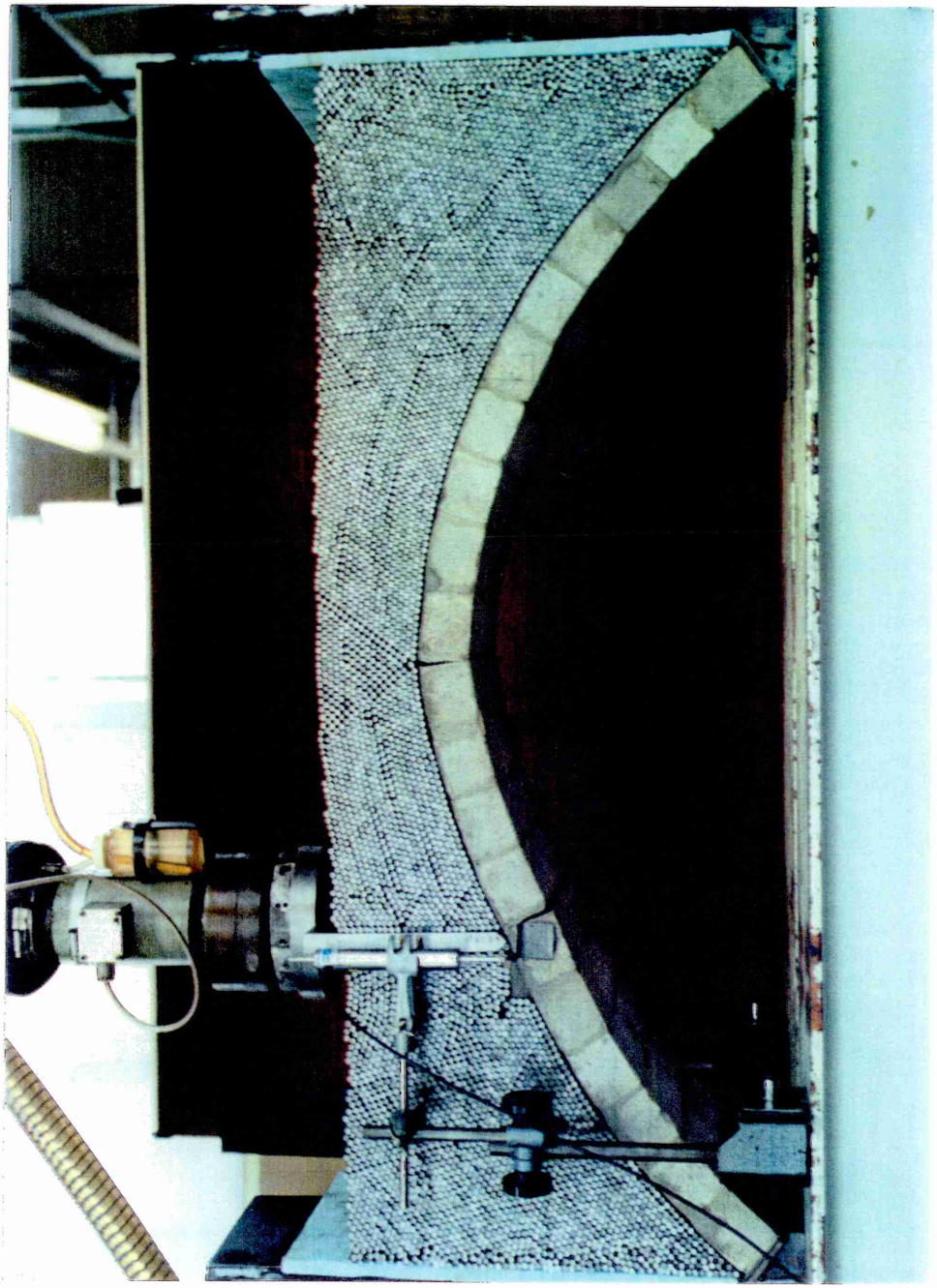

An arch under test. Note linear shear planes through steel rod fill above extrados.

PLATE 5.6

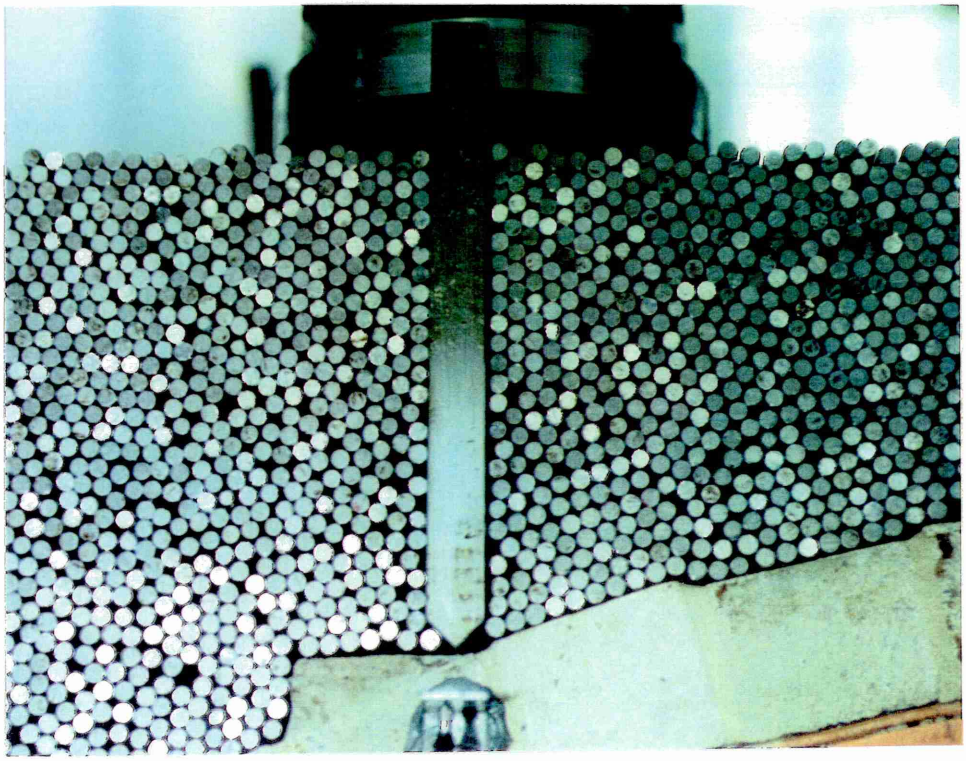

Steel plate transmitting knife edge load through fill to extrados.

PLATE 5.7

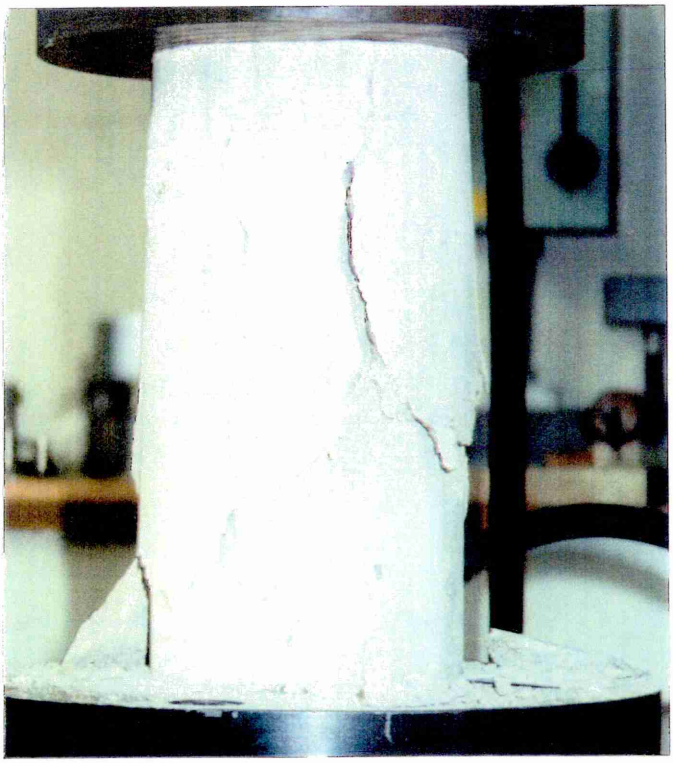

A core of voussoir concrete after load testing.

Some models were also loaded to a low value as a pretest in the parallel load dispersal experimental studies, the object being to study load dispersal without damaging the model. There remains some doubt, however, regarding whether or not the models were pre-weakened in this way. One model was also loaded to failure through the fill, rather than via the KEL plate described above. The full set of results is presented in Table 5.15 below, including notes as to which models were pre-loaded in the above-mentioned load dispersal tests. The directly relevant KEL results are underlined.

Model #	Failure Load (kN)	σ_m Vouss. (N/mm^2)	σ_m Mortar (N/mm^2)	Note
1	N.A.	N.A.	N.A.	Load dispersal test[1] using polystyrene load indicator, ie. loaded through rod fill.
1	<u>2.0</u>	7.11 (av. of 2)	1.99 (av. of 3)	Two voussoir mixes used[2]. K.E. loading.
2	N.A.	N.A.	N.A.	Load dispersal test[3] employing sheet paper and carbon paper "load indicator".
2	<u>1.93</u>	6.27	1.72	Model pre-cracked by above test[4]. K.E. loading.
3	N.A.	N.A.	N.A.	Load dispersal test employing mortar skim, cartridge paper and carbon paper[5].
3	<u>2.49</u>	7.41	None	Front face of model whitewashed to better reveal cracking. K.E. loading.
4	<u>2.35</u>	7.97	0.77	Again whitewashed front face. K.E. loading.
5	2.63	5.85	0.89	Load applied through fill to failure[6], ie. not a K.E.L. test. Softer carbon paper load dispersal indicator and white grid pattern on front face.

Table 5.15 In-house model arch tests: first series

1 The polystyrene was placed at the interface between the extrados and the rod fill and was intended to give a preliminary qualitative indication of the extent of dispersal of live load pressure. However, the results were disappointing.
2 Two separate voussoir mixes were used and the material strengths for both are presented.
3 The carbon paper was used in place of the polystyrene to give a better indication of the varying live load pressure. Again, the result was poor.
4 Whilst care was taken to avoid damaging the models during the preliminary load dispersal tests, in this instance it was observed that cracking did occur. This may may have influenced the load achieved in the subsequent ultimate load test, which it will be noted provided the lowest collapse load of the series.
5 A penultimate attempt to produce a good live load dispersal impression involved a thin mortar skim on the extrados (to give a smooth base) followed by cartridge paper and then carbon paper with the rod fill above. Yet again the result was not sufficiently good to be useable here. The mortar skim may have strengthened the arch and it will be noted that the subsequent ultimate test on this model produced the highest value in the series.
6 The final load dispersal attempt employed a softer carbon paper, again with little effect. A surcharge load was also applied at deck level by means of steel weights. This test was taken to ultimate in the dispersal mode and is therefore not comparable with the preceding five tests and further reference to it will not be made.

The result of direct relevance to the present studies, the mean collapse load for the KEL tests, was 2.19 kN, including averaging the two results suspected of being unduly high and unduly low.

The characteristic load deflection curve for the tests is portrayed in Figure 5.8. The jaggedness of the curve arises for two reasons; firstly because the load was applied by manually turning a knob on the loading apparatus and this is a necessarily discontinuous operation, and secondly because the rod fill continually readjusted itself under arch deformation and this tended to occur as a "stick-slip" process. The mass of rods moving at each slip appeared to be quite large, jolting the whole system.

Otherwise the curve may be observed to be non linear throughout with a long falling branch. Peak load was typically obtained at a deflection of 2 to 3mm, measured at the load position.

Referring again to Plate 5.5, a typical arch deformed under test may be observed.

Plates 5.8 to 5.12 are close-up images of hinges formed in the vault.

Although particles of masonry were observed to fall from the hinge areas under test, it is not possible from any of these plates alone to be certain that local crushing did indeed occur. However, after failure and on close examination of the masonry hinge interfaces (see Plates 5.13 to 5.16), some rounding of the corners may be seen suggesting that some limited crushing did occur.

FIGURE 5.8

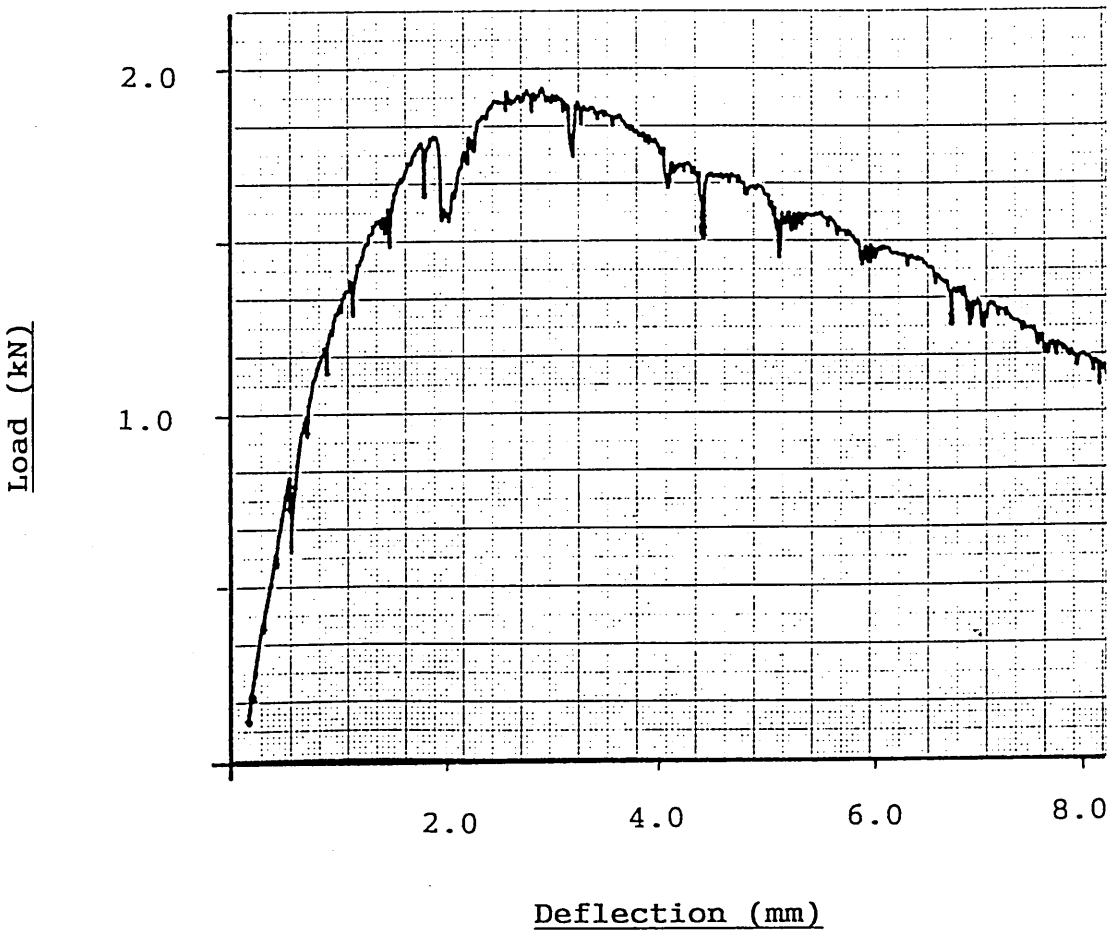

Typical load-deflection plot for a model arch test
(Series One, number 3)

PLATE 5.8

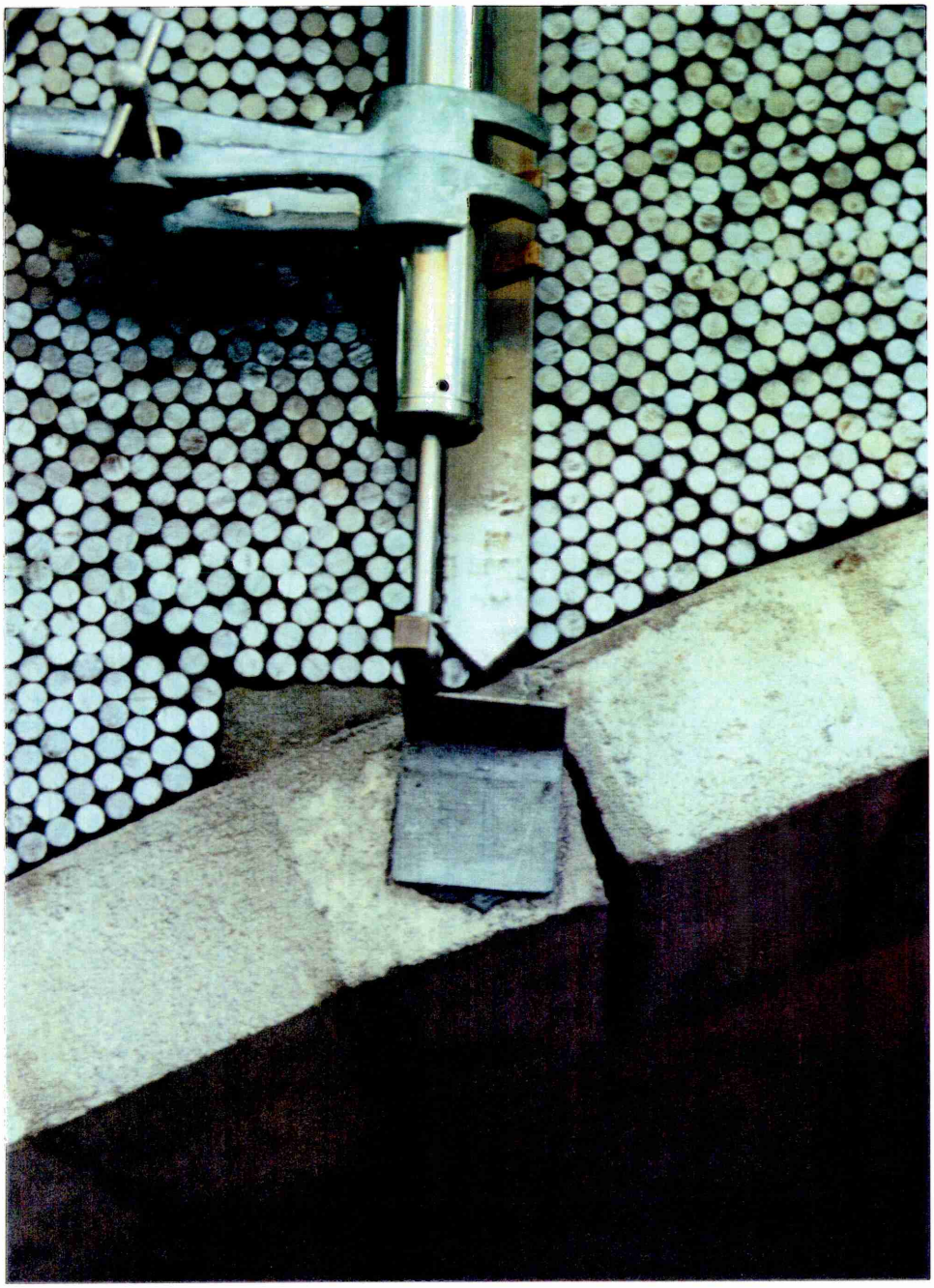

Close-up view of a typical hinge formed beneath the load position

PLATE 5.9

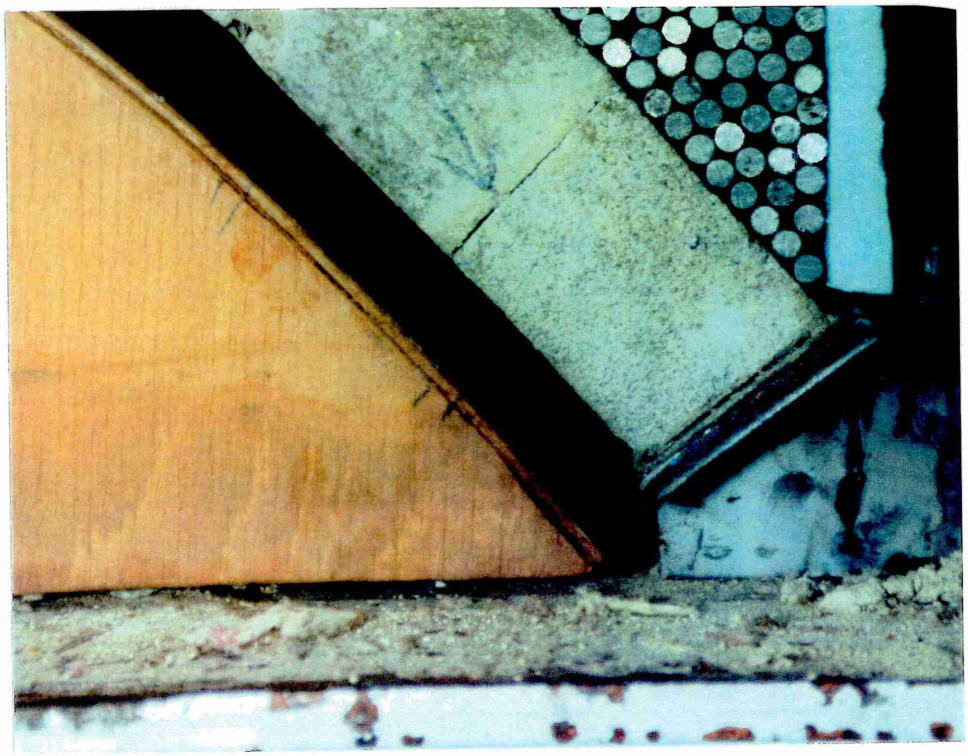

A typical hinge at the springing remote from the load.
Note that it is one voussoir into the span.

PLATE 5.10

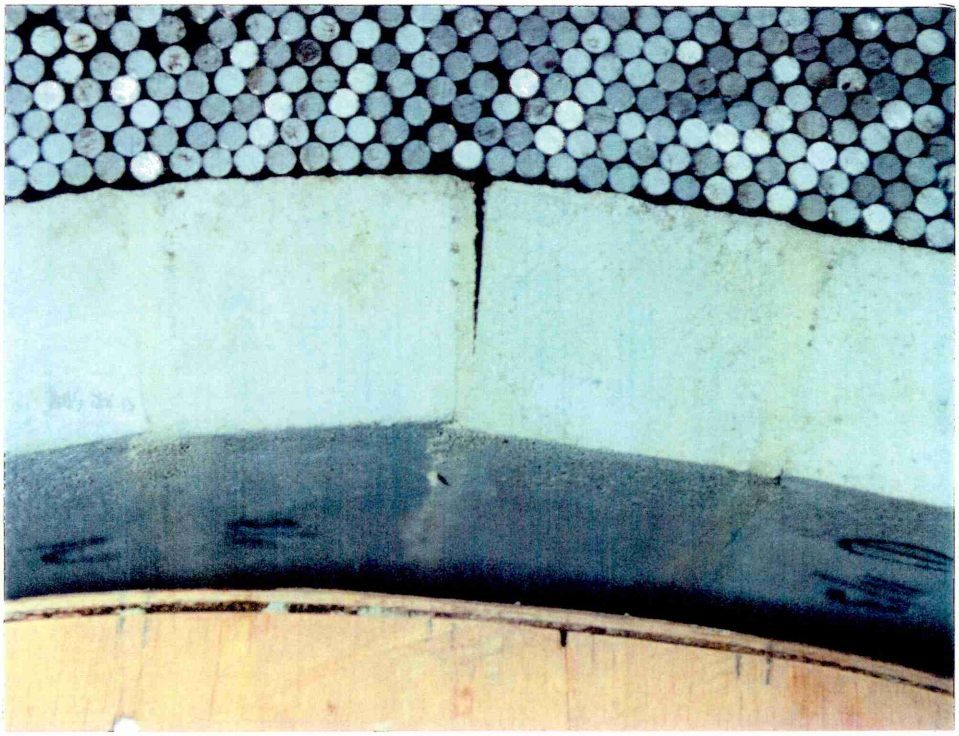

A typical in-span hinge remote from the load position

PLATE 5.11

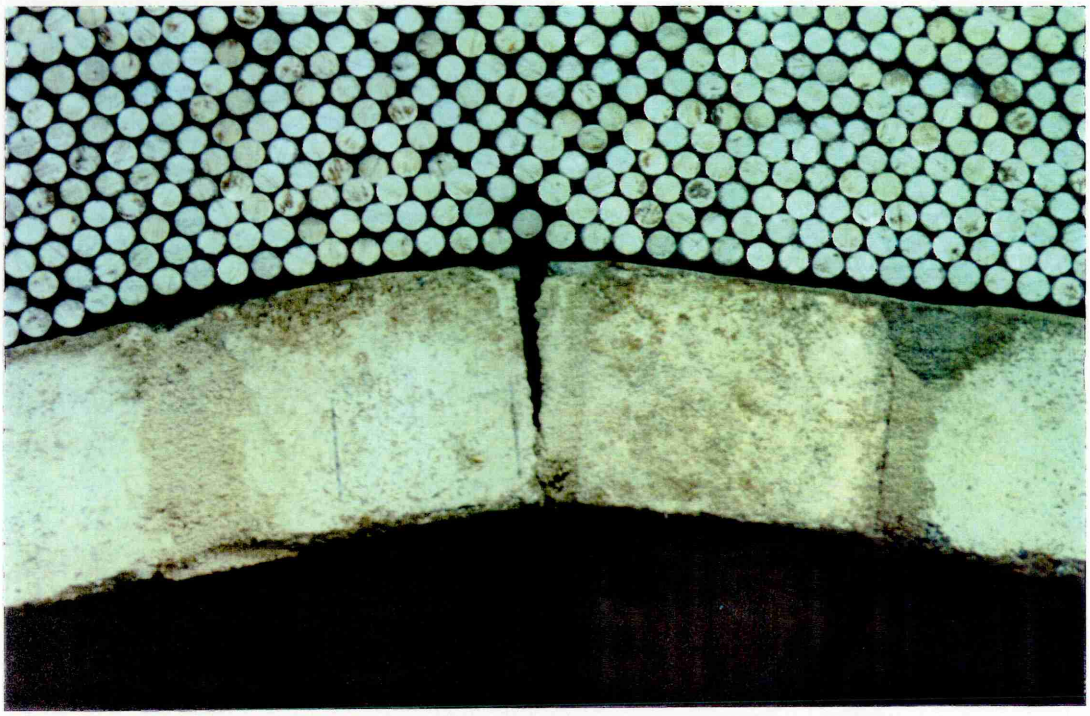

A typical in-span hinge remote from the load at high strain

PLATE 5.12

A typical hinge at the springing nearest the load position.
Note that it is truly at the springing.

PLATE 5.13

Typical voussoir edges post hinge formation - 1

PLATE 5.14

Typical voussoir edges post hinge formation - 2

PLATE 5.15

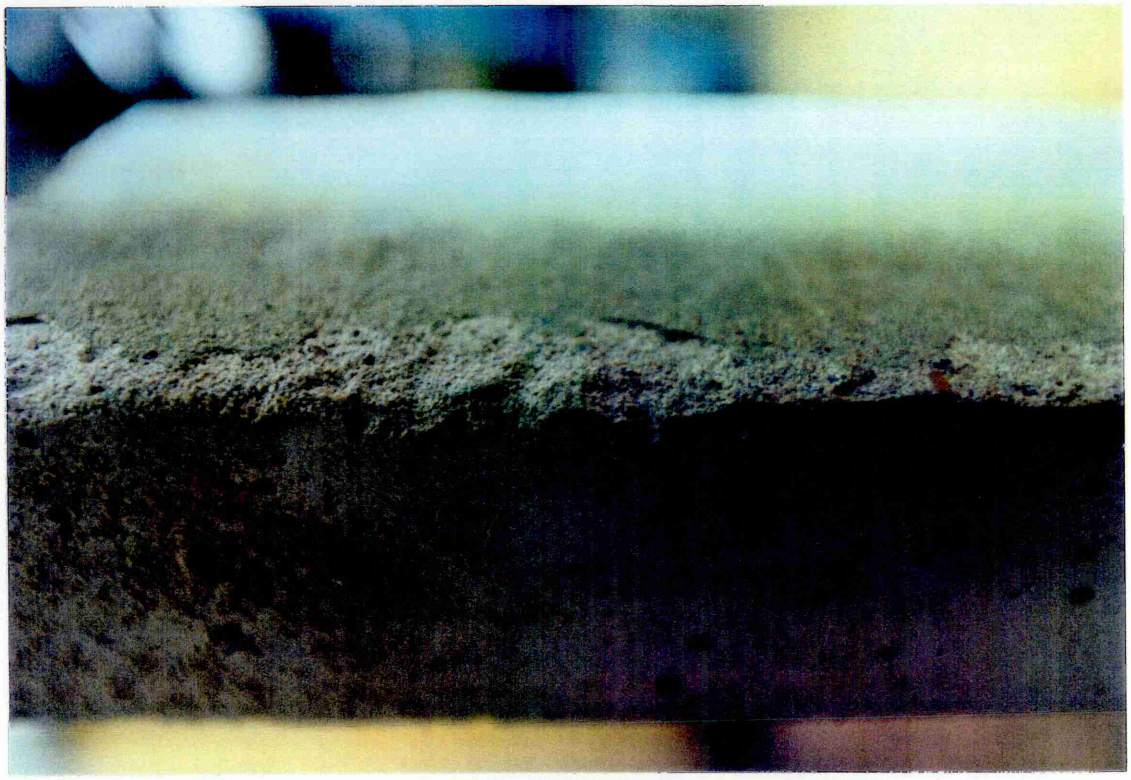

Typical voussoir edges post hinge formation - 3

PLATE 5.16

Typical voussoir edges post hinge formation - 4

On examining the broken arch pieces after the tests it was considered that all tensile failure in the vault was due to bond failure rather than material failure. Referring again to Plates 5.12 and 5.9, it will be noted that the opening hinge (Plate 5.12) occurs at the springing, whereas the closing hinge (Plate 5.9) occurs one joint into the span. The latter is a consequence of fill "trapping" in the closing corner and this effect may have strengthened the arch models. This suggests that one undesirable variable was in fact present. On reflection it would have been preferable to overspan the fill beyond the ends of the model arch to reduce the problem.

However, it is considered that the configuration was basically successful and a second series was undertaken to provide more data and without some of the uncertainties raised by the load dispersal pre-test exercise. At the same time, some of the earlier tests had been video filmed employing equipment associated with a further research programme at Sheffield Hallam University and a potential spinoff technique for deflection monitoring was becoming apparent. To develop this aspect, more controlled conditions (from a video point of view) were necessary.

5.4.4 Second model arch series

The second series consisted of four tests and it was hoped that the first series scatter on ultimate collapse load could be improved upon. Other than the fact that the Sheffield Hallam University structures laboratory had been relocated, these tests were similar in all respects to the earlier ones and no further description is necessary.

The results obtained are given in Table 5.16 below.

Model #	Failure Load (kN)	σ_m Vouss. (N/mm^2)	σ_m Mortar (N/mm^2)	Note
1	≈2.0	16.1 15.5	1.31 1.40	Problem reading maximum load
2	2.25	8.5 8.2	1.10 1.00	
3	1.9	7.8 8.4	1.88 1.97	Transducer problem, so reset after reaching 1.8 kN
4	2.33	5.82 6.24	1.50	

Table 5.16 In-house model arch tests: second series

The overall results are very similar to those in the first series, and the mean collapse load (from four tests) is 2.12 kN, which compares well with the earlier mean of 2.19 kN, also from four tests. The overall mean is 2.16 kN. Further, the scatter is reduced from 2.63-1.93 to 2.25-1.90, the latter indicating some -10% to +6% on the mean. The inevitable conclusion to be drawn is that to accurately and repeatably construct a model of this kind is very difficult, even under laboratory conditions. It also suggests the previous series was not so prejudiced by load dispersal variations as had been imagined.

5.4.5 SMARTMEC analysis applied to the in-house scale model arches

As both the series one and series two models were basically identical, a single set of input parameters will suffice for all. However, the material strength has a range of possible values (from the weakest mortar to the strongest voussoir), and the "earth pressure coefficient" for rod fill is uncertain and so SMARTMEC upper and lower bound, and optimum, and Archie analyses will once more be made. The input data is tabulated below.

Data Item	Value	Note
Span (m)	1.060	(I)
Rise (m)	0.250	
Quarter point rise (m)	-	
Shape	Segmental	
Barrel thickness at springing (m)	0.050	
Barrel thickness at crown (m)	0.050	
Cover at crown (m)	0.100	
Mean material specific weight (kN/m^3)	72.30	
Earth pressure coefficient	0.2-0.3	(II)
Earth pressure enhancement	1.00-1.25	
σ_m (N/mm^2)	0.77-16.1	(III)
k	2	(IV)
λ	1.25	
Distance of load from RHS (m)	0.25	
UDL over whole span (kN, total)	0	
Live load distribution type	KEL	(V)

Table 5.17 SMARTMEC input data: in-house model arch tests

(I) The nominal span was one metre but the true span was 1.06m.
(II) Assumed range based on advice from geotechnics staff.

(Ⅲ) 0.77 is the weakest mortar value; 16.1 the strongest voussoir value.
(Ⅳ) Assumed value for concrete.
(V) True KEL due to steel plate (see Plate 5.6)

The resulting SMARTMEC output is tabulated below.

Prototype mean collapse loads 2.19 kN and 2.12 kN (series 1 and 2)		
No.	Output Item	Value
1.	Upper bound collapse load, kN, (% of prototype)	2.44 (113.2)
2.	Optimum collapse load, kN, (% of prototype)	1.96 (90.9)
3.	Lower bound collapse load, kN, (% of prototype)	1.22 (56.6)
4.	'n' for hinge under load position at optimum	0.064
5.	Archie, kN, (% of prototype)	6.25 (290.0)

Table 5.18 SMARTMEC output: in-house model arch tests

Note: SMARTMEC optimum run is based on σ_m = 3 N/mm^2, an earth pressure coefficient of 0.25, an earth pressure enhancement factor of 1.2 and K.E. loading.

5.5 Summary

5.5.1 SMARTMEC results

A convenient overview for all the results obtained is shown in Figure 5.9. This plots the range of results for each individual case against the prototype, as a percentage. In most cases SMARTMEC brackets the prototype, though not necessarily symmetrically, with models faring best. The latter point illustrates the need for good, representative input, this generally being available for the laboratory models but not for the full size bridges.

It must be borne in mind that, to reflect a fair picture of SMARTMEC, the lower and upper bound results have been obtained by grouping together all the 'high' and 'low' input parameters, respectively. This has resulted in large ranges between upper and lower bound answers. In practice one would never combine input parameters quite so severely as this; a mixture of 'best guess' parameters would always tend to provide a single 'optimum' result somewhere towards the middle of the range and so results of this kind are also depicted for each example.

FIGURE 5.9

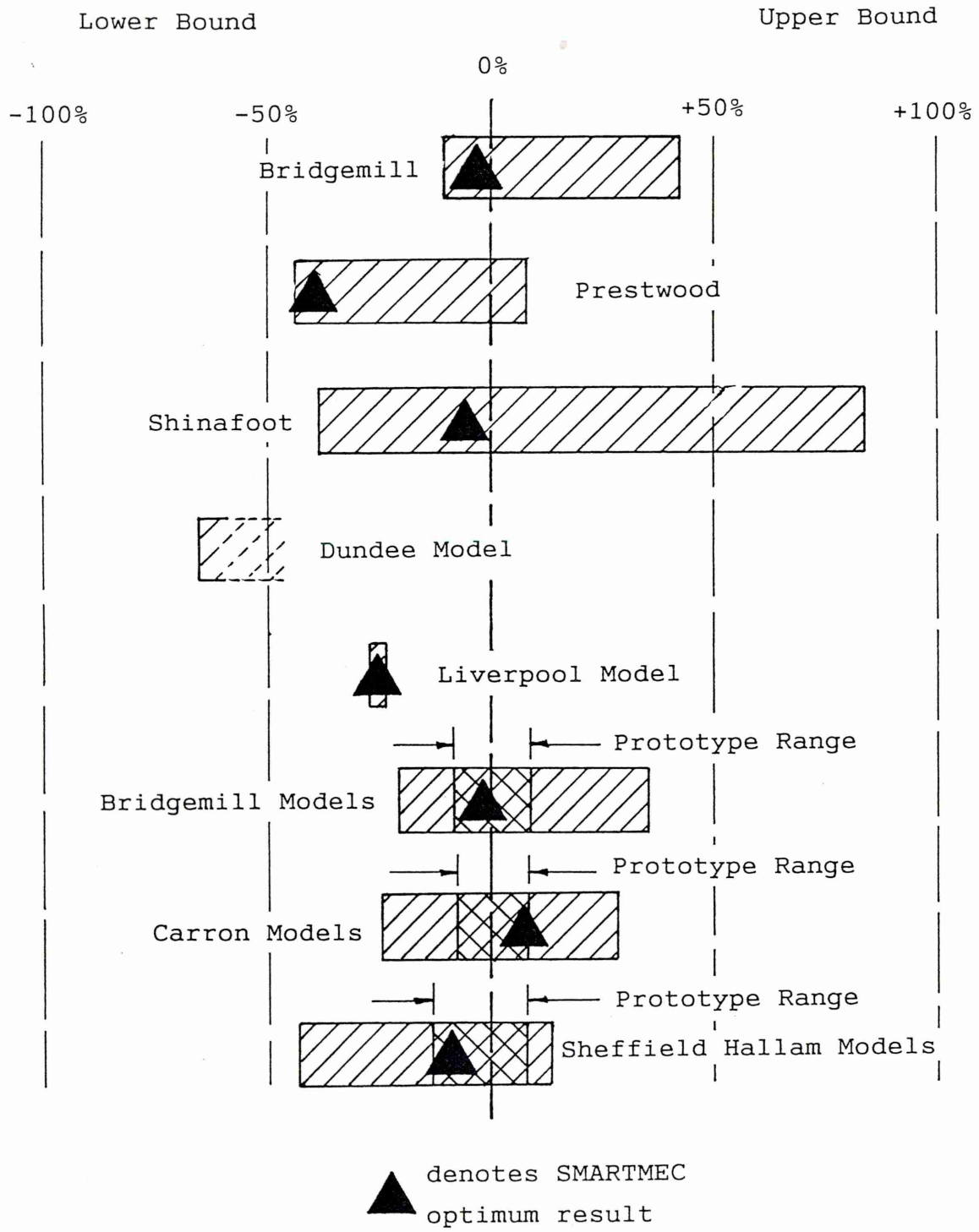

SMARTMEC results summary.

Results are shown as a percentage deviation from the prototype failure load(s)

It is considered that SMARTMEC's results exhibit good correlation with the various prototypes across a very wide range of arch configurations, sizes and material types. The comparison with Archie is limited in value, but does serve to illustrate that SMARTMEC's results are comparable with those obtainable from commercial software.

5.5.2 A simple parametric study (1): the influence of material strength

SMARTMEC may be used to demonstrate the effect of material strength on collapse load. Applied to Edinburgh University's Bridgemill Bridge model tests, and the Bridgemill prototype, it provides the data depicted in Figure 5.10 a) and b) respectively.

With reference to Figure 5.10 a), it may be seen that, as would be expected, the locus begins at the origin - no material strength results in no structural strength! The locus then rises rapidly to (virtually) a plateau. The plateau is assymptotic to infinite material strength, with increases in material strength now producing very little increase in structure strength.

Although the precise shape of the curve will no doubt be unique to an individual arch (and possibly to other factors as well), the general trend seems clear. The inference is that *increasing material strength up to a point produces dramatic increases in arch strength.* Beyond a point, however, very little benefit derives from improving material strength.

The marked non-linearity of the effect of material strength at the low end casts some doubt upon the use of a material partial factor of safety, γ_m, in bridge assessment. If the analysis used models the effect of material strength accurately, use of γ_m may produce unintentionally disproportionate reductions in the arch strength.

It is noteworthy that mortar strength (especially lime-based mortar) may commonly lie in the former region, and voussoir strength in the latter. It would thus seem important to choose a representative value for overall use in analysis and this is an area with scope for further study. Edinburgh University's model Bridgemill Bridge's brick and mortar strengths are superimposed on Figure 5.10 a) as is the range of model collapse loads. The consequences for collapse load prediction by choosing either the mortar or brick material strength can be seen. In this instance using the brick value alone would seem to give the best result, but this is of course fortuitous and by no means a general conclusion.

FIGURE 5.10

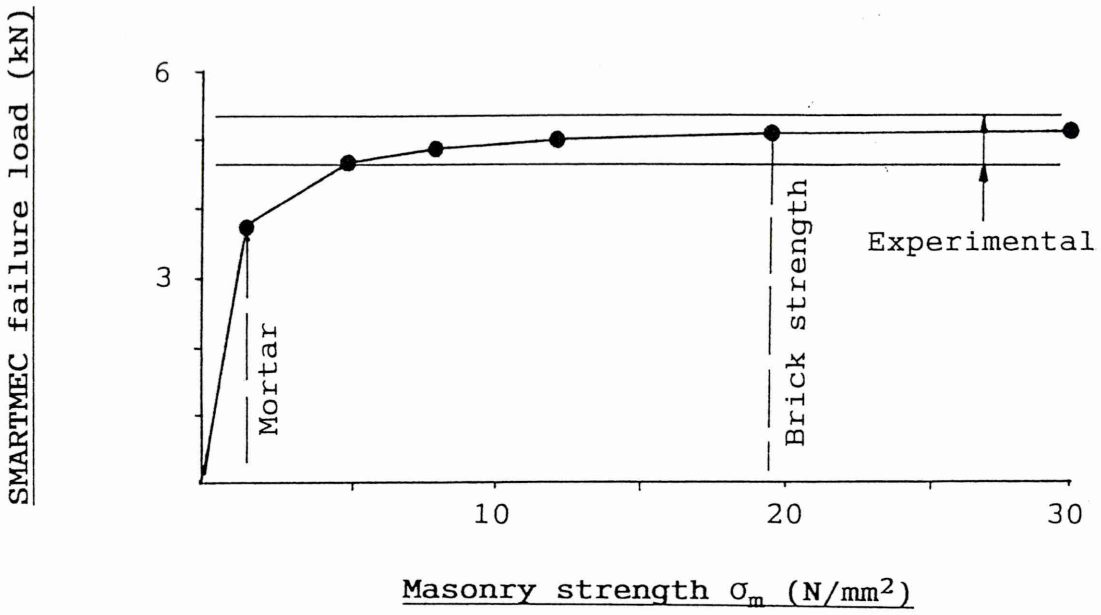

a) effect of material strength on Edinburgh's Bridgemill Bridge scale model

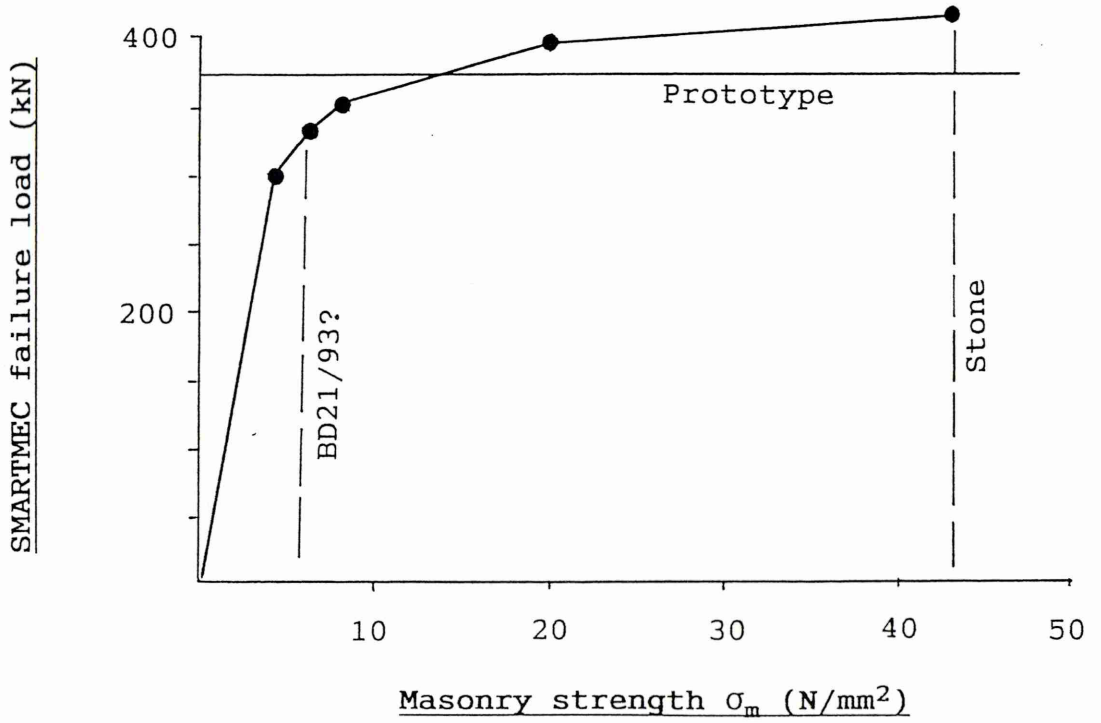

b) effect of material strength on Bridgemill Bridge full-size prototype

Figure 5.10 b) similarly shows the Bridgemill prototype and the same general locus profile is evident. In contrast to the above, use of the stone strength upon which to base a collapse load prediction would result in an overestimate. A better value would be obtained by use of the guidance given in BD21/93, though still producing a slight overestimate of collapse load.

The the two above examples highlight the difficulty in choosing a representative *single* value for material strength, even if both the mortar and masonry individual values are known. In practice, neither or perhaps only one may be known, compounding the problem.

Accepting that material strength is relevant to both the Bridgemill prototype and to the Bridgemill models, the steeper rise and earlier, flatter plateau to the models' locus tend to suggest the question is more relevant to the full size bridge. This also supports the hypothesis that there is a scale effect, and justifies the attempts made in the in-house model tests to obtain as high a loading with as weak a material as possible.

Finally on this point, Figure 5.11 plots mean 'n' values for the hinges beneath the load against span for all the case studies considered. This demonstrates a (weak) correlation - the smaller the bridge, the nearer the interaction diagram origin are the hinges at failure. The marked aberration of the in-house data point on this figure shows that the attempt to "weaken" the material to induce some compressive yielding was to some extent successful.

Data of this kind could be used to extrapolate the absolute maximum size of arch bridge capable of being built of traditional materials in traditional form, having first decided a limit on the interaction diagram - possibly the peak.

Finally, it is interesting to take data from the SMARTMEC analysis of the Bridgemill prototype for the hinge under the load position, and to input this to computer programme PSTRESS1. The resulting stress and strain plots across the section at the hinge position are depicted in Figure 5.12.

It is quite evident that an appreciable depth of arch barrel is in compression, and thus that the thrust line is not at the extreme fibre at collapse. Note also that the curved stress block locus indicates that the peak stress is not quite at the extremity of the section.

FIGURE 5.11

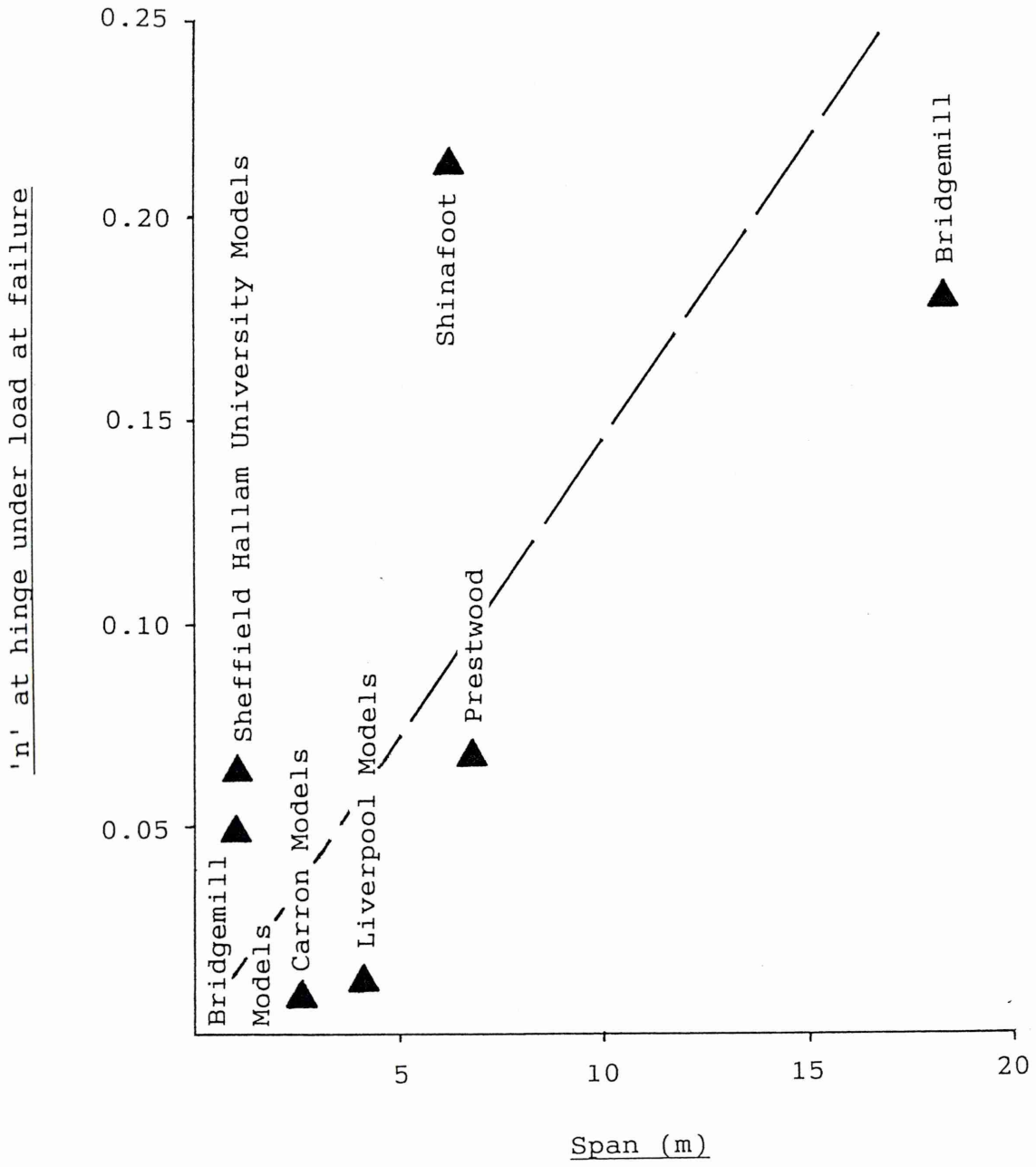

A plot of 'n' value for hinge beneath load versus span for the case studies

FIGURE 5.12

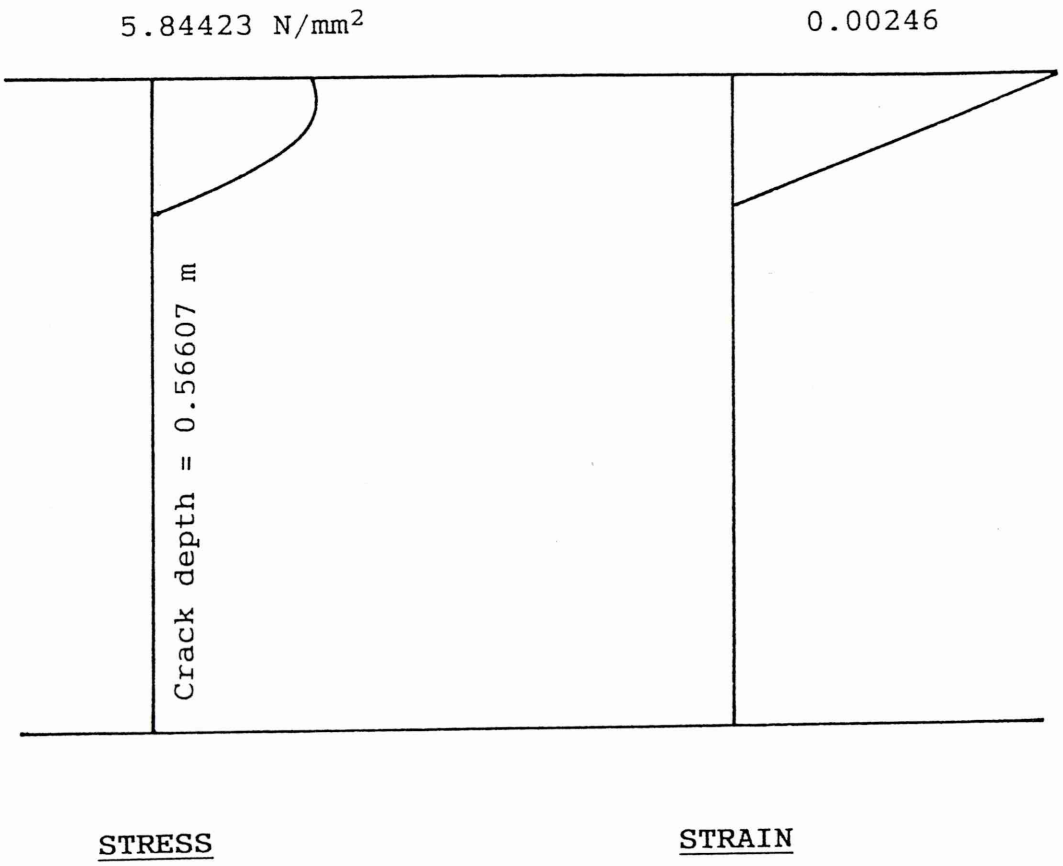

PSTRESS1 "predicted" stress and strain distributions for hinge under load position - Bridgemill Bridge prototype

It is concluded that the studies relating to material properties have been amply justified in the finding that material strength can be a significant contributor to arch ultimate load capacity and furthermore the means to make sophisticated allowance has been developed and incorporated in a mechanism type-analysis computer programme.

5.5.3 A simple parametric study (2): the influence of 'k'

Figure 5.10 a) can be expanded upon by adding further loci corresponding to further, fictitious, materials with the same σ_m value but with varying k. This is done in Figure 5.13 and reveals that, unlike varying σ_m, varying k has minimal effect. This might have been expected; k is related to stiffness and as such has little effect on collapse load.

The parameter 'k' is related to 'E' (Young's modulus) and is some measure of stiffness for a non-linear constitutive material, just as is 'E' for a linear material[44].

It is postulated that consideration of 'k' would have a much greater influence on any analytical method which traced the load path history, since predicted structural deformations from such a method may be a function of 'k'.

Other fields of research may yield the most fruitful application of the 'k' concept, but such work is left to others.

Figure 5.14 speculates (in an exaggerated, schematic manner) what might happen by varying 'k'.

Practical masonry materials possess values of 'k' in the range 2 to about 12, but it is likely that if materials with values of 'k' ranging much lower existed, then their loci they would tend, in the manner shown, towards the asymptote, which is itself suggested represents k=0, ie. the infinite compressive strength and stiffness Heyman model.

FIGURE 5.13

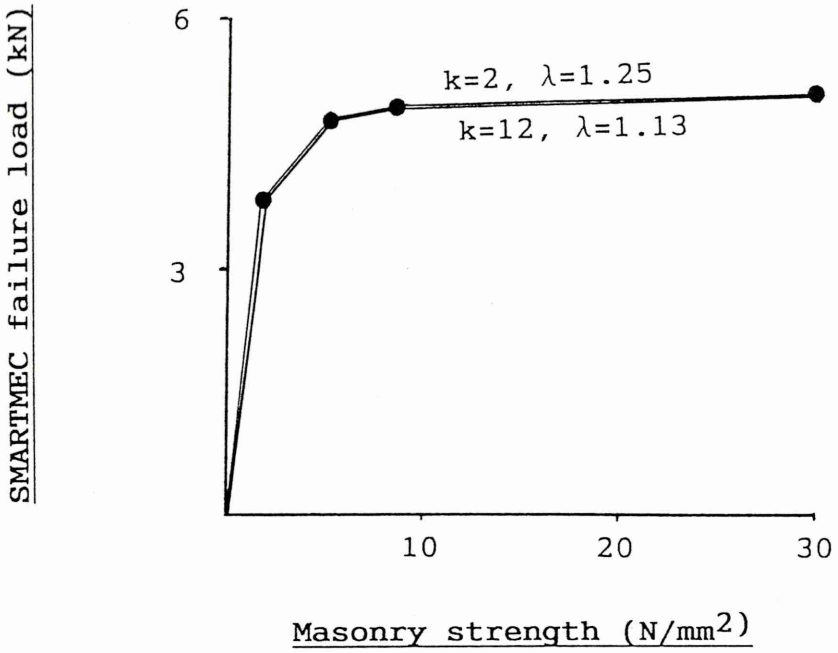

Effect of 'k' on collapse load
(SMARTMEC applied to Edinburgh's Bridgemill Bridge models)

FIGURE 5.14

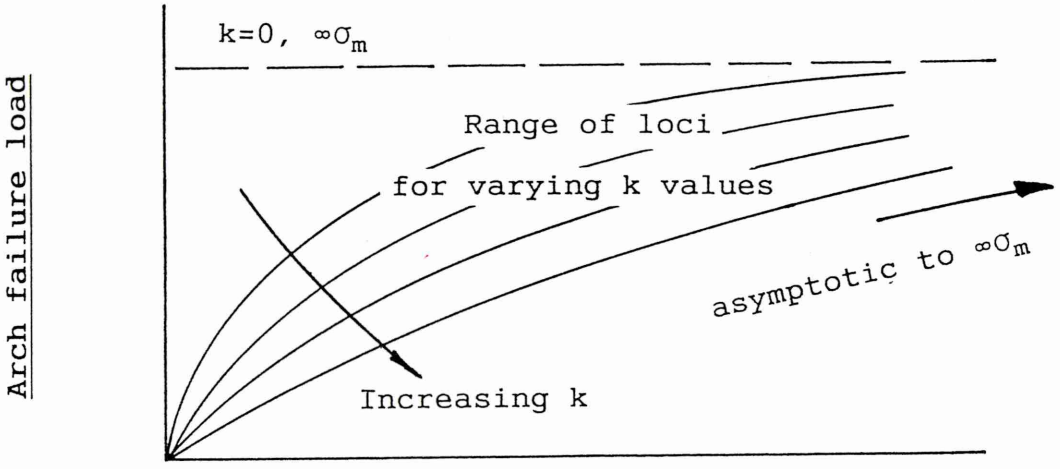

Possible effect of 'k' on collapse load (schematised hypothesis only)

5.6 Conclusions

The five key conclusions from this chapter are:

1. Material strength can be important to masonry vault behaviour.

2. Sophisticated masonry strength modelling may be incorporated into practical mechanism analysis.

3. The degree of effect of material strength is dependant on the scale of the structure.

4. Aside from the use of 'k' values of zero, which is non-conservative, and infinity, which is over conservative, the actual value employed has little effect on collapse load.

5. The 'k' concept is most probably appropriate to the wider field of masonry mechanics, especially in applications dealing with stiffness and hence deflection.

CHAPTER SIX

The Kinematics of Collapse Through Computer Vision

6.1 Synopsis

The concept of computer vision, an information technology (IT) tool, is introduced and its novel potential in the structures field outlined.

Computer vision techniques are adapted to the monitoring of model arches tested to destruction in the Sheffield Hallam University structures laboratory. By using an edge detection algorithm, numerical deflection data is obtained which demonstrates the potential accuracy of this approach and prompts further work in the field.

A full level masonry arch viaduct test to destruction, conducted by the TRL, is video monitored and the results studied by computer vision. By this means a speculative theory regarding the mode of failure is formed.

To test the viaduct failure hypothesis an adaptation and generalisation of the constitutive-based mechanism model theory is developed which demonstrates both the viability of the failure hypothesis and the usefulness of the constitutive studies.

6.2 A Description of Computer Vision

Computer vision is a comparatively new science which aims to understand, mimic and enhance the properties of biological vision. Vision itself is a means of describing the physical world, whereby images are input for interpretation by the system to produce a symbolic representation of the viewed scene. There is a huge physiological literature describing biological vision systems yet many visual processes are at best

only partly understood, and to date computer vision techniques cannot match their biological equivalents.

A key difference between computer and biological vision is that the former is largely *quantitative* and the latter largely qualitative[53]. A human observer may know where viewed objects are to a high degree of precision and be able to use that information to manoeuvre within and manipulate the physical environment. However, the individual will not be precisely aware of the exact distances between objects, unlike in a computer vision parallel. Computer vision centres upon the interpretation of grey level, pixel-based data which may be quantified to provide required measurements.

The potential for test monitoring offered by the quantitative aspect became apparent during the video recording of the model arch tests described in the last chapter and it was decided to explore the possibilities.

Mainstream applications of computer vision in industry have to date been limited to inspection tasks, bin picking exercises and for robotic guidance. These systems usually operate within a controlled environment where the areas of interest are limited and only occupy a small part of the viewed world.

Despite the fact that qualitative monitoring of arch tests would be in a relatively unstructured environment and the region of interest encompassed the entire field of view, the demands in other respects were low; the need to process the visual data in real time, for example, was not a requirement. Furthermore, neither special camera nor film were considered essential and images could be captured under normal lighting leaving them usable in other contexts.

The aim was to obtain deflection data of a unique and more comprehensive nature than that available from conventional transducers. Whereas transducer measurement only provides data at the gauging points, computer vision measurement offers a complete field of information for subsequent analysis, providing numerical values without the need to have pre-determined the points of interest. In other words, measurement by transducer is at discrete points; measurement by computer vision is potentially continuous across the entire field of view and may be selected at leisure subsequent to the test. That is not to say that the application computer vision is entirely unpredetermined, since optimisation of lighting, viewing position and subject tonal qualities are desirable for best results. Nevertheless, the technique is more robust than traditional methods in its tolerance of measurement setting-up assumptions as will be seen later.

The next section describes the application of the computer vision technique to the Sheffield Hallam University model arch tests described in Chapter Five.

6.3 Computer Vision in the Structures Laboratory

6.3.1 Data collection

A tripod mounted, domestic video camera was set up to monitor the pilot arch test described in the last chapter and the images were recorded on a normal VHS video cassette. The results were then input to a software package called 'Tina', which was available in the Sheffield Hallam University Information Technology Laboratory (by courtesy of Sheffield University where it was developed*) and the results are shown as grey level images in Plates 6.1 and 6.2. Note that these images are not photographs, but digital images displayed on a computer monitor. Plate 6.1 shows the pilot arch test at the unloaded (datum) state and Plate 6.2 at high deflection state. Both images were "grabbed" from the stream of frames covering the entire load test. In principle any moment or key event during the test could have been chosen.

6.3.2 Edge detection

To enable useful deflection data to be extracted from these images, it is necessary to precisely identify the same points for measurement on the arch before and after loading, ie. in the datum and deflected positions. Without the use of purpose-made marker devices applied to the arch, the most useable data are the edges of the arch itself. However, the edges appear as a graduation of intensity across several pixels and this places a limit on accuracy. To overcome this an edge detection algorithm can be employed.

Edge detection relies on assumption rather than hard facts. Many edge detection algorithms exist and all rely on a 'step' change in image intensity to mark the boundary between two regions. A step edge is a change in intensity marking the boundary between two image regions with approximately constant but very different intensities, and is readily detectable. All such algorithms are based on image differentiation; the first derivative of the image intensity values are taken and the peaks marked.

* The author expresses his thanks to Sheffield University for giving access to the Tina software.

PLATE 6.1

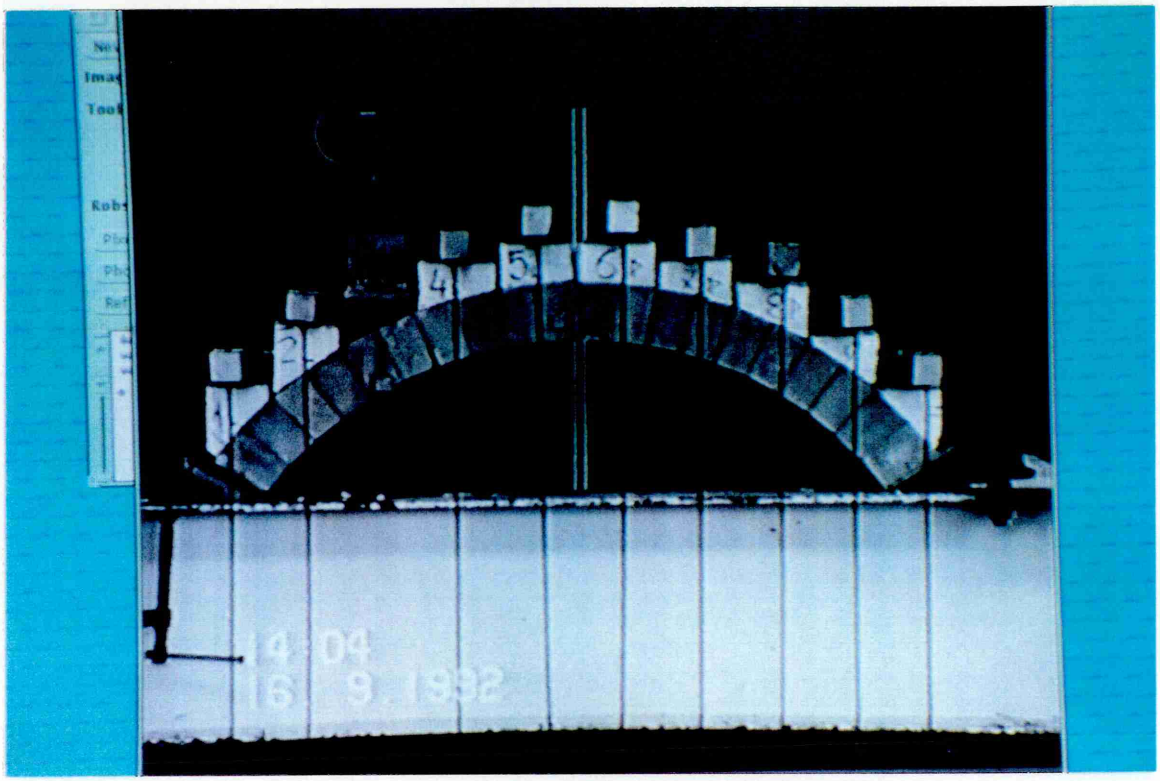

Digital grey level datum image

PLATE 6.2

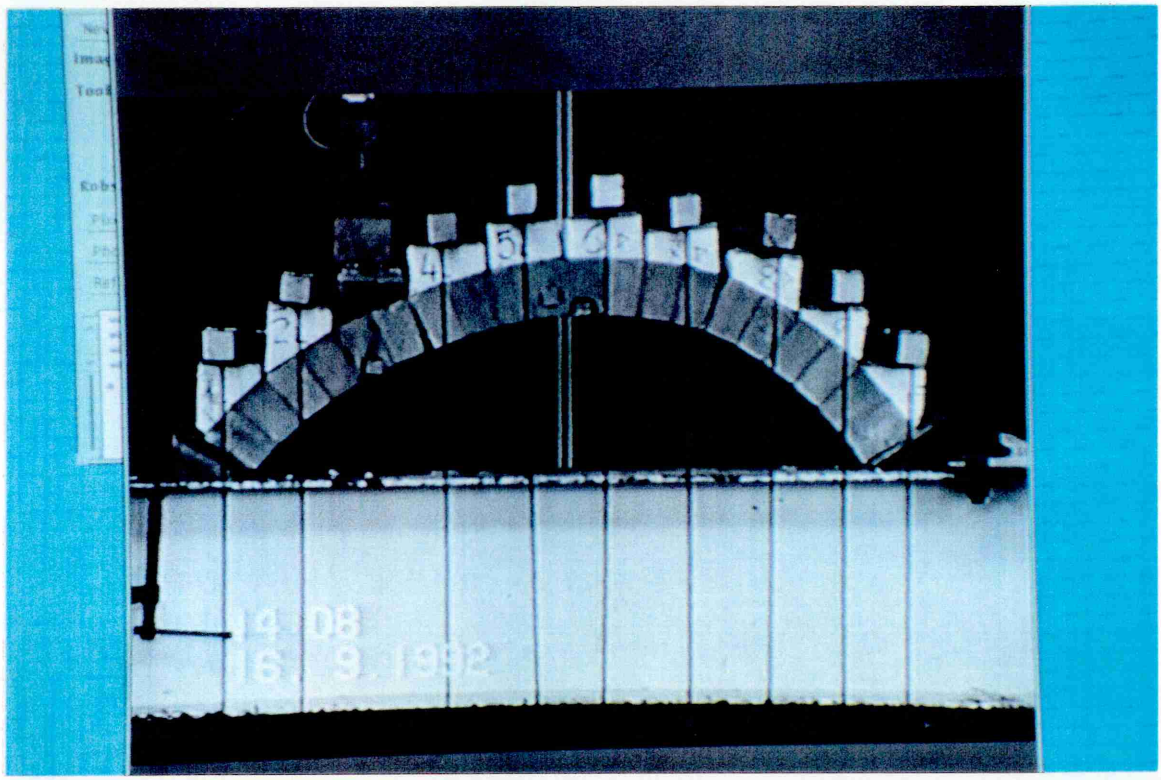

Digital grey level deflected image

The Canny algorithm[54], provided within the Tina software and rapidly becoming an industry standard, was employed in this instance to repeatably define the required edges. Figure 6.1 depicts the basic principles of edge detection.

The Canny algorithm first involves the removal of image noise by Gaussian smoothing followed by differentiation and a search for significant peaks.

The first variable parameter of note is σ, the standard deviation of a Gaussian smoothing filter, which effectively determines the degree of Gaussian smoothing, maintaining sharp boundary detail but generating a high volume of edge data, some of which may be the result of noise. A high sigma value gives greater noise reduction but will blur edge boundaries and may lose significant structures.

A step edge is given by its position, orientation and possibly magnitude (strength). It can be shown that convolving an image with a symmetric 2D Gaussian and then differentiating in the direction of the gradient (perpendicular to the edge direction forms a ready and effective directional operator.

A second parameter, the line length threshold, enables short edge strings to be discarded, discounting unwanted edge detail. Illumination or other effects may however cause significant line structures to be fragmented. High length will subsequently lose these details. A sigma of 30 and a line length threshold of 20 were considered suitable values for this application.

6.3.3 Results

The Canny algorithm was applied, by means of an automated procedure carried out by the computer software, to the images of Plates 6.1 and 6.2 to give the edges displayed in Plates 6.3 and 6.4, respectively. It can be seen that in addition to the required edges there are also spurious noise elements together with valid edges from the loading rig and so forth, both of which are not required. The number of rogue edges is however small, and is considered to be good given the arbitrary illumination of the arch and the uncontrolled environment. Manual editing of the two images next produces the cleaned versions depicted in Plates 6.5 and 6.6. From this point onwards, a variety of options is open. Superposition of the datum and deflected edges provides a foundation from which any desired measurements may be taken (Plate 6.7). This is again done manually, essentially by counting pixels between chosen points (Tina takes care of the actual counting), and relating this to known

FIGURE 6.1

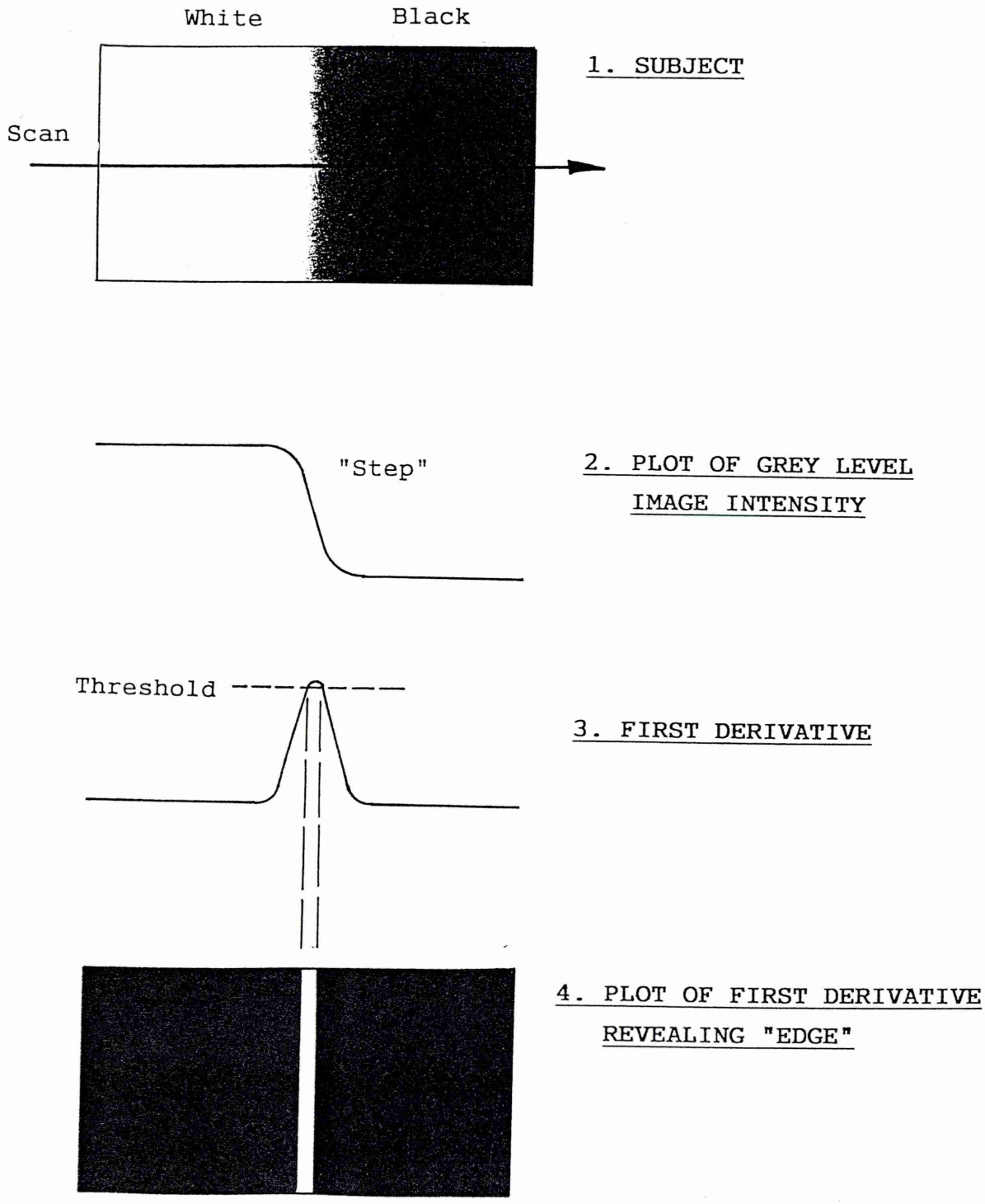

The basic principles of edge detection

PLATE 6.3

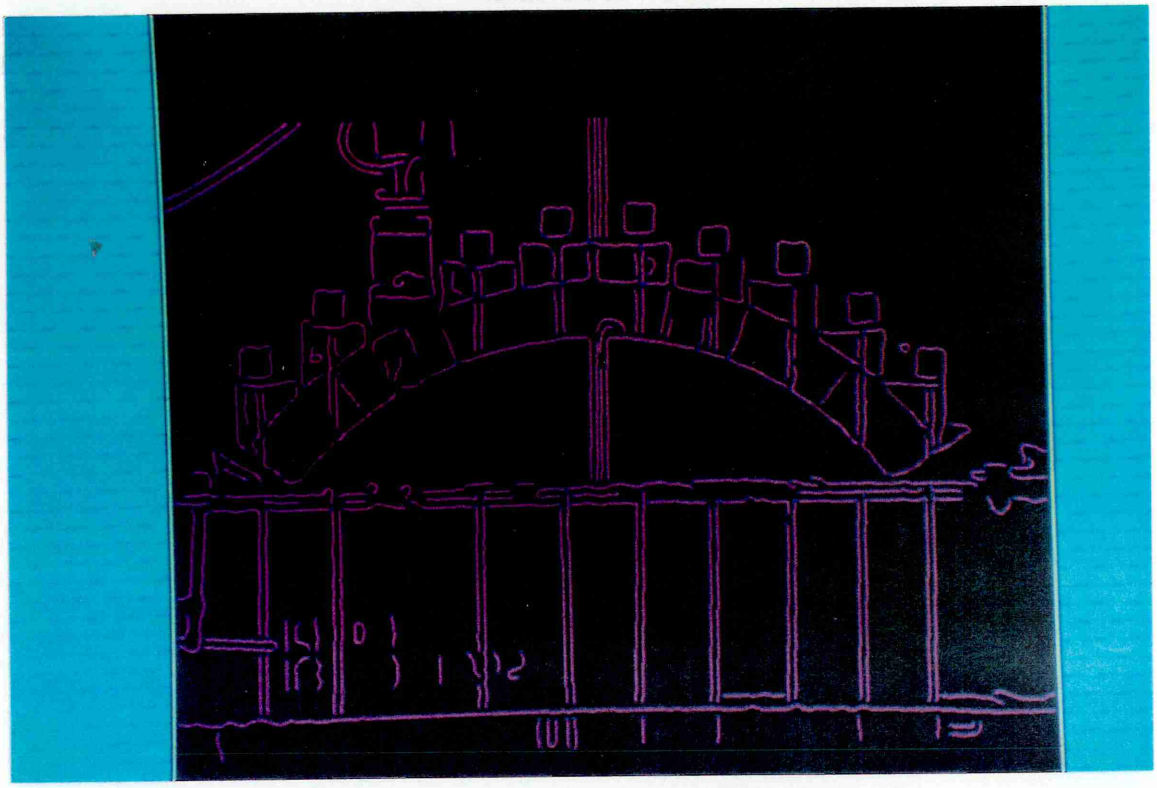

Datum edge detection

PLATE 6.4

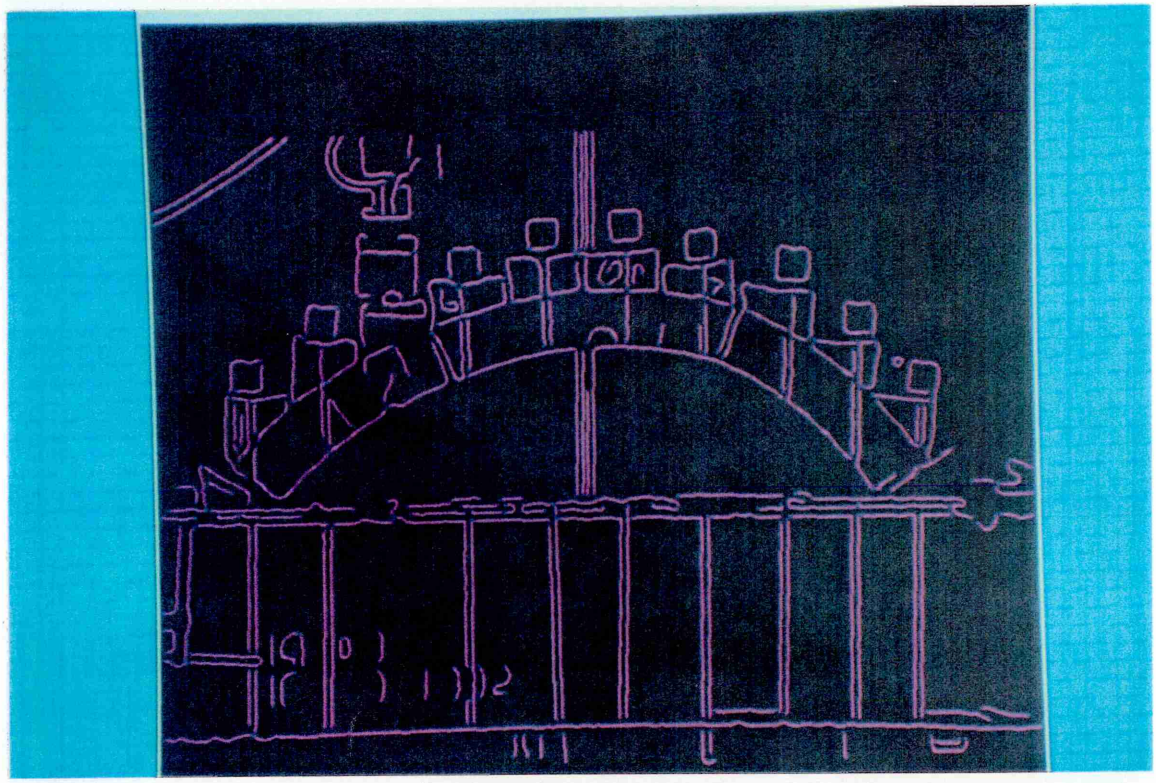

Deflected edge detection

PLATE 6.5

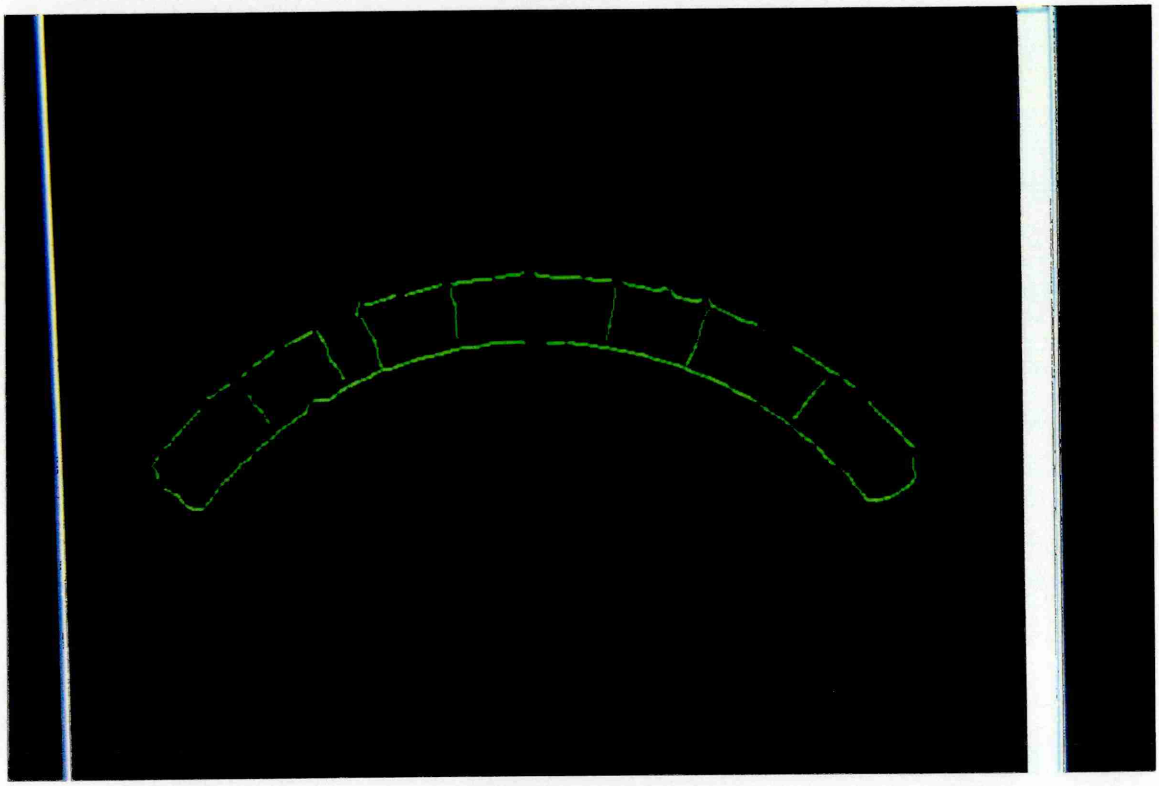

Datum cleaned edges

PLATE 6.6

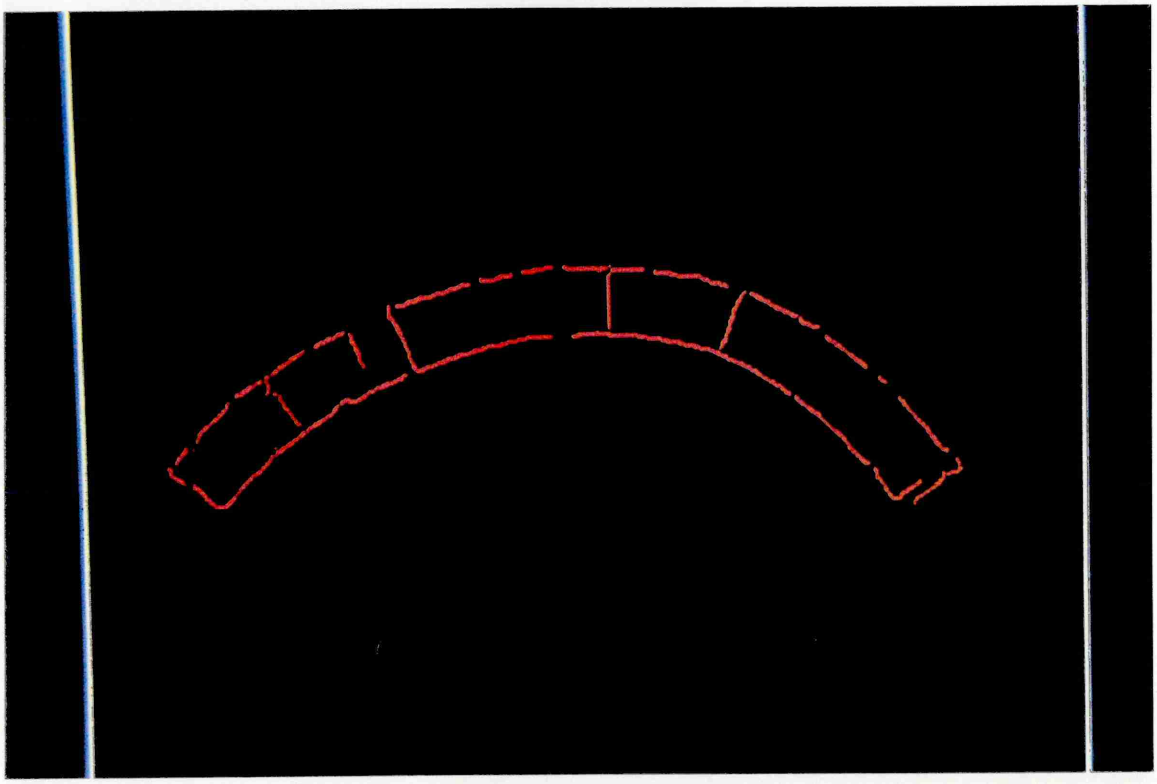

Deflected cleaned edges

PLATE 6.7

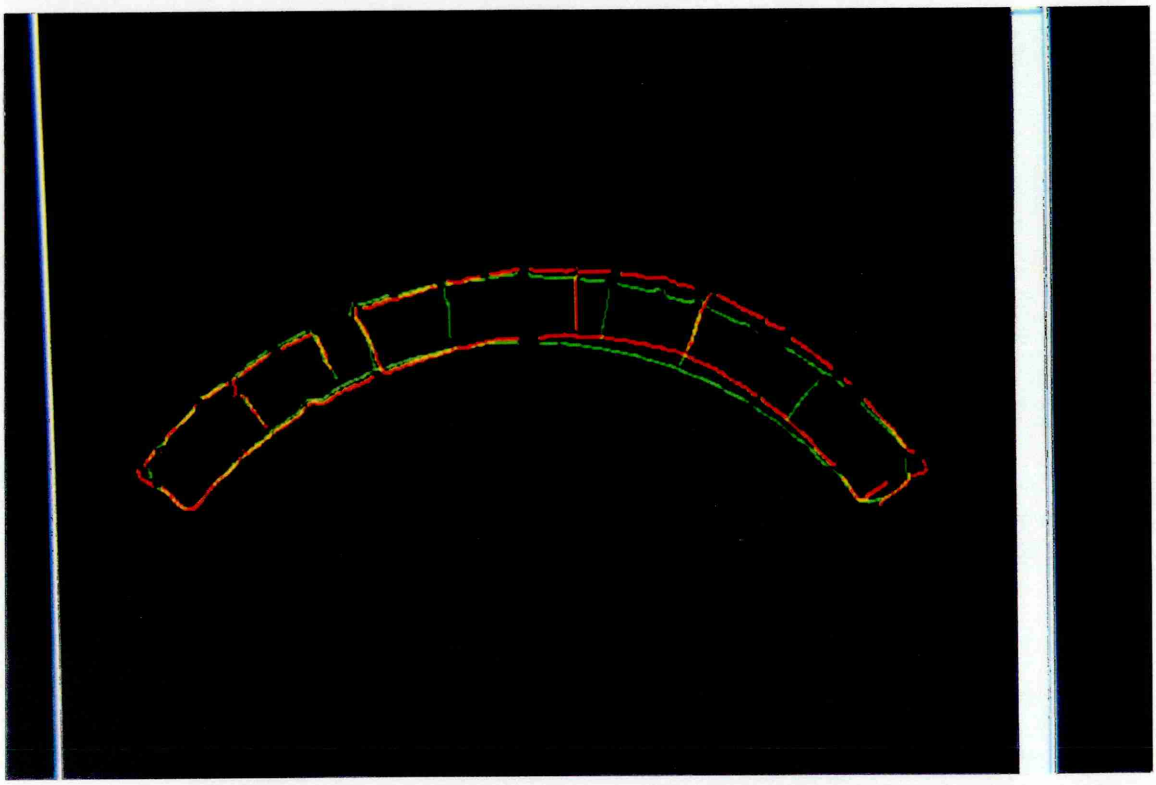

Composite cleaned edges only (7.5mm displacement estimated)

PLATE 6.8

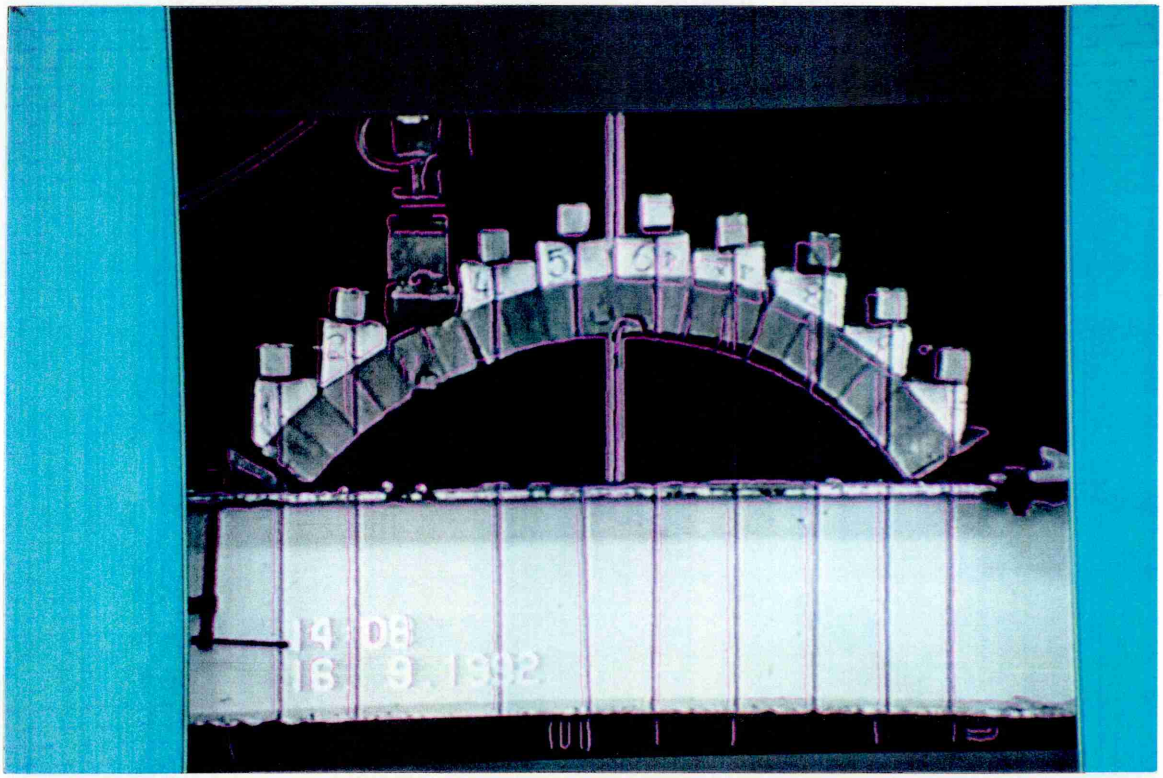

Composite deformed grey level and datum edges

dimensions in the image, such as the arch span. Using this method the deflection of the arch beneath the load is estimated to be a credible 7.5mm. Alternatively, the edges may be superimposed on source grey level images to give a qualitative impression of how elements of the test subject are tending to move. Plate 6.8 shows the deflected edges superimposed on the datum grey level image to illustrate the point.

Encouraged by this application of the computer vision technique it was decided to extend it into the field and this is the subject of the next section.

6.4 Computer Vision in the Field: Railtrack Overbridge Number 124

6.4.1 Description of the test

The opportunity to monitor a full level load test at first hand occurred when the latest in the series of TRL full level arch tests was planned for a date convenient to the further development of this study. The test was the first on a multi span arch bridge and took place on the 19th March, 1994, at Beighton, near Sheffield, on a redundant three span highway viaduct whose centre span crossed a watercourse.

The load test was mainly intended to give data on the degree of interaction between adjacent spans, and thus a single span was loaded by TRL whilst monitoring all three spans by means of conventional transducers.

Plate 6.9 gives an overall view of the loading topology. The massive masonry buttress in the right of the plate previously supported the railway-spanning metal deck, now removed for the test.

Load was applied by means of four hydraulic jacks connected to steel ties which were taken down through holes cored in the deck to ground anchors below. The jacks are mounted on a loading frame which sat astride the deck on a transverse "knife edge" which was effectively drawn down towards the ground anchors during the test sequence. The viaduct's spandrel walls have been removed since they would provide an unwanted additional dimension to the structural behaviour. Plate 6.10 shows the loading frame in detail and Plate 6.11 shows the set up from the opposite side.

PLATE 6.9

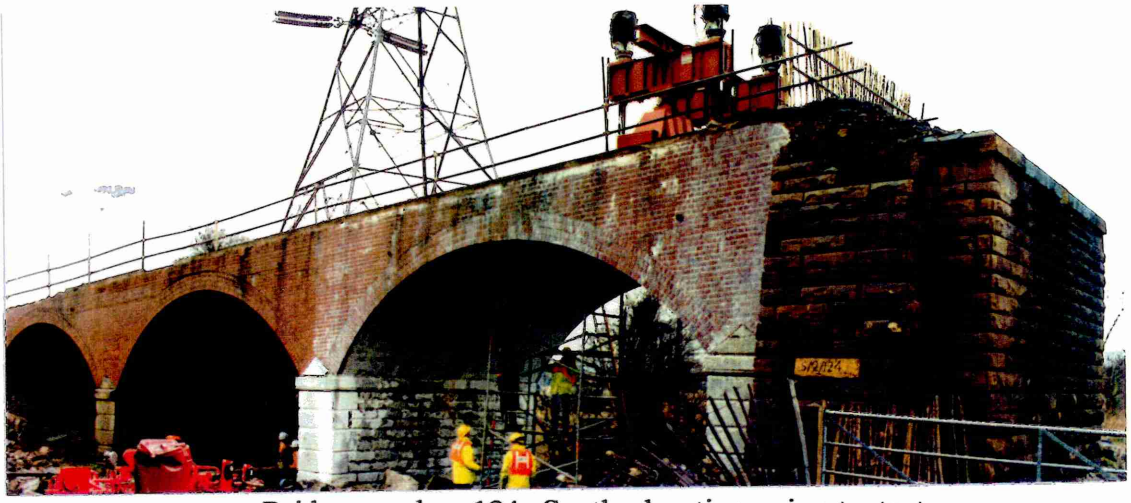

Bridge number 124: South elevation prior to test

PLATE 6.10

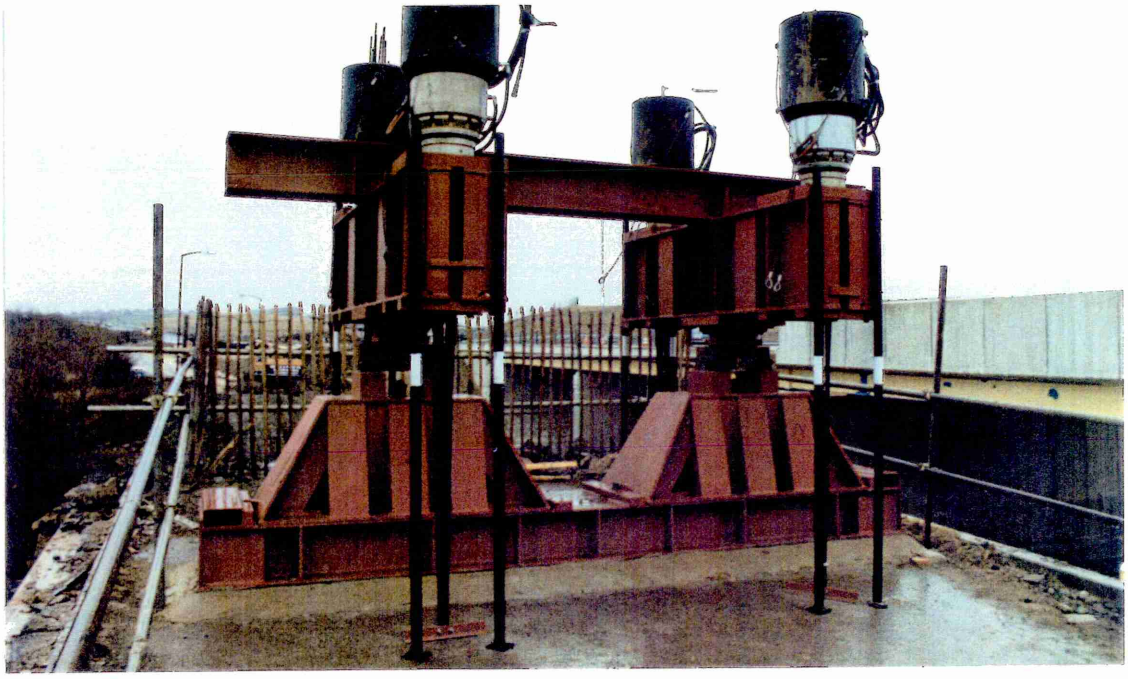

Bridge number 124: Loading arrangement

PLATE 6.11

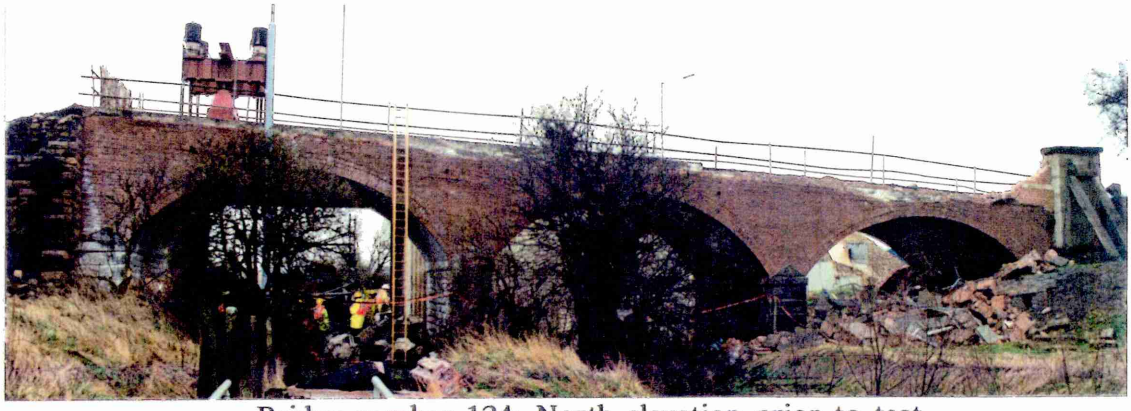

Bridge number 124: North elevation prior to test

The test necessarily took place during a railway "possession" because of the possibility of debris falling onto the adjacent tracks. This meant that the test took place overnight during a "no trains period", a term used by Railtrack to describe a type of possession not requiring diversion or rescheduling of their normal services. The implication of the night time testing for the purposes of this study was that arbitrary artificial floodlighting would be employed. TRL, for their own purposes, whitewashed the near face of the viaduct before the test with the aim of highlighting crack patterns, but a fortuitous spinoff would be increased contrast between the viaduct and its background, of benefit to the computer vision technique. Unfortunately, heavy rain during the days before the test washed off nearly all the whitewash!

Owing to the length of the test, which ran for several hours, continuous recording with one VHS cassette was not possible and so intermittent coverage was used, mainly while load increments were being applied. Eventual failure of the loaded span took place at a load of about 320 kN, a value lower than most had expected. It was conjectured by some present that a three hinge snap-through failure occured, thus limiting the value of the exercise. Resolution of the problem was clearly going to be difficult, but sufficient doubt must have existed since the usual TRL report on the test has yet to be published (spring 1997).

The application of computer vision techniques to the video cassette clearly offered a means of clarifying the issue.

6.4.2 Computer vision applied

The practicalities of obtaining a good camera viewpoint were immediately apparent, and the presence of the new road bridge (which had rendered bridge 124 redundant) prevented the desired central, normal position. Nevertheless, good VHS colour images were obtained and the two shown in Plates 6.12 and 6.13 depict the datum (unloaded) and just-prior-to-collapse conditions.

A similar treatment to before, employing the Canny edge detection algorithm by means of an automated computer process, yields the corresponding Plates 6.14 and 6.15.

The edges detected in this second application of the computer vision technique are more numerous than hitherto, many are obviously spurious. The temptation to interpret the edges on the spandrels as crack development should be questioned, and in the main these are more probably due to changing lighting on uneven brickwork.

PLATE 6.12

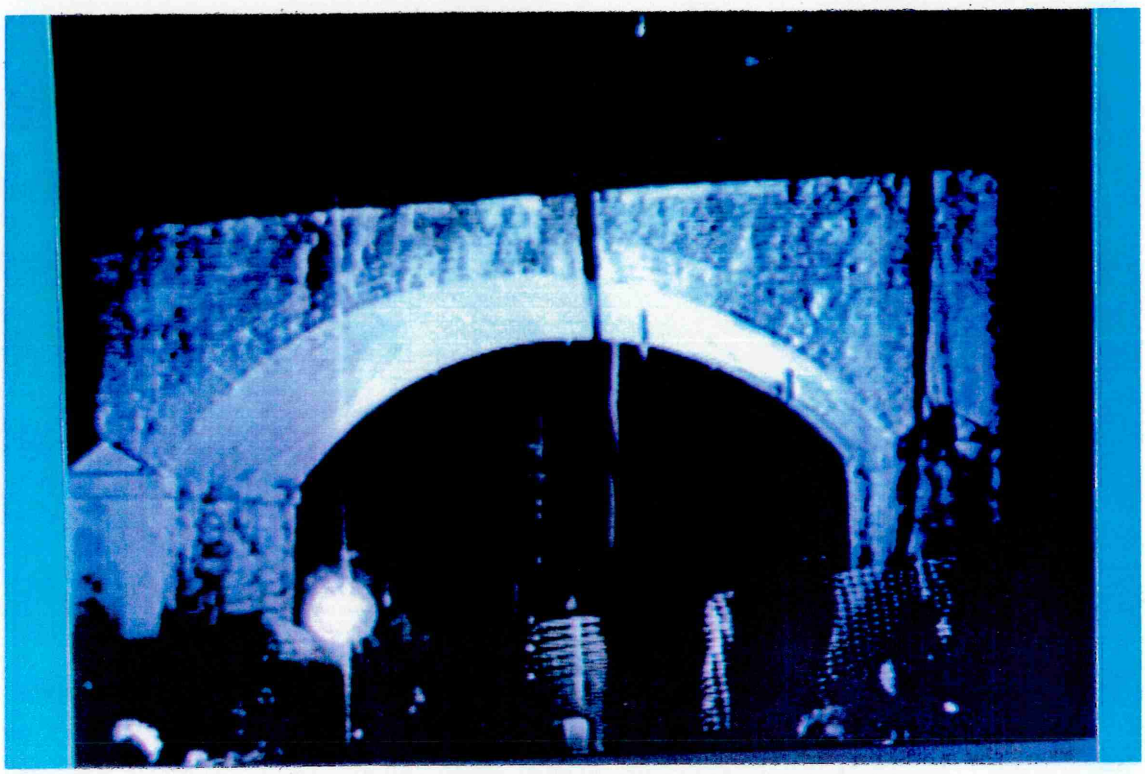

Bridge number 124: Digital grey level datum image

PLATE 6.13

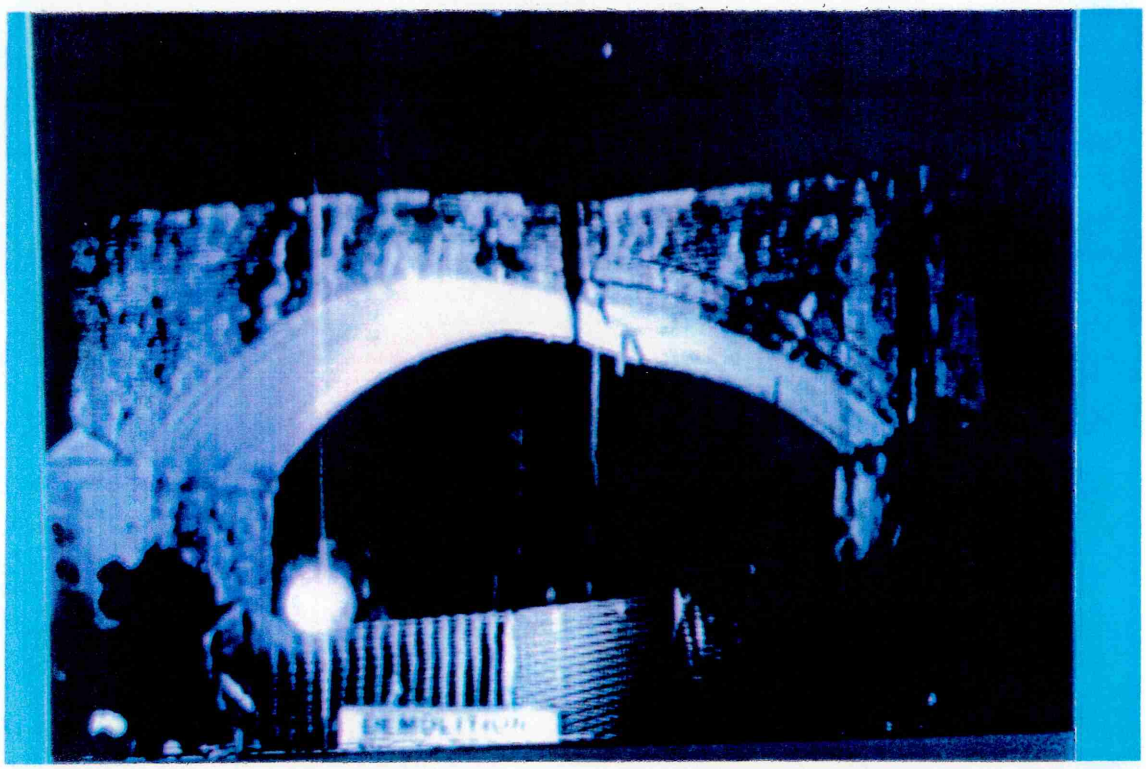

Bridge number 124: Digital grey level deflected image

PLATE 6.14

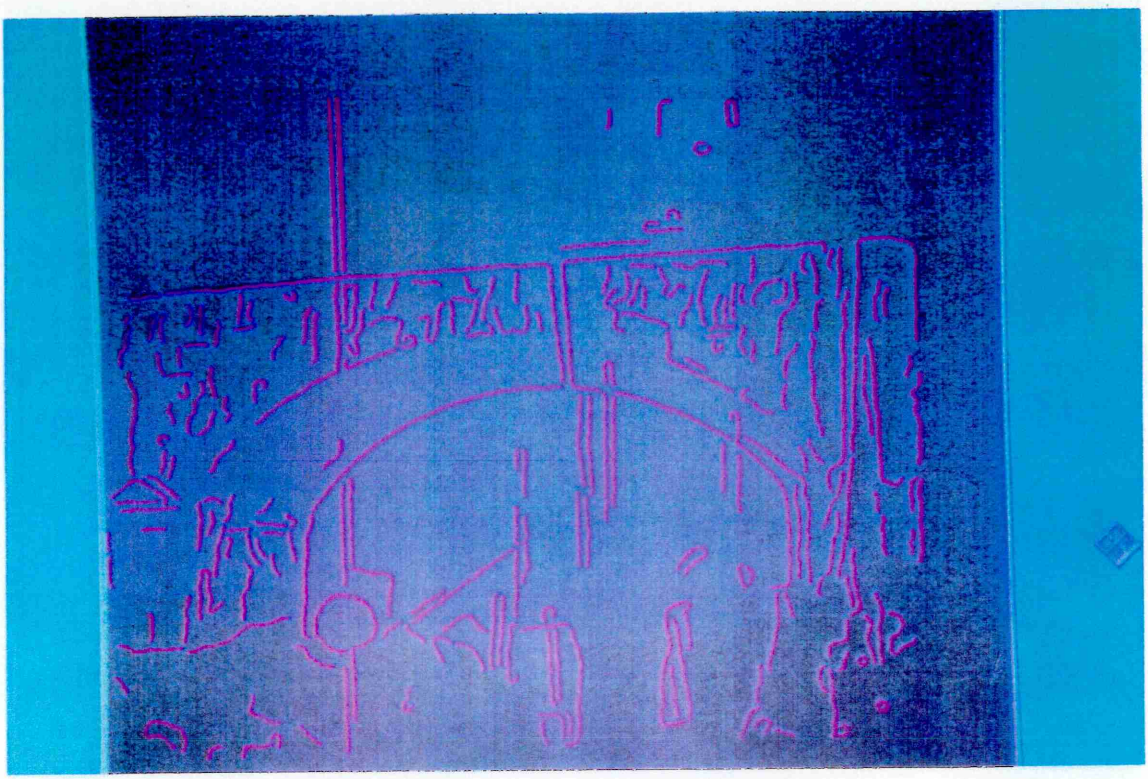

Bridge number 124: Datum edges only

PLATE 6.15

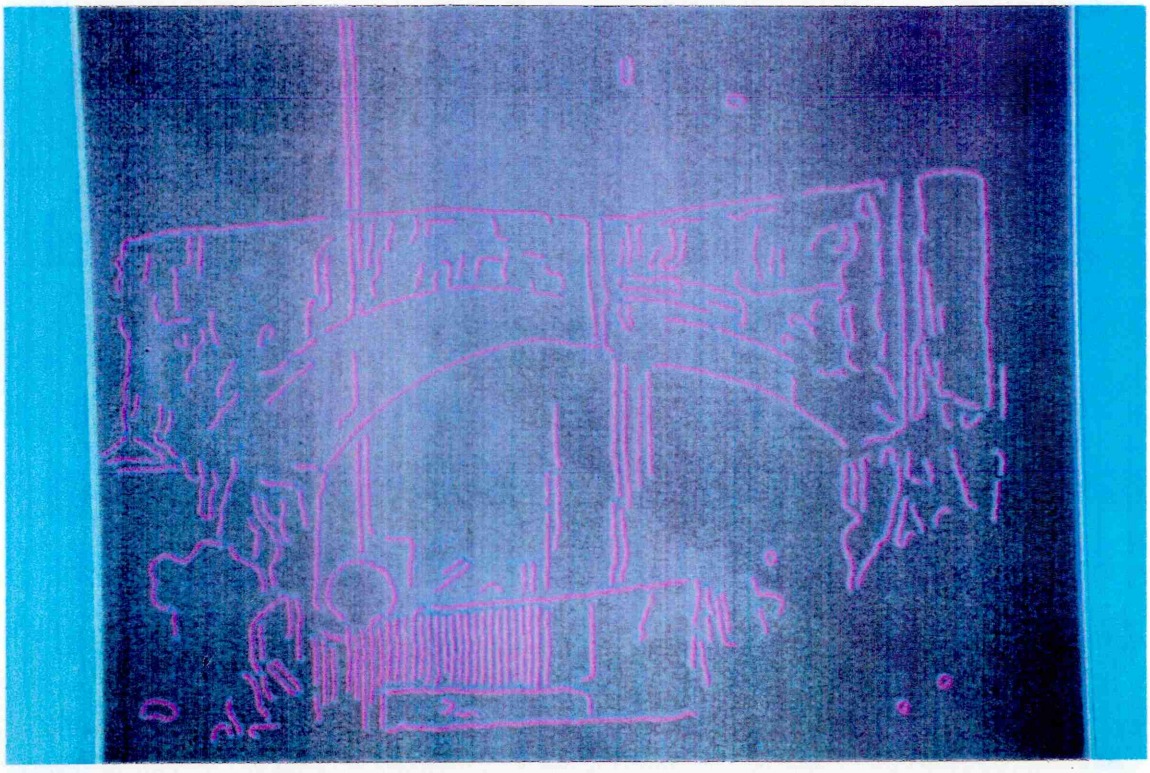

Bridge number 124: Deflected edges only

The vagaries of the lighting during the long test were probably substantial, and include the increasing onset of night, passing clouds, passing road traffic on the adjacent new bridge and frequent individuals moving between the floodlighting and the subject. In all, this was a severe test in terms of ambient lighting.

Rejecting, then, all but the main outlines of the arch itself (by manual editing as before), leads to the cleaned up images in Plates 6.16 and 6.17. Superposition once more provides the key image from which the major deflections under load can be seen.

Plate 6.18 portrays quite vividly the downward deflection of the right hand portion of the arch under load. Looking from left to right, only extremely slight traces of outward movement of the left support (pier) exist.

There is no evidence of hinge formation at the left springing.

Moving attention into the span, a hinge may clearly be seen just to the left of the crown, with a second hinge beneath the load position.

The topology at the right hand side of the span is much less clear. What is apparent is that the top of the right support (pier) has moved to the right, but the fact that the lower parts of the support are obscured by safety fencing in the foreground prevents a definite statement as to whether the support has bodily translated to the right, rotated to the right about its base or perhaps a combination of the two. Examination of the extreme right hand "edge" behind the support suggests at least some rotation of the support, but whether sliding at its base was an accompanying feature is impossible to assess.

Turning attention to whether or not a hinge formed at the right springing, it may be observed that the right hand intrados is moving downwards, rotating about the springing and so a hinge must be present. However, the upper extreme right hand "edge" delineating the back of the spandrel has not yet rotated to the left, suggesting separation between elements of the right hand side of the bridge.

Finally, Plate 6.19 is a colour photograph taken during the collapse.

By measuring the number of pixels across the (known) span, it is possible to derive a roughly calibrated "scale" for the digital images. Using this information to measure the translation of the right springing, as indicated in Plate 6.18, gives Table 6.1.

PLATE 6.16

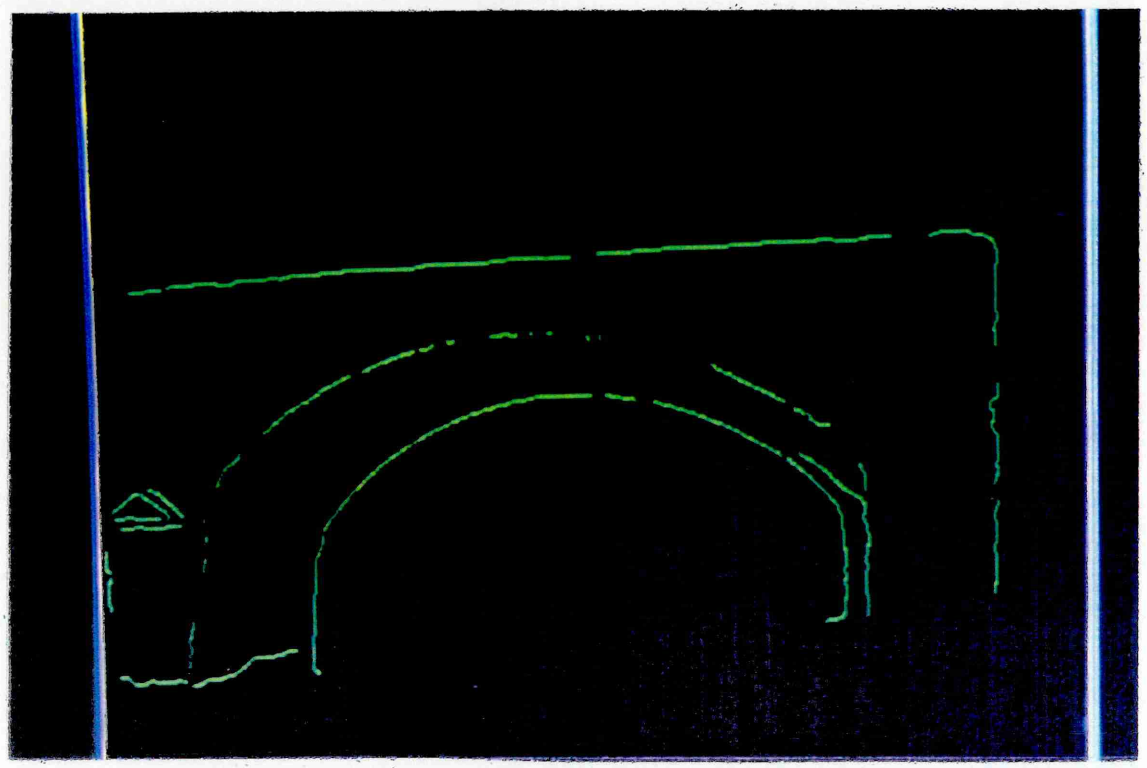

Bridge number 124: Datum cleaned edges

PLATE 6.17

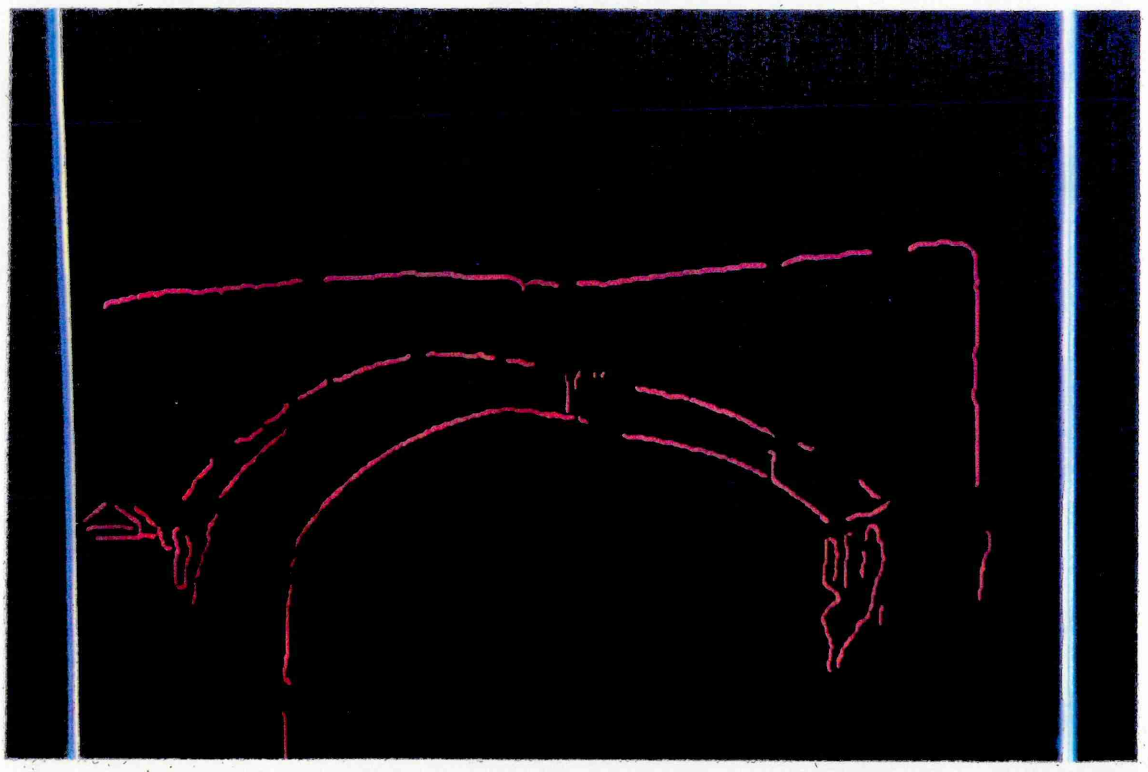

Bridge number 124: Deflected cleaned edges

PLATE 6.18

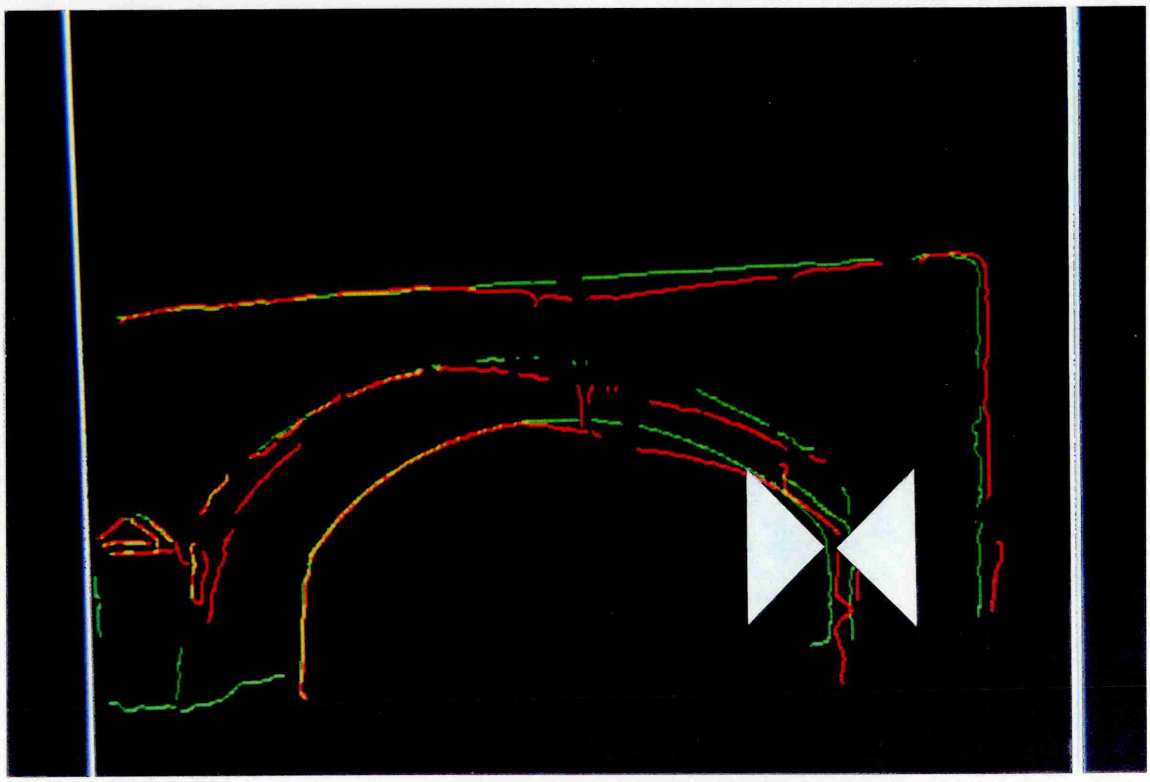

Bridge number 124: Composite datum and deflected cleaned edges.
Deflection of right hand abutment is indicated.

PLATE 6.19

Bridge number 124: Conventional colour photograph of final collapse

Image type	Location	X co-ord.	Y co-ord.
Datum state	LH Springing	162	353
	RH Springing	713	342
Deflected state	LH Springing	162	355
	RH Springing	731	351

Table 6.1 Pixel data

Note: Origin is at image top left corner.

Knowing the span this provides a value for the translation of the right springing of approximately 150mm. It is considered that a normal three hinge snap-through is unlikely in such a brittle system and a four hinge mechanism appears more likely; it remains a moot point as to whether a fourth hinge (perhaps in the pier) or lateral translation of the abutment facilitated eventual collapse.

6.4.3 Analysis of the test using k-based hinge methods

Speculation on the mode of failure prompted an attempt to analyse the collapse using the k-based theory developed earlier. However, the peculiarities of the failure, with one conjectured hinge in a pier, meant that SMARTMEC could not be used directly, and for present purposes required a generalisation of the basic procedure with only the resulting equations being solved by computer. The computer programme was called "Beighton".

It would clearly be difficult to analyse such a multi-span based mode of failure, especially in the absence of any material properties. However, it was hoped to demonstrate that the horizontal restraint provided by the right hand support to the loaded span would be insufficient to support a conventional, full four hinge collapse within the span and that a lower collapse load would naturally follow if the support were to move permitting a three hinge snap-through in the span.

Due to the one-off nature of the exercise significant approximations have been made, as will be described. What follows is therefore an after-the-fact conjectural appraisal using the same basic principles as for SMARTMEC. Figure 6.2 depicts the topology employed wherein force 'Q' represents the key lateral restraint offered by the adjacent buttress - it is a matter of engineering judgement as to its magnitude. Figures 6.3 to 6.5 present the full statical analysis upon which 'Beighton' is based. Two key approximations are, firstly, that the position of the hinges have been scaled from the

FIGURE 6.2

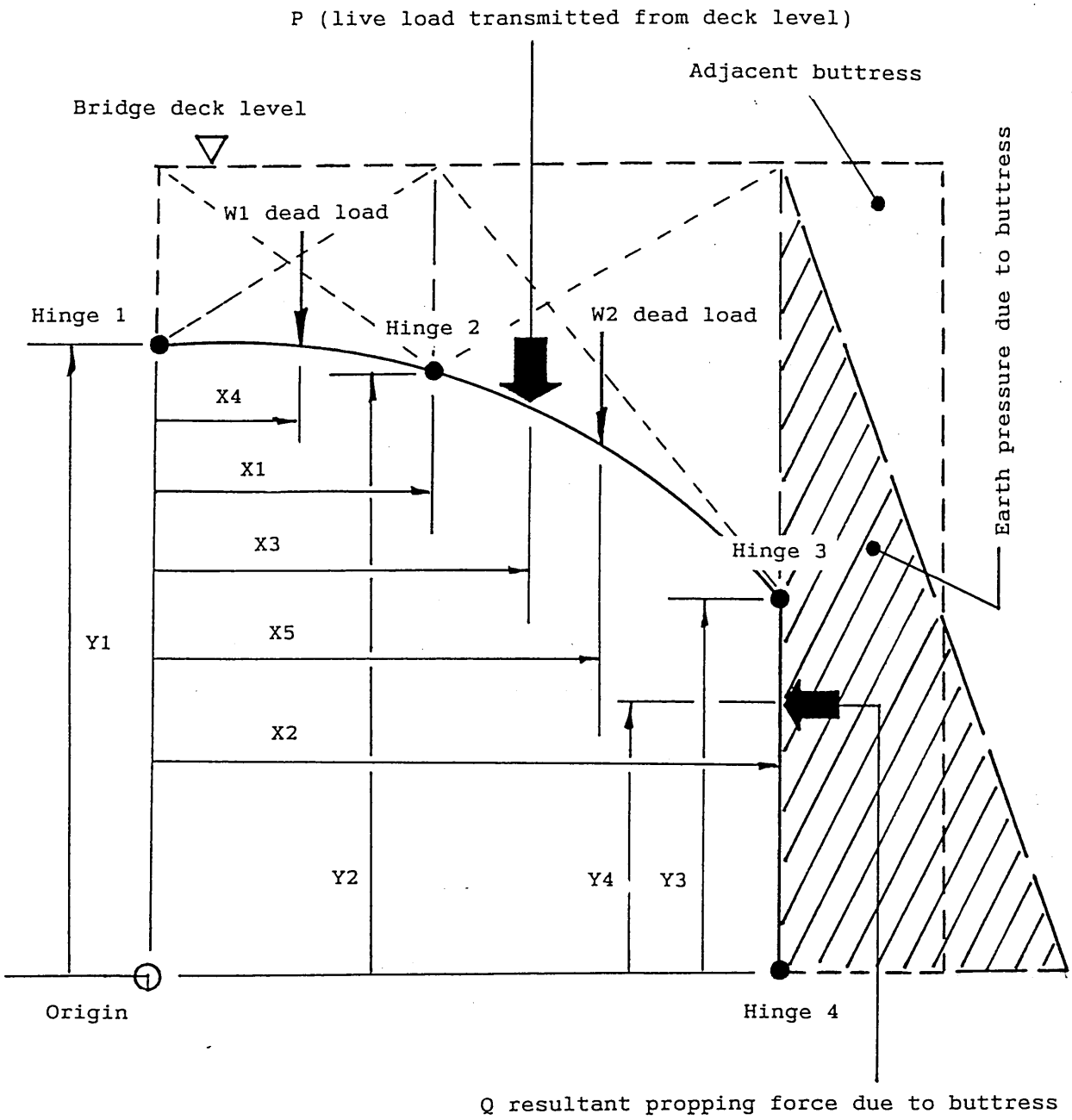

(Note: Analysis relates to a unit metre strip of structure)

Structure topology for analysis of
Railtrack Bridge number 124

FIGURE 6.3

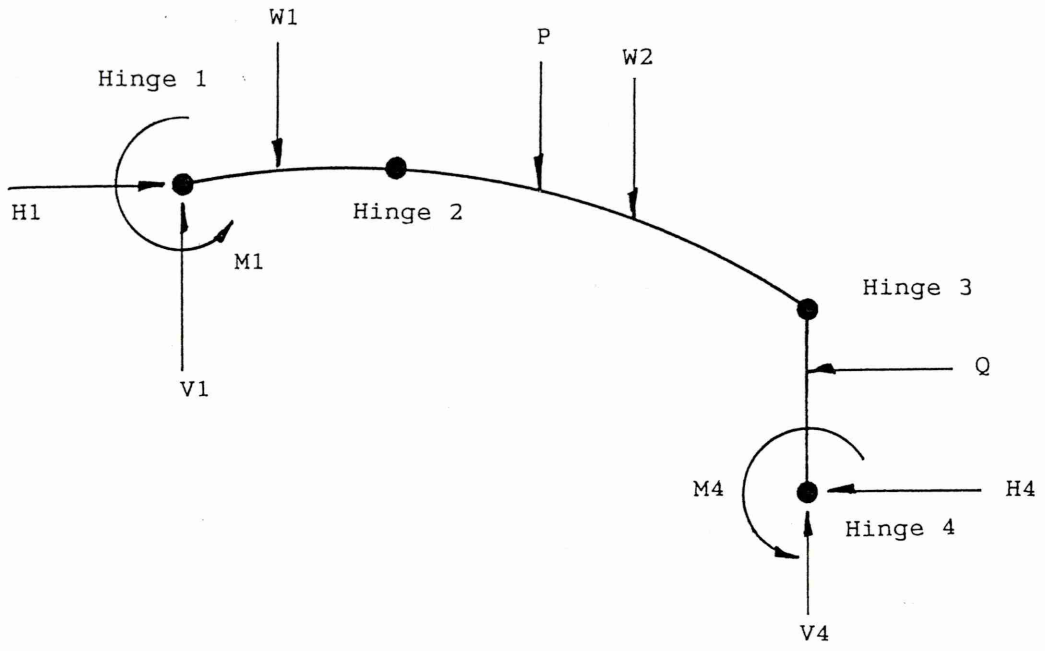

Taking moments about hinge 1: $V_4=(W_1X_4+W_2X_5+PX_3+H_4Y_1+Q(Y_1-Y_4)-M_1-M_4)/X_2$

Resolving vertically: $V_1=W_1+W_2+P-V_4$

Resolving horizontally: $H_4=H_1-Q$

a) Whole structure: equations BN1, BN2 & BN3

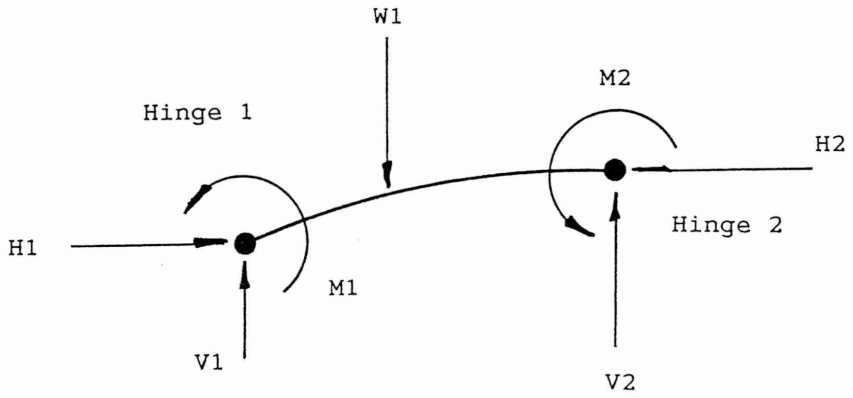

Taking moments about hinge 2:

$H_1=(V_1X_4-M_1-M_2-W_1(X_1-X_4))/(Y_2-Y_1)$

b) Substructure 1-2: equation BN4

Bridge number 124: statical analysis - 1

FIGURE 6.4

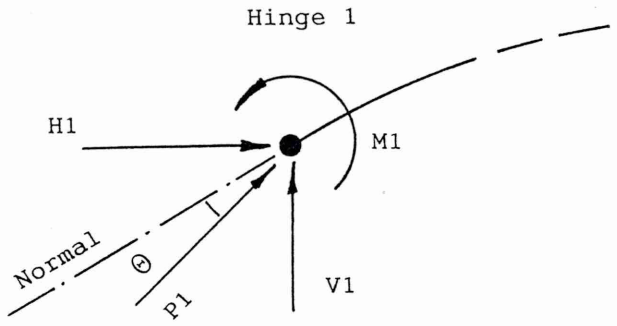

Resolving forces at hinge 1: $P_1=\sqrt{V_1^2+H_1^2}\cos\Theta$ ($\cos\Theta$ taken as 1, Θ assumed small)

a) Substructure 1-2: equation BN5

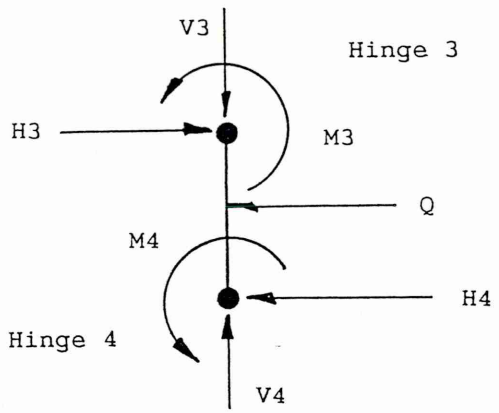

Taking moments about hinge 3: $H_4=(M_3+M_4-Q(Y_3-Y_4))/Y_3$

b) Substructure 3-4: equation BN6

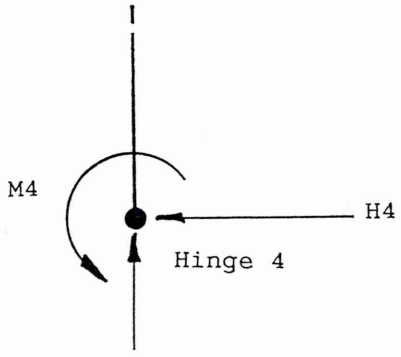

At hinge 4: $P_4=V_4$

c) Substructure 3-4: equation BN7

FIGURE 6.5

Equation 4.1 relating moment and thrust at hinge 1
Equation 4.1 relating moment and thrust at hinge 2
Equation 4.1 relating moment and thrust at hinge 3
Equation 4.1 relating moment and thrust at hinge 4

a) Hinge theory: equations BN8 to BN11

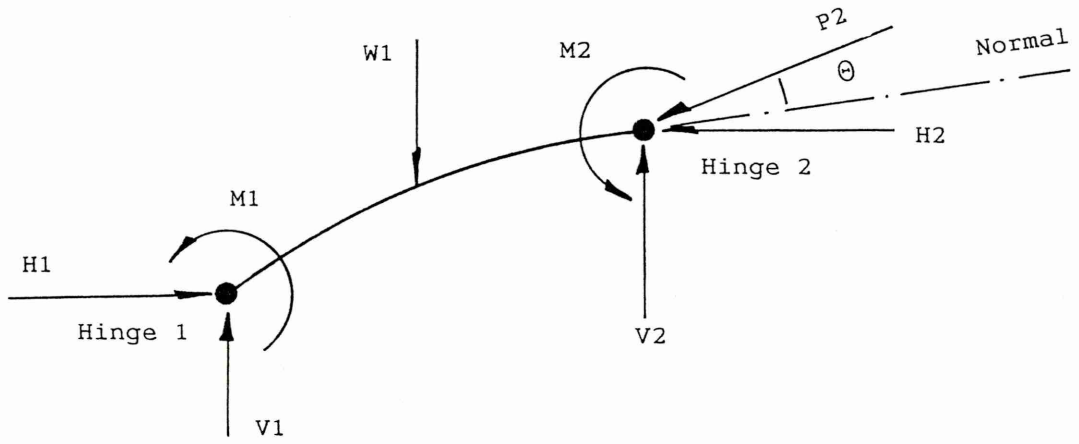

Resolve forces at hinge 2: $P_2=\sqrt{H_2^2+(W_1-V_1^2)}\ \cos\Theta$
($\cos\Theta$ taken as unity since Θ assumed small)

b) Substructure 1-2: equation BN12

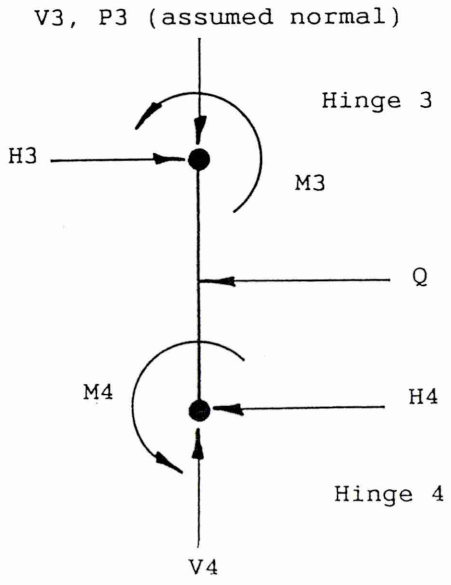

Resolving vertically: $V_4=P_3$

c) Substructure 3-4: equation BN13

images taken during the test - clearly direct measurement was not safely possible! Secondly, the thrust at the hinges has been assumed normal to the section (as noted in the figures). SMARTMEC, in contrast, corrects for non-axial thrust but experience with this programme had shown that the angular deviation was typically small, and the cosine of the angle very near unity and thus the approximation in 'Beighton' is considered justified. As a check, interrogation of 'Beighton' after convergence provides values for H_4 and V_4, leading to the computation of the angle between V_4 and the normal as 7°, and its cosine 0.992, representing an error of less than 1%.

In order to quantify 'Q', it is postulated that the buttress may have consisted of a rubble core (perhaps unbound) within a masonry skin. As such it is premised that the resistance it offered to lateral movement may be modelled by earth pressure methods. The lateral force 'Q' is thus $K\rho h$, where 'K' is the earth pressure coefficient, ρ the soil density and h the soil depth, 'Q' being applied at h/3. See Figure 6.2. In this study ρ is taken as 20 kN/m^3 and h as 6m.

With regard to 'K', it is suggested that nothing remotely appoaching a passive resistance value would be mobilised for two reasons. First and most importantly, passive resistance is dependent on the presence of a semi-infinite body of fill, rather than the finite and in fact fairly slender buttress actually present. Second, even in a semi-infinite body, full passive pressure is not mobilised until the lateral movement is a relatively large proportion of the soil depth. Using the lateral displacement figure of 150mm evaluated in the above computer vision study, the proportion (of the buttress height) here is quantified as 150mm/6000mm x 100%, ie. 2.5%. Whilst significant, a larger proportion is considered necessary to mobilise full passive resistance. On balance, therefore, it was decided to adopt a 'K' value appropriate to earth pressure at rest. Tabulated values of 'K' for passive earth pressure are 0.8 for dense sand and 1.0 for over-consolidated clay. Subjectively, it is considered that the buttress would provide at least these values and thus 'Beighton' has been run for both K=1.0 and K=1.2. The results are presented below.

Prototype collapse load 3200 kN			
Earth pressure at rest 'K' value	'Q' for 1m strip, kN	Collapse load for 1m strip of structure, kN	Full structure collapse, kN
1.0	414.0	418.4	2710
1.2	496.8	482.8	3127

Table 6.2 'Beighton' output

Given the significant assumptions made it must be accepted in part as fortuitous that 'Beighton' yields such creditable results. Neverthless, and discounting the apparent accuracy, the whole exercise does at least support the hypothesis that lack of lateral restraint from the buttress may have accounted for bridge 124's premature collapse.

The computer vision technique has been applied both *qualitatively*, yielding information on which to base a collapse hypothesis, and *quantitatively*, yielding a lateral translation dimension which assisted in the presumption of an appropriate earth pressure coefficient.

It is to be noted that computer vision has also combined powerfully with an adaptation of the novel hinge modelling technique, reinforcing the failure mode hypothesis and facilitating a simplistic quantification of the collapse load.

A full listing of programme 'Beighton' appears in Appendix 'A'.

6.5 Conclusions

With regard to the usefulness of computer vision techniques for quantitative data gathering, the author's studies formed but an early part of Sheffield Hallam University's research in this field. Parallel and ongoing work by others has provided a degree of refinement to the point where, under controlled conditions, the accuracy of the technique is comparable to that of conventional transducers. Using further model arches of the type employed by the author, transducer data and video data correlation has been demonstrated by others to be capable of being very good.

It is noteworthy that one of the main advantages of computer vision monitoring was, by chance, highlighted in the TRL load test at Bridge Number 124 thus; conventional displacement measurement is undertaken at discrete, pre-chosen locations. However, in the case of Bridge Number 124, an unexpected mode of failure occurred and one may assume that the positioning of transducers was not appropriately tailored. On the contrary, the computer vision approach requires few preconceptions and in this example proved its worth in approximately quantifying unpredicted displacements which were possibly not measured by any other method.

The lack of any specific preparation in terms of optimisation of viewpoint, lighting and calibration limited the usefulness of the technique in this case. However, with

purposeful planning the technique should offer considerable merit, initially (perhaps always) in the presence of conventional data gathering for calibration and corroboration, though the extent of this and its accompanying expense should perhaps be reduced.

Overall it is considered that the benefits and potential of computer vision have been demonstrated, and in tandem with a one-off application of the interaction curve-based hinge model theory, has proven both qualitatively and quantitatively a mode of failure in a full scale test that may have remained otherwise conjectural. The usefulness of both techniques is thus to be noted.

CHAPTER SEVEN

Comments and Conclusions

7.1 Context

The masonry vault is a structural form of great antiquity and its presence is commonplace in the built environment of the United Kingdom. It is a deceptively simple structure requiring little or no calculation for its construction but only a basic understanding of how its gravity-friendly shape works; to fail under a four hinge mechanism, approximately half of the vault has to be "lifted". Its durable simplicity and origin in antiquity ensure that there are numerous ancient examples still in use, especially on the nation's road network.

Arched road bridges are under continual pressure to carry ever greater loads, both in magnitude and frequency. The fundamental problem is thus one of prudent expenditure of bridge maintenance budgets given that these arches were built without the need for calculation at the time and are of uncertain strength (and often of uncertain construction) today.

In relatively recent times, structural analysts have attempted to resolve the arch's behaviour and a gradually increased understanding has come about. In the 1930's this lead to the origin of what is still one of the foremost tools, MEXE, arising from the work of Professor Pippard. MEXE is, however, relatively inexact and is specifically excluded for use on arches that possess a deformed profile, are greater than 18 metres in span or are multi-span. Skewed arches are a problem for MEXE, although this is also true for all present assessment methods.

The MEXE approach has gradually led to dissatisfaction resulting in the current search for alternatives, coupled with a re-appreciation of the merits of these structures for new build in situations where the potential problem of headroom may be overcome by a shallow profile, possibly, however, requiring pre-stressing.

One current analytical school to forward an alternative is that of the mechanism method and it is primarily in this area that the author's thesis seeks to make a contribution. The constitutive studies, however, have applications beyond this immediate field and are of probable value in the wider field of structural masonry.

Unlike elastic methods, plastic methods (such as mechanism analysis) do not provide a load path history and need an allowance for the interaction between arch and fill if they are to give reasonable results for deep arches. Indeed, not all arches fail as a four hinge mechanism and a variety of failure modes have been observed in tests.

However, mechanism computer programmes are simple and quick to use and are undemanding of the computer hardware required and as a tool for application in appropriate circumstances, mechanism analysis possesses merit. The lack of data in practice surely precludes over-elaborate procedures.

It has therefore been the particular aim of this research programme to study masonry hinges in the context of masonry vault mechanism analysis.

7.2 Present Findings

7.2.1 Constitutive considerations

Traditionally, masonry materials were assumed to have no tensile strength and a linear stress-strain property, and furthermore in "plastic" analysis were assumed to possess infinite stiffness and strength. In recent years it has become accepted that masonry does in fact exhibit a non-linear stress-strain property and this thesis supports that view. Indeed, the universality of non-linear stress-strain laws for *all* masonry materials is considered probable.

A novel equation for modelling masonry stress-strain laws has been presented thus

$$\frac{\sigma}{\sigma_m} = \frac{1}{k-1}\left[\frac{k\varepsilon}{\varepsilon_m} - \left(\frac{\varepsilon}{\varepsilon_m}\right)^k\right]$$

Its strength lies in the fact that, by varying one parameter, 'k', it may be configured to mimic the behaviour of real materials, as well as the behaviour of the theoretical infinite strength, infinite stiffness law (k=0) and the linear law (k=∞).

The use of k=0 is clearly non-conservative and k=0 may be over conservative. In practice, real masonry materials possess 'k' values in the range 2 to about 12 (noting the equation's singularity at k=1), but mechanism analysis is insensitive to the particular value used in this range and k=2 will generally suffice for simplicity. The key finding is thus that moving away from either k=0 or k=∞ is important, but the precise 'k' value chosen between these is relatively unimportant in the consideration of masonry vault mechanisms. Nonetheless, other analyses dependent upon stiffness and deflection may be more sensitive to 'k'.

Using the new equation, a computerised numerical analytical procedure has been developed to 'solve' the states of stress and strain for a rectangular masonry section under combined bending and thrust, and thus it is possible to solve a section irrespective of the constitutive properties of the material under study. The previous simplistic approaches of assuming infinite compressive strength and the use of either an unrepresentative linear or a second order parabolic stress-strain relationship have been rendered unnecessary, and the difference between those approaches and the new may be readily demonstrated and quantified by further use of the new equation.

7.2.2 Moment, thrust and the limit state

Further manipulation has lead to the ability to determine *limit state characteristics* using the above numerical approach. The basic non-linear k-based formulations have been developed to provide a set of equations, unamenable to formal computational manipulation, which have been solved numerically to furnish both a static limit state axial thrust/bending moment interaction diagram and a corresponding serviceability limit state, prevention of cracking interaction diagram.

Differentiation is now possible between hitherto identically-treated natural materials; an immediate observation from this work is that that sectional resistance is enhanced as the constant 'k' decreases (see Figure 3.7).

A distinction should be made between γ, the fracture strain coefficient, and λ, the theoretical maximum strain coefficient occurring at the static limit state. If the former does not exceed the latter in practice, then the sectional capacity (ie. the extent of the limit state moment-thrust interaction diagram) will be diminished.

It has been shown that, for any material with a non-linear stess-strain characteristic, the middle third rule does not strictly apply and may be non-conservative in prevention of cracking. The difference is, however, minimal at low strains.

A further finding, of similar 'rule-of-thumb' value to the traditional middle third rule, is that all loci maxima lie on the middle half rule. Unlike the (now queried) middle third rule, however, the middle half rule for maximisation of sectional bending resistance applies to *all constitutive types,* and is thus valid for all masonry materials.

7.2.3 Masonry hinges

It has been postulated that any point on a static limit state interaction diagram 'k' locus represents a masonry hinge and an extensive series of model hinge tests has been undertaken in the laboratory to demonstrate the point and to validate the foregoing theoretical studies.

It is considered to be well demonstrated in the laboratory that this supposition is correct. To facilitate practical application, a single mathematical expression (equation 4.1) has been derived for the cracked condition, this condition having been shown to be generally applicable to the consideration of the ultimate limit state in masonry vaults. This enables the solution of moment and thrust at any masonry hinge at the point of failure, incorporating the constitutive parameter 'k', and is thus applicable to all masonry materials.

A qualitative conclusion from the laboratory hinge tests is the observation that very little distress normally occurs prior to maximum load being reached. This has implications for the detection of hinges in the field when inspecting the condition of masonry arches.

A further observation deriving from examination of the laboratory hinge study's (nominally) moment-rotation curves is that peak loads occur at lower rotations with increasing 'n', and that the rate of attack (rotational stiffness) increases with increasing 'n', and so hinge formation becomes more brittle with increasing 'n'. Allied with the later supposition that model scale arches occupy regions of n,m space closer to the origin than full scale arches, simply, the bigger the bridge, the more brittle its onset of hinge formation is thought to be.

7.2.4 Computerised mechanism analysis

The findings to date have been incorporated into a four hinge mechanism-type computer analysis (SMARTMEC) for the study of masonry vaults at the ultimate limit state. Crucially, the analysis is different from other mechanism analyses in that the

hinge model equation 4.1 is employed, together with equations derived from consideration of statics, to arrive at a collapse load. The constitutive-based, finite strength interaction locus hinge theory is thus intrinsic to the method and the effects of varying material parameters may be studied. SMARTMEC is applied to arch collapse test data from three sources; full-scale bridges, laboratory model tests by other organisations, and models constructed at Sheffield Hallam University. The results obtained are encouraging overall and are considered to demonstrate that the underlying method is valid.

7.2.5 The effects of material properties on four hinge mechanisms

A simple parametric study has been undertaken, utilising the software described above, to study the effect of both material strength, σ_m, and material stiffness, 'k'.

The effect of masonry strength on collapse is shown provide a locus rising rapidly to almost a plateau, which then tapers off very slowly to the asymptote of infinite material strength. Once on the "plateau", further increases in material strength produce very little increase in structure strength.

The precise form of the response curve will no doubt be a function of many parameters, but the basic finding is that material strength should have a marked bearing on arch vault strength at the low, or weak material end of the spectrum. Of interest to new arch construction, at higher strengths virtually no improvement is brought about beyond a certain point (which may be quantified) and expenditure on stronger materials for construction will be wasted.

For the structural assessment of existing arches, the effect on collapse load prediction by choosing either the mortar or brick material strength alone can also be seen. This highlights the difficulty in choosing a representative single value for material strength, even if both the mortar and masonry individual values are known, which is rarely the case anyhow.

It has been demonstrated that material strength is relevant to both the Bridgemill prototype and to Edinburgh University's Bridgemill scale models. However, it can be seen that the effect is different at model scale to full size.

Using computer programme PSTRESS1 to plot the SMARTMEC data from the Bridgemill prototype analysis for the hinge under the load position (ie. taking the moment and thrust values coexistant at collapse), an appreciable depth of arch barrel

is found to be in compression. The thrust line is not at the extreme fibre at collapse as would have been the case using the infinite strength/stiffness assumption. A curved stress block here is also a consequence of the non-linear constitutive modelling. Furthermore, the 'n' value is noticeably higher than in the model studies, again pointing to the presence of a scale effect.

The overall effect of material properties may thus be summarised as follows. For the static limit state (collapse), material strength, σ_m, is found to be relevant, more so if the material is "weak" and less so if it is "strong". Model arches and full scale arches respond somewhat differently to the effects of material strength, with the assumption of infinite compressive strength bringing marked inaccuracy to "large" arches, but less inaccuracy at model scale. Material stiffness, represented by 'k', in contrast has little bearing on collapse (irrespective of scale), but is considered to be relevant to the load-deflection response of the arch vault and to serviceability. Further work is considered necessary in this latter area.

It is noteworthy that these studies have enabled the above conclusions to be made in a sophisticated and quantifiable manner which had hitherto not been possible.

7.2.6 Computer vision and extension of the theory into the field

Computer vision is a technique that is relatively novel to the structures field. It is adapted here to the monitoring of model arch tests to destruction in the Sheffield Hallam University structures laboratory, and then extended to the monitoring of a full scale *multi span* masonry arch bridge test (by TRL) in the field.

The technique works by use of an edge detection algorithm applied to datum and deflected structural conditions. This allows quantification of the deflection data, at any desired location within the field of view.

Following encouraging use of the technique in the laboratory, a full scale masonry arch viaduct test to destruction on railway bridge number 124, Beighton, Sheffield, is video monitored and the results studied by computer vision permitting the formulation of a hypothesis regarding the (unexpected) mode of failure of this multi-span bridge. The mode of failure is then modelled using an adaptation and generalisation of the constitutive-based mechanism model theory which demonstrates both the viability of the failure hypothesis and the usefulness of the constitutive studies.

With regard to computer vision, beyond providing qualitative information, under controlled conditions the accuracy of the technique is comparable to that of conventional transducers and furthermore the latter only carry out displacement measurement at *discrete, pre-chosen* locations. In this study, the TRL did not expect the mode of failure that occurred and their positioning of transducers was not appropriately tailored to what actually occurred. In contrast, computer vision requires few preconceptions and proved its potential in this instance by quantifying unpredicted displacements.

The lack of any specific preparation in terms of optimisation of viewpoint, lighting and so forth limited the usefulness of the technique in this case, but nevertheless the potential of computer vision is considered to be well demonstrated, as is a generalisation of the hinge model theory.

7.3 Suggestions for Further Work

The consequences for collapse load prediction by choosing either the mortar or brick material strength can be seen from these studies and relatively little guidance is available on the derivation of a representative, single value for use in masonry vault mechanism analysis. This is an area which merits further research as indeed would the investigation of methods for readily and cheaply determining values in the field – a device akin to a Schmidt hammer for masonry would be ideal.

Further sensitivity studies concerning the response of different structures to changes in masonry strength may be warranted now that the means to do this have been developed.

Interesting further areas of study are the effect of cyclic loading (arches may flex in service) on hinge behaviour over time; the effect of moisture on hinge properties (most arches are wet); the effect of loss of mortar, and it would also be intriguing to try to locate hinges in in-service bridges to resolve the problem of whether or not the formation of a first hinge could be regarded as a serviceability limit state, which the author doubts. Much attention has been focussed in recent years on ultimate arch behaviour (strength/safety), but relatively little work appears to have been done on serviceability (usefulness), which, in truth, is the more important issue. Again this is put forward as an area for future study.

The effect of 'k' in other masonry fields, for example in the general structural masonry field should be investigated, and the use of this kind of masonry constitutive modelling may have application in "elastic" masonry arch analysis software which attempts to predict deformation.

With regard to "plastic" arch analysis, it would be rewarding for the hinge modelling herein presented to be incorporated in a far improved computer package to give a comprehensive assessment tool.

The novel potential of computer vision in the structures field appears promising and indeed this work is continuing under other research programmes at Sheffield Hallam University. It may eventually be possible to develop a routine monitoring method to indicate stuctural deterioration over time.

In conclusion, it is hoped that these studies have afforded valuable and novel findings of equal interest to the practising structural engineer and the theoretician; that they have given insights into masonry vault hinge behaviour and have provided useful tools with direct practical use.

APPENDIX 'A'

Software listings: PSTRESS1, SMARTMEC, BEIGHTON.

```
   10REM PROGRAM PSTRESS1
   20:
   30REM P. A. MALLINDER
   40:
   70REM NOTE - NEWTON & METRE UNITS
   80:
   90:
  100REM------------------------ D A T A  I N P U
T ----------------------------
  110:
  120@%=&20509:MODE0:CLS
  130PRINT"P R O G R A M  'P S T R E S S 1'":PRINT
"---------------------------------":PRINT:PRINT
  140PRINT"To solve a rectangular masonry section.
 of parabolic stress-strain law,":PRINT
  150PRINT"subject to thrust and uniaxial bending
moment.":PRINT:PRINT:PRINT
  160PRINT"MATERIAL PROPERTIES:":PRINT:INPUT"Sigma
 max. (N/mm2 units, typical value 16 N/mm2) ",SIGm
:SIGm=SIGm*1E6:REM CONVERT TO N/m2 UNITS
  170PRINT:INPUT"E max. (typical value 0.0024) ";E
m
  180PRINT:PRINT:PRINT"SECTION DIMENSIONS:":PRINT:
INPUT"Section depth (metres) ".d
  190PRINT:PRINT"(unit metre strip assumed)":PRINT
:b=1:REM UNIT METRE STRIP ASSUMED
  200PRINT:PRINT"LOADING:":PRINT
  210INPUT"Axial thrust (kN units) ",P:P=P*1000:RE
M CONVERT TO NEWTONS
  220PRINT:INPUT"Bending moment (kNm units) ",M:M=
M*1000:REM CONVERT TO NEWTON METRES
  230CLS
  240:
  250PROCaxisdraw
  260:
  270REM---------------- U N C R A C K E D  A N A L
 Y S I S --------------------
  280:
  290REM   P L O T T I N G  P O L Y N O M I A L
  300:
  310I=0
  320FOR E2=-1.5*Em TO 1.5*Em STEP 3*Em/50
  330I=I+1
  340X=(2*(E2/Em)^2-5*E2/Em+3*P/SIGm/b/d-12*M/SIGm
/b/(d^2))/(1-E2/Em)
  350ANSWER=SIGm*b*d^2/6*(-.5*X^2+X-E2/Em+.5*(E2/E
m)^2)-M
  360PRINT TAB(20,4);"E2=";E2;" E1=";X*Em;" poly.=
";ANSWER;"      "
  370IF500+ANSWER/1000>1200 OR500+ANSWER/1000<-120
```

```
0 GOTO390
  380DRAW I/52*1200,500+ANSWER/1000
  390NEXT E2
  400:
  410REM   P L O T T I N G  E 2
  420:
  430VDU5
  440MOVE0,500
  450I=0
  460FOR E2=-1.5*Em TO 1.5*Em STEP 3*Em/50
  470I=I+1
  480X=(2*(E2/Em)^2-5*E2/Em+3*P/SIGm/b/d-12*M/SIGm
/b/(d^2))/(1-E2/Em)
  490ANSWER=SIGm*b*d^2/6*(-.5*X^2+X-E2/Em+.5*(E2/E
m)^2)-M
  500DRAW I/52*1200,500+E2/(1.5*Em)*500
  510NEXT E2
  520:
  530:
  540REM   P L O T T I N G  E 1
  550:
  560MOVE0,500
  570I=0
  580FOR E2=-1.5*Em TO 1.5*Em STEP 3*Em/50
  590I=I+1
  600X=(2*(E2/Em)^2-5*E2/Em+3*P/SIGm/b/d-12*M/SIGm
/b/(d^2))/(1-E2/Em)
  610E1=X*Em
  620IF500+E1/(1.5*Em)*500 >1200 OR500+E1/(1.5*Em)
*500 <-1200 GOTO640
  630DRAW I/52*1200,500+E1/(1.5*Em)*500
  640NEXT E2
  650VDU4
  660:
  670:
  680REM   S O L V E  F O R  U N C R A C K E D  S
 E C T I O N
  690:
  700IFP>0THEN720
  710CLS:PRINT"SECTION IN TENSION!":STOP
  720E2=1.5*Em+0.00010001:STIP=Em/24
  730X=(2*(E2/Em)^2-5*E2/Em+3*P/SIGm/b/d-12*M/SIGm
/b/(d^2))/(1-E2/Em)
  740RLAST=SIGm*b*d^2/6*(-.5*X^2+X-E2/Em+.5*(E2/Em
)^2)-M
  750E2=E2-STIP:IF E2>-0.0024 GOTO770
  760FORDD=1TO3000:NEXT:CLS:PRINT"NO SOLUTION FOUN
D - SECTION BEYOND SQUASH LOAD OR PLASTIC MOMENT":
STOP
  770MOVE E2/(1.5*Em)*600+600,400
  780DRAW E2/(1.5*Em)*600+600,600
  790X=(2*(E2/Em)^2-5*E2/Em+3*P/SIGm/b/d-12*M/SIGm
/b/(d^2))/(1-E2/Em)
  800RNOW=SIGm*b*d^2/6*(-.5*X^2+X-E2/Em+.5*(E2/Em)
^2)-M
  810IF ABS(RNOW)<10 GOTO850
  820IF SGN(RLAST)=SGN(RNOW) GOTO840
  830STIP=-STIP/2
```

```
  840RLAST=RNOW:GOTO750
  850E1=X*Em
  860PRINTTAB(10,5);"*** Solution: E1=";E1;" E2=";
E2;", at poly.=";X;" ***          "
  870PRINT"CHECK:      "
  880KK=SIGm*b*d*(-1/3*(E1/Em)^2+E1/Em-1/3*(E1*E2/
Em^2)+E2/Em-1/3*(E2/Em)^2)
  890PRINT"COMPUTED P=";KK/1000;" kN"
  900JJ=SIGm*b*d^2/6*(-1/2*(E1/Em)^2+E1/Em-E2/Em+1
/2*(E2/Em)^2)
  910PRINT"COMPUTED M=";JJ/1000;" kNm"
  920IF ABS(KK-P)<ABS(5/100*P) AND (ABS(JJ-M)<ABS(
5/100*M) OR ABS(JJ-M)<50) THEN 940:REM CHECK THAT
CORRECT P & M FOUND TO WITHIN 5% OR .05 kNm
  930PRINT"COMPUTED P AND M NOT CORRECT":VDU4:STOP
  940PROCcopy
  950:
  960:
  970REM D R A W  S T R E S S  &  S T R A I N  D I
 A G S.
  980:
  990CLS:VDU5
 1000MOVE0,950:PLOT21,1279,950
 1010MOVE0,400:PLOT21,1279,400
 1020MOVE300,400:DRAW300,950
 1030MOVE900,400:DRAW900,950
 1040MOVE220,300:PRINT"S T R E S S"
 1050MOVE830,300:PRINT"S T R A I N"
 1060MOVE280,50:PRINT"*** U N C R A C K E D  A N A
 L Y S I S ***"
 1070MOVE900,950:DRAW 900+E1*150000,950:DRAW 900+E
2*150000,400:DRAW900,400
 1080MOVE820,990:PRINTE1
 1090MOVE820,390:PRINTE2
 1100MOVE300,950
 1110FORI=0TO10
 1120J=E1-(I/10)*(E1-E2)
 1130J=SIGm*(2*J/Em-(J/Em)^2)/1E6:REM STRESS IN N/
mm^2
 1140DRAW J*20+300,950-I/10*550
 1150NEXTI
 1160DRAW300,400
 1170MOVE220,990:PRINT SIGm*(2*E1/Em-(E1/Em)^2)/1E
6;" N/sq.mm"
 1180MOVE220,390:PRINT SIGm*(2*E2/Em-(E2/Em)^2)/1E
6;" N/sq.mm"
 1190:
 1200REM F I N D  M E A N 'E'
 1210K=0
 1220FORI=0TO10
 1230J=ABS(E1-(I/10)*(E1-E2)):REM STRAIN
 1240K=K+SIGm*(2*J/Em-(J/Em)^2)/J:REM STRESS/STRAI
N = E
 1250NEXTI
 1260Elocal=K/11:REM MEAN 'E'
 1270MOVE300,200:PRINT"Averaged local 'E' = ";Eloc
```

```
al;" N/sq.m"
 1280MOVE0,30
 1290PROCcopy
 1300:
 1310REM   D E C I D E  I F  C R A C K E D  A N A
L Y S I S  R E Q D.
 1320:
 1330IF E1<0 OR E2<0 THEN 1380
 1340VDU4:CLS:STOP
 1350:
 1360REM------------------ C R A C K E D  A N A L
Y S I S --------------------
 1370:
 1380CLS:J=SGN(M):M=ABS(M)
 1390PROCaxisdraw
 1400I=0
 1410FOR E1=-1.5*Em TO 1.5*Em+3*Em/50 STEP 3*Em/50
+1E-9
 1420I=I+1
 1430dd=3*P/(SIGm*b*(3*E1/Em-(E1/Em)^2))
 1440ANSWER=4*SIGm*b*P*(M/P-(d-dd)/2)*(3*E1/Em-(E1
/Em)^2)^2-3*P^2*(2*E1/Em-(E1/Em)^2)
 1450IF500+ANSWER/1E10>1200 OR 500+ANSWER/1E10<-12
00 GOTO1480
 1460DRAW I/52*1200,500+ANSWER/1E10
 1470PRINT TAB(20,4);" E1=";E1;" d'=";dd;"m, poly.
=";ANSWER;"       "
 1480NEXT E1
 1490:
 1500REM   P L O T T I N G  E 1
 1510:
 1520MOVE0,500
 1530I=0
 1540FOR E1=-1.5*Em TO 1.5*Em STEP 3*Em/50
 1550I=I+1
 1560DRAW I/52*1200,500+E1/(1.5*Em)*500
 1570NEXT E1
 1580:
 1590REM   S O L V E  F O R  C R A C K E D  S E C
T I O N
 1600:
 1610E1=0.0000001:STIP=Em/24:REM J=SGN(M):M=ABS(M)
 <-.NEED IN PSTRESS2
 1620dd=3*P/(SIGm*b*(3*E1/Em-(E1/Em)^2))
 1630RLAST=4*SIGm*b*P*(M/P-(d-dd)/2)*(3*E1/Em-(E1/
Em)^2)^2-3*P^2*(2*E1/Em-(E1/Em)^2)
 1640E1=E1+STIP:IF E1<1.5*Em GOTO1660
 1650VDU4:CLS:PRINT"NO SOLUTION FOUND - SECTION BE
YOND SQUASH LOAD OR PLASTIC MOMENT":STOP
 1660MOVE E1/(1.5*Em)*600+600,400
 1670DRAW E1/(1.5*Em)*600+600,600
 1680dd=3*P/(SIGm*b*(3*E1/Em-(E1/Em)^2))
 1690RNOW=4*SIGm*b*P*(M/P-(d-dd)/2)*(3*E1/Em-(E1/E
m)^2)^2-3*P^2*(2*E1/Em-(E1/Em)^2)
 1700IF ABS(RNOW)<1E5 GOTO1740
 1710IF SGN(RLAST)=SGN(RNOW) GOTO1730
```

```
1720STIP=-STIP/2
1730RLAST=RNOW:GOTO1640
1740VDU4
1750dd=3*P/(SIGm*b*(3*E1/Em-(E1/Em)^2))
1760PRINTTAB(10,5);"*** Solution: d'=";dd;" E1=";
E1;", at poly.=";RNOW;" ***                "
1770PRINT"Check:      "
1780PRINT"Computed P=";SIGm*b*dd/3*(3*E1/Em-(E1/E
m)^2)/1000;" kN"
1790XX=SIGm*b*dd^2/12*(2*E1/Em-(E1/Em)^2)
1800PRINT"Computed M'=";XX/1000;" kNm"
1810PRINT"Giving a computed M =";(XX/P+(d-dd)/2)*
P/1000*SGN(J);" kNm"
1820PROCcopy
1830:
1840REM D R A W  S T R E S S  &  S T R A I N  D I
A G S.
1850:
1860CLS:VDU5
1870MOVE0,950:PLOT21,1279,950
1880MOVE0,400:PLOT21,1279,400
1890MOVE300,400:DRAW300,950
1900MOVE900,400:DRAW900,950
1910MOVE220,300:PRINT"S T R E S S"
1920MOVE830,300:PRINT"S T R A I N"
1930MOVE280,50:PRINT"*** C R A C K E D  A N A L Y
S I S ***"
1940MOVE900,950:DRAW 900+E1*100000,950:DRAW 900,9
50-dd/d*550:DRAW900,400
1950MOVE820,990:PRINTE1
1960MOVE770,370:PRINT"Crack depth = ";d-dd;" m"
1970MOVE300,950
1980FORI=0TO10
1990J=E1-(I/10)*E1
2000J=SIGm*(2*J/Em-(J/Em)^2)/1E6:REM STRESS IN N/
mm^2
2010DRAW J*20+300,950-I/10*dd/d*550
2020NEXTI
2030DRAW300,400
2040MOVE220,990:PRINT SIGm*(2*E1/Em-(E1/Em)^2)/1E
6;" N/sq.mm"
2050:
2060REM F I N D  M E A N 'E'
2070:
2080K=0
2090FORI=0TO9
2100J=ABS(E1-(I/10)*E1):REM STRAIN
2110K=K+SIGm*(2*J/Em-(J/Em)^2)/J:REM STRESS/STRAI
N = E
2120NEXTI
2130Elocal=K/10:REM MEAN 'E'
2140MOVE300,200:PRINT"Averaged local 'E' = ";Eloc
al;" N/sq.m"
2150Ilocal=b*dd^3/12:REM LOCAL 'I'
2160MOVE300,150:PRINT"Local 'I' = ";Ilocal;" m4"
2170MOVE300,100:PRINT"ALL MOMENTS ASSUMED +VE"
2180MOVE0,30
```

```
2190PROCcopy
2200:
2210VDU4:CLS:PRINT"P R O G R A M  F I N I S H E D
":STOP
2220:
2230REM   H A R D  C O P Y  S U B R O U T I N E
2240:
2250DEFPROCcopy
2260INPUT"C FOR COPY",A$
2270IFA$="C"THEN2290
2280ENDPROC
2290*FX5,1
2300*FX6,0
2310VDU2
2320*GDUMP1,1,3,1,0
2330VDU3
2340ENDPROC
2350:
2360REM  S U B R O U T I N E  T O  D R A W  A X E
S  Et C.
2370:
2380DEFPROCaxisdraw
2390MOVE0,500
2400DRAW1200,500
2410VDU5
2420I=0
2430FOR E2=-1.5*Em TO 1.5*Em STEP 1.5*Em/6
2440I=I+1
2450MOVE I/6*1200,505
2460DRAW I/6*1200,495
2470MOVE0,500+E2/(1.5*Em)*500
2480PRINTE2
2490MOVE150,500+E2/(1.5*Em)*500
2500DRAW1200,500+E2/(1.5*Em)*500
2510NEXTE2
2520VDU4
2530@%=&20109:PRINT"   Axial force = ";P;" Newton
s. Bending moment = ";M;" Newton metres    ":PRINT
"  ********************************************
*****************************":@%=&20509
2540MOVE0,0
2550ENDPROC
```

```
10 REM#####################################################################
20 REM#####################################################################
30 REM                                                                  ###
40 REM                                                                  ###
50 REM     P . A .  M A L L I N D E R     -    J A N   1 9 9 3         ###
60 REM                                                                  ###
70 REM            P R O G R A M  ' S M A R T M E C '                    ###
80 REM                                                                  ###
90 REM                                                                  ###
100 REM###################################################################
110 REM###################################################################
120 :
130 :
140 SCREEN 0:COLOR 1,3:PI=3.141592654#:UDL=0:KAFACTOR=1
150 DIM D(50),WD(50),WL(50),X(50),Y(50),VX(50),VY(50),PIN(4),KA(50)
160 GOSUB 4810:REM INITIALISE
170 :
180 GOSUB 4010:REM PRINT SCREEN HEADING
190 :
200 :
210 REM DATA INPUT ************************************************************
220 INPUT "Clear span (m) ";L
230 INPUT "Clear rise (m) ";RISE
240 INPUT"Is the profile segmental (Y/N) ";Y$
250 IF Y$="Y" OR Y$="y" THEN 270
260 INPUT"Quarter span rise (m) ";HQ
270 INPUT"Barrel thickness at springing (m) ";DSPRING
280 INPUT"Barrel thickness at crown (m) ";DCROWN
290 INPUT"Depth of fill over extrados at crown (m) ";D1
300 B=1:REM UNIT WIDTH
310 REM MODIFY SPAN TO DESIGN LINE:
320 XRAD=(L^2+4*RISE^2)/8/RISE+DSPRING:REM ARCH RADIUS TO EXTRADOS <- NOTE!
330 XL=SQR(XRAD*8*(RISE+DCROWN)-4*(RISE+DCROWN)^2):REM SPAN ACROSS EXTRADOS
340 L=(XL+L)/2:REM MODIFY SPAN TO DESIGN LINE
350 RISE=RISE+DCROWN/2:REM MODIFY RISE TO DESIGN LINE
360 IF Y$="Y" THEN 380
370 HQ=HQ+(DSPRING+DCROWN)/4:REM MODIFY 1/4 SPAN RISE TO DESIGN LINE FOR NON
    SEG PROFILE (APPROXIMATION)
380 IF Y$="N" THEN 420
390 R=(L^2+4*RISE^2)/8/RISE:REM ARCH RADIUS FOR SEGMENTAL PROFILE
400 HQ=SQR(R^2-L^2/16)-SQR(R^2-L^2/4):REM 1/4 SPAN RISE FOR SEGMENTAL PROFI
    LE
410 :
420 GOSUB 3260:REM COMPUTE NODE COORDINATES
430 :
440 GOSUB 3330:REM COMPUTE BARREL THICKNESS AT EACH NODE
450 :
460 YDECK=(192*RISE-256*H1)/3/L^4*(L/2)^4+(512*H1-384*RISE)/3/L^3*(L/2)^3+(228
    *RISE-320*H1)/3/L^2*(L/2)^2+(64*H1-36*RISE)/3/L*(L/2)+D1+DCROWN/2
470 :
480 GOSUB 4010:REM PRINT SCREEN HEADING
490 :
500 INPUT"Estimated mean material unit weight (kN/m3) ";RO
510 INPUT"Earth pressure coefficient (Ka-Ko-Kp) ";KA
520 IF KA=0 THEN KAPLUS$="N"
530 IF KA=0 GOTO 580
540 INPUT"Do you require enhanced earth pressures (Y/N) ";KAPLUS$
550 IF KAPLUS$="N" THEN 580
560 INPUT"Enhancement factor (suggested range: between 1 and 2) ",KAFACTOR
570 :
580 GOSUB 4220:REM INITIALISE EARTH PRESSURE COEFFICIENT ARRAY
590 :
600 INPUT"Sigma max for arch barrel material (N/mm2) ";SIGM
610 INPUT"k value for arch barrel material ";K
```

```
620 INPUT"Lambda for arch barrel material ";LAMBDA
630 :
640 GOSUB 4010:REM PRINT SCREEN HEADING
650 :
660 INPUT"Distance of load from rhs springing (m) ";XP
670 XP=XP+(XL-L)/2:REM MAKE LIVE LOAD POSITION RELATIVE TO DESIGN LINE
680 INPUT"UDL to apply (kN, total for whole span, 1m strip) ",UDL
690 PRINT:PRINT"Choose the type of live load dispersal:":PRINT
700 PRINT"    1 .... Modified Boussinesq":PRINT
710 PRINT"    2 .... Knife edge (no dispersal)":PRINT
720 PRINT"    3 .... 2:1 angle with triangular pattern":PRINT
730 PRINT"    4 .... 2:1 angle with UDL":PRINT
740 INPUT"Your choice (1, 2, 3 or 4) ";LIVE:PRINT
750 IF LIVE=1 OR LIVE=2 THEN 800
760 :
770 GOSUB 3890:IF LLL<>999 AND LLR<>999 THEN 800:REM EXTENT OF LOAD SPREAD
780 :
790 PRINT:PRINT"The load spills off the span. Please choose again.":GOTO 690
800 INPUT"The springing hinges are held. Do you wish to hold the other two
    (Y/N) ";Y$
810 IF Y$="N" THEN GOTO 830
820 INPUT"Enter all four node numbers, left to right ",PIN(1),PIN(2),PIN(3),
    PIN(4)
830 :
840 :
850 REM INITIAL ESTIMATES OF PA, PB, PC, PD FOR SOLUTION ROUTINE
860 :
870 GOSUB 3190:REM COMPUTE DEAD LOAD ARRAY
880 :
890 TOTALDL=0
900 FOR I=1 TO 50:TOTALDL=TOTALDL+WD(I):NEXT I
910 PA=SQR((TOTALDL/2)^2+(25*L*TOTALDL/2/RISE/128)^2)
920 PD=PA
930 PB=25*L*TOTALDL/RISE/128
940 PC=PB
950 H1=PA:H4=PA
960 CLS
970 :
980 SCREEN 2:GOSUB 3460:REM DRAW DECK & WHEEL
990 :
1000 :
1010 REM ITERATIVE SOLUTION ROUTINE **********************************
1020                                                                  :REM
1030 P=TOTALDL/2:LASTP=9.9E+37                                        :REM
1040 GOSUB 3830:REM DRAW BOXES                                        :REM
1050 LASTRUN%=0                                                       :REM
1060 IF Y$="Y" THEN 1150                                              :REM
1070 PIN(1)=1:PIN(3)=INT((L-XP)/L*50): PIN(2)=INT(PIN(3)/2):PIN(4)=50
1080 FOR II%=2 TO 3                                                   :REM
1090 PINORIG=PIN(II%)                                                 :REM
1100 PLAST=1E+30                                                      :REM
1110 FOR JJ%=PIN(II%)-1 TO PIN(II%)+1                                 :REM
1120 COL=0:GOSUB 3540:REM ERASE HINGES                                :REM
1130 IF LASTRUN%=1 GOTO 1150                                          :REM
1140 PIN(II%)=JJ%                                                     :REM
1150 COL=1:GOSUB 3540:REM DRAW HINGES                                 :REM
1160                                                                  :REM
1170 XX=P/4:ELAST=1E+20:E=0:JOLT=0:REM***********                     :REM
1180 ELAST=E                                  :REM                    :REM
1190 P=P+XX:JOLT=JOLT+1                       :REM                    :REM
1200 ON LIVE GOTO 1210,1220,1230,1240:REM L.L.:REM                    :REM
1210 GOSUB 2770:GOTO 1250:REM MOD. BOUSSINESQ :REM                    :REM
1220 GOSUB 2910:GOTO 1250:REM TRUE KEL        :REM                    :REM
1230 GOSUB 2950:GOTO 1250:REM 2TO1 SPREAD(TRI):REM                    :REM
```

```
1240 GOSUB 3110:GOTO 1250:REM 2TO1 SPREAD(UDL):REM                :REM
1250 GOSUB 4080:REM ERASE & DRAW LOAD VECTORS :REM OPTMISE LOAD:REM OPT HNGES
1260 GOSUB 1570:REM FIND TOTAL ERROR          :REM                :REM
1270 GOSUB 3510:REM DRAW LIVE LOAD            :REM                :REM
1280 GOSUB 3640:REM DRAW TEXT                 :REM                :REM
1290 IF JOLT=200 THEN XX=500                  :REM                :REM
1300 IF JOLT=200 THEN JOLT=0                  :REM                :REM
1310 IF ABS(E)>.005 THEN 1320 ELSE 1360       :REM                :REM
1320 IF ABS(E)<ABS(ELAST) THEN 1180           :REM                :REM
1330 XX=-XX/2                                 :REM                :REM
1340 GOTO 1180:REM*******************************                 :REM
1350                                                              :REM
1360 BEEP:IF Y$="Y" THEN 1480                                     :REM
1370 IF P>PLAST THEN 1390                                         :REM
1380 PLAST=P:PINORIG=PIN(II%):GOTO 1420                           :REM
1390 COL=0:GOSUB 3540:  REM ERASE HINGES                          :REM
1400 PIN(II%)=PINORIG                                             :REM
1410 COL=1:GOSUB 3540:  REM DRAW HINGES                           :REM
1420 IF LASTRUN%=1 GOTO 1480                                      :REM
1430 NEXT JJ%                                                     :REM
1440 NEXT II%                                                     :REM
1450 IF ABS(LASTP-P)<.2 GOTO 1470                                 :REM
1460 LASTP=P:GOTO 1080                                            :REM
1470 LASTRUN%=1:GOTO 1120                                         :REM
1480 FOR I=1 TO 3:SOUND 800,7:SOUND 300,3:NEXT I                  :REM
1490 LOCATE 15,30:PRINT"* * * D O N E * * *"                      :REM
1500 LOCATE 15,32:INPUT"Edit and re-run (Y/N) ";YY$               :REM
1510 IF YY$="Y" THEN GOSUB 4370 ELSE STOP                         :REM END
1520 REM*************************************************************
1530 :
1540 :
1550 REM SUBROUTINE TO COMPUTE TOTAL NON-CLOSURE OF EQUATIONS ***************
1560 :
1570 PSA=SIGM*D(PIN(4))*1000:REM PS IN kN AT 'A'
1580 MSA=1225/10560*PSA*D(PIN(4)):REM MS IN kNm AT 'A'
1590 MA=SIGM*1000*B*((K-1)*PA/(SIGM*1000*B*(K/2*LAMBDA-1/(K+1)*LAMBDA^K)))^2
     /(12*(K-1))*(K*LAMBDA-LAMBDA^K*(6/(K+1)-12/((K+1)*(K+2))))+PA*(D(PIN(4))
     )/2-((K-1)*PA/(SIGM*1000*B*(K/2*LAMBDA-1/(K+1)*LAMBDA^K)))/2):REM EQN 6
1600 IF MA<0 THEN MA=0
1610 :
1620 PSB=SIGM*D(PIN(3))*1000:REM PS IN kN AT 'B'
1630 MSB=1225/10560*PSB*D(PIN(3)):REM MS IN kNm AT 'B'
1640 MB=SIGM*1000*B*((K-1)*PB/(SIGM*1000*B*(K/2*LAMBDA-1/(K+1)*LAMBDA^K)))^2/
     (12*(K-1))*(K*LAMBDA-LAMBDA^K*(6/(K+1)-12/((K+1)*(K+2))))+PB*(D(PIN(3))
     /2-((K-1)*PB/(SIGM*1000*B*(K/2*LAMBDA-1/(K+1)*LAMBDA^K)))/2):REM EQN 7
1650 IF MB<0 THEN MB=0
1660 :
1670 PSC=SIGM*D(PIN(2))*1000:REM PS IN kN AT 'C'
1680 MSC=1225/10560*PSC*D(PIN(2)):REM MS IN kNm AT 'C'
1690 MC=SIGM*1000*B*((K-1)*PC/(SIGM*1000*B*(K/2*LAMBDA-1/(K+1)*LAMBDA^K)))^2/
     (12*(K-1))*(K*LAMBDA-LAMBDA^K*(6/(K+1)-12/((K+1)*(K+2))))+PC*(D(PIN(2))
     /2-((K-1)*PC/(SIGM*1000*B*(K/2*LAMBDA-1/(K+1)*LAMBDA^K)))/2):REM EQN 8
1700 IF MC<0 THEN MC=0
1710 :
1720 PSD=SIGM*D(PIN(1))*1000:REM PS IN kN AT 'D'
1730 MSD=1225/10560*PSD*D(PIN(1)):REM MS IN kNm AT 'D'
1740 MD=SIGM*1000*B*((K-1)*PD/(SIGM*1000*B*(K/2*LAMBDA-1/(K+1)*LAMBDA^K)))^2
     /(12*(K-1))*(K*LAMBDA-LAMBDA^K*(6/(K+1)-12/((K+1)*(K+2))))+PD*(D(PIN(1))
     )/2-((K-1)*PD/(SIGM*1000*B*(K/2*LAMBDA-1/(K+1)*LAMBDA^K)))/2):REM EQN 9
1750 IF MD<0 THEN MD=0
1760 :
1770 SUMV=0                                                       :REM
1780 FOR I=PIN(1)+1 TO PIN(4)-1                                   :REM
1790 SUMV=SUMV+(WD(I)+WL(I))*(X(I)-X(PIN(1)))                     :REM
```

```
1800 NEXT I                                                                    :REM
1810 SUMV=SUMV+(WD(PIN(1))+WL(PIN(1)))/2*L/49/4                                :REM
1820 SUMV=SUMV+(WD(PIN(4))+WL(PIN(4)))/2*(L-L/49/4)                            :REM
1830 SUMH=0                                                                    :REM
1840 FOR I=PIN(1)+1 TO 25                                                :REM EQN 1
1850 GOSUB 3410:REM GRADIENT AT I                                              :REM
1860 SUMH=SUMH+KA(I)*SIN(J)*(WL(I)+WD(I))*(Y(I)-Y(PIN(1)))                     :REM
1870 NEXT I                                                                    :REM
1880 I=PIN(1):GOSUB 3410:REM GRADIENT AT PIN1                                  :REM
1890 SUMH=SUMH+KA(PIN(1))*SIN(J)*(WL(PIN(1))+WD(PIN(1)))/2*(Y(PIN(1)+1)-Y(PIN
     (1)))/4                                                                   :REM
1900 FOR I=26 TO PIN(4)-1                                                      :REM
1910 GOSUB 3410:REM GRADIENT AT I                                              :REM
1920 SUMH=SUMH-KA(I)*SIN(J)*(WL(I)+WD(I))*(Y(I)-Y(PIN(1)))                     :REM
1930 NEXT I                                                                    :REM
1940 I=PIN(4):GOSUB 3410:REM GRADIENT AT PIN4                                  :REM
1950 SUMH=SUMH-KA(PIN(4))*SIN(J)*((WL(PIN(4))+WD(PIN(4)))/2*(Y(PIN(4)-1)-Y(P
     IN(4)))/4)                                                                :REM
1960 H4=H1-SUMH                                                                :REM
1970 VA=(MD+MA+SUMV+SUMH+H4*(Y(PIN1)-Y(PIN4)))/(X(PIN(4))-X(PIN(1)))          :REM
1980 :
1990 SUMV=0                                                                    :REM
2000 FOR I=PIN(1)+1 TO PIN(4)-1                                                :REM
2010 SUMV=SUMV+WL(I)+WD(I)                                                :REM VD
2020 NEXT I                                                                    :REM
2030 SUMV=SUMV+(WL(PIN(1))+WD(PIN(1)))/2                                       :REM
2040 SUMV=SUMV+(WL(PIN(4))+WD(PIN(4)))/2                                       :REM
2050 VD=SUMV-VA                                                                :REM
2060 :
2070 SUMV=0:SUMH=0                                                             :REM
2080 FOR I=PIN(1)+1 TO PIN(2)-1                                                :REM
2090 SUMV=SUMV+(WD(I)+WL(I))*(X(PIN(2))-X(I))                            :REM EQ 2
2100 GOSUB 3410:REM GRADIENT AT I                                              :REM
2110 SUMH=SUMH+KA(I)*SIN(J)*(WL(I)+WD(I))*(Y(PIN(2))-Y(I))                     :REM
2120 NEXT I                                                                    :REM
2130 SUMV=SUMV+((WD(PIN(1))+WL(PIN(1)))/2)*(X(PIN(2))-X(PIN(1))-L/49/4)        :REM
2140 I=1:GOSUB 3410:REM GRADIENT AT PIN1                                       :REM
2150 SUMH=SUMH+KA(PIN(1))*SIN(J)*(WL(PIN(1))+WD(PIN(1)))/2*((Y(PIN(2))-Y(PIN
     (1)))-(Y(PIN(1)+1)-Y(PIN(1)))/4)                                          :REM
2160 SUMV=SUMV+((WD(PIN(2))+WL(PIN(2)))/2*L/49/4)                              :REM
2170 I=2:GOSUB 3410:REM GRADIENT AT PIN2                                       :REM
2180 SUMH=SUMH+KA(PIN(2))*SIN(J)*((WL(PIN(2))+WD(PIN(2)))/2)*((Y(PIN(2))-Y(P
     IN(2)-1))/4)
2190 H1=(MC+MD-SUMH-SUMV+VD*(X(PIN(2))-X(PIN(1))))/(Y(PIN(2))-Y(PIN(1))):REM
2200 :
2210 I=PIN(1):GOSUB 3420:REM GRADIENT AT PIN1                            :REM EQ 3
2220 PD=SQR(VD^2+H1^2)*COS(ABS(ABS(ATN(VD/H1))-J))                             :REM
2230 :
2240 SUMV=0:SUMH=0                                                             :REM
2250 FOR I=PIN(3)+1 TO PIN(4)-1                                                :REM
2260 SUMV=SUMV+(WD(I)+WL(I))*(X(I)-X(PIN(3)))                                  :REM
2270 GOSUB 3420:REM GRADIENT AT I                                              :REM
2280 SUMH=SUMH+KA(I)*SIN(J)*(WL(I)+WD(I))*(Y(PIN(3))-Y(I))                     :REM
2290 NEXT I                                                                    :REM
2300 SUMV=SUMV+(WD(PIN(3))+WL(PIN(3))/2)*L/49/4                          :REM EQ 4
2310 I=3:GOSUB 3420:REM GRADIENT AT PIN3                                       :REM
2320 SUMH=SUMH+KA(PIN(3))*SIN(J)*(WL(PIN(3))+WD(PIN(3)))/2*((Y(PIN(3))-Y(PIN
     (3))+1)/4)                                                                :REM
2330 SUMV=SUMV+(WD(PIN(4))+WL(PIN(4)))/2*(X(PIN(4))-X(PIN(3))-L/49/4)          :REM
2340 I=4:GOSUB 3420:REM GRADIENT AT PIN4                                       :REM
2350 SUMH=SUMH+KA(PIN(4))*SIN(J)*(WL(PIN(4))+WD(PIN(4)))/2*(Y(PIN(3))-Y(PIN(
     4))-(Y(PIN(4)-1)-Y(PIN(4)))/4)                                            :REM
2360 E=H4*(Y(PIN(3))-Y(PIN(4)))+MA+MB+SUMV+SUMH-VA*(X(PIN(4))-X(PIN(3))):REM
2370 :
```

```
2380 I=PIN(4):GOSUB 3420:REM GRADIENT AT PIN4                          :REM EQ 5
2390 PA=SQR(VA^2+H4^2)*COS(ABS(ABS(ATN(VA/H4))-J))                     :REM
2400 :
2410 SUMV=0:SUMH=0                                                     :REM
2420 FOR I=PIN(3)+1 TO PIN(4)-1                                        :REM
2430 SUMV=SUMV+WD(I)+WL(I)                                             :REM
2440 GOSUB 3420:REM GRADIENT AT I                                      :REM
2450 SUMH=SUMH+KA(I)*SIN(J)*(WD(I)+WL(I))                              :REM
2460 NEXT I                                                          :REM EQ 11
2470 SUMV=SUMV+(WD(PIN(3))+WL(PIN(3)))/2                               :REM
2480 I=PIN(3):GOSUB 3420:REM GRADIENT AT PIN3                          :REM
2490 SUMH=SUMH+KA(PIN(3))*SIN(J)*(WD(PIN(3))+WL(PIN(3)))/2             :REM
2500 SUMV=SUMV+(WD(PIN(4))+WL(PIN(4)))/2                               :REM
2510 I=PIN(4):GOSUB 3420:REM GRADIENT AT PIN4                          :REM
2520 SUMH=SUMH+KA(PIN(4))*SIN(J)*(WD(PIN(4))+WL(PIN(4)))/2             :REM
2530 I=PIN(3):GOSUB 3420:REM GRADIENT AT PIN3                          :REM
2540 H3=H4-SUMH                                                        :REM
2550 PB=SQR(H3^2+(SUMV-VA)^2)*COS(ABS(ABS(ATN((SUMV-VA)/H3))-J))       :REM
2560 :
2570 SUMV=0:SUMH=0                                                     :REM
2580 FOR I=PIN(1)+1 TO PIN(2)-1                                        :REM
2590 SUMV=SUMV+WD(I)+WL(I)                                             :REM
2600 GOSUB 3420:REM GRADIENT AT I                                      :REM
2610 SUMH=SUMH+KA(I)*SIN(J)*(WD(I)+WL(I))                            :REM EQN 10
2620 NEXT I                                                            :REM
2630 SUMV=SUMV+(WD(PIN(1))+WL(PIN(1)))/2                               :REM
2640 I=PIN(1):GOSUB 3420:REM GRADIENT AT PIN1                          :REM
2650 SUMH=SUMH+KA(PIN(1))*SIN(J)*(WD(PIN(1))+WL(PIN(1)))/2             :REM
2660 SUMV=SUMV+(WD(PIN(2))+WL(PIN(2)))/2                               :REM
2670 I=PIN(2):GOSUB 3420:REM GRADIENT AT PIN2                          :REM
2680 SUMH=SUMH+KA(PIN(2))*SIN(J)*(WD(PIN(2))+WL(PIN(2)))/2             :REM
2690 I=PIN(2):GOSUB 3420:REM GRADIENT AT PIN2                          :REM
2700 H2=H1-SUMH                                                        :REM
2710 PC=SQR(H2^2+(SUMV-VD)^2)*COS(ABS(ABS(ATN((SUMV-VD)/H2))-J))       :REM
2720 RETURN                                                            :REM
2730 :
2740 :
2750 REM LIVE LOAD ARRAY SUBROUTINES ****************************************
2760                                                                   :REM
2770 REM LIVE LOAD SUBROUTINE (MODIFIED BOUSSINESQ) ***************    :REM
2780 JK=0                                                              :REM
2790 FOR I=1 TO 50                                                     :REM
2800 XL=ABS(X(50)-XP-X(I))                                             :REM
2810 ZL=YDECK-Y(I)                                                     :REM
2820 WL(I)=3*P/(2*PI*ZL^2)*(1/(1+(XL/ZL)^2))^(5/2)                     :REM
2830 JK=JK+WL(I)                                                       :REM
2840 NEXT I                                                            :REM
2850 IF JK=0 THEN 2890                                                 :REM
2860 FOR I=1 TO 50                                                     :REM
2870 WL(I)=WL(I)*P/JK:REM MAKE TOTAL OF W(I) = TOTAL APPLIED LIVE LOAD  :REM
2880 NEXT I                                                            :REM
2890 RETURN                                                            :REM
2900                                                                   :REM
2910 REM LIVE LOAD SUBROUTINE (KEL - NO DISPERSAL) ****************    :REM
2920 WL(50-INT(XP/L*51))=P                                             :REM
2930 RETURN                                                            :REM
2940                                                                   :REM
2950 REM LIVE LOAD SUBROUTINE (2 TO 1 - TRIANGULAR) ***************    :REM
2960 J=0:Q=0                                                           :REM
2970 FOR I=1 TO INT((LLR-LLL+1)/2)                                     :REM
2980 Q=Q+1:J=J+Q                                                       :REM
2990 NEXT I                                                            :REM
3000 J=J+J                                                             :REM
3010 IF (LLR-LLL)/2=INT((LLR-LLL)/2) THEN J=J+Q+1                      :REM
```

```
3020 Q=0                                                                    :REM
3030 FOR I=1 TO INT((LLR-LLL+1)/2)                                          :REM
3040 Q=Q+1                                                                  :REM
3050 WL(LLL+I-1)=Q/J*P                                                      :REM
3060 WL(LLR-I+1)=Q/J*P                                                      :REM
3070 NEXT I                                                                 :REM
3080 IF(LLR-LLL)/2=INT((LLR-LLL)/2) THEN WL(LLL+INT(LLR-LLL)/2)=(Q+1)/J*P:REM
3090 RETURN                                                                 :REM
3100                                                                        :REM
3110 REM LIVE LOAD SUBROUTINE (2 TO 1 - UDL) **********************         :REM
3120 FOR I=LLL TO LLR                                                       :REM
3130 WL(I)=P/(LLR-LLL+1)                                                    :REM
3140 NEXT I                                                                 :REM
3150 RETURN                                                                 :REM
3160                                                                        :REM
3170 REM*************************************************************************
3180 :
3190 REM SUBROUTINE FOR DEAD LOAD ******************************************
3200 FOR I=1 TO 50
3210 WD(I)=RO*(YDECK-Y(I)+D(I)/2)*L/51
3220 WD(I)=WD(I)+UDL/50
3230 NEXT I
3240 RETURN
3250 :
3260 REM SUBROUTINE TO COMPUTE NODE COORDINATES ******************************
3270 FOR I=1 TO 50
3280 X(I)=(I-1)*L/49
3290 Y(I)=(192*RISE-256*HQ)/3/L^4*X(I)^4+(512*HQ-384*RISE)/3/L^3*X(I)^3+(228
     *RISE-320*HQ)/3/L^2*X(I)^2+(64*HQ-36*RISE)/3/L*X(I)
3300 NEXT I
3310 RETURN
3320 :
3330 REM SUBROUTINE TO COMPUTE BARREL THICKNESS AT EACH NODE *****************
3340 D(25)=DCROWN+(DSPRING-DCROWN)*(L/2-X(25))/(L/2)
3350 FOR I=1 TO 25
3360 D(I)=DSPRING-(DSPRING-D(25))*(X(I)/X(25))
3370 D(51-I)=D(I)
3380 NEXT I
3390 RETURN
3400 :
3410 REM SUBROUTINE TO COMPUTE PROFILE GRADIENT AT I *************************
3420 J=ATN(ABS(4*(192*RISE-256*HQ)/3/L^4*X(I)^3+3*(512*HQ-384*RISE)/3/L^3*X(I
     )^2+2*(228*RISE-320*HQ)/3/L^2*X(I)+(64*HQ-36*RISE)/3/L))
3430 RETURN
3440 :
3450 REM GRAPHICS SUBROUTINE - DECK & WHEEL **********************************
3460 PRESET(25,115-YDECK/L*440/2.5),1:DRAW"R600C1"
3470 CIRCLE(540-XP/L*440,109-YDECK/L*440/2.5),12:DRAW"BU1":DRAW"C5P1,3"
3480 RETURN
3490 :
3500 REM GRAPHICS SUBROUTINE - LIVE LOAD LEGEND ******************************
3510 LOCATE INT((105-YDECK/L*440/2.5)/190*24+1),INT((530-XP/L*440)/640*80)+5)
     :PRINT USING"####.##";P;:PRINT" kN"
3520 RETURN
3530 :
3540 REM GRAPHICS SUBROUTINE - HINGES ****************************************
3550 FOR J=1 TO 4
3560 X=100+X(PIN(J))/L*440:Y=115-Y(PIN(J))/L*440/2.5
3570 PRESET(X,Y),1
3580 CIRCLE STEP(0,0),3,COL
3590 CIRCLE STEP(0,0),7,COL
3600 NEXT J
3610 RETURN
3620 :
```

```
3630 REM GRAPHICS SUBROUTINE - TEXT OUTPUT ***********************************
3640 LOCATE 18,5:PRINT"M (kNm) _______":LOCATE 18,22:PRINT USING"###.###";MD:
     LOCATE 18,37:PRINT USING"###.###";MC:LOCATE 18,52:PRINT USING"###.###";M
     B:LOCATE 18,67:PRINT USING"###.###";MA
3650 LOCATE 19,5:PRINT"P (kN) ________":LOCATE 19,21:PRINT USING"####.###";PD
     :LOCATE 19,36:PRINT USING"####.###";PC:LOCATE 19,51:PRINT USING"####.##
     #";PB:LOCATE 19,66:PRINT USING"####.###";PA
3660 MSA=MA/MSA:MSB=MB/MSB:MSC=MC/MSC:MSD=MD/MSD
3670 LOCATE 20,5:PRINT"m _____________":LOCATE 20,22:PRINT USING"###.###";MSD
    :LOCATE 20,37:PRINT USING"###.###";MSC:LOCATE 20,52:PRINT USING"###.###";
     MSB:LOCATE 20,67:PRINT USING"###.###";MSA
3680 PSA=PA/PSA:PSB=PB/PSB:PSC=PC/PSC:PSD=PD/PSD
3690 LOCATE 21,5:PRINT"n _____________":LOCATE 21,22:PRINT USING"###.###";PSD
    :LOCATE 21,37:PRINT USING"###.###";PSC:LOCATE 21,52:PRINT USING"###.###";
    PSB:LOCATE 21,67:PRINT USING"###.###";PSA
3700 LOCATE 23,5:PRINT USING "Non-closure=###.##";ABS(E),:PRINT"   "
3710 LOCATE 23,25:PRINT USING "LH=####.#";H4,:PRINT"kN"
3720 LOCATE 23,38:PRINT USING "LV=####.#";VD,:PRINT"kN"
3730 LOCATE 23,52:PRINT USING "RH=####.#";H1,:PRINT"kN"
3740 LOCATE 23,65:PRINT USING "RV=####.#";VA,:PRINT"kN"
3750 IF LASTRUN%=1 THEN II%=0
3760 LOCATE 17,22:PRINT PIN(1);:IF II%=1 THEN PRINT"<FREE " ELSE PRINT "<HEL
     D "
3770 LOCATE 17,37:PRINT PIN(2);:IF II%=2 THEN PRINT"<FREE " ELSE PRINT "<HEL
     D "
3780 LOCATE 17,52:PRINT PIN(3);:IF II%=3 THEN PRINT"<FREE " ELSE PRINT "<HEL
     D "
3790 LOCATE 17,67:PRINT PIN(4);:IF II%=4 THEN PRINT"<FREE " ELSE PRINT "<HEL
     D "
3800 RETURN
3810 :
3820 REM GRAPHICS SUBROUTINE - BOXES ****************************************
3830 PRESET(25,125),1
3840 DRAW"D60R590U60L590"
3850 DRAW"D48R590U48L590"
3860 LOCATE 17,5:PRINT"Hinge nodes"
3870 RETURN
3880 :
3890 REM SUBROUTINE TO FIND EXTENT OF 2 TO 1 SPREAD (2 NODES, LLL AND LLR) ***
3900 LLL=(50-INT(XP/L*51)):LLR=LLL
3910 LLL=LLL-1
3920 IF LLL=0 THEN LLL=999
3930 IF LLL=999 THEN 3990
3940 IF (YDECK-Y(LLL))<2*((L-XP)-X(LLL)) THEN 3950 ELSE 3910
3950 LLR=LLR+1
3960 IF LLR=50 THEN LLR=999
3970 IF LLR=999 THEN 3990
3980 IF (YDECK-Y(LLR))<2*(X(LLR)-(L-XP)) THEN 3990 ELSE 3950
3990 RETURN
4000 :
4010 REM SUBROUTINE TO PRINT SCREEN HEADING **********************************
4020 CLS:COLOR 10,4
4030 PRINT"
          ":PRINT "          <  <  <    S    M    A    R    T    M    E    C
 >  >  >            "
4040 PRINT"
          "
4050 COLOR 1,3:PRINT:PRINT
4060 RETURN
4070 :
4080 REM GRAPHICS SUBROUTINE TO ERASE & DRAW LOAD VECTORS ********************
4090 PRESET(100,115),1
4100 FOR I=0 TO 50
4110 LINE-(100+X(I)/L*440,115-Y(I)/L*440/2.5),1:REM DRAWS ARCH SEGMENT
```

```
4120 LINE-(VX(I),VY(I)),0:REM ERASES VECTOR
4130 PRESET(100+X(I)/L*440,115-Y(I)/L*440/2.5),1:REM PRESETS TO BOTTOM OF VECT
     OR
4140 VX(I)=(100+X(I)/L*440)-SGN(25-I)*KA(I)*2.5*SIN(J)*(WD(I)+WL(I))*25/L
4150 VY(I)=(115-Y(I)/L*440/2.5)-(WD(I)+WL(I))*25/L
4160 GOSUB 3410
4170 LINE-(VX(I),VY(I)),1,,-16:REM DRAWS VECTOR
4180 PRESET(100+X(I)/L*440,115-Y(I)/L*440/2.5),1:REM PRESETS TO BOTTOM OF VECT
     OR
4190 NEXT I
4200 RETURN
4210 :
4220 REM SUBROUTINE TO INITIALISE EARTH PRESSURE COEFFICIENT ARRAY ***********
4230 FOR I=1 TO 50
4240 KA(I)=KA
4250 NEXT I
4260 IF KAPLUS$="y"OR KAPLUS$="Y" THEN 4270 ELSE 4350
4270 FOR I=1 TO 10
4280 KA(I)=KA(I)*KAFACTOR
4290 KA(51-I)=KA(51-I)*KAFACTOR
4300 NEXT I
4310 FOR I=11 TO 25
4320 KA(I)=KA(I-1)-(KAFACTOR-1)*KA/15
4330 KA(51-I)=KA(I)
4340 NEXT I
4350 RETURN
4360 :
4370 REM EDITOR SUBROUTINE ****************************************************
4380 CLS
4390 PRINT"Current primary data values:"
4400 PRINT"_____________________________":PRINT
4410 PRINT"    1 ... Mean material unit weight                    ";RO;" kN/
     mm3":PRINT
4420 PRINT"    2 ... Earth pressure coefficient (Ka-Ko-Kp)        ";KA:PRINT
4430 PRINT"    3 ... Enhanced earth pressure factor               ";KAFACTOR
     :PRINT
4440 PRINT"    4 ... Sigma max for arch barrel material           ";SIGM;" N
     /mm2":PRINT
4450 PRINT"    5 ... k value for arch barrel material             ";K:PRINT
4460 PRINT"    6 ... Lambda for arch barrel material              ";LAMBDA:P
     RINT
4470 PRINT"    7 ... Distance of load from rhs springing          ";XP-(XL-L
     )/2;" m":PRINT
4480 PRINT"    8 ... UDL applied (total for whole span, 1m strip) ";UDL;" kN
     ":PRINT
4490 PRINT"    9 ... The live load dispersal is currently";
4500 ON LIVE GOTO 4510,4520,4530,4540
4510 PRINT" modified Boussinesq":GOTO 4550
4520 PRINT" knife edge":GOTO 4550
4530 PRINT" 2:1, triangular":GOTO 4550
4540 PRINT" 2:1, UDL":GOTO 4550
4550 PRINT
4560 INPUT"                Enter number for change or 99 to continue ",ED
4570 CLS
4580 GOSUB 4810:REM INITIALISE
4590 IF ED=99 THEN 850
4600 ON ED GOTO 4610,4620,4630,4640,4650,4660,4670,4690,4700
4610 INPUT"New material unit weight (kN/m3) ";RO:GOTO 4370
4620 INPUT"New earth pressure coefficient (Ka-Ko-Kp) ";KA:GOSUB 4220:GOTO 4370
4630 INPUT"Enhanced earth pressure factor ";KAFACTOR:KAPLUS$="Y":GOSUB 4220
     :GOTO 4370
4640 INPUT"New sigma max for arch barrel material (N/mm2) ";SIGM:GOTO 4370
4650 INPUT"New k value for arch barrel material ";K:GOTO 4370
4660 INPUT"New lambda for arch barrel material ";LAMBDA:GOTO 4370
```

```
4670 INPUT"New distance of load from rhs springing (m) ";XP
4680 XP=XP+(XL-L)/2:GOTO 4370:REM MAKE LL POSITION RELATIVE TO DESIGN LINE
4690 INPUT"New UDL applied (kN, total for whole span, 1m strip) ";UDL:GOT
     O 4370
4700 PRINT"The types of live load dispersal available are:":PRINT
4710 PRINT"     1) .... Modified Boussinesq":PRINT
4720 PRINT"     2) .... Knife edge (no dispersal)":PRINT
4730 PRINT"     3) .... 2:1 angle with triangular pattern":PRINT
4740 PRINT"     4) .... 2:1 angle with UDL":PRINT
4750 INPUT"Your choice (1, 2, 3 or 4) ",LIVE
4760 IF LIVE=1 OR LIVE=2 THEN 4370
4770 GOSUB 3890:IF LLL<>999 AND LLR<>999 THEN 4370:REM EXTENT OF LOAD SPREAD
4780 PRINT:PRINT"The load spills off the span. Please choose again.":GOTO 4590
4790 CLS:RETURN
4800 :
4810 REM SUBROUTINE TO INITIALISE VARIABLES **********************************
4820 FOR I=1 TO 50:WL(I)=0:WD(I)=0:VX(I)=100:VY(I)=115:NEXT I:REM INITIALISE
4830 RETURN
```

```
10 REM##########################################################################
20 REM##########################################################################
30 REM                                                                        ###
40 REM                                                                        ###
50 REM     P . A .  M A L L I N D E R     -     J U N   1 9 9 5              ###
60 REM                                                                        ###
70 REM              P R O G R A M  ' B E I G H T O N '                        ###
80 REM                                                                        ###
90 REM                                                                        ###
100 REM#########################################################################
110 REM#########################################################################
120 :
130 :
140 SCREEN 0:COLOR 1,3:CLS
150 :
160 :
170 REM DATA ***************************************************************
180 X1=2.16                         :REM m
190 X2=5.49                         :REM m
200 X3=2.16                         :REM m
210 X4=1.95                         :REM m
220 X5=5.49                         :REM m
230 Y1=4.77                         :REM m
240 Y2=4.69                         :REM m
250 Y3=2.5                          :REM m
251 Y4=2!                           :REM m
260 W1=51.8                         :REM kN
270 W2=146.5                        :REM kN
280 Q=496.8                         :REM Est. horiz. restraint, kN, via K earth
290 DA=.483                         :REM Arch barrel thickness, m
300 DP=1.5                          :REM Estimated effective pier thickness, m
310 B=1                             :REM Unit width, m
320 SIGM=4.5                        :REM Sigma max for arch barrel matl, N/mm2
330 K=2                             :REM k value for arch barrel material
340 LAMBDA=1.25                     :REM Lambda for arch barrel material
350 PSA=SIGM*DA*1000                :REM Pquash in kN for arch barrel
360 MSA=1225/10560*PSA*DA           :REM Msquash in kNm for arch barrel
370 PSP=SIGM*DP*1000                :REM Pquash in kN for pier/abutment
380 MSP=1225/10560*PSP*DP           :REM Msquash in kNm for pier/abutment
390 :
400 :
410 REM INITIAL ESTIMATES ***************************************************
420 M1=90:M2=90:M3=90:M4=90
430 P1=600:P2=600:P3=600:P4=600
440 P=500
450 H1=50:H4=50:V1=50:V4=50
460 :
470 :
480 REM ITERATIVE SOLUTION ROUTINE ***********************
490 XX=P/4:ELAST=1E+20:E=1E+15:GOTO 520                   :REM
500 ELAST=E                                               :REM
510 P=P+XX                                                :REM
520 GOSUB 610:REM FIND TOTAL ERROR                        :REM OPTIMISE LOAD
530 GOSUB 790:REM PRINT OUTPUT                            :REM
540 IF ABS(E)>.005 THEN 550 ELSE 580                      :REM
550 IF ABS(E)<ABS(ELAST) THEN 500                         :REM
560 XX=-XX/2                                              :REM
570 GOTO 500                                              :REM
580 LOCATE 1,1:PRINT "PROGRAMME FINISHED":STOP            :REM PROG END
590 :
600 :
610 REM SUBROUTINE TO COMPUTE TOTAL NON-CLOSURE OF EQUATIONS **************
620 V4=((W1*X4)+(W2*X5)+(P*X3)+(H4*Y1)-M1-M4+Q*(Y1-Y4))/X2     :REM EQN 1
630 V1=W1+W2+P-V4                                             :REM V1
640 E=((M1+M2+(W1*(X1-X4))-(V1*X1))/(Y1-Y2))-H1               :REM EQN 2
```

```
650 H1=H4+Q                                                    :REM H1
660 P1=SQR(V1^2+H1^2)                                          :REM EQN 3
670 H4=(M3+M4-Q*(Y3-Y4))/Y3                                    :REM EQN 4
680 P4=V4                                                      :REM EQN 5
690 M4=SIGM*1000*B*((K-1)*P4/(SIGM*1000*B*(K/2*LAMBDA-1/(K+1)*LAMBDA^K)))^2
    /(12*(K-1))*(K*LAMBDA-LAMBDA^K*(6/(K+1)-12/((K+1)*(K+2))))+P4*(DP/2-((K
    -1)*P4/(SIGM*1000*B*(K/2*LAMBDA-1/(K+1)*LAMBDA^K)))/2):REM EQN 6 - PIER
700 M3=SIGM*1000*B*((K-1)*P3/(SIGM*1000*B*(K/2*LAMBDA-1/(K+1)*LAMBDA^K)))^2
    /(12*(K-1))*(K*LAMBDA-LAMBDA^K*(6/(K+1)-12/((K+1)*(K+2))))+P3*(DA/2-((K
    -1)*P3/(SIGM*1000*B*(K/2*LAMBDA-1/(K+1)*LAMBDA^K)))/2):REM EQN 7 - ARCH
710 M2=SIGM*1000*B*((K-1)*P2/(SIGM*1000*B*(K/2*LAMBDA-1/(K+1)*LAMBDA^K)))^2
    /(12*(K-1))*(K*LAMBDA-LAMBDA^K*(6/(K+1)-12/((K+1)*(K+2))))+P2*(DA/2-((K
    -1)*P2/(SIGM*1000*B*(K/2*LAMBDA-1/(K+1)*LAMBDA^K)))/2):REM EQN 8 - ARCH
720 M1=SIGM*1000*B*((K-1)*P1/(SIGM*1000*B*(K/2*LAMBDA-1/(K+1)*LAMBDA^K)))^2
    /(12*(K-1))*(K*LAMBDA-LAMBDA^K*(6/(K+1)-12/((K+1)*(K+2))))+P1*(DA/2-((K
    -1)*P1/(SIGM*1000*B*(K/2*LAMBDA-1/(K+1)*LAMBDA^K)))/2):REM EQN 9 - ARCH
730 H2=-H1:P2=SQR(H2^2+(W1-V1)^2)                              :REM EQN 10
740 P3=V4                                                      :REM EQN 11
750 RETURN
760 :
770 :
780 REM OUTPUT SUBROUTINE ************************************************
790 LOCATE 3,21:PRINT"*** APPLIED LOAD = ";:PRINT USING"####.##";P;:PRINT"
    kN ***"
800 LOCATE 4,21:PRINT"---------------------------------"
810 LOCATE 7,28:PRINT USING "Non-closure = ###.##";ABS(E),:PRINT"  "
820 LOCATE 10,23:PRINT"Hinge 1        Hinge 2        Hinge 3        Hinge 4
    "
830 LOCATE 12,5:PRINT"M (kNm) _______":LOCATE 12,22:PRINT USING"###.###";M1
    :LOCATE 12,37:PRINT USING"###.###";M2:LOCATE 12,52:PRINT USING"###.###"
    ;M3:LOCATE 12,67:PRINT USING"###.###";M4
840 LOCATE 14,5:PRINT"P (kN) ________":LOCATE 14,21:PRINT USING"####.###";P
    1:LOCATE 14,36:PRINT USING"####.###";P2:LOCATE 14,51:PRINT USING"####.#
    ##";P3:LOCATE 14,66:PRINT USING"####.###";P4
850 MS4=M4/MSP:MS3=M3/MSA:MS2=M2/MSA:MS1=M1/MSA
860 LOCATE 16,5:PRINT"m _____________":LOCATE 16,22:PRINT USING"###.###";MS
    1:LOCATE 16,37:PRINT USING"###,###";MS2:LOCATE 16,52:PRINT USING"###.##
    #";MS3:LOCATE 16,67:PRINT USING"###.###";MS4
870 PS4=P4/PSP:PS3=P3/PSA:PS2=P2/PSA:PS1=P1/PSA
880 LOCATE 18,5:PRINT"n _____________":LOCATE 18,22:PRINT USING"###.###";PS
    1:LOCATE 18,37:PRINT USING"###.###";PS2:LOCATE 18,52:PRINT USING"###.##
    #";PS3:LOCATE 18,67:PRINT USING"###.###";PS4

890 LOCATE 21,8:PRINT USING "L HORIZ. REACT.=####.#";H1,:PRINT"kN"
900 LOCATE 22,8:PRINT USING "L VERT. REACT. =####.#";V1,:PRINT"kN"
910 LOCATE 21,40:PRINT USING "R HORIZ. REACT.(INC. Q)=####.#";H4+Q,:PRINT"k
    N"
920 LOCATE 22,40:PRINT USING "R VERT. REACT. =####.#";V4,:PRINT"kN"
930 RETURN
```

APPENDIX 'B'

The model hinge experimental data referred to in Chapter Three

PLATE B1

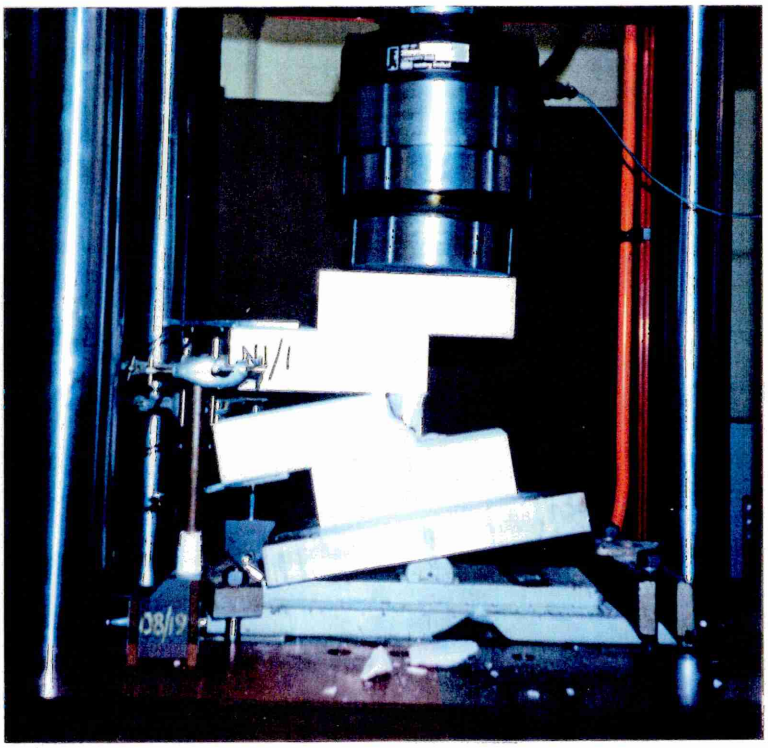

Hinge test N1/1 post failure

PLATE B2

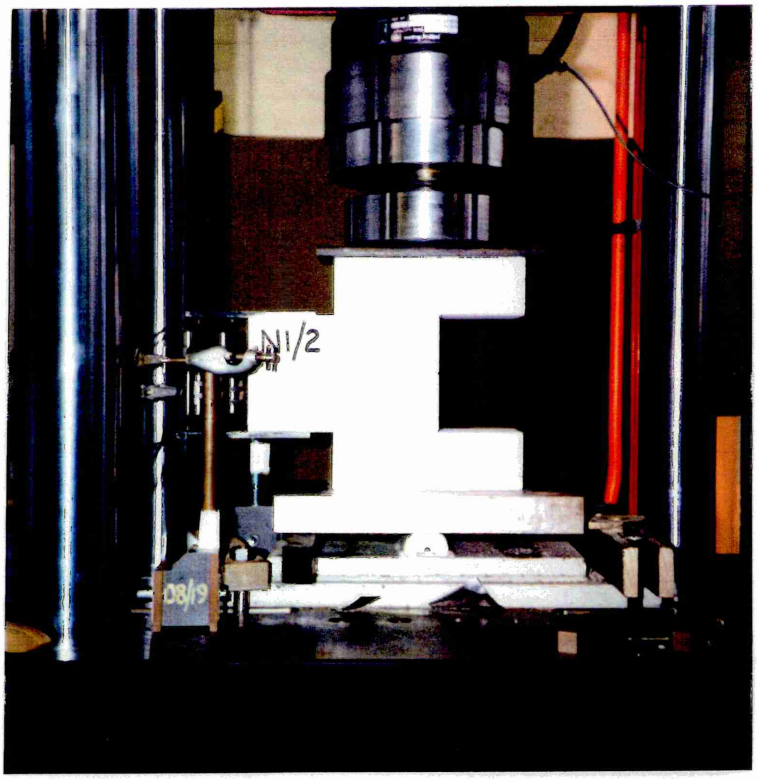

Hinge test N1/2 before testing

PLATE B3

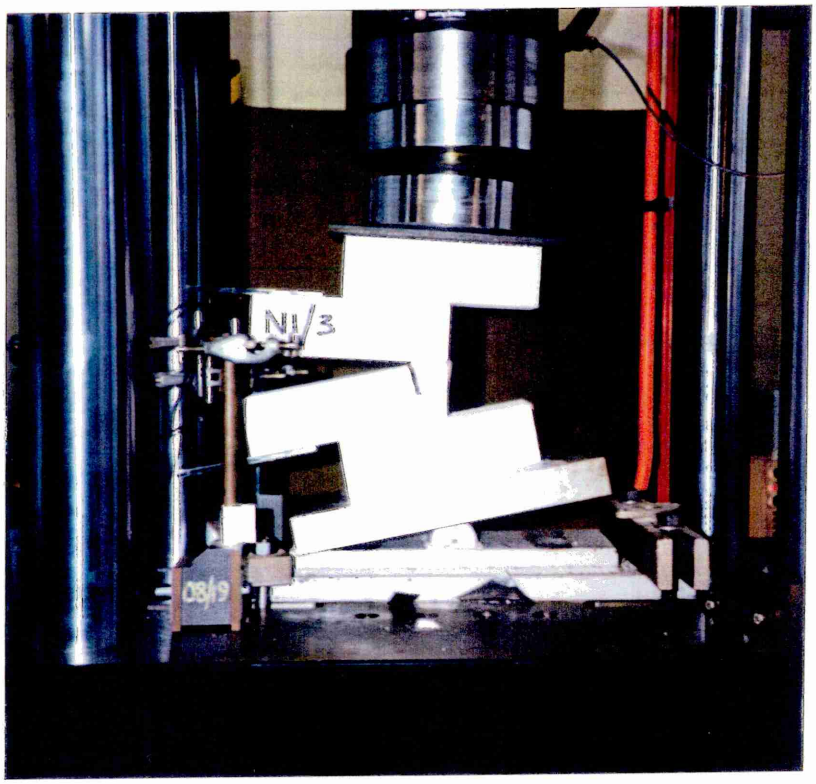

Hinge test N1/3 post failure

PLATE B4

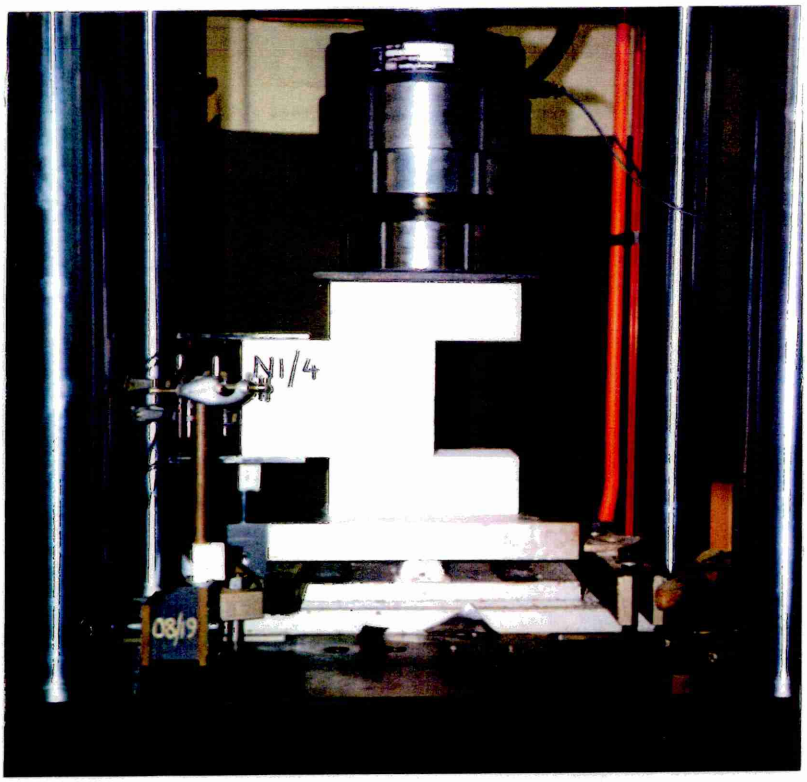

Hinge test N1/4 before testing

PLATE B5

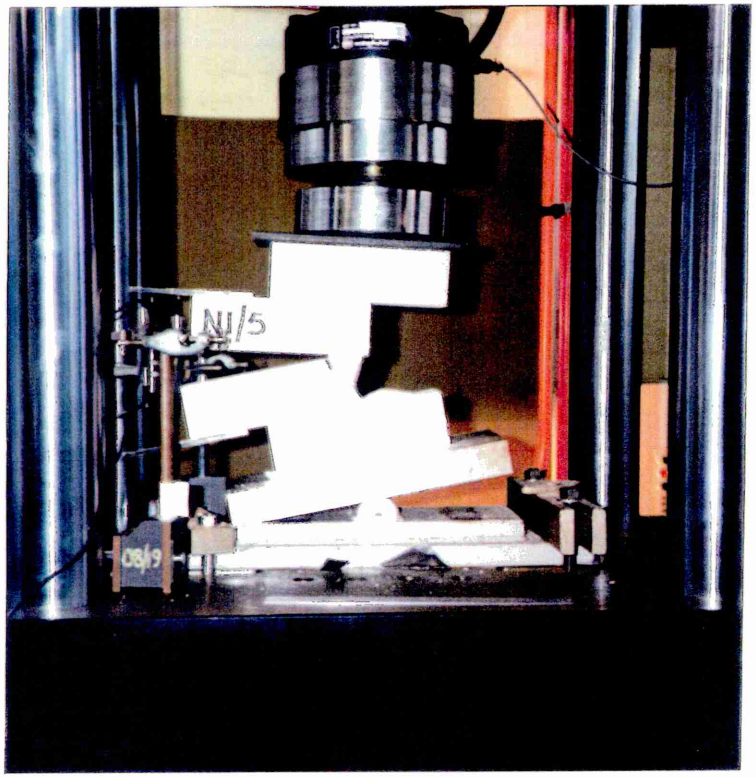

Hinge test N1/5 post failure

PLATE B6

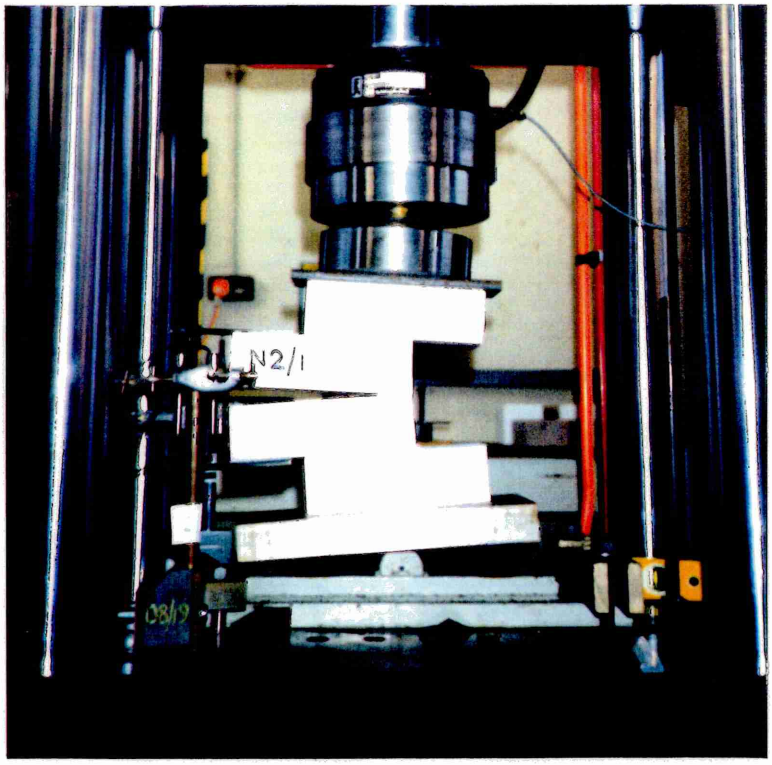

Hinge test N2/1 post failure

PLATE B7

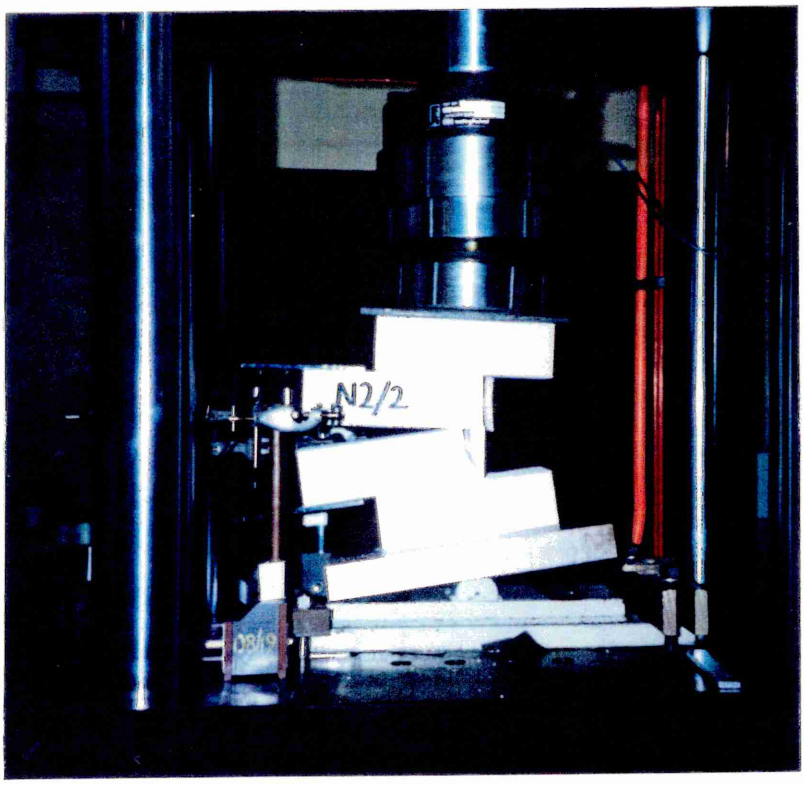

Hinge test N2/2 post failure

PLATE B8

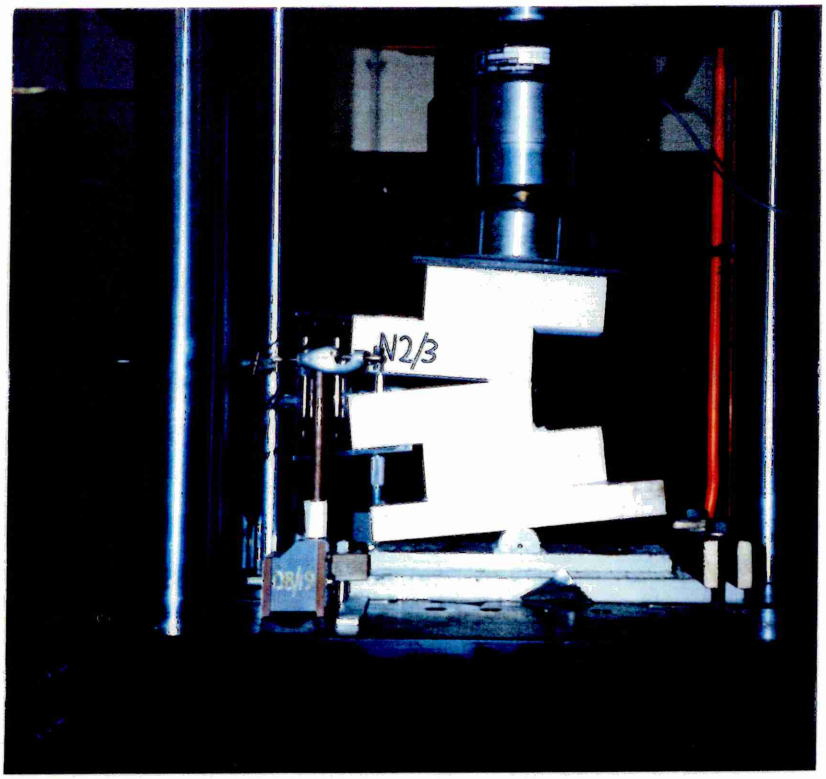

Hinge test N2/3 post failure

PLATE B9

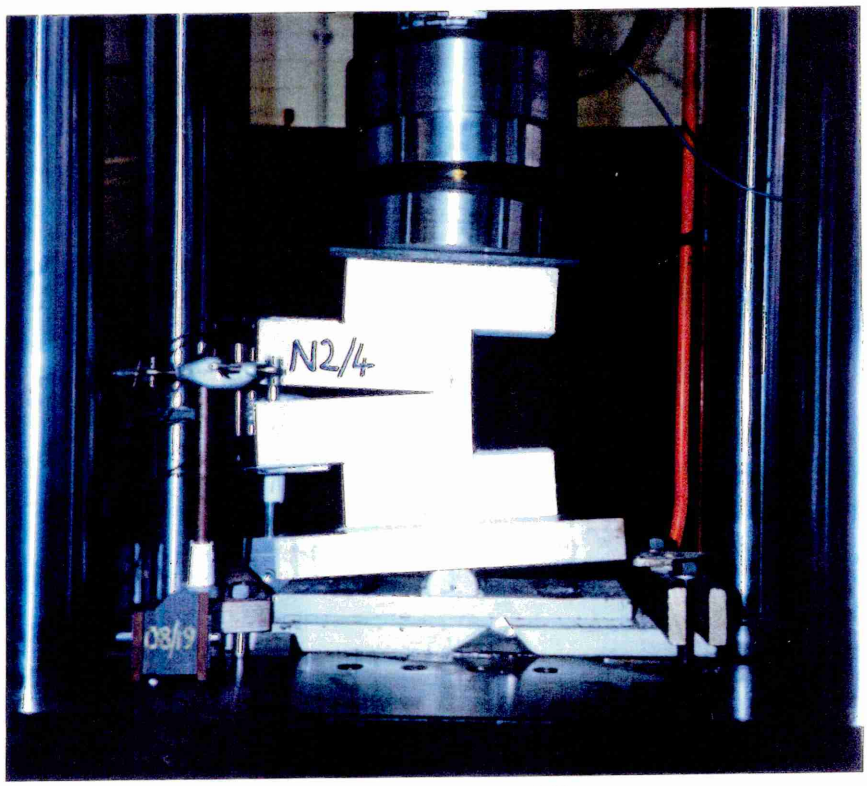

Hinge test N2/4 post failure

PLATE B10

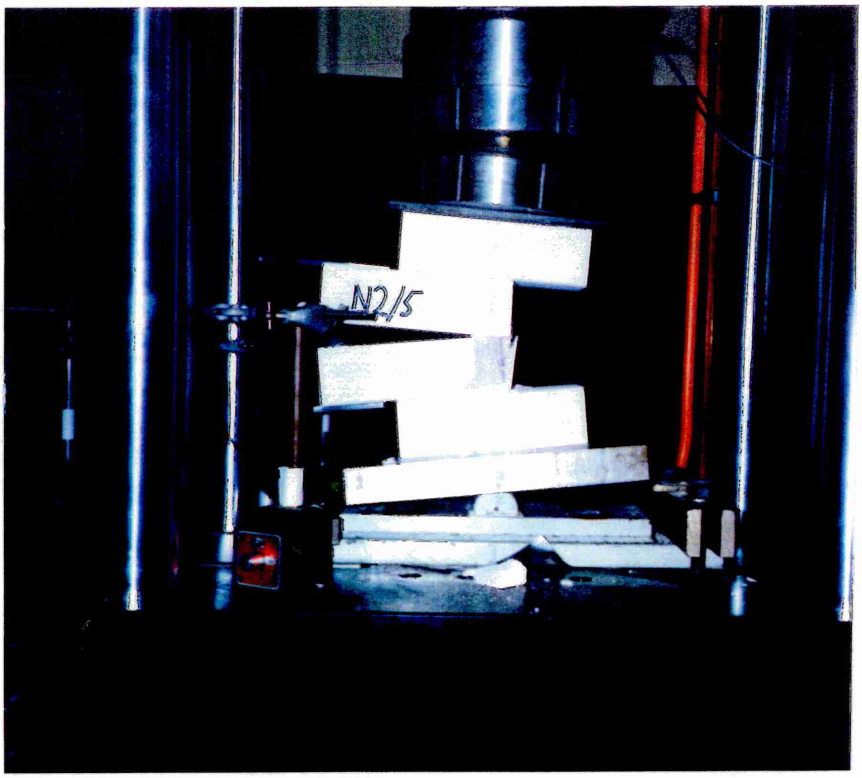

Hinge test N2/5 post failure

PLATE B11

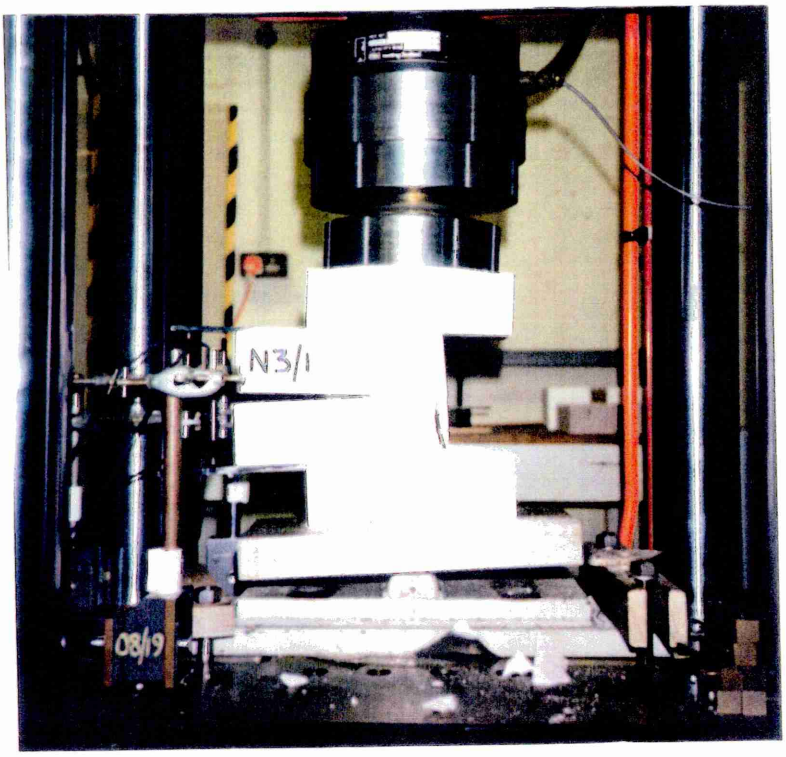

Hinge test N3/1 post failure

PLATE B12

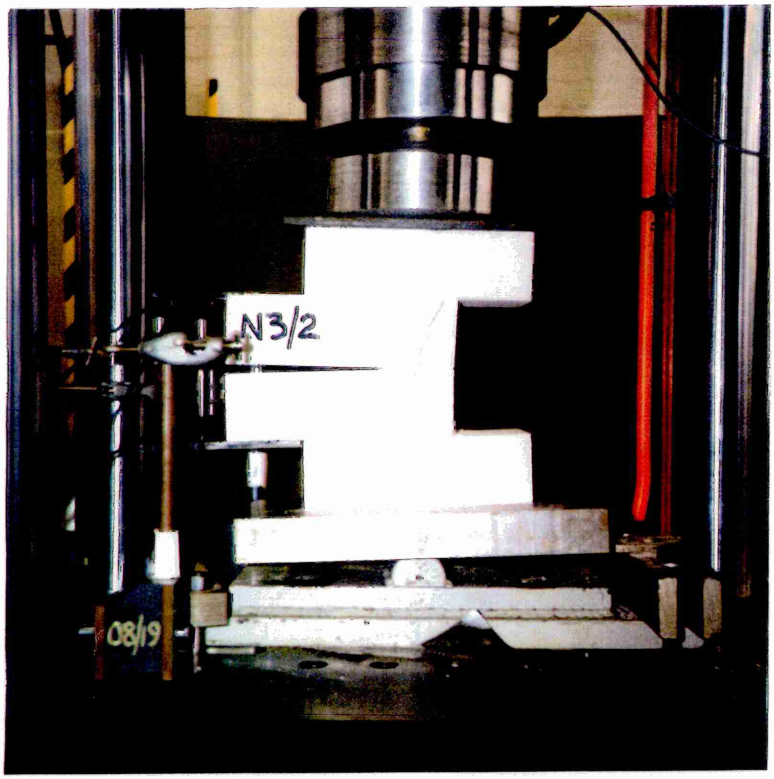

Hinge test N3/2 post failure

PLATE B13

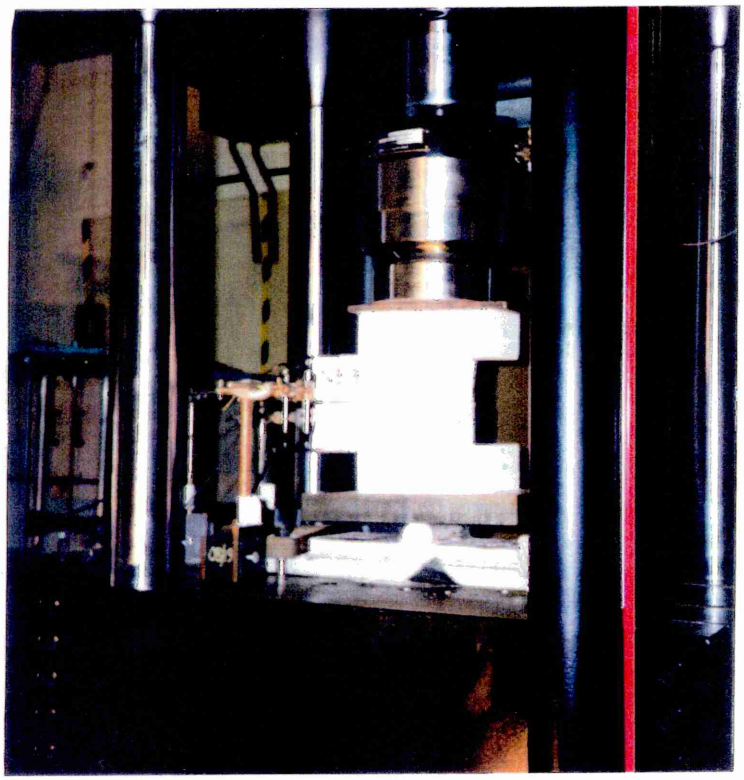

Hinge test N3/3 post failure

PLATE B14

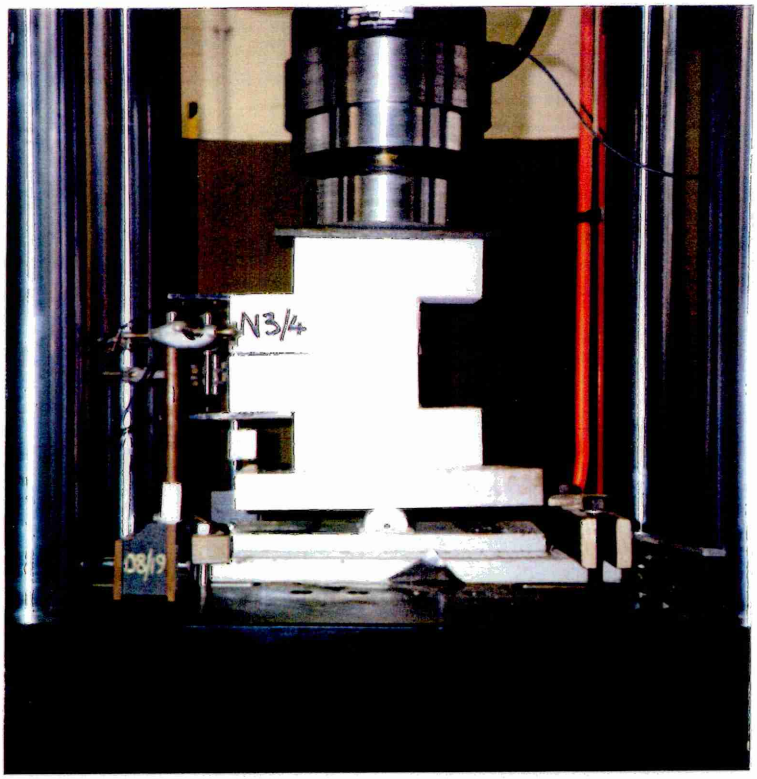

Hinge test N3/4 post failure

PLATE B15

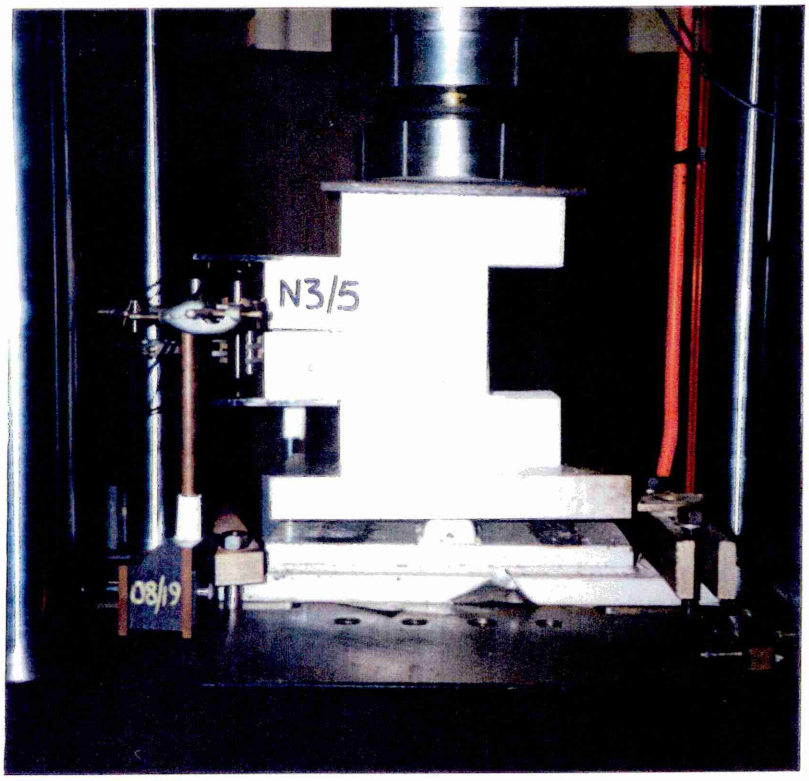

Hinge test N3/5 post failure

FIGURE B1

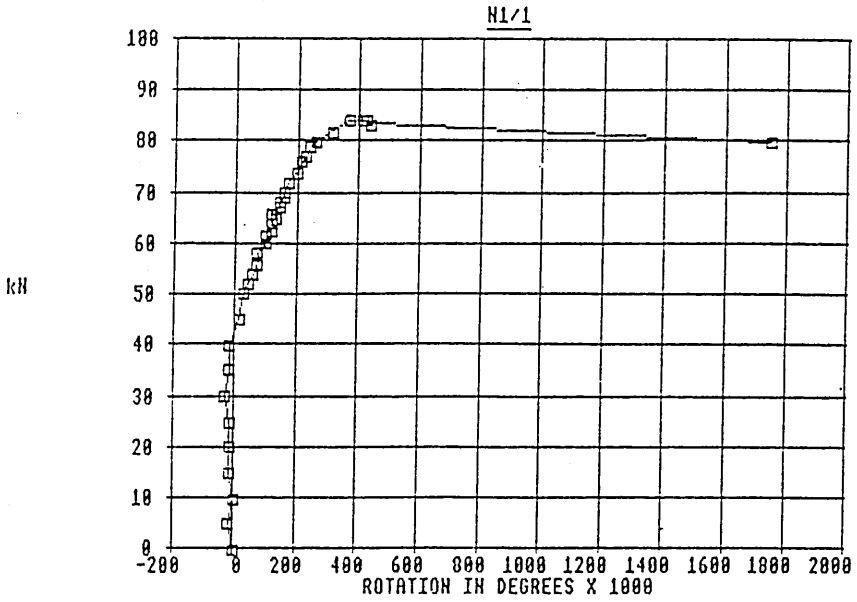

Force-rotation plot for N1/1

FIGURE B2

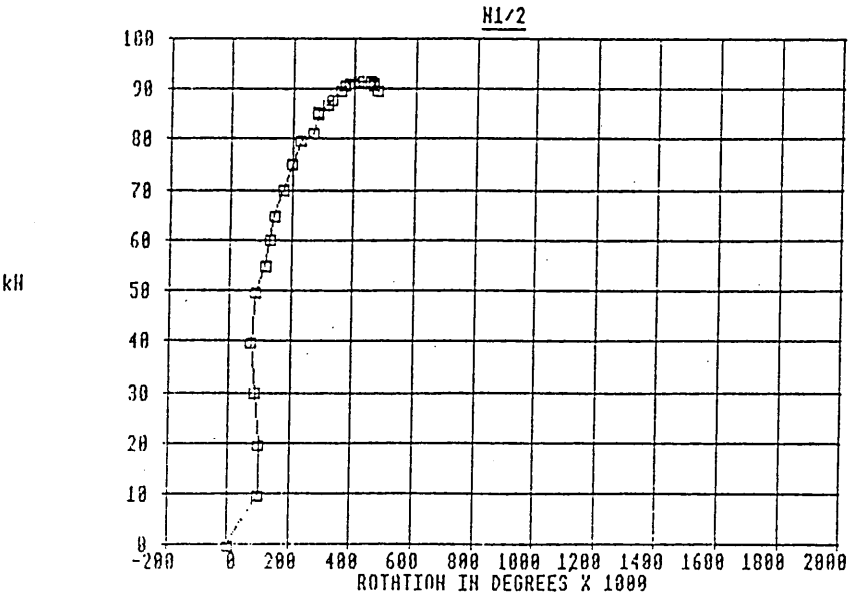

Force-rotation plot for N1/2

FIGURE B3

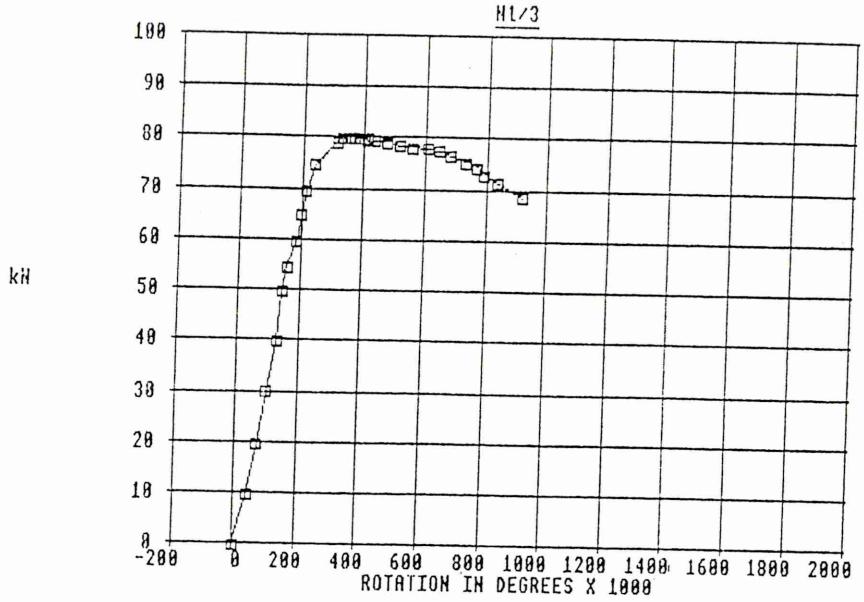

Force-rotation plot for N1/3

FIGURE B4

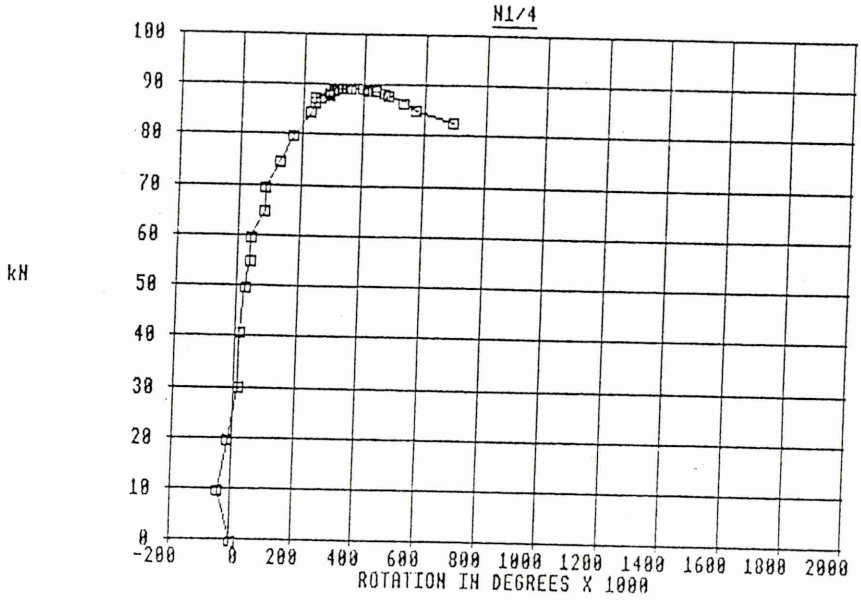

Force-rotation plot for N1/4

FIGURE B5

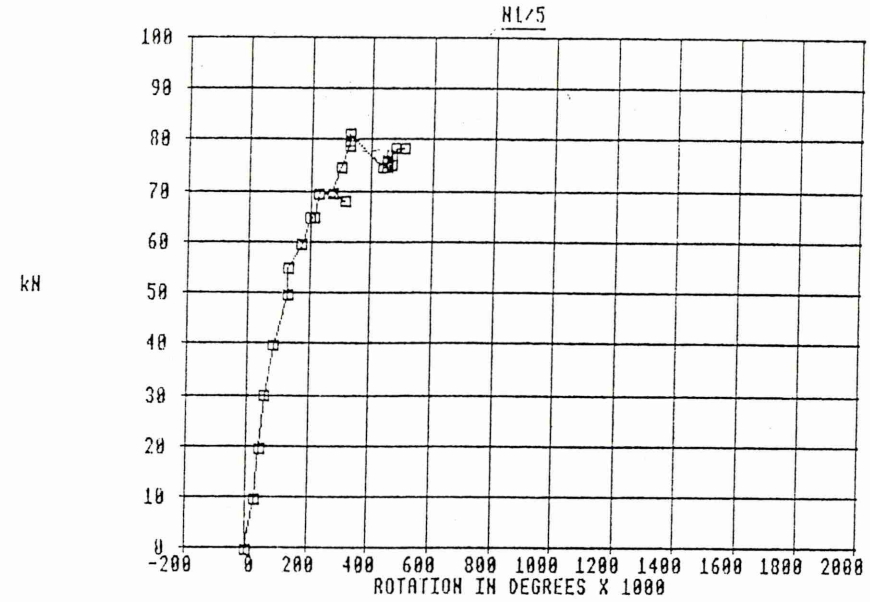

Force-rotation plot for N1/5

FIGURE B6

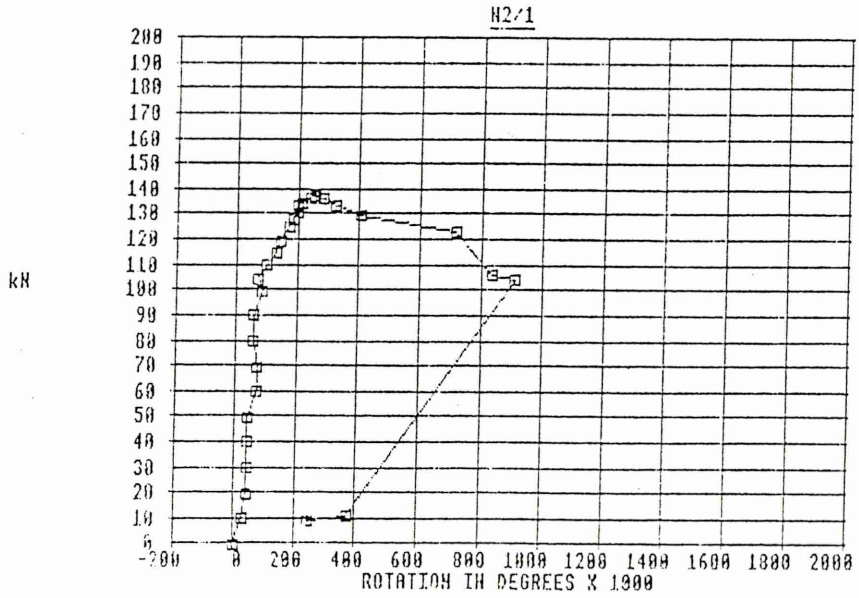

Force-rotation plot for N2/1

FIGURE B7

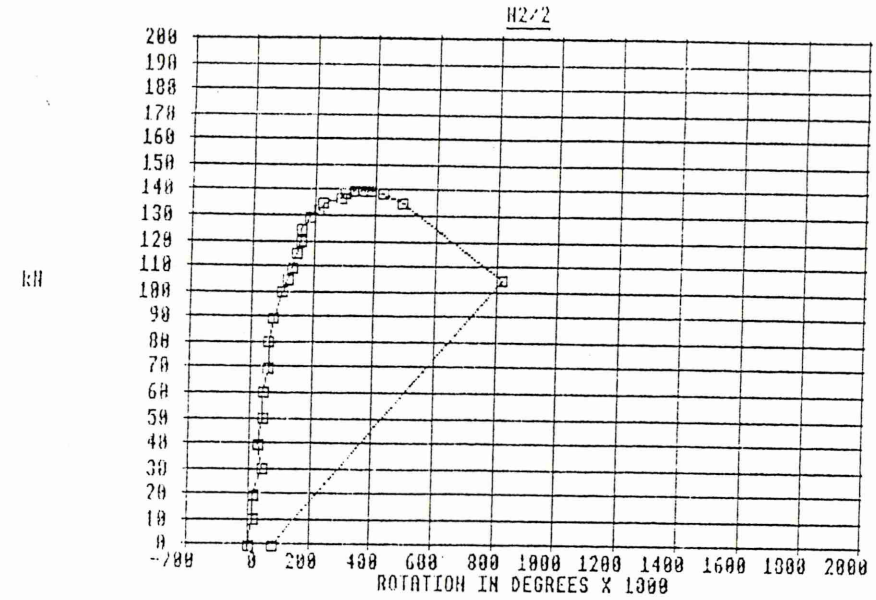

Force-rotation plot for N2/2

FIGURE B8

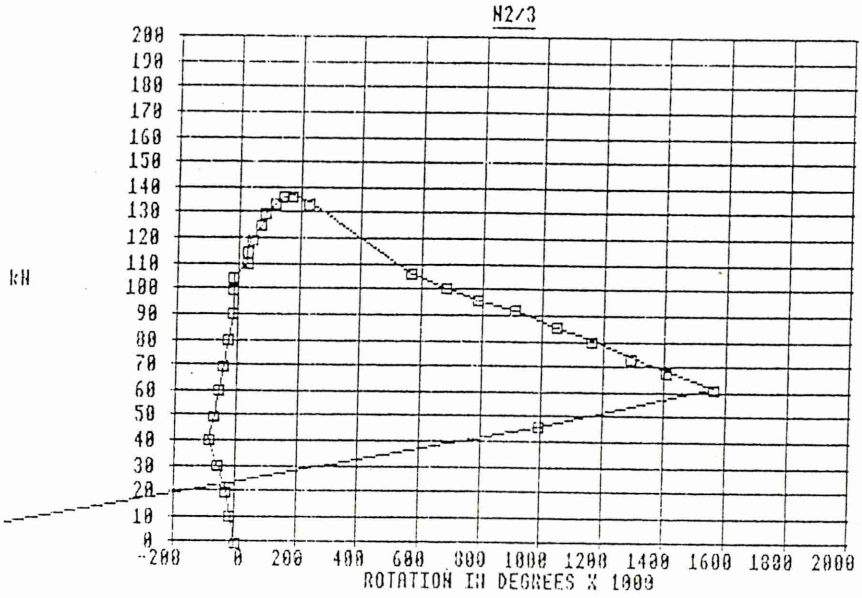

Force-rotation plot for N2/3

FIGURE B9

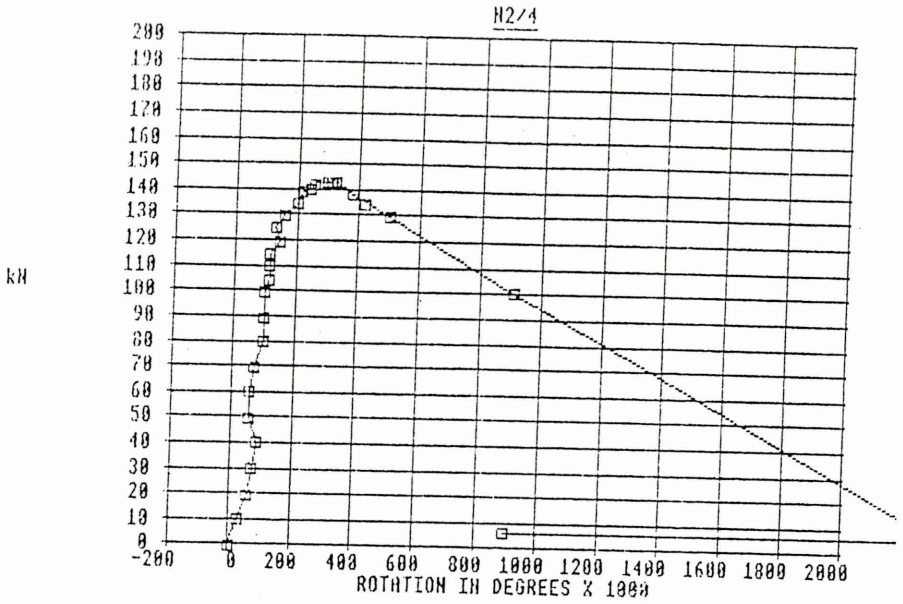

Force-rotation plot for N2/4

FIGURE B10

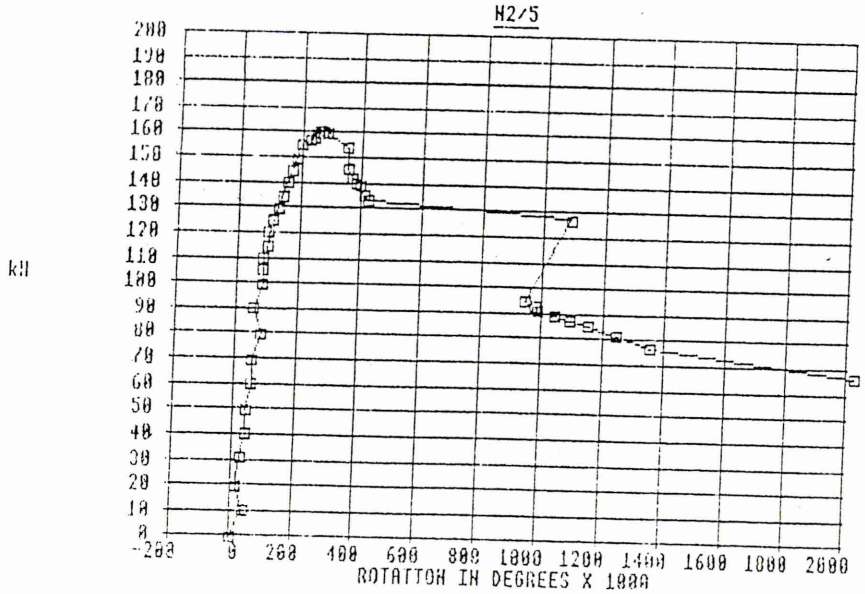

Force-rotation plot for N2/5

FIGURE B11

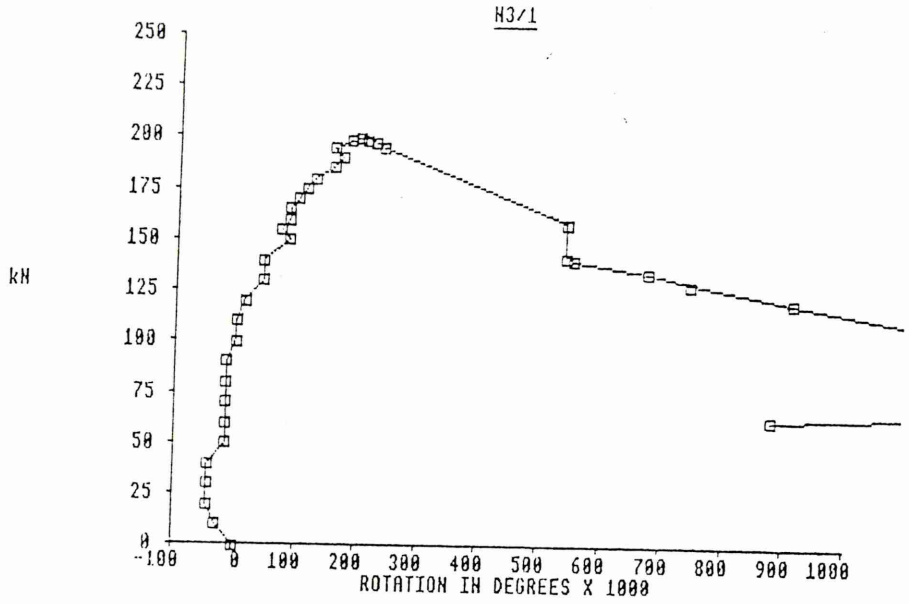

Force-rotation plot for N3/1

FIGURE B12

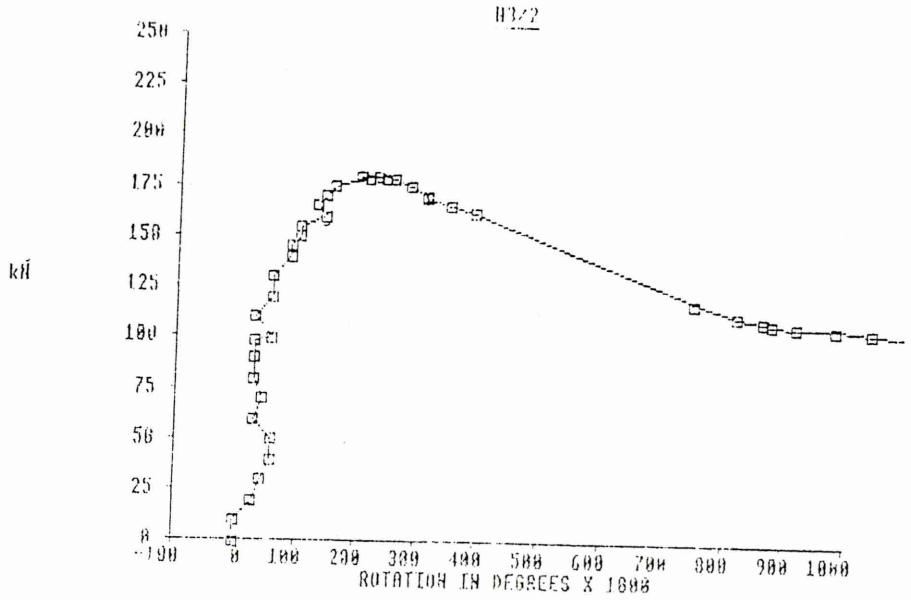

Force-rotation plot for N3/2

FIGURE B13

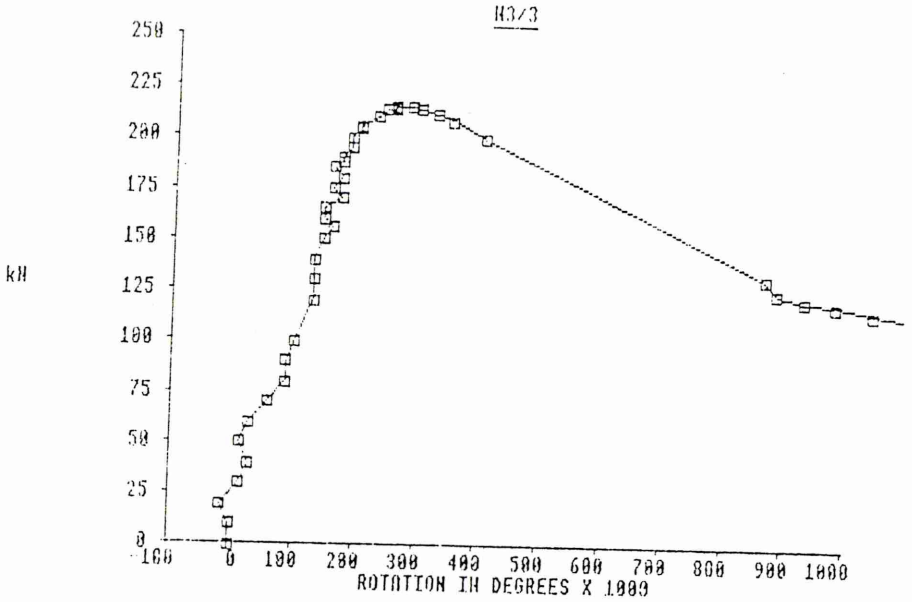

Force-rotation plot for N3/3

FIGURE B14

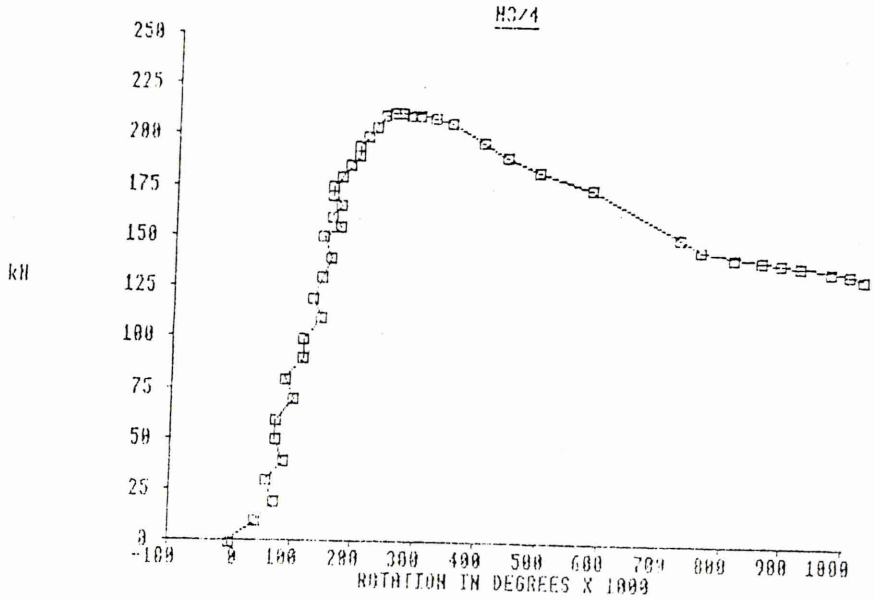

Force-rotation plot for N3/4

FIGURE B15

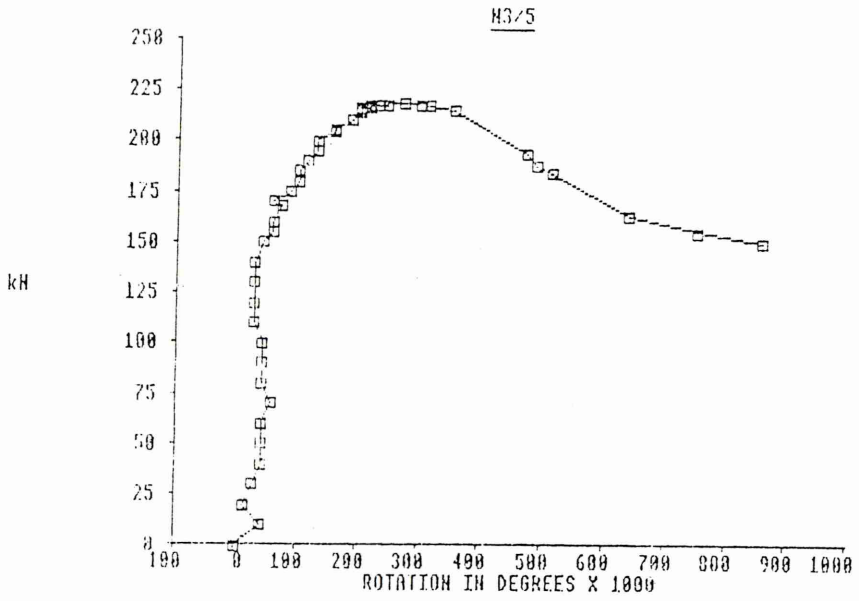

Force-rotation plot for N3/5

APPENDIX 'C'

Publications:

Taylor, Mallinder and Davies, Discussion on technical note 381, Proceedings of The Institution of Civil Engineers, Part 2, December 1984.

Taylor and Mallinder, On the limit state properties of masonry, Proceedings of The Institution of Civil Engineers, Part 2, March 1987.

Taylor and Mallinder, The brittle hinge in masonry arch mechanisms, The Structural Engineer, October 1993.

Taylor, Draper, Broadhurst and Mallinder, Static and kinematic limit states of masonry vaults, Centenary Year Bridge Conference, Cardiff, U.K., 26-30 September 1994.

Proc. Instn Civ. Engrs, Part 2, 1984, 77, Dec., 503–504

DISCUSSION ON TECHNICAL NOTE 381

On the stiffness properties of masonry

F. Sawko and M. A. Rouf

Dr N. W. Taylor, Sheffield City Polytechnic, Mr. P. A. Mallinder and Mr. B. L. Davies, South Yorkshire County Council

The Authors have presented an interesting study with regard to the analysis of masonry materials subject to axial loading in the presence of bending moment. The following points are, perhaps, worthy of consideration.

36. Do the discrete points denoted on the curves in Fig. 1 relate to actual experimental readings or to curve fitting empiricism? The peak stress values given do not concur with stress ordinate values.

37. It would be interesting to receive the Authors' comments regarding the nature of the stress–strain curves equivalent to those of Fig. 1 for natural stone types. This bears directly on the study of masonry arches constructed of stone, a common structural form.

38. The adoption of a parabolic stress–strain distribution negates the well established middle third rule. Surely this is to be noted. Indeed, employing an approach equivalent to that given in the Technical Note, it can be shown that the eceentricity e at which a compressive load will cause the onset of cracking is given by

$$e = f(T)/6$$

where T is the depth of the section and f is a parabolic factor of the form

$$f = 6 - 3(\varepsilon_l/\varepsilon_m)/6 - 2(\varepsilon_l/\varepsilon_m)$$

where ε_l and ε_m are as defined by the Authors. This expression has been programmed on a micro-computer and the corresponding graphical output is depicted in Fig. 12. Clearly, care must be taken in its interpretation at high strain ratios.

Professor Sawko and Mr Rouf

In reply to the specific points raised by the contributors, the Authors would like to make the following comments.

40. The empirical curves in Fig. 1 are based on mean curves obtained from twenty-six pillar tests carried out by Powel and Hodgkinson at the laboratories of the British Ceramic Research Association at Stoke-on-Trent. The individual curves are presented as Figs 3–6 in reference 1. The peak stress values used by the Authors are numerically approximate; more accurate values are 27·4, 19·2 and 9·3 for the three brickwork types considered.

41. In the opinion of the Authors, stress–strain curves for natural stone and also for concrete blockwork are certainly comparable to those in Fig. 1, and would, therefore, be applicable to stone masonry arches.

Paper published: *Proc. Instn Civ. Engrs*, Part 2, 1984, 77, Mar., 1–12.

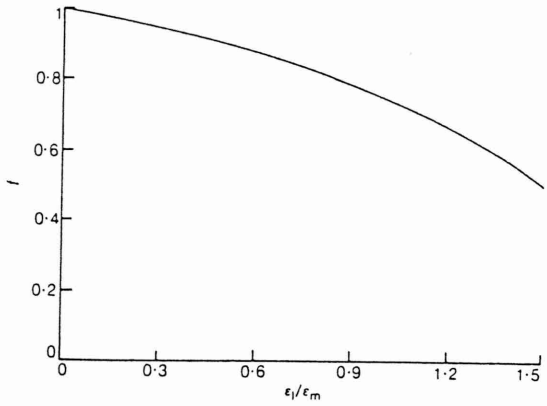

Fig. 12. Middle third factor

42. The adoption of the parabolic stress–strain law does indeed negate many well-known concepts derived on the basis of linear elasticity, such as the middle third rule and the parabolic shear stress distribution in masonry sections. The expressions for f quoted by the contributors are derived from the zero tension criterion. At the onset of cracking the strain distribution in a section is as shown in Fig. 13.

43. From simple geometry, centroidal strain $\varepsilon_c = \varepsilon_1/2$ and curvature $C = \varepsilon_1/T$. Substituting these expressions into equations (24) and (25), the corresponding expressions for axial force and bending moment at the onset of cracking are

$$P = \frac{E_0 A_0 \varepsilon_m}{2}\left(\frac{\varepsilon_1}{\varepsilon_m} - \frac{\varepsilon_1^2}{3\varepsilon_m}\right)$$

$$M = \frac{E_0 I_0 \varepsilon_m}{2T}\left(2\frac{\varepsilon_1}{\varepsilon_m} - \frac{\varepsilon_1^2}{\varepsilon_m^2}\right)$$

Thus the eccentricity at the onset of cracking is

$$e = \frac{M}{P} = \left[\frac{6 - 3(\varepsilon_1/\varepsilon_m)}{6 - 2(\varepsilon_1/\varepsilon_m)}\right]\left(\frac{T}{6}\right)$$

where the expression in square brackets is the contributors' value of f.

44. The Authors are grateful to the contributors for pointing out the practical significance of this result.

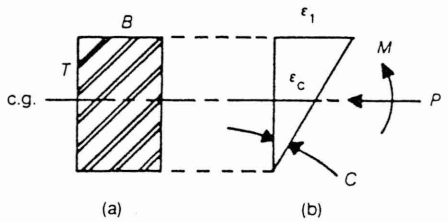

Fig. 13. Strain distribution at the onset of cracking: (a) section; (b) strain

Proc. Instn Civ. Engrs, Part 2, 1987, **83**, Mar., 33–41
PAPER 9014 STRUCTURAL ENGINEERING GROUP

On the limit state properties of masonry

N. TAYLOR, BTech, MSc, PhD*

P. A. MALLINDER, BEng, MICE†

An axial force/bending moment interaction diagram for the limit state of rectangular masonry sections is presented. The strain distribution across the section is taken to be linear, and the stress–strain relationship for the material is assumed to be parabolic. Tensile strength is taken to be insignificant in comparison with the compressive strength. The interaction curve generated represents the limit state configurations of axial thrust and bending moment; this curve is discussed in the context of masonry design to BS5628 Part 1.

Notation

b	breadth of section
d	depth of section
d'	effective depth of cracked section
e	eccentricity, $e\|_{zz} = 0$
m	non-dimensional bending moment parameter, $m = M_m/M_s$
M	bending moment
M_m	limit state bending moment
M_s	maximum limit state bending moment
M_t	tensile component of bending moment
n	non-dimensional axial compression parameter, $n = P_m/P_s$
P	axial compression
P_m	limit state axial compression
P_s	squash load
y	sectional spatial co-ordinate, $y\|_{zz} = 0$
y_m	distance from centroid to fibres suffering maximum stress
zz	flexural axis
ε	compressive strain
ε_m	compressive strain accompanying maximum compressive stress
ε_{om}	centroidal strain at limit state
ε_1	top fibre strain
ε_2	bottom fibre strain
ν_m	curvature at limit state
σ	compressive stress
σ_m	maximum compressive stress
σ_1	top fibre stress
σ_2	bottom fibre stress

Introduction

Developments in the use of masonry in new structural forms[1,2] and concern with the safe-load assessment of existing and often elderly structures such as the vous-

Written discussion closes 15 May 1987; for further details see p. ii.
* Senior Lecturer, Department of Civil Engineering, Sheffield City Polytechnic.
† Assistant Structural Engineer, Sheffield Metropolitan City Council.

soir arch[3,4] have led to considerable research on the structural behaviour of masonry. Recent studies have included investigation into the fundamental properties of structural masonry.[5–8] This has resulted in the adoption of a parabolic stress–strain relationship acting in conjunction with a linear strain distribution across a rectangular masonry section subject to a singly-eccentric compressive normal load.

2. Employing equations relating sectional strain response to any specified loading combination of axial thrust and bending moment so established,[8] the respective limit state combinations can be derived for both cracked and uncracked sectional topologies; tensile strength is considered to be negligible in the context of limit state configurations.

Non-linear theory

3. An idealized parabolic stress-strain locus is shown in Fig. 1. The relationship is of the form

$$\sigma/\sigma_m = 2\varepsilon/\varepsilon_m - (\varepsilon/\varepsilon_m)^2 \tag{1}$$

where σ and ε are the general stress and strain parameters, σ_m is the maximum stress, and ε_m is the corresponding strain.

4. A masonry section subject to a compressive normal force P acting at an eccentricity e is shown in Fig. 2(a); the corresponding uncracked strain distribution is shown in Fig. 2(b). Incorporation of equation (1) gives the stress distribution shown Fig. 2(c). The equivalent cracked section configurations are given in Fig. 3. Stresses σ_m are present at the limit state (see below). However, the general stress responses of Figs 2(c) and 3(c), noting equation (1), are given by

$$\frac{\sigma}{\sigma_m} = \left[\left(\frac{\varepsilon_1 + \varepsilon_2}{2\varepsilon_m}\right) + \frac{y}{d}\left(\frac{\varepsilon_1 - \varepsilon_2}{\varepsilon_m}\right)\right]\left\{2 - \left[\left(\frac{\varepsilon_1 + \varepsilon_2}{2\varepsilon_m}\right) + \frac{y}{d}\left(\frac{\varepsilon_1 - \varepsilon_2}{\varepsilon_m}\right)\right]\right\} \tag{2}$$

for the uncracked case, with $\varepsilon_2 \geqslant 0$ ($\varepsilon_2 \leqslant \varepsilon_1 \leqslant 1{\cdot}5\varepsilon_m$), and by

$$\frac{\sigma}{\sigma_m} = \frac{\varepsilon_1}{\varepsilon_m}\left(1 + \frac{y}{d'} - \frac{d}{2d'}\right)\left\{2 - \left[\frac{\varepsilon_1}{\varepsilon_m}\left(1 + \frac{y}{d'} - \frac{d}{2d'}\right)\right]\right\} \tag{3}$$

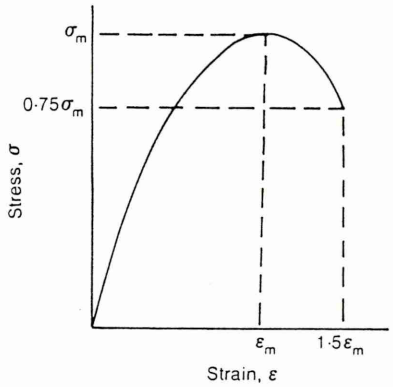

Fig. 1. Idealized stress–strain locus for masonry (compression)

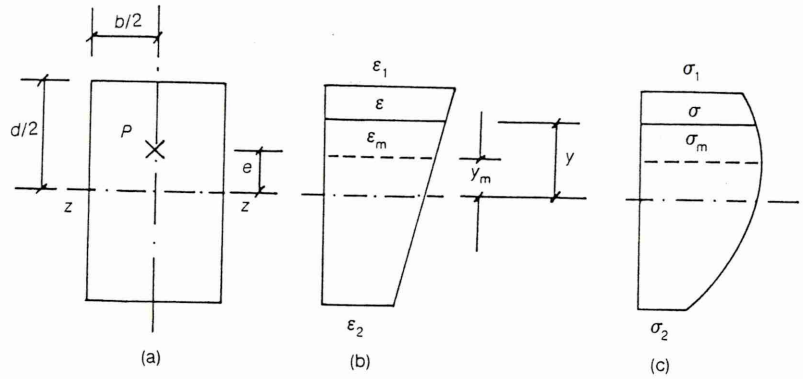

Fig. 2. General strain and stress distributions in an uncracked section: (a) section; (b) strain; (c) stress

for the cracked case, with $\varepsilon_1 \leqslant 1{\cdot}5\varepsilon_m$ ($0 \leqslant d' \leqslant d$). d denotes the full depth of the section, d' denotes the effective depth in the cracked case, y is the sectional spatial co-ordinate, and ε_1 and ε_2 represent the extreme fibre strains.

5. Interpreting the eccentric loading P as being statically equivalent to an axial thrust P and a bending moment M acting about the flexural (zz) axis (i.e. $M = Pe$), then for the uncracked configuration, integration across the section, incorporating equation (2), gives

$$P = \int_{-d/2}^{d/2} \sigma b \, \mathrm{d}y = \sigma_m bd\left(\frac{(\varepsilon_1 + \varepsilon_2)(3\varepsilon_m - \varepsilon_1 - \varepsilon_2) + \varepsilon_1\varepsilon_2}{3\varepsilon_m^2}\right) \tag{4}$$

(where b is the breadth of the section), and

$$M = \int_{-d/2}^{d/2} \sigma b y \, \mathrm{d}y = \sigma_m bd^2\left(\frac{(\varepsilon_2 - \varepsilon_1)(\varepsilon_1 + \varepsilon_2 - 2\varepsilon_m)/2}{6\varepsilon_m^2}\right) \tag{5}$$

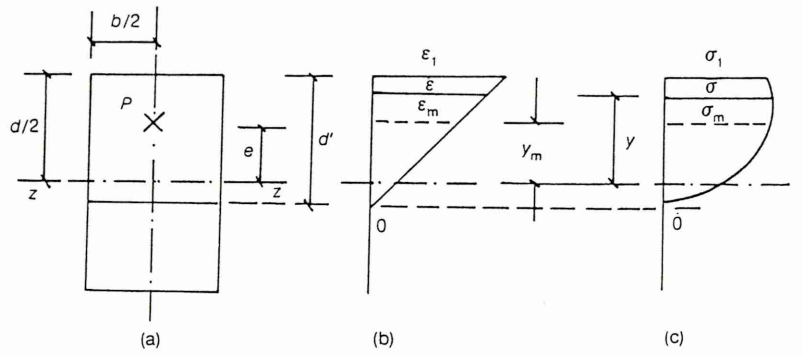

Fig. 3. General strain and stress distributions in a cracked section: (a) section; (b) strain; (c) stress

Similarly, for the cracked configuration, noting equation (3)

$$P = \int_{d/2-d'}^{d/2} \sigma b \, \mathrm{d}y = \sigma_m b d' \left(\frac{\varepsilon_1 \varepsilon_m - \varepsilon_1^2/3}{\varepsilon_m^2} \right) \tag{6}$$

and

$$M = \int_{d/2-d'}^{d/2} \sigma b y \, \mathrm{d}y = \sigma_m b d' \left(\frac{\varepsilon_1 (6\varepsilon_m d - 2\varepsilon_1 d + \varepsilon_1 d' - 4\varepsilon_m d')}{12\varepsilon_m^2} \right) \tag{7}$$

Sagging bending moments ($0 \leqslant e \leqslant d/2$) will be considered first.

Limit state configuration: uncracked section

6. The limit state is determined by obtaining the maximum force P_m that the section can withstand at any given value of bending moment M. This is achieved by employing $\partial P/\partial \varepsilon_1 = 0$ in conjunction with prescribed values of $M(\varepsilon_2)$ with respect to equations (4) and (5). Differentiating equation (4) accordingly generates the limiting condition

$$\varepsilon_1 = (3\varepsilon_m - \varepsilon_2)/2 \tag{8}$$

recalling $\varepsilon_1 \leqslant 1{\cdot}5\varepsilon_m$, $\varepsilon_2 \geqslant 0$. The appropriate expressions for P_m and the corresponding limit state bending moment $M \equiv M_m$ are obtained by back-substituting equation (8) into equations (4) and (5):

$$P_m = \frac{\sigma_m b d}{4} [3 + 2(\varepsilon_2/\varepsilon_m) - (\varepsilon_2/\varepsilon_m)^2] \tag{9}$$

and

$$M_m = \frac{\sigma_m b d^2}{16} [1 - 2(\varepsilon_2/\varepsilon_m) + (\varepsilon_2/\varepsilon_m)^2] \tag{10}$$

Equations (9) and (10) thus give the requisite limit state interaction locus, subject to the delineation of the range of validity of the uncracked case studies.

7. Intuition demands that the squash load P_s represents an upper bound on P_m, with

$$P_m \Big|_{M_m = 0} \equiv P_s = \sigma_m b d \tag{11}$$

wherein, noting Fig. 2(c), a uniform axial stress distribution $\sigma_1 = \sigma_2 = \sigma_m$ acts across the entire section. Equation (11) can also be obtained using $\partial P_m/\partial \varepsilon_2 = 0$ with respect to equation (9), such that

$$\varepsilon_2 \Big|_{P_m = P_s} = \varepsilon_m \tag{12}$$

which gives equation (11) on back-substitution into equations (9) and (10). The lower bound value for P_m with respect to the uncracked section studies is obtained by setting $\varepsilon_2 = 0$. At this state, equation (8) gives $\varepsilon_1 = 3\varepsilon_m/2$, which accords with the limiting permissible extreme fibre strain. Furthermore, substitution into equa-

tion (9) identifies the lower bound of P_m to be $P_m = 0{\cdot}75\sigma_m bd$, at which state equation (10) gives $M_m = \sigma_m bd^2/16$. Introducing the non-dimensional parameter $n = P_m/P_s$, then equations (9) and (10) afford the limit state locus for the section in the range $0{\cdot}75 \leqslant n \leqslant 1$.

8. Finally, it is instructive to determine the position, y_m, at which the maximum stress, σ_m, occurs under limit state conditions. This can be achieved employing the geometry of the corresponding strain distribution, with ε_1 in Fig. 2(b) being defined by equation (8), such that

$$y\Big|_{\sigma_m} = y\Big|_{\varepsilon_m} = y_m = d/6 \tag{13}$$

for $0{\cdot}75 \leqslant n < 1$. That is, at the limit state the most highly stressed fibres occur at $d/6$ above the centroidal axis, while the most highly strained fibres occur at the top of the section (note Fig. 2(c)). This separation of maximum effects relates directly to the presence of the falling branch in the stress–strain curve given in Fig. 1. For completeness, the centroidal strain ε_{om} and the sectional curvature ν_m corresponding to the uncracked limit state configuration can also be obtained from Fig. 2(b), ε_1 being as defined in equation (8)

$$\varepsilon_{om} = (\varepsilon_1 + \varepsilon_2)/2 = (3\varepsilon_m + \varepsilon_2)/4 \tag{14}$$

$$\nu_m = (\varepsilon_1 - \varepsilon_2)/d = 3(\varepsilon_m - \varepsilon_2)/(2d) \tag{15}$$

Limit state configuration: cracked section

9. The approach used to determine the limit state locus for $0 \leqslant n \leqslant 0{\cdot}75$ is similar to that employed in the previous section. Employing the limiting criterion $\partial P/\partial\varepsilon_1 = 0$ in conjunction with prescribed values of $M(d')$ with respect to equations (6) and (7) gives the explicit limiting condition $\varepsilon_1 = 1{\cdot}5\,\varepsilon_m$, which when back-substituted into equations (6) and (7) gives

$$P_m = 3\sigma_m bd'/4 \tag{16}$$

and

$$M_m = \sigma_m bd'(6d - 5d')/16 \tag{17}$$

respectively. These expressions define the limit state interaction locus for $0 \leqslant n \leqslant 0{\cdot}75$; they interface with equations (9) and (10) at $n = 0{\cdot}75$ ($d' = d$), with a lower bound at $n = 0$ ($d' = 0$), whereupon equations (16) and (17) afford $n = P_m = d' = M_m = 0$.

10. Intuition suggests that a turning point is present in the interaction locus $0 \leqslant n \leqslant 0{\cdot}75$. Employing

$$\frac{\partial M_m}{\partial P_m} = \frac{\partial M_m}{\partial d'} \cdot \frac{\partial d'}{\partial P_m} = 0 \tag{18}$$

then, from equations (16) and (17),

$$d'\Big|_{\partial M_m/\partial P_m = 0} = 3d/5 \tag{19}$$

with a maximum turning point at $n = 0{\cdot}45$. The absolute maximum bending moment the section can resist, M_s, is therefore, from equation (17)

$$M_m\Big|_{n=0{\cdot}45} \equiv M_s = 9\sigma_m bd^2/80 \tag{20}$$

11. Employing the geometry of Fig. 3(b) with $\varepsilon_1 = 1{\cdot}5\ \varepsilon_m$ gives the location of the fibres undergoing maximum stress, with

$$y\Big|_{\sigma_m} = y\Big|_{\varepsilon_m} = y_m = (3d - 2d')/6 \tag{21}$$

which interfaces with equation (13) at $n = 0{\cdot}75$. As the tension crack develops, the location of these fibres moves towards the top of the section (Fig. 3(c)). Again employing Fig. 3(b) with $\varepsilon_1 = 1{\cdot}5\ \varepsilon_m$, the centroidal strain ε_{om} and the sectional curvature ν_m corresponding to the cracked limit state configuration take the form

$$\varepsilon_{om} = 0{\cdot}75\varepsilon_m(2d' - d)/d' \qquad (d/2 \leqslant d' \leqslant d) \tag{22}$$

$$\nu_m = 3\varepsilon_m/(2d') \tag{23}$$

both interfacing with equations (14) and (15) at $n = 0{\cdot}75$.

Axial force/bending moment interaction diagram

12. Noting the identities of equations (11) and (20), and introducing the non-dimensional parameter $m = M_m/M_s$, then the interaction diagram can be conveniently presented in n–m space. For this purpose, equations (9), (10), (16) and (17) are written in the form

$$n = [3 + 2(\varepsilon_2/\varepsilon_m) - (\varepsilon_2/\varepsilon_m)^2]/4 \tag{24}$$

$$m = 5[1 - 2(\varepsilon_2/\varepsilon_m) + (\varepsilon_2/\varepsilon_m)^2]/9 \tag{25}$$

$$n = 0{\cdot}75(d'/d) \tag{26}$$

and

$$m = 5[d'(6d - 5d')/d^2]/9 \tag{27}$$

respectively. The interaction diagram (Fig. 4) can thus be constructed for $0 \leqslant e \leqslant d/2$ using equations (24) and (25) for $0{\cdot}75 \leqslant n \leqslant 1$ and equations (26) and (27) for $0 \leqslant n \leqslant 0{\cdot}75$. These equations are in parametric form, and are most conveniently evaluated in increments of ε_2 and d' respectively. For $-d/2 \leqslant e \leqslant 0$ (hogging moment) the interaction diagram is simply a mirror image of Fig. 4 about the abscissa.

13. As the axial compression reduces from P_s to $0{\cdot}75\ P_s$, the falling branch effect is immediately realized as maximum strains in excess of ε_m (see Fig. 1) are experienced ($\varepsilon_m < \varepsilon_1 \leqslant 3\varepsilon_m/2$). The maximum stress occurs at the 'middle third'. These two effects are intimately connected with a degradation in the minimum compressive strain ε_2. Compressive stress response is thereby critical for $0{\cdot}75 \leqslant n \leqslant 1$. Details of the interface state (0·75, 0·55) are given in Fig. 5. All parameters interface smoothly. Maximum compressive strain now becomes crucial, with $\varepsilon_1 = 3\varepsilon_m/2$ as n decreases. Flexural resistance increases up to a maximum at (0·45, 1), whereupon crack propagation becomes crucial, resulting in a degradation of sectional strength. Fig. 6 shows a detail of the maximum flexural

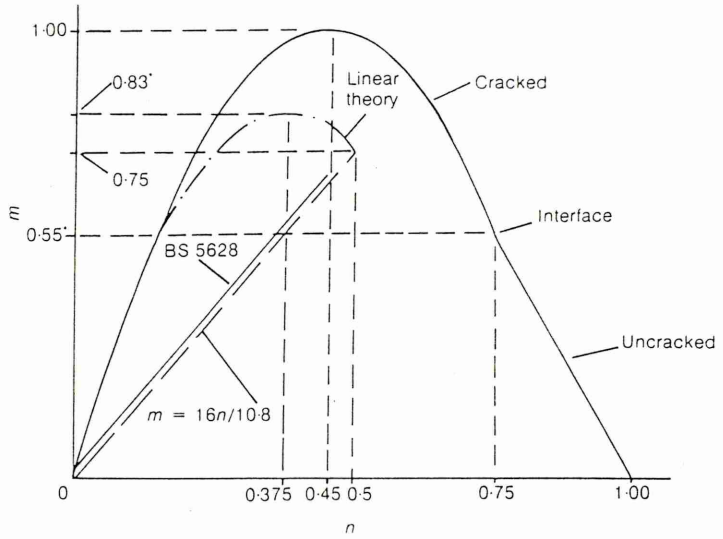

Fig. 4. Limit state masonry moment–thrust interaction diagram

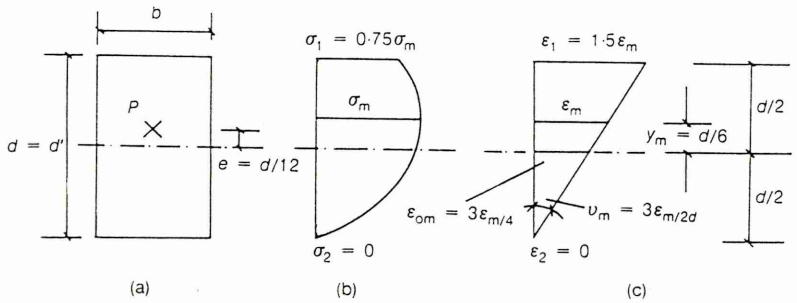

Fig. 5. Stress–strain states at n = 0·75

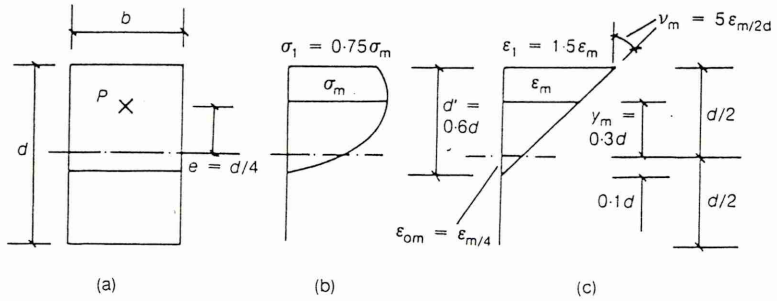

Fig. 6 Stress–strain states at n = 0·45

response state; the tension crack extends to 40% of the section depth at this state. The movement of the location of the fibres undergoing maximum compressive stress σ_m as n decreases from 0·75 can be seen by comparing Figs 5 and 6. The extreme fibre compressive stress remains unaltered throughout $0 < n \leqslant 0{\cdot}75$ at $\sigma_t = 0{\cdot}75\,\sigma_m$. Curvature ν_m increases throughout as n decreases from unity, while crack depth $d - d'$ increases as n decreases from 0·75. Centroidal strain ε_{om} decreases from ε_m at $n = 1$ to zero at $n = 0{\cdot}375$; this lower limit is readily determined from equations (16) and (22) with cracking reaching up to the centroidal axis. The (0, 0) state is effectively trivial; it is predictable, since zero tensile strength has been assumed.

Design considerations

14. The relationship between axial compression and moment of resistance with regard to present design practice[9] includes the section modulus term $bd^2/6$. This suggests a linear interpretation of the appropriate stress–strain characteristics, and the respective n, m limit state moment–thrust interaction locus corresponding to the cracked configuration is included in Fig. 4. This locus is derived from the familiar elastic basis, with stress–strain characteristics being linear up to the limiting case of σ_m, ε_m (Fig. 1). While the expressions for squash load are the same for both the elastic theory and the non-linear theory discussed here, it is important to note that the maximum moment in the latter exceeds that in the former by 20% (Fig. 4); i.e. $m = 1$ corresponds to $M_m = M_s = 9\sigma_m bd^2/80$.

15. For design practice, the expression for the respective moment of resistance,[9] M_m, can be written in the form

$$M_m = M_t + Pd/6 \tag{28}$$

where M_t is the permitted tensile resistance (and is not a function of P). Neglecting this tensile component, then the relationship $M_m = Pd/6$ conforms to the unique linear theory limit state $n = 0{\cdot}5$, $m = 0{\cdot}75$, corresponding to the respective cracked/uncracked interface state.

16. Interpreting equation (28) as a design limit state locus, initially for $0 \leqslant P \leqslant P_s/2$ and neglecting the tensile component, generates the non-dimensionalized expression $m = 16n/10{\cdot}8$, $0 \leqslant n \leqslant 0{\cdot}5$, which is also depicted in Fig. 4. Including the variable tensile component and noting code constraints[9] on n,

$$m = \left(\frac{96M_t}{P_s d} + 16n\right) \Big/ 10{\cdot}8 \qquad (0 \leqslant n \leqslant 0{\cdot}44) \tag{29}$$

is the n–m equivalent of equation (28); this is sketched in Fig. 4 with the tensile term being, typically, responsible for a few percent of the total resistance moment at the prescribed upper limit value of n. This upper limit has an 'absolute' maximum value of 0·44 ($= [0{\cdot}9 \times 2{\cdot}5]^{-1}$) as denoted in equation (29). The relationship between this design locus and that corresponding to the non-linear theory presented previously can be seen in Fig. 4. It is suggested that some relaxation of present design criteria, leading to more economic design practice, could be considered; the availability of constitutive loci of the form typified by Fig. 1 would be an essential prerequisite, however.

Conclusions

17. An axial force/bending moment interaction diagram for masonry employing a parabolic stress-strain relationship has been produced, and the effect of the

falling branch demonstrated. The diagram provides appropriate data with respect to the limit state characterisitics of masonry. The area enclosed by the limit state locus and the abscissa defines 'safe' combinations of axial force and bending moment with regard to a rectangular masonry section. The study affords insight into masonry mechanics and invites further consideration of present design practice.

Acknowledgements

18. The Authors thank J. Ducker, J. Ducker and Associates, Consulting Engineers, Rotherham, and B. L. Davies, formerly Chief Engineer, Bridges and Structures, South Yorkshire County Council, for their advice and assistance.

References

1. CURTIN W. G. Brick diaphragm walls in tall single storey buildings. *Design guide No. 3* (revised edition), The Brick Development Association, 1979.
2. CURTIN W. G. *et al.* Design of brick fin walls in tall single storey buildings. *Design Guide No. 8*, The Brick Development Association, 1980.
3. HEYMAN J. *The masonry arch.* Ellis Horwood Ltd, Chichester, 1982.
4. WALKLATE R. P. and MANN J. W. A method for determining the permissible loading of brick and masonry arches. *Proc. Instn Civ. Engrs*, Part 2, 1983, **75**, Dec., 585–597.
5. TOWLER K. D. S. *The structural behaviour of brickwork arches.* PhD thesis, University of Liverpool, 1981.
6. POWELL B. and HODGKINSON H. R. *Determination of stress-strain relationship of brickwork.* TN249, British Ceramic Research Association, Stoke-on-Trent, 1976.
7. TOWLER K. and SAWKO F. Limit state behaviour of brickwork arches. *Proc. 6th Int. Conf. on Brick Masonry, Rome, 1982.* ANDIL, Rome, 412–421.
8. SAWKO F. and ROUF M. A. On the stiffness properties of masonry. *Proc. Instn Civ. Engrs*, Part 2, 1984, **77**, Mar., 1–12.
9. BRITISH STANDARDS INSTITUTION. *Code of practice for structural use of masonry.* BSI, London, 1978, BS 5628, Part 1.

Paper

The brittle hinge in masonry arch mechanisms

N. Taylor, BTech, MSc, PhD
School of Construction, Sheffield Hallam University

P. Mallinder, BEng, MPhil, CEng, MICE
DBS Bridges, Sheffield City council

Synopsis

Hinge formation in the presence of local crushing is studied in the context of limit state masonry arch mechanisms. Empirical constitutive modelling is developed to produce a range of corresponding axial force/bending moment interaction diagrams appertaining to rectangular masonry sections subject to singly-eccentric compressive normal loading, and these archetypal design charts are assessed against experimental data. It is considered that masonry hinges are of distinctly brittle form, rotation becoming significant only as hinge resistance decays. Preliminary arch bridge case-studies serve to encourage confidence in the brittle hinge model, and serviceability factors are also considered.

Notation

b is the breadth of section
d is the depth of section
d' is the effective depth of cracked section
e is the eccentricity
k is a constant
m is the normalised bending moment parameter
m_i is the cracked/uncracked interface limit state coordinate
m_{nc} is the prevention of cracking normalised moment
n is the normalised axial compression parameter
n_i is the cracked/uncracked interface limit state coordinate
n_{nc} is the prevention of cracking normalised thrust
y is the sectional spatial coordinate
y_m is the sectional coordinate to σ_m
z-z is the flexural axis

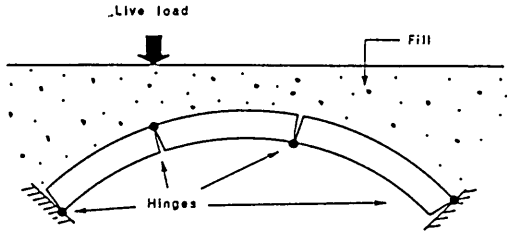

(a) *Topology*

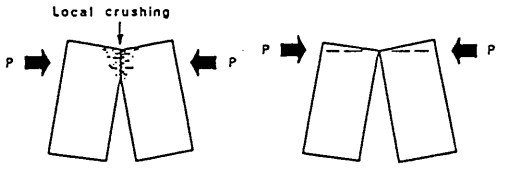

(b) *Proposed hinge model* (c) *Existing hinge model*

Fig 1. Four hinge masonry arch collapse mechanism

E_i is the incremental modulus
M is the bending moment
M_c is the middle-half rule bending moment at $P = P_c$
P is the axial compression
P_c is the squash load
γ is the fracture strain coefficient
ε is the compressive strain
ε_m is the compressive strain accompanying maximum compressive stress
ε_1 is the maximum compressive fibre strain
ε_2 is the minimum compressive fibre strain
λ is the static limit state hinge strain coefficient
σ is the compressive stress
σ_m is the maximum compressive stress
σ_1 is the stress accompanying ε_1
σ_2 is the stress accompanying ε_2

Introduction

Constituting a considerable proportion of the United Kingdom's bridge stock[1], aging masonry arch structures continue to attract considerable engineering attention[2-6], particularly with regard to scientifically-based safe-load assessment[7,8]. The formation of arch barrel mechanistic hinges, as typified in Fig 1(a), is central to any limit state procedure[2,9-11], and engineers often base bridge strength judgments on the mechanistic capacity of the arch barrel alone[2], the fill serving primarily as an arch-compressing and a live load dispersal medium. The present study attempts to set out the nature of hinge formation in voussoir arches in the presence of local compressive crushing as indicated in Fig 1(b), with P denoting arch thrust; this requires *a priori* establishment of the respective constitutive properties. Previous mechanistic modelling assumes validity of the infinite compressive strength rule[9] which implies the somewhat unappealing and non-conservative hinge mechanism illustrated in Fig 1(c)[2,9]. Alternative finite element studies have yet to prove attractive in practice because of their excessive demands on input data definition and computer resource requirements[2,12].

Herein, mechanistic response to singly-eccentric compressive normal loading is interpreted in terms of limit state axial thrust/bending moment relationships[10,13-16] which employ an empirically-based non-linear constitutive modelling applicable to a wide range of masonry materials, both natural and synthetic.

An experimental investigation identifies the appropriate physics, and theoretical/experimental correlation is provided. Experimental moment-thrust-rotation characteristics are also discussed, and masonry arch analysis developments *per se* are suggested accordingly.

Constitutive modelling

Fig 2 illustrates a complete stress-strain locus for natural masonry obtained from a circular section core sample subjected to uniaxial compression in a modern, stiff, servohydraulic testing machine[17]. The rock was acquired from a damaged voussoir belonging to a recently saddled masonry arch bridge on the A57 Sheffield to Manchester trunk road. The bridge dates from 1819, the strengthening works being undertaken by Sheffield City Council engineers. The locus in Fig 2 is typical of structural masonry being non-linear throughout and including a definitive 'falling branch'[16, 17]. Importantly, the flatbed-produced experimental locus is essentially indistinguishable from a theoretical locus of the form

$$\sigma/\sigma_m = [k/(k-1)]\,[\varepsilon/\varepsilon_m - (\varepsilon/\varepsilon_m)k/k] \qquad \ldots.(1)$$

where σ and ε are the general stress and strain parameters, σ_m denotes the maximum stress with ε_m the corresponding strain, and k is a constant; here, $\sigma_m = 33\text{N/mm}^2$, $\varepsilon_m = 0.00378$, and $k = 7$.

Experimentally, fracture does not occur until $\varepsilon = \gamma\varepsilon_m$, while $\varepsilon = \lambda\varepsilon_m$ relates

TABLE 1 – Calcium silicate test data

Test no.	Cores: Peak load (kN)	Cores: Peak stress σ_m (N/mm²)	Cores: Strain at peak stress ε_m	Bricks: Peak load (kN)	Bricks: Peak stress σ_m (N/mm²)
1	68.00	34.63	0.00480	625	28.4
2	68.80	35.04	0.00406	615	27.9
3	69.40	35.34	0.00408	622	28.2
4	67.60	34.43	0.00400	606	27.5
5	72.27	36.81	0.00344	617	28.0
6	69.69	35.49	0.00412	575	26.1
7	70.41	35.86	0.00400	616	27.9
8	69.28	35.28	0.00404	606	27.5
9	69.28	35.28	0.00344	613	27.8
10	70.40	35.85	0.00396	613	27.8
Mean*	69.51	35.40*	0.00399	611	27.7*
Std dev.	1.325	1.325	0.00379	13.9	13.9
Coef. var. %	±1.91	±1.91	±9.49	±2.28	±2.28

*NOTE. Average peak stress = 31.6 N/mm²

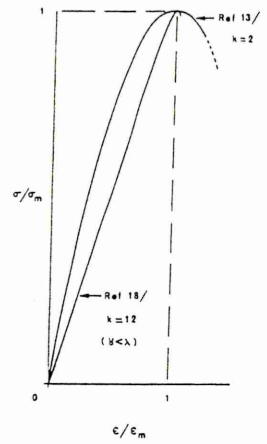

Fig 3. Interpretation of brick pier constitutive loci

to the maximum strain occurring at the static limit state according to the singly-eccentric studies discussed in the following; in Fig 2, $\gamma = 1.47$ and $\lambda = 1.16$. Further experimental masonry constitutive data are available elsewhere, relating for example, to brick *pier* testing, and proposed appropriate versions of eqn. (1) are illustrated in Fig 3[13, 18].

A recently completed experimental programme serves to develop this theme, and the results of 10 uniaxial compression tests on 50mm diameter, 2.5:1 aspect ratio, circular section calcium silicate class 4 brick cores are summarised in Fig 4 and Table 1. As indicated in Fig 4, nine of the 10 constitutive loci are indistinguishable from eqn. (1) with $k = 3$ for $\varepsilon/\varepsilon_m \leq \lambda$ ($\lambda > 1$), while Table 1 also affords corresponding full brick compression test data obtained in accordance with BS 187:1978. It is considered that Fig 4 provides excellent data characteristics for $\varepsilon/\varepsilon_m \leq \lambda = 1.227$ with experimental fracture not being completed prior to $\gamma = 2.5$. The peak load data of Table 1 are also considered to show distinct consistency, due allowance being required when comparing core and full brick peak stress values.

The foregoing studies ($k = 2$, 3, 7 and 12) suggest eqn. (1) to be capable of modelling a variety of structural masonry materials, and the key constitutive factors are accordingly summarised in Fig 5. Briefly, $k = 0$ corresponds to the infinite stiffness/strength rule underpinning Heyman's established 'plastic' hinge model[9,11], while $k = \infty$ corresponds to the equally familiar linear constitutive modelling of masonry associated with the middle-third rule[9, 18]. It is proposed that for $0 < k < \infty$ there is an array of loci of the form given by eqn. (1) suited to a variety of structural masonry materials.

Rectangular section under singly-eccentric compression

An uncracked rectangular masonry section of breadth b and depth d is shown subject to a compressive normal force P acting at an eccentricity e in Fig 6(a); the corresponding linear strain distribution is illustrated in Fig 6(b) with ε_1 and ε_2 denoting maximum and minimum compressive strains, respectively. Incorporation of eqn. (1) gives the stress distribution shown in Fig 6(c). (Peak stress σ_m and corresponding strain ε_m are present under static limit state conditions – see *post.*) The general stress response to Fig 6(c) can be written in the form

$$\sigma/\sigma_m = f(\varepsilon_1, \varepsilon_2, \varepsilon_m, y, d, k) \qquad \ldots.(2)$$

with $0 \leq \varepsilon_2 \leq \varepsilon_1 \leq \gamma\varepsilon_m$ and spatial co-ordinate $-d/2 \leq y \leq d/2$. Explicit presentation of all key equations is given in Appendix A. Interpreting the eccentric load P as being statically equivalent to an axial thrust P, together with a bending moment M acting about the z-z ($y = 0$) axis – i.e. $M = Pe$, $-d/2 \leq e \leq d/2$ – and integrating through the section, incorporating eqn. (2), affords

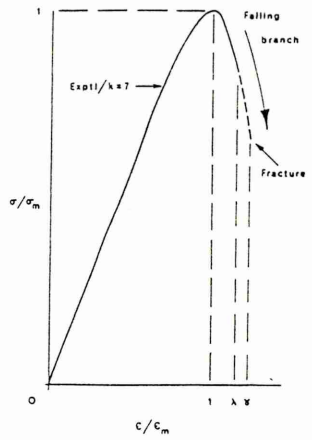

Fig 2. Typical natural stone stress-strain locus

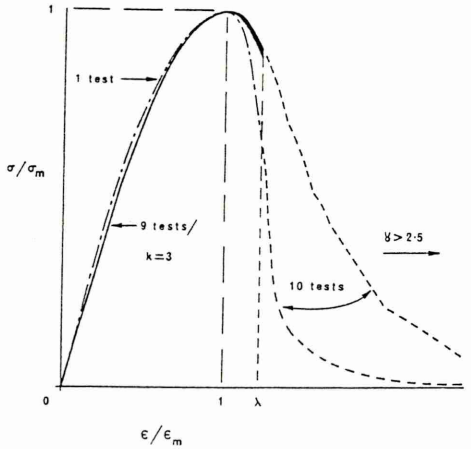

Fig 4. Calcium silicate constitutive core loci

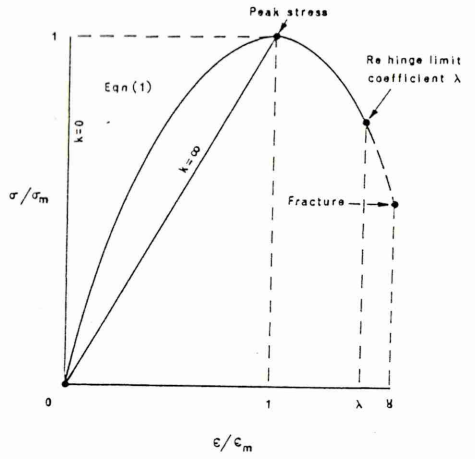

Fig 5. Idealised constitutive locus

$$P = \int_{-d/2}^{d/2} \sigma b\, dy = f_1(\varepsilon_1, \varepsilon_2, \varepsilon_m, \sigma_m, b, d, k) \quad \ldots.(3)$$

and

$$M = \int_{-d/2}^{d/2} \sigma b y\, dy = f_2(\varepsilon_1, \varepsilon_2, \varepsilon_m, \sigma_m, b, d, k) \quad \ldots.(4)$$

Fig 7 illustrates the corresponding strain and stress distributions with respect to the cracked section configuration; following the above, the general stress response is now given by

$$\sigma/\sigma_m = f(\varepsilon_1, \varepsilon_m, y, d', k) \quad \ldots.(5)$$

with d' denoting effective section depth such that $-d'/d \le (d'-d)/d \le 0 \le \varepsilon_1 \le \gamma\varepsilon_m$. The cracked section axial compression and bending moment expressions are thereby obtained with

$$P = \int_{-d/2-d'}^{d/2} \sigma b\, dy = f_1(\varepsilon_1, \varepsilon_m, \sigma_m, b, d', d, k) \quad \ldots.(6)$$

and

$$M = \int_{-d/2-d'}^{d/2} \sigma b y\, dy = f_2(\varepsilon_1, \varepsilon_m, \sigma_m, b, d', d, k) \quad \ldots.(7)$$

respectively.

Eqns. (3) and (4) together with (6) and (7) therefore describe the general response of rectangular masonry sections, in both uncracked and cracked configurations, respectively, to singly-eccentric compressive normal loading as typified by masonry arch bridge barrels or vaults. Their specific static limit state characteristics are now to be determined.

Static limit state considerations: axial force/bending moment interaction diagram

Static limit states are determined by obtaining the maximum bending moment that the section can withstand at any given value of axial compression. Unfortunately, the respective pairs of response equations, explicitly presented in Appendix A, are quite unamenable to formal computational manipulation, and recourse to numerical techniques is necessary. Some simplification is available from normalising eqns. (3) and (6) employing the squash load $P_s = \sigma_m bd$ and eqns. (4) and (7) employing $M_s = P_s d/4$, a notional middle-half rule moment with $P = P_s$. An overview of the maximisation procedure adopted is given in the simplified flowchart of Fig 8. Recalling Figs 2–7, the key observation is that static limit states occur for $\varepsilon_1 = \lambda\varepsilon_m$ and $\varepsilon_1 = \lambda\varepsilon_m - (\lambda-1)\varepsilon_2$ for the cracked and uncracked configurations, respectively, with $\lambda > 1$ being a constant for any specified k. Numerical treatment of the uncracked section eqns. (3) and (4) generally

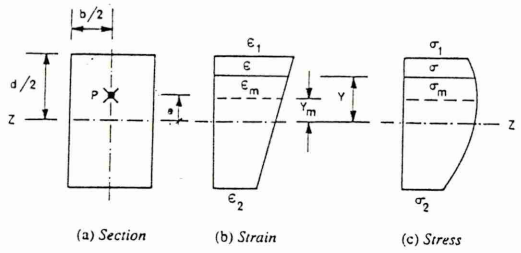

Fig 6. General strain and stress distributions in an uncracked section

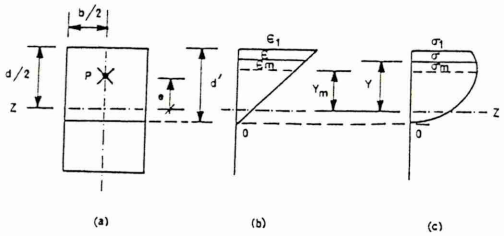

Fig 7. General strain and stress distribution in a cracked section
(a) *Section* (b) *Strain* (c) *Stress*

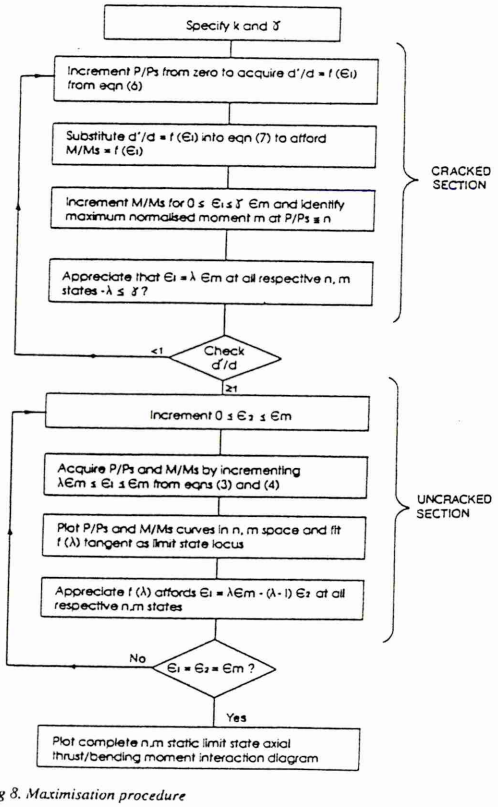

Fig 8. Maximisation procedure

(i.e. $k > 2$[10]) involves multiple roots that are difficult to treat and requires appreciation that $o \le \varepsilon_2 \le \varepsilon_m$ and $\lambda\varepsilon_m \le \varepsilon_1 \le \varepsilon_m$ *a priori*, the static limit state cracked/uncracked section interface occurring when $d' = d$ and $\varepsilon_2 = 0$ at $\varepsilon_1 = \lambda\varepsilon_m$ regarding eqns (3), (4), (6) and (7).

Summarising, for $0 \le k \le \infty$ static limit states for the cracked configuration coincide with the maximum compressive strain obeying

$$\varepsilon_1 = \lambda\varepsilon_m \qquad \text{....(8)}$$

while those for the uncracked configuration coincide with

$$\varepsilon_1 = \lambda\varepsilon_m - (\lambda - 1)\,\varepsilon_2 \qquad \text{....(9)}$$

with λ a constant coefficient for any specified k. Eqns. (8) and (9) represent *simulated* algebraic expressions deduced from a considerable numerical database in k. Typical values for k and λ are given in Table 2. Static limit state values for structural masonry are therefore available from eqns. (6) and (7) and eqns. (3) and (4), subject to the conditions given in eqns. (8) and (9), with, in normalised terms,

$$n = P/P_s\Big|_{\varepsilon_1 = \lambda\varepsilon_m} \quad \text{and } m = M/M_s\Big|_{\varepsilon_1 = \lambda\varepsilon_m} \qquad \text{....(10)}$$

for the cracked configuration $0 \le n \le n_i$ as $0 \le d' \le d$ and

$$n = P/P_s\Big|_{\varepsilon_1 = \lambda\varepsilon_m - (\lambda-1)\varepsilon_2} \quad \text{and } m = M/M_s\Big|_{\varepsilon_1 = \lambda\varepsilon_m - (\lambda-1)\varepsilon_2} \qquad \text{....(11)}$$

for the uncracked configuration $n_i \le n \le 1$ as $0 \le \varepsilon_2 \le \varepsilon_m$.

Eqns. (10) and (11) are represented most conveniently by means of a static limit state axial thrust/bending moment interaction diagram, and Fig 9 accordingly illustrates the static limit state interaction loci for $k = 2$, 3, 7 and 12 with the $k = 2$ locus representing the most enveloping or most resistant case concerned. Safe combinations of axial compression and bending moment (sagging, $0 \le e \le d/2$) lie between the respective k locus and the abscissa. For hogging moments, $-d/2 \le e \le 0$, the interaction loci adopt a mirror image about the abscissa.

Pertinent features to note are that the sectional resistance is enhanced as constant k decreases, to recall Figs 2 to 5, to recall that all loci maxima can be shown to lie on the middle-half rule, to note Table 3, which also includes cracked/uncracked configuration interface state data (n_i, m_i), and to note that $\lambda > 1$, as shown in Table 2, such that the falling branch (Fig 5) is crucial to limit state definition, and that each point on any k interaction locus represents a brittle hinge as illustrated in Fig 1 (a) and (b). For example, with $k = 2$ and $n = m = 0.464$, the effective depth $d' = 0.638d$ and not zero as required by Fig 1(c). Further, and also recalling Figs 6 and 7, it is to be noted that maximum stress is neither located at the extreme fibres nor at the loading eccentricity $e = M/P = 0.25d(m/n)$. For the foregoing data which corresponds to the middle-half rule, as noted in Table 3, maximum stress occurs at $y = 0.372d \ne d/2 \ne d/4$.

The foregoing presumes material integrity is available for strains up to at least $\lambda\varepsilon_m$ - i.e. $\lambda\varepsilon_m$ must clearly not exceed fracture strain $\gamma\varepsilon_m$ as suggested in Figs 2, 4, and 5. This condition, $\gamma > \lambda$ or otherwise, is checked in the procedure given in Fig 8. Being a physical parameter, γ varies independently of k so that masonry materials effectively sharing a common k value can readily possess individual values of fracture strain $\gamma\varepsilon_m$. Herein, the $k = 12$ case involves the corresponding mathematical parameter $\lambda = 1.13$ exceeding or violating the physical parameter $\gamma = 1.03$ for the particular material under consideration. In such cases, the theoretical static limit state as set out above is unachievable, and a slightly modified maximisation procedure[16] is required which-simply leads to γ replacing λ in eqns. (10) and (11). Accordingly, two $k = 12$ loci are included in Fig 9, one corresponding to cases wherein $\lambda = 1.13 \le \gamma$, the other to the particular case illustrated in Fig 3 wherein practical fracture restrictions apply to the static limit state with $\gamma = 1.03 \le \lambda$.

TABLE 2 – Limit state parameters

Material specimen	k	λ	γ
Rivelin Mill (ref. Fig 2)	7	1.16	1.23
Hodgkinson & Davies[18] (ref. Fig 3)	12	1.13*	1.03*
Towler & Sawko[13] (ref. Fig 3)	2	1.25	1.34
Calcium silicate (ref. Fig 4)	3	1.227	>2.5

*NOTE. Here, $\gamma < \lambda$ with implications (see text)

TABLE 3 – Key limit state interaction loci data

k	Middle-half rule moment maxima co-ordinates (n,m)	Cracked/uncracked interfacing state co-ordinates (n_i,m_i)
2	0.464, 0.464	0.729, 0.312
3	0.456, 0.456	0.689, 0.336
7	0.436, 0.436	0.618, 0.360
12	0.422, 0.422	0.586, 0.359
12*	0.408, 0.408	0.552, 0.358

*NOTE: Denotes γ-restricted values for $\gamma < \lambda$ as Table 2

Prior to applying the foregoing theory, and Fig 9 in particular, to arch bridge mechanism case-studies, it is now pertinent to consider the theory in the context of experimental evidence.

Brittle hinge experimentation

The experimental system adopted inhouse is illustrated in Fig 10. The test samples consisted of whole calcium silicate class 4 bricks, the pair under combined axial thrust and bending moment action being sandwiched between two further bricks mounted centrally in a servohydraulic, stiff testing machine[17] to minimise end effects. All brick interfaces were initially smoothed, and the topology was carefully set up. All joints were dry under test in order to isolate precisely the masonry material under consideration. Transducers were employed to monitor rotation, and constitutive properties were established from the previously discussed axial compression tests summarised in Table 1.

Three eccentricities corresponding to $n = 0.1$, 0.2 and 0.3 were chosen for investigation – limit state analysis of the Bridgemill[19] test-to-destruction affords $n = 0.2$ – each eccentricity being tested five times. Compressive

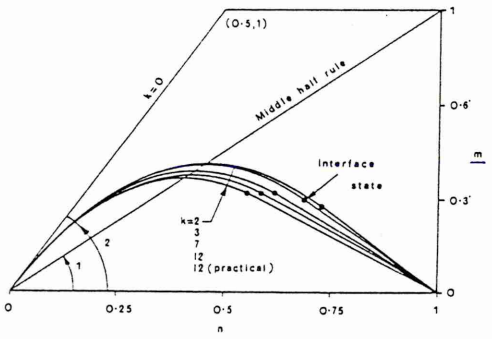

Fig 9. Static limit state interaction diagram

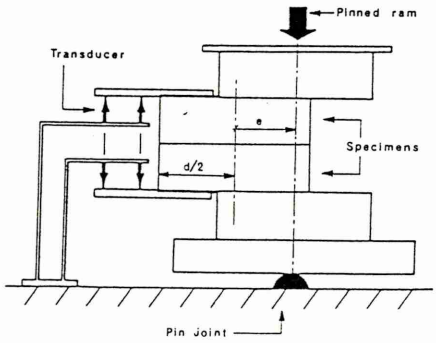

Fig 10. Brittle hinge experimental topology

TABLE 4 – Brittle hinge tests: peak load data

Ecc e (n)	Peak loads (kN) Test no. /1	/2	/3	/4	/5	Mean peak load (kN)	Std dev. (+/–)	Coef. var. (%)	Theo. peak load* (kN)
0.1	84.2	91.9	80.2	89.7	81.5	85.5	5.108	5.97	70
0.2	137.9	140.2	137.2	143.9	161.1[R]	144.1	9.878	6.85	139
0.3	200.1	221.1[R]	214.7	211.8	218.2	213.2	8.112	3.80	209

[R] Indicates replacement test
* Theoretical peak load employs average σ_m from corresponding core and whole brick tests (see Table 1)

displacement action was applied up to the corresponding peak load and continued until virtually no loading remained. It is important to note that visible signs of physical breakdown in the form of cracking and spalling were not observed until action resulted in high compressive strains well beyond the peak load static limit state. Typical high strain plates are shown in Figs 11 and 12, and key data are summarised in Table 4. The theoretical peak load values given in Table 4 employ the average of the mean peak stress data as noted in Table 1 (i.e.σ_m=31.6 N/mm²) in conjunction with eqn. (10) for k=3 and λ=1.227 as stipulated in Table 2; it is considered that overall experimental consistency and good experimental/ theoretical correlation are exhibited. The validity of averaging the mean full brick and core values for σ_m for use with the brittle hinge experimentation lies with the fact that, while full brick constitutive testing effectively corresponds to the use of the same prototype model voussoirs as employed in the brittle hinge studies, the cores, with their smaller cross-section, are more representative of the corresponding voussoir strain gradient topology (recall Figs 6 and 7) encountered therein[20].

A graphical interpretation that enables theoretical/experimental correlation to be put in the context of *both* flexural and compressive actions is to be seen in Fig 13, which superposes experimental data on the appropriate portion of the k=3 interaction diagram (note Fig 9). Good overall experimental/theoretical correlation is again displayed. Fig 13 also includes the corresponding limit state locus based on the basic linear constitutive model illustrated in Fig 5 (k=∞).

The superiority of the proposed non-linear k=3 modelling over the established linear model is clearly shown. Such findings support the development of a masonry arch bridge mechanism model based on the proposed non-zero but finite k brittle hinge formulation, typified by Fig 9, regarding which the following qualitative experimental observations can also be drawn.

The average moment/thrust-rotation loci illustrated in Fig 14 for each of the three eccentricity cases display clearly the primary characteristics of the 'brittle hinge' with rotation relatively slow to develop before resistance peaks but with rapid loss of resistance beyond. These loci are quite distinct from their familiar *ductile* steel counterparts; this is not surprising in view of their lack of a constitutive yield surface in accordance with Fig 5. The key implications with regard to masonry arch bridge mechanism analyses are that deformations are unlikely to be significant until hinge formation is imminent and that any early formed hinge in a four-hinge collapse mechanism such as that illustrated in Fig 1(a) undergoes fluctuations in resistance while awaiting development of the fourth, mechanism-completing hinge. Fig 14 is not to suggest, however, that eccentricity would remain constant in this process. Load/deformation path history is not essential to a four-hinge mechanism limit state model; the primary requirement is that, for any particular case-study, the proposed mechanism must be statically admissible.

Fig 11. Experimental hinge at high strain

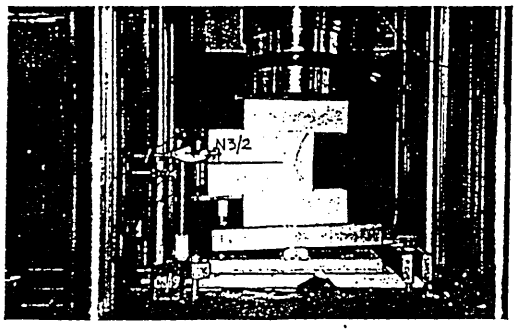

Arch bridge case-studies

With two hinges dedicated to the springings and the fill restricted to a role of (quarter-point) live load dispersal and arch ring precompression, preliminary four-hinge mechanism case-studies have been implemented on the basis of Fig 9 and in the manner illustrated in Fig 1(a). Results are summarised in Table 5 and typified in Fig 15. The data appertaining to the spandrel-less Bridgemill scale-model experiments carried out at Edinburgh University[3] are particularly gratifying; noting the above planar mathematical restrictions, this case-study represents precisely the structural form with which the brittle hinge mechanism model is presently concerned. Importantly, the brittle hinge's superiority over the infinite compression model (k=0) is shown clearly in Fig 15. Arch bridge strength due to passive/active fill resistance and spandrel presence, contributing to both longitudinal and lateral strength components[3], serves to induce a larger (though not excessively so) degree of conservatism with respect to the

Fig 12. End view of localised crushing

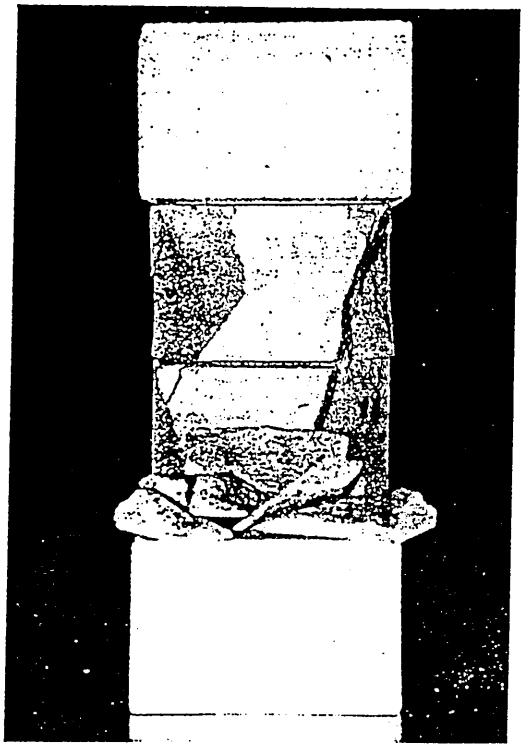

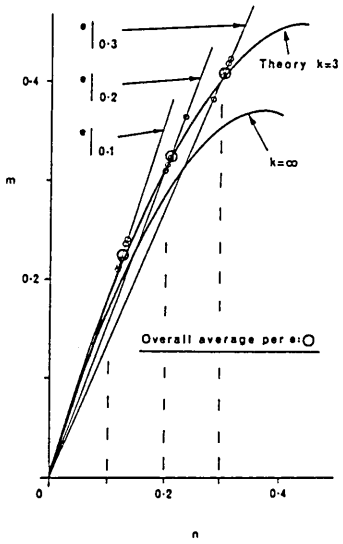

Fig 13. Experimental interaction data

corresponding full-scale prototype characteristics[19] as anticipated. Noting Table 5 further, the proposed model suggests the two full-scale prototypes to be subjected to mechanistic hinges suffering axial compressions in the range $0.12 \leq n \leq 0.19$ (the former figure relating to Shinafoot[21], unloaded side springing, the latter to both[19,21] loaded side springing). Hinge axial compression values for the Edinburgh model test analyses are approximately 40 % corresponding Bridgemill prototype values, indicating an effect of scale[3].

Serviceability considerations

While limit state masonry arch bridge mechanism studies have received purposeful attention over recent years[2-6], the vexed question of serviceability requirements remains largely unanswered[2, 4, 16]. Kinematic, as opposed to static, considerations can be developed in conjunction with the foregoing with a view to tackling this matter.

A non-linear-k-based prevention of cracking formulation equivalent to the linear-based middle-third rule[9, 16] is readily available by substituting $d'=d$ in eqns. (6) and (7) such that, by normalising as previously,

$$n_{nc} = P/P_s\Big|_{d'=d} \quad \text{and} \quad m_{mc} = M/M_s\Big|_{d'=d} \qquad 0 \leq n_{nc} \leq n_t \qquad \ldots.(12)$$

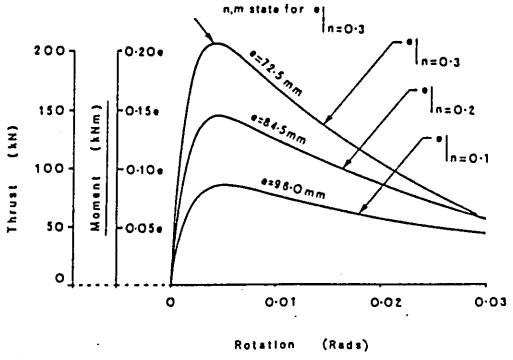

Fig 14. Moment/thrust-rotation curve

TABLE 5 – Arch bridge case-studies (k=2)

Structure case-study	σ_m' (N/mm²)	Experimental collapse load (kN, 1m strip)	Brittle hinge collapse load (kN, 1m strip)	% difference*
Mean of three Bridgemill models[3]	5	4.94	4.75	- 3.8
Bridgemill prototype[19]	6	373.5	334.0	-10.6
Shinafoot[21]	3	359.0	315.2	-12.2

* Brittle hinge theory is conservative throughout

resulting in the n, m prevention of cracking interaction loci for k=2, 3, 7 and 12 illustrated in Fig 16. Each curve is initially tangential to the linear-based middle-third rule and terminates at the respective cracked/uncracked interface state (n_t, m_t).

For $n_t \leq n_{nc} \leq 1$, the respective k prevention of cracking envelope is simply completed by eqn. (11). That the non-linear equivalent k-based envelopes are superior to their linear ($k=\infty$) is clearly shown – but there is a minor problem. If masonry arch bridge systems[19] involve axial compressions in the vicinity of $n=0.25$, say, the k-based loci are actually more restrictive than the middle-third rule. This factor is, however, relatively small in effect, as can be seen from Fig 16, and eqn. (13) provides a basis, it is contended, for developing a *systematic* ruling on serviceability.

Finally, it needs to be stated that the loci corresponding to eqn. (12) theoretically continue beyond the interface states shown in Fig 16. Each locus decays rapidly 'below' the respective uncracked static limit state locus, with each terminating at an unshown intersection (e.g. 0.75, 0.25 for k=2) with a corresponding kinematic *physical breakdown* limit state locus[16]. This latter locus can be derived for any $0 < k < \infty$, $0 \leq n \leq 1$, from eqns. (3), (4), (6) and (7) with, typically[16], λ replaced by γ in eqns. (10) and (11). These kinematic physical breakdown limit state loci typified by the $k=12$ (practical) locus in Fig 9 lie wholly within their static equivalents' envelopes and represent the states to which the static limit states degenerate as collapse, preceded by local crushing, finally occurs.

Discussion

That a masonry arch bridge modelling based on infinite compressive strength is incongruous is indisputable[3,11]. Herein postulated is a consistent non-zero but finite k brittle hinge theory which henceforth prohibits the *need* for this assumption (wherein $k=0$) which can be seen to be non-conservative from Figs 9 and 15. While further work is required before claims can be made that a masonry arch bridge assessment package suited to industrial practice is now available, a number of key observations regarding future such 'packaging' can be discerned.

The constitutive relationship of eqn. (1) is considered to offer a generalised interpretation of structural masonry's stress–strain characteristics and the ensuing limit state interaction diagram illustrated in Fig 9 is initially proposed as a k/λ–based design chart given the findings of the experimental

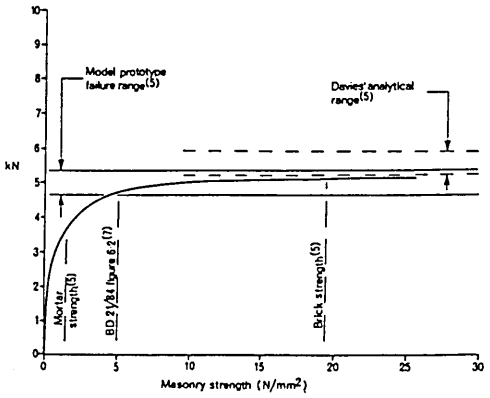

Fig 15. Bridgemill scale model case-study

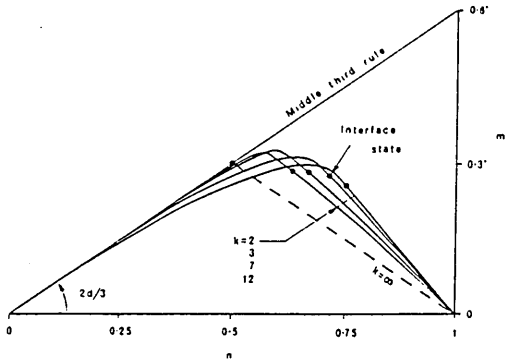

Fig 16. Prevention of cracking interaction diagram

programme as interpreted in Table 4 and Fig 13. The restricted data scatter available when dealing with synthetic masonry is similarly displayed in Tables 1 and 2, together with Fig 4 regarding material values for σ_m, ε_m and k. Dry hinge testing was employed in order that the modelling provided by eqn. (1) could be *uniquely* assessed for any specified material in the context of combined axial force and bending moment. As noted in Table 4, replacement hinge tests were required on two occasions owing to problems of surface grit and specimen component alignment; dry testing is clearly sensitive to these matters. In the absence of an internationally recognised standard for compression testing, it is perhaps worth noting that the extent of the falling branch in masonry constitutive tests, as typified by Figs 2-5, is highly dependent on the testing machine's stiffness or effective loading *and unloading* rates[17].

The results of the preliminary arch bridge case-studies summarised in Table 5 and Fig 15 lend further and distinct confidence to the proposed theory. It should be noted that $k=2$ was employed throughout the case studies in the absence of more definitive constitutive data[5, 19, 21]. However, the collapse loads concerned proved quite insensitive to variations in k for $2 \leq k \leq 12$, suggesting the crucial matter is to employ non-linear constitutive functions, i.e. $k \neq 0, \infty$, with the limit state accessible falling branch characteristics denoted in Fig 5. Inspection of Fig 9 regarding the $0 < n \leq 0.2$ range (which, as noted previously, approximates to arch bridge limit state values of vault compression) shows the convergence of the various $2 \leq k \leq 12$ loci, which underlies the insensitivity of arch bridge collapse loads to the *specific* finite value of k within non-zero but finite k brittle hinge models. The collapse loads are also relatively insensitive to the actual value of σ_m employed: regarding Fig 15, for example, a 500% increase in σ_m[7] results in a < 10% increase in collapse load[1].

The limit state arch bridge model requires the presence of a statically admissible four-hinge mechanism. Fig 14 serves to display appropriate brittle hinge force-rotation characteristics which imply changes will occur in the limit state bending moment/axial compression ratio appertaining to a mechanism hinge following its initial formation. Given the claim that there is a considerable *delay* between the formation of the first and last three hinges comprising an arch collapse mechanism[3], this could be a pertinent feature. Indeed, this feature provides support for the changing nature and, in view of the discrete voussoir construction involved, location of brittle hinges discussed elsewhere[2, 4].

Full-scale arch bridge tests-to-destruction are considered to exhibit a lesser degree of local crushing than that displayed in Figs 11 and 12; refs. 19 and 21 serve to typify this factor, although it should be appreciated that, where the most developed or first formed hinge occurs under the familiar quarter-point loading, the state of the appropriate portion of the extrados would not readily permit close visual inspection. Further, and as noted previously, Figs 11 and 12 illustrate brittle hinge behaviour at strains far in excess of those pertaining to the static limit state and primarily serve to demonstrate physical response through exaggeration. At the static limit states tested inhouse, there was little visible sign of rotation and no sign of physical breakdown. Because of its strain-softening characteristics[22], inclusion of a mortar bed would serve to reduce local crushing effects, however, and future developments of the proposed brittle hinge mechanics will need to consider the attendant complexities of composite behaviour in the context of more vault-like aspect ratios.

Notwithstanding the above, the present model's results for the spandrel-less Edinburgh small-scale bridge tests[5] remain highly acceptable, as shown in Table 5 and Fig 15. Although the Edinburgh testing programme, involving quality construction, suggests that the restraint of lateral straining by means of the spandrel and wing walls substantially enhances arch bridge strength, this enhancement could be disputed in practice, as many of these ancient structures exhibit poor highway geometry resulting in frequent parapet wall damage through impact. Further, spandrel walls are sometimes of poor or even dry stone construction and can become detached from the barrel, allowing the latter to flex independently. Similar concern could be expressed regarding the inclusion of passive and active fill pressure effects within the mathematical model, given the general lack of as-built detailed drawings. The anticipated conservatism associated with spandrel-less theoretical models when applied to full-scale masonry arch bridge prototypes is clearly evident from Table 5. Perhaps this degree of conservatism is acceptable for bridges constructed from natural stone which inherently possesses a relatively high degree of material variability.

Should the construction of new arch bridges, employing reliably testable synthetic masonry components, be undertaken with a view to providing the minimal maintenance bridging structures so long sought by public authorities, full 3-dimensional analysis would perhaps possess more appeal. Presently, however, it is considered that the incorporation of the foregoing brittle hinge expressions (i.e. eqns. (10) and (11) noting eqns. (3), (4), (6) and (7)) within a mechanism analysis should serve to improve modelling capabilities for safe load assessment schemes. Fig 9 is intended to serve as a design chart to this end[20]. Unlike its ductile steel counterparts, the limit state interaction diagram of Fig 9 is not necessarily everywhere convex. The normality theorem[23] with its attendant plastic behaviour is not an issue here with, for $k=\infty$ and 2 at least, the uncracked static limit state locus taking a linear, m, n path[10]. It should finally be noted that masonry arch bridges can alternatively collapse because of either material failure or snap buckling[1]. A load path-history model is being developed to deal with the former configuration, employing an incremental modulus $E_t = \partial\sigma/\partial\varepsilon = (\sigma_m/\varepsilon_m)(k/[k-1])(1-[\varepsilon/\varepsilon_m]^{k-1})$ from eqn. (1). Load-deformation characteristics, including serviceability considerations, are unlikely to prove as insensitive to variations in non-zero but finite values of k (or E_t[24]) as limit state strengths.

Serviceability remains a major issue in the appraisal of masonry arch bridges. However, the proposed non-linear prevention of cracking criterion supports the suggestion made elsewhere that a linear constitutive model is valid for serviceability states despite the acceptance that a non-linear constitutive modelling is more definitive[1], with Fig 16 illustrating this point to advantage regarding low values of n. Furthermore, and unlike with infinite compressive stiffness/strength modelling, the proposed brittle hinge inherently requires *finite* values for peak stress σ_m and corresponding strain ε_m, and finite σ_m, ε_m values are considered to be important parameters regarding *full-scale* prototype behaviour[3]. It has even been suggested that three-hinge topologies form immediately on decentring[2] with possible inservice redistribution of loading ensuing[4]. The earlier noted lack of obvious signs of physical distress until hinges have developed beyond their peak load states suggests that these propositions cannot be refuted on the basis of visual site inspection. Indeed, it could thereby be argued on aesthetic grounds that the presence of such hinges would not be detrimental to serviceability considerations.

Conclusions

The behaviour of rectangular masonry sections under singly-eccentric compressive loading has been considered in both theoretical and experimental terms. Static limit state combinations of axial force and bending moment have been established from a consistent non-linear constitutive basis. Both experimental hinge testing on definitive masonry material and preliminary masonry arch bridge mechanism case-studies suggest the proposed brittle hinge model possesses distinct advantages over the familiar, but more restrictive, linearised constitutive approach and the less conservative infinite compressive strength modelling widely employed in engineering practice. It is considered that the key improvement in modelling so produced is due to the incorporation of non-linear constitutive properties in the presence of a falling branch. By including material deformation effects that lead to local crushing at high strains, the masonry hinge *per se*, a central feature of masonry arch bridge mechanism studies, has been fundamentally reassessed, and a variety of further potential developments have been identified.

Acknowledgement

The authors are grateful to Sheffield City Council Engineers for the provision of supporting field data.

Appendix A

Explicit expressions for

Eqn. (2)

$$\sigma/\sigma_m = \{[(\varepsilon_1+\varepsilon_2)/2 + y(\varepsilon_1-\varepsilon_2)/d]/[(k-1)\varepsilon_m]\} \{k - ([(\varepsilon_1+\varepsilon_2)/2 + y(\varepsilon_1-\varepsilon_2)/d]/\varepsilon_m)^{k-1}\} \quad \text{....(A.2)}$$

Eqn. (3)

$$P = \int_{-d/2}^{d/2} \sigma b\,dy = \sigma_m bd\{k[\varepsilon_1+\varepsilon_2]/2 + [\varepsilon_2^{k+1} - \varepsilon_1^{k+1}]/[(k+1)(\varepsilon_1-\varepsilon_2)\varepsilon_m^{k-1}]\}/\{[k-1)\varepsilon_m\} \quad \text{....(A.3)}$$

Eqn. (4)

$$M = \int_{-d/2}^{d/2} \sigma b y\,dy = \sigma_m bd^2\{k[\varepsilon_1-\varepsilon_2]/12 - [\varepsilon_1^{k+1} + \varepsilon_2^{k+1}]/[2(k+1)(\varepsilon_1-\varepsilon_2)\varepsilon_m^{k-1}] + [\varepsilon_1^{k+2} - \varepsilon_2^{k+2}]/[(k+1)(k+2)(\varepsilon_1-\varepsilon_2)^2\varepsilon_m^{k-1}]\}/\{[k-1]\varepsilon_m\} \quad \text{....(A.4)}$$

Eqn. (5)

$$\sigma/\sigma_m = \{\varepsilon_1[1 + y/d' - d/(2d')]/[(k-1)\varepsilon_m]\}\{k - [1 + y/d' - d/(2d')]^{k-1}\varepsilon_1^{k-1}/\varepsilon_m^{k-1}\} \quad \text{....(A.5)}$$

Eqn. (6)

$$P = \int_{d/2-d'}^{d/2} \sigma b\,dy - \sigma_m b\varepsilon_1 d'[k/2 - (\varepsilon_1/\varepsilon_m)^{k-1}/(k+1)]/[(k-1)\varepsilon_m] \quad \text{....(A.6)}$$

Eqn. (7)

$$M = \int_{d/2-d'}^{d/2} \sigma b y\,dy = \sigma_m b\varepsilon_1 d'\{k[3d - 2d']/6 - [d - 2d']/(k+2)]/[(k+1)\varepsilon_m^{k-1}]\}/\{2[k-1]\varepsilon_m^{k-1}\} \quad \text{....(A.7)}$$

References

1. Department of Transport: 'The assessment of highway bridges and structures', *Bridge Census and Sample Survey*, DTp, 1987
2. Smith, F. W., Harvey, W. J., and Vardy, A. E.: 'Three-hinge analysis of masonry arches', *The Structural Engineer*, **68**, No. 11, June 1990, pp203-213
3. Harvey, W. J.: 'Stability, strength, elasticity and thrustlines in masonry structures', *The Structural Engineer*, **69**, No. 9, May 1991, pp181-184
4. Smith, F. W., Harvey, W. J., and Vardy, A. E.: 'Three-hinge analysis of masonry arches', correspondence, *The Structural Engineer*, **69**, No. 1, January 1991, pp9-10
5. Royles, R., Hendry, A. W.: 'Model tests on masonry arches', *Proc. ICE*, Part 2, **91**, 1991, pp299-321
6. Bridle, R. J., Hughes, T. G.: 'An energy method for arch bridge analysis', *Proc. ICE*, Part 2, **89**, 1990, pp375-385
7. Department of Transport: 'The assessment of highway bridges and structures', *Departmental Standard BD21/84*, 1984
8. Department of Transport: 'The assessment of highway bridges and structures', *Advice Note BA16/84*, 1984
9. Heyman, J.: *The masonry arch*, Chichester, Ellis Horwood, 1981
10. Taylor, N.: 'Moment-thrust limit state properties of masonry', *Masonry International*, **5**, No. 2, 1991, pp55-58
11. Harvey, W. J.: 'The application of the mechanism analysis to arch bridges', *The Structural Engineer*, **66**, No. 5, March 1988, pp77-84
12. Crisfield, M.: 'Finite element mechanism methods for the analysis of masonry and brickwork arches', TRRL, *Research Report 19*, DTp, 1986
13. Towler, K., Sawko, F.: 'Limit state behaviour of brickwork arches', *Proc. 6th Int. Conf. on Brick Masonry*, Rome, 1982, pp412-42
14. Powell, B., Hodgkinson, W. R.: 'Determination of the stress-strain relationship for brickwork', *TN249*, Stoke-on-Trent, British Ceramic Research Association, 1976
15. Sawko, F., Rouf, M. A.: 'On the stiffness properties of masonry', *Proc. ICE*, Part 2, **77**, March 1984, pp1-12
16. Taylor, N., Mallinder, P. A.: 'On the limit state properties of masonry', *Proc. ICE*, Part 2, **83**, March 1987, pp33-41
17. Hudson, J. A., Crouch, S. L., and Fairhurst, C.: 'Soft, stiff and servocontrolled testing machines: a review with reference to rock failure', *Engineering Geology*, **6**, 1972, pp155-189
18. Hodgkinson, H. R., Davies, S.: 'The stress–strain relationships of brickwork when stressed in directions other than normal to the bed face', *Proc. 6th Int. Conf. on Brick Masonry*, Rome, 1982, pp290-299
19. Hendry, A. W., Davies, S. R., and Royles, R.: 'Test on stone masonry arch at Bridgemill – Girvan', DTp, TRRL, Crowthorne, *Cont. Rept. 7*, 1985
20. Edgell, G. J.: 'Stress-strain relationships for brickwork – their application in the theory of unreinforced slender members', *TN319*, Stoke-on-Trent, British Ceramic Research Association, 1981
21. Page, J.: 'Load tests to collapse on two arch bridges at Torksey and Shinafoot', DTp, TRRL, Crowthorne, *Res. Rept. 159*, 1988
22. Loo, Y. C., Yang, Y.: 'Cracking and failure analysis of masonry arch bridges', *Jnl. Struc. Eng.*, ASCE, **117**, No. 6, June 1991, pp1641-1659
23. Taylor, N.: 'Combined axial force and bending moment on a Tee-section beam – an illustration of the normality rule in plasticity', *IJMEE*, **14**, No. 2, 1986, pp141-150
24. Choo, B. S. *et al:* 'Finite element analysis of masonry arch bridges using tapered elements', *Proc. ICE*, Part 2, **91**, December 1991, pp755-770

Bridge Assessment Management and Design
B.I.G. Barr, H.R. Evans, J.E. Harding (Editors)
1994 Elsevier Science B.V.

Static and kinematic limit states of masonry vaults

N. Taylor[a], R. Draper[b], S. Broadhurst[b] and P. A. Mallinder[c]

[a]Reader, School of Construction, Sheffield Hallam University (SHU), UK.

[b]Research Students, Centre for Engineering Research, SHU, UK.

[c]Acting Principal Engineer, Design and Building Services, Sheffield City Council, UK.

1. SYNOPSIS

An ongoing programme of research at Sheffield Hallam University is directed towards understanding the limit state behaviour of masonry arch vault mechanisms; non-linear mathematical modelling of masonry hinge behaviour has been supported by laboratory testing and field observation. It is postulated that masonry hinges are brittle in nature with rotation only becoming significant as hinge resistance decays. Significantly, theory predicts definitive and distinct static and kinematic limit states.

Herein, key limit state developments to-date are summarised in the context of the recent full-scale multi-span arch load test at Beighton, Sheffield, at which the static/kinematic separation was noticeably evident. In conjunction with recent developments in Information Technology (IT), task dedicated computer vision algorithms are used to speculate on the likely mode of failure at Beighton.

2. NOTATION

k	material response factor
P	arch thrust
ε	compressive strain
ε_m	compressive strain accompanying σ_m
σ	compressive stress
σ_m	maximum compressive stress

3. INTRODUCTION

Constituting a considerable proportion of the United Kingdom's bridge stock[1], ageing masonry arch structures continue to attract considerable engineering attention[2-10], particularly with regard to scientifically-based safe-load assessment[11,12]. The formation of arch barrel mechanistic hinges, as typified in Fig 1(a), is

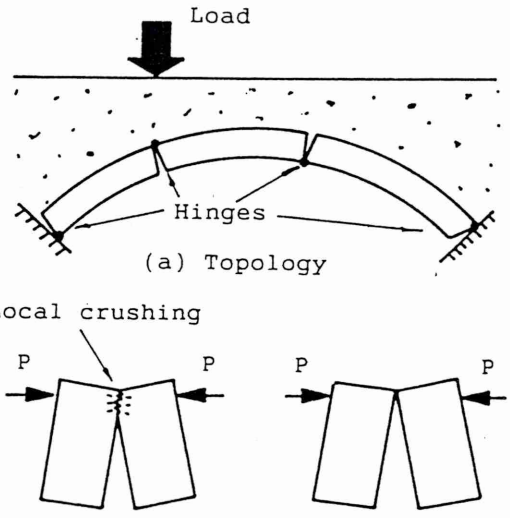

(b) Proposed hinge model (c) Existing hinge model

Fig 1. Four hinge masonry arch collapse mechanism

central to any limit state procedure, and engineers often base strength judgements on the mechanistic capacity of the arch barrel alone[2], the fill serving primarily as an arch-compressing and a live load dispersal medium. Present concern lies with the nature of hinge formation in voussoir arches in the presence of local compressive crushing as indicated in Fig 1(b), with P denoting arch thrust: this requires *a priori* establishment of the respective constitutive properties. Alternative mechanistic modelling assumes validity of the infinite compressive strength rule[11] which implies the mechanism illustrated in Fig 1(c).

Under stroke-controlled loading, physical collapse onsets with the kinematic limit state. Collapse provides effects quantifiable by modern computer vision facilities[13] and preliminary computer vision studies consider the collapse of BR Bridge No. 124 at Beighton.

4. CONSTITUTIVE MODELLING

Fig 2 illustrates an idealised complete stress-strain locus for masonry based upon empirical data[2-4]. Generally, the locus takes the form

$$\sigma/\sigma_m=(\varepsilon/\varepsilon_m)(1+k-[\varepsilon/\varepsilon_m]^k)/k \quad 0<k<\infty \qquad (1)$$

where σ and ε represent general compressive stress and strain respectively, subscript m denoting their maxima, and k is a material response factor. *Exceptional* cases include the basic linear

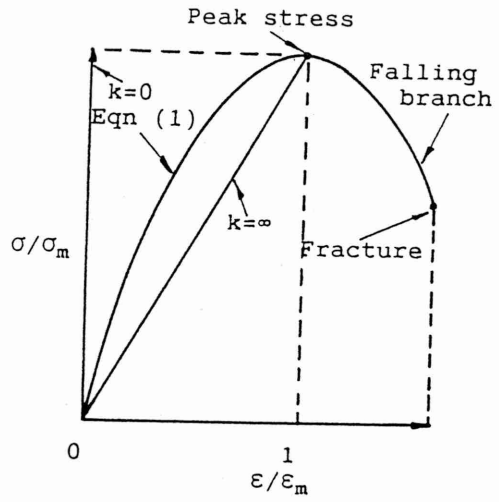

Fig 2. Idealised Constitutive Locus

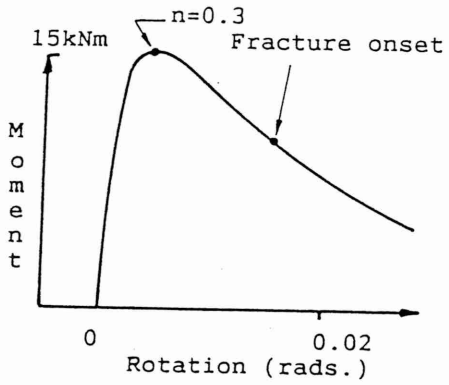

Fig 3. Experimental Moment-Rotation (n=0.3)

model (k=∞), whilst k=0 corresponds to the infinite stiffness/strength rule underpinning Heyman's established "plastic" hinge model[11]; a yield surface is actually suggested by k=-1.

5. BRITTLE HINGE CHARACTERISTICS

General bending moment and axial compression expresssions corresponding to both uncracked and cracked rectangular masonry sections under the action of singly-eccentric compression, typical of arch vault behaviour, are available elsewhere[2-4]. Computational manipulation of these expressions leads to distinct static and kinematic limit state relationships being obtained such that, for example, with k=2, the associated cracked section topologies generate maximum compressive strains of $1.25\varepsilon_m$ and $1.5\varepsilon_m$ respectively[3]. Significantly, the maximum strains associated with both static and kinematic limit states occupy locations within the falling branch of Fig 2. It is considered that the actual value of the collapse load of masonry vaults employing k-modelling is relatively insensitive to the actual value of k so long as it is *non-zero but finite*[4].

Supportive experimentation has included the eccentric loading of pairs of class 4 calcium silicate bricks. Figure 3 shows the typical considerable separation between the static and kinematic limit states with the former occurring at approximately 200kN of eccentric compression (M≃15kNm) whilst the latter occurs, following this, at approximately 120kN (M≃9kNm) under fixed eccentricity conditions. Notably, visible signs of rotation and cracking are unavailable prior to the static limit state.

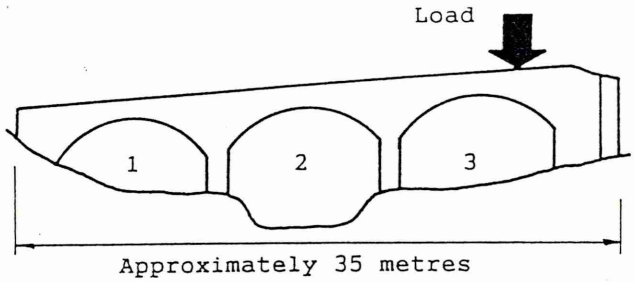

Fig 4. BR Bridge No. 124 schema

Static and kinematic limit states are, as predicted, quite distinct.

6. COMPUTER VISION APPLICATION TO BR BRIDGE No. 124

The recent full-scale multi-span bridge test at Beighton, Sheffield was video recorded. The bridge (see Fig 4) was subject to stroke-controlled loading applied in the proximity of the right support which, significantly, was free standing given the removal of the formerly adjacent main girder structure. The maximum load recorded was of the order of 320 tonnes whilst physical breakdown occurred much later, after jack re-setting, at a lower load.

Vision is a sensory system; there is a huge physiological and psychological literature describing biological vision systems. Computer vision[13] employs digital data to represent images and can provide, unlike its biological counterpart, quantitative descriptions of the perceived world or image.

As part of ongoing, in-house, multi-disciplinary, research activities[14], the bridge test recording was subject to preliminary computer analysis employing SUN IPC hardware and the TINA programming environment. Individual video frames were "grabbed" and digitised, and three hard copies are illustrated in Fig 5. Frame (a) relates to the datum state, (b) to a state just prior to collapse whilst (c) relates to collapse *per se*. Pixel coordinates were derived for locations on both springings as shown in (a) and (b); limited calibration was available by comparing pixel data for (a) with bridge geometry available from drawings. The respective approximate movements of the springings are given in Fig 5. Whilst that for the left springing is considered within current vision system tolerance, that for the right-hand support suggests significant horizontal translation. Accordingly, it is suggested that this translation of the free standing support downgraded any tendency for multi-span collapse, reducing rotational movement requirements, and thereby limit (static) strength, at the left springing with regard to mechanism failure of the loaded span.

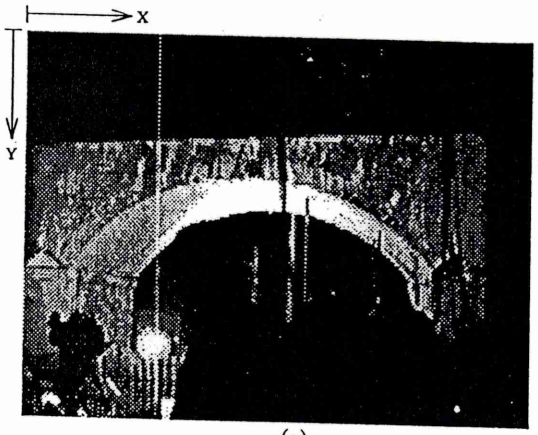

(a)

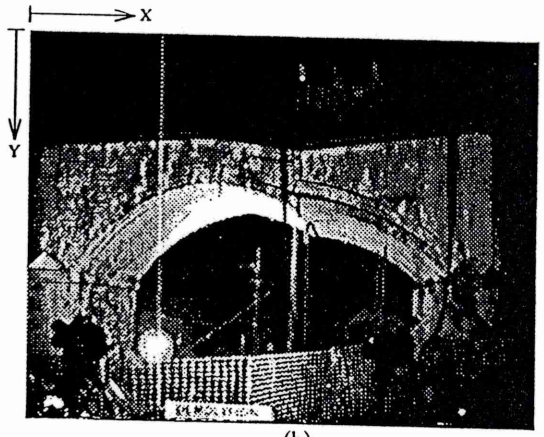

(b)

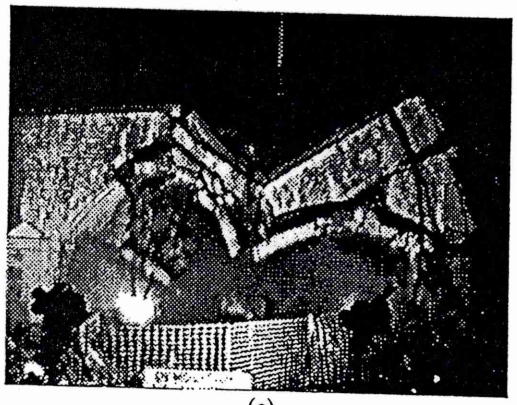

(c)

Table 1. Pixel Data	X	Y
(a) LH Springing	162	353
RH Springing	713	342
(b) LH Springing	162	355
RH Springing	731	351

Horizontal Translation Of RH Springing = 731 - 713 = 18 Pixels, Of Order 150mm.

Figure 5. Digitised Images Of Bridge No 124 Under Test

7. CONCLUSIONS

Static and kinematic limit states are quite distinct in masonry vaults subject to stroke-controlled loading. This distinction demands falling branch constitutive behaviour. Computer vision offers considerable scope for the monitoring of masonry vaults under test given that the brittle, sudden nature of collapse, which onsets with the kinematic limit state, lends itself to continuous video recording and thereby the provision of digital data. The current study involves an initial attempt to utilise computer vision techniques in this field and further efforts are to involve more thorough calibration and edge detection techniques in order to improve digital data accuracy.

8. ACKNOWLEDGEMENTS

TINA is kindly made available through the good offices of the AIVRU at Sheffield University.

REFERENCES

1. Department of Transport: "The assessment of highway bridges and structures", Bridge Census and Sample Survey, DTp, 1987.
2. Taylor, N., Mallinder, P. A.: "On the limit state properties of masonry", Proc, ICE, Part 2, 83, March 1987, pp33-41.
3. Taylor, N.: "Moment-thrust limit state properties of masonry", Masonry International, 5, No. 2, 1991, pp55-58.
4. Taylor, N., Mallinder, P. A.: "The brittle hinge in masonry arch mechanisms", The Structural Engineer, 71, No. 20, October 1993, pp359-366.
5. Smith, F. W., Harvey, W. J., and Vardey, A. E.: "Three-hinge analysis of masonry arches", The Structural Engineer, 68, No, 11, June 1990, pp203-213.
6. Harvey, W. J.: Stability, strength, elasticity and thrustlines in masonry structures", The Structural Engineer, 68, No. 9, May 1991, pp181-184.
7. Royles, R., Hendry, A. W.: "Model tests on masonry arches", Proc. ICE, Part 2, 91, 1991, pp299-321.
8. Bridle, R. J., Hughes, T. G.: "An energy method for arch bridge analysis". Proc. ICE, Part 2, 89, 1990, pp375-385.
9. Department of Transport: "The assessment of highway bridges and structures", Departmental Standard BD21/93, 1993.
10. Department of Transport: ""The assessment of highway bridges and structures", Advice Note BA16/93, 1993.
11. Heyman, J.: "The masonry arch", Chichester, Ellis Horwood, 1981.
12. Harvey, W. J.: "The application of the mechanism analysis to arch bridges", The Structural engineer, 66, No. 5, March 1988, pp77-84.
13. Ballard, D. H. et al: "Computer Vision", Prentice-Hall Inc., 1982.
14. Broadhurst, S. J., Pridmore, T. P., and Taylor, N.: "Sensing for feature identification in sewers", Proc. XI Int. Symp. on Automation and Robotics in Construction (ISARC), Brighton UK, Ed. D. A. Chamberlain, Elsevier, 1994, pp675-682.

NOMENCLATURE

b	breadth of section
d	depth of section
d'	effective depth of cracked section
e	eccentricity
E_i	incremental modulus
m	non-dimensional bending moment parameter, $m=M_m/M_s$
m_i	cracked/uncracked interface limit state coordinate
m_{nc}	prevention of cracking normalised moment
M	bending moment
M_m	limit state bending moment
M_s	maximum limit state bending moment
M_t	tensile component of bending moment
n	non-dimensional axial compression parameter, $n=P_m/P_s$
n_i	cracked/uncracked interface limit state coordinate
n_{nc}	prevention of cracking normalised thrust
P	axial compression
P_m	limit state axial compression
P_s	squash load
y	sectional spatial coordinate
y_m	distance from centroid to σ_m
zz	flexural axis
ε	compressive strain
ε_m	compressive strain accompanying maximum compressive stress
ε_{om}	centroidal strain at limit state
ε_1	top fibre strain
ε_2	bottom fibre strain
v_m	curvature at limit state
σ	compressive stress
σ_m	maximum compressive stress
σ_1	top fibre stress
σ_2	bottom fibre stress
k	stress-strain locus shape constant
γ	fracture strain coefficient
λ	static limit state hinge strain coefficient

REFERENCES

1. Das P. C., *The design of unreinforced arch bridges*, Proceedings of the Centenary Year Bridge Conference, Elsevier, Cardiff, 1994.

2. Rocke R. S. and Bridle R. J., *The INCA arch bridge system*, Proceedings of the Centenary Year Bridge Conference, Elsevier, Cardiff, 1994.

3. Melbourne C. and Irvine B., *Mass concrete arches*, Proceedings of the Centenary Year Bridge Conference, Elsevier, Cardiff, 1994.

4. Ferguson H., *Bridge checks to be huge and costly*, New Civil Engineer, Thomas Telford, 23rd June 1983.

5. Harvey, W. J., *Arches stand the test of time*, New Scientist, 15th May 1986.

6. *Dales bridge collapses with frostbite*, New Civil Engineer, Thomas Telford, 28th February, 1985.

7. *A chance for old bridges*, New Civil Engineer Editorial, Thomas Telford, 19th April 1984.

8. Chatterjee S., *Assessment of old bridges*, Highways and Transportation, February 1985.

9. Page J., *Load tests to collapse on masonry arch bridges*, Proceedings of The First International Conference on Arch Bridges, Thomas Telford, Bolton, 1995.

10. Heyman J., *The safety of masonry arches*, International Journal of Mechanical Science, 11, 363, 1969.

11. Heyman J., *The estimation of the strength of masonry arches*, Proceedings of The Institution of Civil Engineers, Part 2, December 1980, pp921-937.

12. Heyman J., *The Masonry Arch*, Ellis Horwood, 1984.

13. Page J., *Mechanism computer programmes for the prediction of masonry arch bridge collapse loads*, Department of Transport, April 1986.

14. Crisfield M. A., *A finite element computer programme for the analysis of masonry arches*, Transport and Road Research Laboratory, Laboratory Report LR 1115, 1984.

15. Mann P. and Gunn M., *Computer modelling of the construction and load testing of a masonry arch bridge*, Proceedings of The First International Conference on Arch Bridges, Thomas Telford, Bolton, 1995.

16. Bridle R. J. and Hughes T. G., *An energy method for arch bridge analysis*, Proceedings of The Institution of Civil Engineers, 1990.

17. Chandler C. M., *The analysis of skew arches using shell theory*, Proceedings of The First International Conference on Arch Bridges, Thomas Telford, Bolton, 1995.

18. Choo B. S. and Gong N. G., *Effect of skew on the strength of masonry arch*

bridges, Proceedings of The First International Conference on Arch Bridges, Thomas Telford, Bolton, 1995.

19. *The assessment of highway bridges and structures*, Departmental Standard BD21/93, Department of Transport, 1993.

20. *The assessment of highway bridges and structures*, Departmental Standard BA21/93, Department of Transport, 1993.

21. Melbourne C., *Analysis of multi-ring brickwork arch bridges*, Proceedings of The First International Conference on Arch Bridges, Thomas Telford, Bolton, 1995.

22. Barlow W. H., *On the presence (practically) of the line of equal thrust in arches and the mode of determining it by geometrical construction*, Proceedings of The Institution of Civil Engineers, Volume 5, 1846, p162.

23. Castigliano C. A. P., *Theorie de l'equilibre des systemes elastiques et ses applications*, Augusto Frederico Negro, Turin, 1879.

24. Shaw G., Southcombe C., Easterbrook D. and Gill G., *Design, buildability and monitoring of the first end-built pre-stressed masonry flat arch box girder footbridges*, Proceedings of the Centenary Year Bridge Conference, Elsevier, Cardiff, 1994.

25. Mair, *A new design standard for unreinforced arch bridges*, Highways Agency (to be published).

26. Pippard A. J. S. et al, *The mechanics of the voussoir arch*, Journal of The Institution of Civil Engineers, 1936.

27. *The road vehicles (construction and use) regulations 1986*, HMSO, 1986.

28. Curtin, Shaw, Beck and Bray, *Structural masonry designers' manual*, Granada, 1982.

29. *Code of practice for the use of masonry*, BS 5628 Parts 1 to 3, British Standards Institution.

30. Mallinder P. A., *The non-linear analysis of masonry arches*, M.Phil. thesis, Sheffield City Polytechnic, 1988.

31. Harvey W. J., Smith F. W. and Wang, X., *Arch fill interaction in masonry bridges - an experimental study*, Proceedings of the Centenary Year Bridge Conference, Elsevier, Cardiff, 1994.

32. Harvey W. J., Vardy A. E., Craig R. F. and Smith F. W., *Load tests on a full scale arch model four metre span masonry arch bridge*, TRL Contractor Report 155, 1989.

33. Towler K. and Sawko F., *Limit state behaviour of brickwork arches*, Proceedings of The 6th International Brick Masonry Conference, Rome, 1982.

34. Towler K., *Structural behaviour of brickwork arches*, PhD thesis, University of Liverpool, 1982.

35. Fuller G., *Curve of equilibrium for a rigid arch under vertical forces*, Proceedings of The Institution of Civil Engineers, 1875.

36. Jennings A., *Use and misuse of Fuller's construction for the analysis of masonry arches*, The Structural Engineer, November 1985, pp352-355.

37. Page J., *Repair and strengthening of masonry arch highway bridges - a user guide*, County Surveyors' Society, 1996.

38. Hodgkinson H. R. and Powell B., *The determination of the stress strain relationship for brickwork*, Proceedings of The 6th International Brick Masonry Conference, Brugge, April 1976.

39. *Specification for calcium silicate (sandlime and flintlime) bricks*, BS 187:1978.

40. Jaeger and Cook, *Fundamentals of rock mechanics*, Macmillan, 1969.

41. Hudson, Crouch and Fairhurst, *Soft, stiff and servo controlled testing machines: a review with reference to rock failure*, Engineering Geology, 1972.

42. Sawko F. and Rouf M. A., *On the stiffness properties of masonry*, Proceedings of The Institution of Civil Engineers, March 1984.

43. Taylor N. W., Mallinder P. A. and Davies B. L., Discussion on technical note 381, Proceedings of The Institution of Civil Engineers, December 1984.

44. Taylor N. W. and Mallinder P. A., *The brittle hinge in masonry arch mechanisms*, The Structural Engineer, Volume 71, October 1993.

45. *Structural use of concrete*, BS 8110:Part 2:1985, HMSO, Figure 2.1.

46. Hodgkinson H. R. and Davies S., *The stress-strain relationships of brickwork when stressed in directions other than normal to the bed face*, Proceedings of The 6th International Conference on Brick Masonry, Rome, 1982.

47. Hendry A. W., Davies S. R. and Royles R., *Test on stone masonry arch at Bridgemill - Girvan*, Department of Transport, 1985.

48. Page J., *Load tests to collapse on two arch bridges at Preston, Shropshire and Prestwood, Staffordshire*, TRRL Research Report 110, Department of Transport, 1987.

49. Page J., *Load tests to collapse on two arch bridges at Torksey and Shinafoot*, TRRL Research Report 159, Department of Transport, 1988.

50. Harvey W. J., Vardy A. E., Craig R. F. and Smith F. W., *Load tests on a full scale model four metre span masonry arch bridge*, Transport and Road Research Laboratory Contractor Report 155, Department of Transport, 1989.

51. Sawko F. and Towler K., *Structural behaviour of brickwork arches*, Proceedings of The 7th International Loadbearing brickwork Conference, November 1981.

52. Royles R. and Hendry A. W., *Model tests on masonry arches*, Proceeding of The Institution of Civil Engineers, 1991.

53. Ballard D. H. et al, *Computer Vision*, Prentice-Hall Inc., New Jersey, 1982.

54. Canny J., *A computational approach to edge detection*, IEEE Transactions on Pattern Analysis and Machine Intelligence, 1986.